

Mechanical Modeling of Natural and Anthropogenic Fluid-Rock Interactions: Volcano  
Deformation and Induced Seismicity

by

Guang Zhai

A Dissertation Presented in Partial Fulfillment  
of the Requirements for the Degree  
Doctor of Philosophy

Approved July 2018 by the  
Graduate Supervisory Committee:

Manoochehr Shirzaei, Chair  
Edward Garnero  
Amanda Clarke  
James Tyburczy  
Mingming Li

ARIZONA STATE UNIVERSITY

December 2018

## ABSTRACT

The dynamic Earth involves feedbacks between the solid crust and both natural and anthropogenic fluid flows. Fluid-rock interactions drive many Earth phenomena, including volcanic unrest, seismic activities, and hydrological responses. Mitigating the hazards associated with these activities requires fundamental understanding of the underlying physical processes. Therefore, geophysical monitoring in combination with modeling provides valuable tools, suitable for hazard mitigation and risk management efforts. Magmatic activities and induced seismicity linked to fluid injection are two natural and anthropogenic processes discussed in this dissertation.

Successful forecasting of the timing, style, and intensity of a volcanic eruption is made possible by improved understanding of the volcano life cycle as well as building quantitative models incorporating the processes that govern rock melting, melt ascending, magma storage, eruption initiation, and interaction between magma and surrounding host rocks at different spatial extent and time scale. One key part of such models is the shallow magma chamber, which is generally directly linked to volcano's eruptive behaviors. However, its actual shape, size, and temporal evolution are often not entirely known. To address this issue, I use space-based geodetic data with high spatiotemporal resolution to measure surface deformation at Kilauea volcano. The obtained maps of InSAR (Interferometric Synthetic Aperture Radar) deformation time series are exploited with two novel modeling schemes to investigate Kilauea's shallow magmatic system. Both models can explain the same observation, leading to a new compartment model of magma chamber. Such models significantly advance the understanding of the physical processes associated with Kilauea's summit plumbing system with potential applications for volcanoes around the world.

The unprecedented increase in the number of earthquakes in the Central and Eastern United States since 2008 is attributed to massive deep subsurface injection of saltwater. The elevated chance of moderate-large damaging earthquakes stemming from increased seismicity rate causes broad societal concerns among industry, regulators, and the public. Thus, quantifying the time-dependent seismic hazard associated with the fluid injection is of great importance. To this end, I investigate the large-scale seismic, hydrogeologic, and injection data in northern Texas for period of 2007-2015 and in northern-central Oklahoma for period of 1995-2017. An effective induced earthquake forecasting model is developed, considering a complex relationship between injection operations and consequent seismicity. I find that the timing and magnitude of regional induced earthquakes are fully controlled by the process of fluid diffusion in a poroelastic medium and thus can be successfully forecasted. The obtained time-dependent seismic hazard model is spatiotemporally heterogeneous and decreasing injection rates does not immediately reduce the probability of an earthquake. The presented framework can be used for operational induced earthquake forecasting. Information about the associated fundamental processes, inducing conditions, and probabilistic seismic hazards has broad benefits to the society.

To my mother, my uncle and aunt, and my wife for their enduring love and support.

献给我的母亲骆桂芬女士，我的舅舅骆哲先生舅妈陈涛女士，以及我的妻子宋宁忆女士，感谢他们长久以来的爱与支持。



## ACKNOWLEDGMENTS

First of all, I deeply and sincerely appreciate my supervisor, Prof. Manoochehr Shirzaei, for his invaluable guidance, support, and encouragement. This dissertation is made possible because he has always believed in me and continuously supported me over the years. I feel very honored to have the opportunity to work with and learn from him, who has been extremely open to and always ready for what I want to discuss. He guided and encouraged me to touch different topics (volcano and earthquake), and he was never out of reach whenever I came into difficulties in my research.

I would like to give my great thanks to my current dissertation committee members Dr. Edward Garnero, Dr. Amanda Clarke, Dr. James Tyburczy, and Dr. Mingming Li as well as previous exam/dissertation committee members Dr. Allen McNamara and Dr. Stanley Williams for their insightful discussions and constructive suggestions along with my path toward completing this dissertation. The diverse lectures they provided in the past years are extremely helpful with my research that not only significantly broaden my scope but also teach me critical thinking.

My graduate study in RaT Lab (Remote Sensing & Tectonic Geodesy Lab) has been a very pleasant journey. I had a great time and office #745 was a great place over the years because of so many wonderful officemates, Dr. Megan Miller, Dr. Jennifer Weston, Mostafa Khoshmanesh, Zac Yung-Chun Liu, Dr. Chandrakanta Ojha, Grace Carlson, and Sonam Sherpa. I also want to give my thanks to Prof. Susanna Werth.

Special thanks go to Mingming Li when I came to ASU in 2013 when he was a senior PhD student. He helped me a lot in my everyday life especially during the stressful first two years. I still remember the time when he picked me up from the airport and hosted me the

first week before I moved to a new apartment. Also, great thanks to Xinming Chen who always drives me everywhere, without which my life would be tough.

There are many other people that I would like to acknowledge, staffs and faculties from SESE and across the University, friends in my everyday life, and far beyond.

Finally, I want to thank all my families for their endless loves, supports, encouragements, and patience, without which I would never make it and complete this dissertation. I also give my deep thanks to my beloved wife who always supports and believes in me. My heartfelt gratitude is extended to my uncle and aunt who are so unselfish to support me both financially and spiritually.

## TABLE OF CONTENTS

	Page
LIST OF TABLES .....	x
LIST OF FIGURES .....	xi
CHAPTER	
1 INTRODUCTION.....	1
Part I Volcano Deformation	
2 SPATIOTEMPORAL MODEL OF KĪLAUEA'S SUMMIT MAGMATIC SYSTEM INFERRED FROM INSAR TIME SERIES AND GEOMETRY-FREE TIME- DEPENDENT SOURCE INVERSION .....	12
2.1 Abstract .....	12
2.2 Introduction.....	13
2.3 Methods.....	18
2.3.1 Multitrack Wavelet-Based InSAR .....	18
2.3.2 Time-Dependent Geometry-Free Source Modeling .....	19
2.3.3 Principal Component Analysis .....	24
2.4 Surface Deformation Data.....	25
2.4.1 GPS Data.....	25
2.4.2 InSAR Deformation Time Series.....	26
2.5 Model Results .....	29
2.6 Discussion .....	39
2.6.1 Distributed PCD Inversion.....	39
2.6.2 Model Implications for Magma Storage .....	40
2.6.3 Model Implications for Magma Supply and Transport .....	42

CHAPTER	Page
2.6.4 Other Implications.....	47
2.7 Conclusions.....	50
3 3-D MODELING OF IRREGULAR VOLCANIC SOURCES USING SPARSITY- PROMOTING INVERSIONS OF GEODETIC DATA AND BOUNDARY ELEMENT METHOD .....	51
3.1 Abstract .....	51
3.2 Introduction.....	52
3.3 Method.....	56
3.3.1 Distributed PCDs as Volcanic Deformation Source .....	56
3.3.2 Magmatic Deformation Source Modeling .....	61
3.4 Algorithm Learning and Synthetic Test.....	70
3.5 Application to Kilauea Volcano.....	74
3.5.1 Data Sets.....	76
3.5.2 Inversion Parameter Setup.....	77
3.5.3 Model Result .....	79
3.6 Discussion .....	82
3.6.1 Advances and Limitations of Two-Step Modeling.....	83
3.6.2 Implications for Volcanic Source Volume Change.....	84
3.6.3 Implications for Reservoir Storage Change.....	87
3.6.4 Implications for Evolution of Kilauea Magma Chamber.....	89
3.7 Conclusion .....	91

## Part II Induced Seismicity

CHAPTER	Page
4 FLUID INJECTION AND TIME-DEPENDENT SEISMIC HAZARD IN THE BARNETT SHALE, TEXAS.....	94
4.1 Abstract .....	94
4.2 Introduction.....	95
4.3 Seismic and Injection Data Sets.....	97
4.4 Method.....	99
4.5 Hydrogeological Background and Model Setup.....	102
4.6 Result .....	103
4.7 Discussion and Summary.....	108
5 PHYSICS-BASED INDUCED EARTHQUAKE FORECASTING IN OKLAHOMA.....	112
5.1 Abstract .....	112
5.2 Introduction.....	112
5.3 Data.....	114
5.3.1 Well Injections .....	114
5.3.2 Seismicity .....	116
5.4 Method.....	116
5.4.1 Declustering the Seismic Catalog.....	116
5.4.2 Poroelastic Modeling .....	117
5.4.3 Seismicity Rate Modeling .....	120
5.5 Result and Discussion .....	122
5.6 Conclusion .....	128
6 SUMMARIES AND CONCLUSIONS.....	129

	Page
REFERENCES.....	132
APPENDIX	
A SUPPLEMENTARY INFORMATION FOR CHAPTER 2.....	150
B SUPPLEMENTARY INFORMATION FOR CHAPTER 3.....	165
C SUPPLEMENTARY INFORMATION FOR CHAPTER 4.....	174
D SUPPLEMENTARY INFORMATION FOR CHAPTER 5.....	200
E APPENDIX REFERENCES.....	218

## LIST OF TABLES

Table	Page
2.1 Summary of the cluster analysis results .....	38
C.1 Parameters for modeling of coulomb stress, seismicity rate and probability.....	191
C.2 List of injection wells.....	192
C.3 Earthquake catalog from ComCat.....	194
C.4 Earthquake catalog from publication.....	198

## LIST OF FIGURES

Figure	Page
2.1. Map view of Kilauea’s summit and rift zones .....	14
2.2. InSAR surface LOS deformation .....	26
2.3. LOS displacement for nine episodes .....	28
2.4. Three-dimensional checkerboard test.....	31
2.5. Inverted 3-D distribution of volume change rate .....	33
2.6. Episodic plane view of zones of major volume change rate.....	35
2.7. PCA results of the time-dependent source model.....	37
2.8. Time series of magma storage rate for PCA clusters .....	42
2.9. Schematics showing magma storage and transport .....	44
2.10. Time series of LOS displacement at summit and ERZ .....	45
2.11. Relation between summit volume change and ERZ normal stress .....	48
2.12. Modeled coulomb stress change distribution.....	49
3.1. Schematics of simple inflationary and deflationary volcanic systems .....	54
3.2. Benchmark tests for oblate and prolate spheroid sources.....	60
3.3. Comparison of different regularization schemes .....	63
3.4. Workflow chart for implementing sparsity-promoting inversion .....	72
3.5. Algorithm learning using synthetic tests.....	73
3.6. Synthetic test considering data noise .....	74
3.7. InSAR LOS velocity map and time series at Kilauea summit.....	77
3.8. Calibration test using spherical source .....	78
3.9. Sparse volume change models of uplift and subsidence periods .....	80
3.10. Tensile slip models using BEM for inflation and deflation periods .....	81



Figure	Page
3.11. Schematic of source volume change as enclosed tensile crack.....	84
4.1. The Barnett Shale injection and seismic date .....	98
4.2. Snapshots of the distribution of the modeled cumulative pore pressure, poroelastic stress, total coulomb stress, and seismicity rate.....	104
4.3. Time series of spatially average parameters in Figure 4.2.....	105
4.4. Annual earthquake magnitude exceedance probability in Barnett.....	107
5.1. Fluid injection and seismicity in Oklahoma.....	115
5.2. Time series of coulomb stressing rate and seismicity rate.....	123
5.3. Observed and predicted M3+ earthquakes.....	125
5.4. Annual earthquake magnitude exceedance probability in Oklahoma.....	127
A.1 InSAR LOS displacement after correcting decollement slip.....	153
A.2 Variance-covariance analysis of inverted volume change.....	154
A.3 Standard deviation of inverted volume change using bootstrapping.....	155
A.4 Data fitting of LOS time series at summit and SWRZ .....	156
A.5 Model misfit RMS of all time steps.....	157
A.6 Observed LOS displacement distribution.....	158
A.7 Modeled LOS displacement distribution .....	159
A.8 Model misfit of residual distribution.....	160
A.9 Integrated volume change in three directions .....	161
A.10 Correlation analysis of all PCA clusters.....	162
A.11 Same as Figure A.9 but with lower PCD resolution.....	163
A.12 Schematic of implementing 3-D Laplacian smoothing.....	164
B.1 Data fitting of synthetic tests without considering data noise.....	167

Figure	Page
B.2 Data fitting of synthetic tests considering data noise .....	168
B.3 Simulated descending LOS deformation for calibration.....	169
B.4 Data fit for the sparsity-promoting inversion for the uplift period.....	170
B.5 Data fit for the sparsity-promoting inversion for the subsidence period.....	171
B.6 Data fit for the BEM modeling for the uplift period .....	172
B.7 Data fit for the BEM modeling for the subsidence period.....	173
C.1 Time series of total annual injection volume versus earthquake count .....	177
C.2 Poroelastic model setup .....	178
C.3 Yearly snapshots of modeled parameters.....	179
C.4 Yearly snapshots of relative earthquake probability .....	180
C.5 Same as Figure C.3 using different hydraulic diffusivity of $0.7 \text{ m}^2/\text{s}$ .....	181
C.6 Annual exceedance probabilities for hydraulic diffusivity of $0.7 \text{ m}^2/\text{s}$ .....	182
C.7 Production well locations at Azle .....	183
C.8 Yearly snapshots of total CFS due to fluid production at Azle .....	184
C.9 Yearly snapshots of total CFS due to both injection and production at Azle .....	185
C.10 Yearly snapshots of seismicity rate due to both injection and production at Azle .....	186
C.11 Time series of modeled parameters due to both injection and production at Azle.....	187
C.12 Annual earthquake magnitude exceedance probabilities due to both injection and production at Azle.....	188
C.13 Cumulative number of earthquakes .....	189
C.14 Sensitivity test for frictional parameter and background stressing rate .....	190
D.1 Monthly injection volume and histogram of observed seismicity in Oklahoma .....	203
D.2 Spatial locations of seismicity before and after declustering.....	204

Figure	Page
D.3 Histograms of M3+ events before and after declustering .....	205
D.4 Subsurface stratigraphic information in Oklahoma .....	206
D.5 Basement depth and injection well depth.....	207
D.6 The fitted surface of basement interface .....	208
D.7 Well bottom to basement relative distance.....	209
D.8 Profile of layered poroelastic model.....	210
D.9 Mechanical parameters of each layer.....	211
D.10 Snapshots of poroelastic modeling result and seismicity rate in CO.....	212
D.11 Snapshots of poroelastic modeling result and seismicity rate in WO .....	213
D.12 Comparison of relative seismicity rates using different fault geometries.....	214
D.13 Background seismicity prior to 2008 in Oklahoma.....	215
D.14 Gutenberg-Richter relationship for CO.....	216
D.15 Cumulative background earthquake number for CO and WO.....	217

## CHAPTER 1

### INTRODUCTION

#### 1.1 Overview

Earth is a dynamic system with mutual interaction between solid and liquid materials [Hefferan and O'Brien, 2010]. The interaction between shallow fluids (both natural and man-made) and rocks changes the stress state in the brittle lithosphere. Driven by this mechanical interaction, many Earth phenomena are widely observed, including volcanic unrest, seismic activities, and hydrological responses [Dzurisin, 2007; Manga and Wang, 2015]. The hazards associated with these activities generally evolves over different spatial and temporal scales, requiring better understanding of the associated physical processes to improve forecasting capacity. Geophysical observations combined with numerical modeling can provide insights into the fundamentals of the dynamics associated with the fluid-rock interaction processes. In this dissertation, I focus on volcanic and seismic processes involving natural and anthropogenic fluid interactions with the solid crust, respectively. The presented work here enhances the understanding of physical processes of both volcanic plumbing system and induced seismicity with broad goals of helping to reduce the associated risks.

##### 1.1.1 Volcano Deformation

Volcanoes are one of the most important components of the Earth system. They act to deliver materials in the Earth's interior to the surface and continue to recycle earth materials [Francis and Oppenheimer, 2004]. This process is partially manifested as volcanic eruptions. Worldwide, millions of people live in volcanically active areas and are exposed to great dangers and economic losses.

Volcanoes are linked to the thermal processes in the deep earth and thus their formation and location are controlled by plate tectonics and mantle dynamics [*Francis and Oppenheimer*, 2004; *Parfitt and Wilson*, 2008]. Various eruption styles and volcano structures reflect the complex internal physiochemical processes that govern magma generation, transport, storage, and eruption. The general working mechanism of a volcano is as follows: magmatic melt is generated in the mantle and moves upward due to buoyance. This rising magma can ascend to surface directly or is stored in a shallow crust forming magma chamber. The shallow magma chamber is the source feeding distinct surface eruptions. Thus, understanding how volcanos form and erupt is dependent on the understanding of how magma is generated, stored, transported, accumulated, and erupted.

Successful forecasting of the timing, style, and intensity of an eruption is made possible by improved understanding of the volcano life cycle as well as building quantitative models incorporating the processes that govern rock melting, melt ascending, magma storage, eruption initiation, and interaction between magma and surrounding host rocks at different scales of time and space. One key part of such model is the shallow magma chamber which is generally directly linked to eruption behaviors at Earth's surface [*Francis and Oppenheimer*, 2004; *Parfitt and Wilson*, 2008]. A magma chamber is formed due to repeated magma intrusions and emplacements and expressed as a connected network of magma bodies [*Fiske and Kinoshita*, 1969]. The chamber shape evolves gradually through internal physical and chemical reactions and interactions with crust rocks [*Gudmundsson*, 1990]. Although the shape of a shallow magma chamber cannot be highly irregular based on thermal and mechanical stability considerations [*Gudmundsson*, 1990], its actual shape, size, and temporal evolution are not entirely known [*Marsh*, 2015].

Magmatic processes associated with shallow magma chambers are generally studied indirectly through seismic and geodetic imaging [Dzurisin, 2007; Lees, 2007]. Seismic imaging uses seismic tomography to estimate the anomalies of physical properties of crustal rocks to infer magma distribution. However, such method used for shallow magmatic system is limited because of low spatial resolution which stems from low seismic ray coverage. In addition, this method cannot be used to constrain the pressure condition of a magma chamber. In contrast, geodetic measurement of surface deformation with high spatial resolution can provide crucial information on the geometrical and physical parameters of magma chamber and the associated magmatic processes.

Due to inaccessibility of the magmatic units at depth, mathematic models provide the link between surface deformation and source at subsurface [Dzurisin, 2007]. These models belong to a wide class of inhomogeneous inclusion problems in elasticity [Davis and Selvadurai, 1996; Mura, 2013]. In general, these models assume that the magma inside the chamber is entirely molten (behaving like fluid) with uniform excess pressure. The volume change in the magma chamber causing the change in excess pressure elastically deforms the crust and results in deformation at the Earth's surface. Despite the significant improvement in the monitoring capacity of geodetic techniques at various spatiotemporal scales, the models and methods to interpret these observations remain very simple. Following the first application of a Mogi-type source to interpret surface deformation at Kilauea, many other analytical models with predefined source geometries have been proposed to explain spatial and temporal observations of surface deformation at volcanos. They often fail to explain the fine details of observed surface deformation as a result of their over simplification of chamber geometries.

In the first part of this dissertation, I focus on the well-studied Kilauea volcano. I explore a large set of SAR images to map the evolution of surface deformation during the time period from 2003 to 2011 at Kilauea. Two different modeling and inversion methods are proposed to investigate the magmatic source responsible for surface deformation: (1) a time-dependent, geometry-free kinematic chamber model and (2) a mechanical irregularly-shaped chamber model. The results significantly improve the understanding of Kilauea's shallow magmatic system with potential extended application to volcanoes around the world. The advanced magma chamber model is helpful for building forecasting models to mitigate volcanic hazards.

#### 1.1.2 Induced Seismicity

The interaction between fluid and faults has been widely documented in historical observations for thousands of years [*Manga and Wang, 2015*]. Specifically, earthquakes can change ground water levels, streamflow and spring discharges, as well as causing rapid well level fluctuations. These records show that earthquakes can modify the hydrological systems. However, fluid can also perturb the fault system leading to the generation of earthquakes since fluid can mechanically modify the stress condition in the crust where most earthquakes occur [*Hubbert and Rubey, 1959*].

Many fluid-related anthropogenic activities can induce earthquakes, including fluid injection, fluid extraction, and water impoundment. The first documented fluid induced earthquake dates back to 1920 due to subsurface water withdrawal [*Pratt and Johnson, 1926*]. The significant advancements in the understanding of fluid induced earthquakes arose from two case studies of fluid injection and earthquakes in Colorado in the 1960s. The first was the Denver earthquakes triggered by water disposal at the Rocky Mountain Arsenal in 1962

[*Healy et al.*, 1968] and the second was the earthquake control experiment in the Rangely oil field, Colorado in 1969 [*Raleigh et al.*, 1976]. These early studies suggested a causal link between fluid injection and earthquake triggering, supported by the strong temporal correlation between seismicity frequency and injection amount.

The understanding of how seismicity is induced by injection requires integrating fluid processes into the framework of earthquake physics [*Segall and Lu*, 2015]. The basic mechanism of induced seismicity is the reduction of frictional strength on pre-existing faults due to fluid injection. Fluid is injected into the targeted subsurface formations and then diffuses away, which can mechanically alter the stress condition in the medium or on the faults. These changes include the direct pore pressure and poroelastic stress changes due to fluid diffusion, stress changes from induced seismic or aseismic slips, stress change due to thermoelastic response caused by temperature difference of injected fluid and host rocks, and change of frictional properties due to increased pore pressure and geochemical alteration of fracture surfaces.

Although the mechanism of induced seismicity is well known, discrimination of them from natural earthquakes is still a great challenge [*Ellsworth*, 2013]. A statistical approach for induced seismicity based on temporal and spatial correlation between injection and seismicity may fail under certain circumstances, such as the region defined for analysis being not large enough. A seismological method for distinguishing induced seismicity is not currently available because no evidence shows that induced earthquakes are inherently different from natural earthquakes. As the pattern of induced seismicity is directly controlled by subsurface mechanical changes [*Segall and Lu*, 2015], one promising way is to study precursory signals of such changes, such as geodetic observation of deformation (e.g., InSAR [*Shirzaei et al.*, 2016]). However, observations show that such precursory signals do not routinely exist,



making it difficult for further application. Hydrogeological models, resulting in the quantitative evaluation of subsurface mechanical changes, provide the most reliable approach to determine the likelihood of fluid injection induced seismicity (e.g., [Keranen *et al.*, 2014]), although in some cases it is complicated by the poor constraints on local hydrogeology, the background stress field, and the initial pore pressure [Ellsworth, 2013].

Most studies addressing the correlation between injection and seismicity quantify the pore pressure change in the subsurface using uncoupled groundwater flow equations [Hornbach *et al.*, 2015; Keranen *et al.*, 2014]. Recent studies consider coupling between pore pressure and matrix deformation to investigate the relationship between injection and earthquakes since poroelastic stress can also contribute to the triggering of earthquakes [Segall and Lu, 2015]. The theory of poroelasticity is widely used for this purpose, accounting for the coupling between deformation of the porous medium and evolution of the pore fluid pressure [Cheng, 2016]. This means a change of pore pressure can deform rocks and vice versa.

The unprecedented increase in the number of earthquakes in the Central and Eastern United States since 2008 is attributed to massive deep subsurface injection of saltwater [Ellsworth, 2013; Frohlich, 2012; Keranen *et al.*, 2014; Weingarten *et al.*, 2015], which is mostly coproduced from unconventional oil and gas production. Many of those events show spatiotemporal correlation with high-volume injection operation based on statistical analysis [Frohlich, 2012; Horton, 2012; Kim, 2013; Rubinstein *et al.*, 2014]. The elevated chance of moderate-large damaging earthquakes stemming from increased seismicity rate, as observed in Oklahoma, Texas, Colorado, Kansas, and Arkansas, causes broad societal concerns among industry, regulators, and the public [Ellsworth, 2013], creating the need to understand the associated seismic hazard due to fluid injection.

In the second part of this dissertation, I focus on Texas and Oklahoma that experienced intensive deep waste fluid injections and seismicity increases. I investigate the large-scale seismic, hydrogeologic, and injection data spanning period 2007-2015 for northern Texas and 1995-2017 for northern-central Oklahoma. I develop an effective induced earthquake forecasting model, considering a complex relationship between injection operations and consequent seismicity. This model incorporates the underlying physics of the process governing fluid diffusion in a poroelastic medium and earthquake nucleation. The results significantly advance the understanding of the time-dependent seismic hazard associated with waste fluid injection. This time-dependent hazard model can be used for operational induced-earthquake forecasting.

## 1.2 Dissertation Objectives and Contributions

In this dissertation, I investigate two different sets of fluid-related geo-problems. The first one is geophysical application of geodetic data (InSAR) to image active magmatic systems. The current models for magmatic deformation source remain highly simplistic, incapable for complex source geometries. I developed two different modeling schemes to invert surface deformation to study complex magmatic sources. The focus is Kilauea volcano with a summit shallow magmatic system which remains elusive. The second one is investigating the waste fluid injection and its link to recent surges of seismicity in the central and eastern United States. I devise an induced earthquake forecasting method to investigate the time-dependent induced seismic hazard and focus on induced seismicity in Texas and Oklahoma. More specifically, I summarize the dissertation contributions as following.

Part one:

(1) I use advanced multitemporal InSAR technique to illuminate surface deformation at high spatial and temporal resolutions.

(2) I develop a kinematic volcanic source modeling scheme using geometry-free, time-dependent source inversion and linear Kalman filtering.

(3) I develop a physics-based volcanic source modeling using sparsity-promoting inversion and boundary element method.

(4) I apply the modeling methods to Kilauea volcano and propose a new magma chamber model.

Part two:

(5) I propose an induced earthquake forecasting model considering the physics of fluid diffusion and earthquake nucleation.

(6) I use a poroelastic model to simulate the evolution of pore pressure and poroelastic stresses as well as coulomb stress change in the medium.

(7) I use a seismicity rate model and probabilistic earthquake model to estimate time-dependent seismic hazards.

(8) I apply the method to Texas and Oklahoma and provide time-dependent earthquake probabilities in both areas.

### 1.3 Dissertation Roadmap

The first part of this dissertation contains Chapters 2 and 3 and the second part of this dissertation contains Chapters 4 and 5. Each of these chapters is written based on an independent manuscript that has been either published in or submitted to a scientific journal.

Chapter 2 proposes a time-dependent, geometry-free kinematic modeling scheme, which implements a static geometry-free inversion and a linear Kalman filtering. This method is applied to Kilauea volcano to image the summit shallow magmatic reservoir using high spatiotemporal InSAR time series. Then principal component analysis is used to decompose the obtained 4-D source model. This chapter has been published as *Zhai and Shirzaei* [2016] in *Journal of Geophysical Research*.

Chapter 3 devises a mechanical 3-D modeling method of irregular volcanic sources, which employs a sparsity-promoting inversion and a boundary element method. This approach is applied to two periods of rapid deformation of uplift and subsidence at Kilauea. This chapter has been published as *Zhai and Shirzaei* [2017] in *Journal of Geophysical Research*.

Chapter 4 focuses on the time-dependent seismic hazard in the Texas using a newly proposed physics-based induced earthquake forecasting model, which incorporates the physics of the processes governing fluid diffusion in poroelastic medium and earthquake nucleation. This chapter has been published as *Zhai and Shirzaei* [2018] in *Geophysical Research Letter*.

Chapter 5 focuses on induced seismicity in Oklahoma where the issue of injection induced earthquakes is far more severe. The physics-based method is applied to large-scale injection, seismic, and hydrogeological data. This chapter has been submitted to *Science Advances*.

Chapter 6 provides a summary of this dissertation.

## Part I

# Volcano Deformation

## CHAPTER 2

# SPATIOTEMPORAL MODEL OF KĪLAUEA'S SUMMIT MAGMATIC SYSTEM INFERRED FROM INSAR TIME SERIES AND GEOMETRY-FREE TIME- DEPENDENT SOURCE INVERSION

The work presented in this chapter has been published as: Zhai, G., and Shirzaei, M. (2016), Spatiotemporal model of Kīlauea's summit magmatic system inferred from InSAR time series and geometry-free time-dependent source inversion. *Journal of Geophysical Research: Solid Earth* **121**, 5425-5446, doi: 10.1002/2016JB012953.

### 2.1 Abstract

Kīlauea volcano, Hawai‘i Island, has a complex magmatic system including summit reservoirs and rift zones. Kinematic models of the summit reservoir have so far been limited to first-order analytical solutions with predetermined geometry. To explore the complex geometry and kinematics of the summit reservoir, a multitrack wavelet-based InSAR (interferometric synthetic aperture radar) algorithm and a novel geometry-free time-dependent modeling scheme are applied. To map spatiotemporally distributed surface deformation signals over Kīlauea's summit, synthetic aperture radar data sets from two overlapping tracks of the Envisat satellite, including 100 images during the period 2003–2010 are processed. Following validation against Global Positioning System data, the surface deformation time series are inverted to constrain the spatiotemporal evolution of the magmatic system without any prior knowledge of the source geometry. The optimum model is characterized by a spheroidal and a tube-like zone of volume change beneath the summit and the southwest rift zone at 2–3 km depth, respectively. To reduce the model dimension, a

principal component analysis scheme, which allows for the identification of independent reservoirs, is applied. The first three PCs, explaining 99% (63.8%, 28.5%, and 6.6%, respectively) of the model, include six independent reservoirs with a complex interaction suggested by temporal analysis. The data and model presented here, in agreement with earlier studies, improve the understanding of Kīlauea’s plumbing system through enhancing the knowledge of temporally variable magma supply, storage, and transport beneath the summit, and verify the link between summit magmatic activity, seismicity and rift intrusions.

## 2.2 Introduction

Kīlauea volcano, one of the world’s most active volcanoes, is located on Hawai‘i Island (Figure 2.1). Its volcanic system includes a summit caldera and two rift zones—the southwest rift zone (SWRZ) and east rift zone (ERZ)—which are regarded as the boundaries of the northern stable sector of Kīlauea’s edifice and the southern mobile flank, as inferred from modeling of rift zone opening [*Cayol et al.*, 2000; *Lundgren et al.*, 2013]. The southern flank is situated on a subhorizontal fault system or decollement, which is located close to the base of the volcanic edifice at a depth of about 7–11 km [*Borgia et al.*, 2000; *Brooks et al.*, 2008; *Delaney and Denlinger*, 1999; *Denlinger and Okubo*, 1995; *Eaton*, 1962; *Got et al.*, 1994; *Owen et al.*, 1995]. Due to the gravitational instability of the south flank, shallow episodic intrusions, and possible steady magma accumulation in the deep rift zone [*Swanson et al.*, 1976], the whole south flank experiences seaward sliding at an average velocity of 8–10 cm/year [*Owen et al.*, 1995; *Owen et al.*, 2000a; *Poland et al.*, 2014]. Deep long-period seismicity and tremors at a depth of about 30 km beneath Kīlauea’s SWRZ suggest a horizontal melt zone as a deep source feeding Kīlauea volcano [*Gonnermann et al.*, 2012; *Wright and Klein*, 2006]. Magma rising from the deep melt zone through a central conduit is believed to be stored in a shallow



magma reservoir at  $\sim 2\text{--}4$  km depth [Baker and Amelung, 2012; Cervelli and Miklius, 2003; Delaney et al., 1990; Owen et al., 2000a; Yang et al., 1992]. This shallow magma reservoir feeds the ERZ and SWRZ through laterally stretched dikes [Duffield et al., 1982; Lundgren et al., 2013; Montgomery-Brown et al., 2010] and sustains the summit eruption [Carbone and Poland, 2012; Carbone et al., 2013; Johnson et al., 2010]. The temporally variable pressure in the magma reservoir causes changes in the stress field, which is the driving force for active dike intrusions and propagation in the ERZ [Lundgren et al., 2013; Montgomery-Brown et al., 2011; Montgomery-Brown et al., 2010].

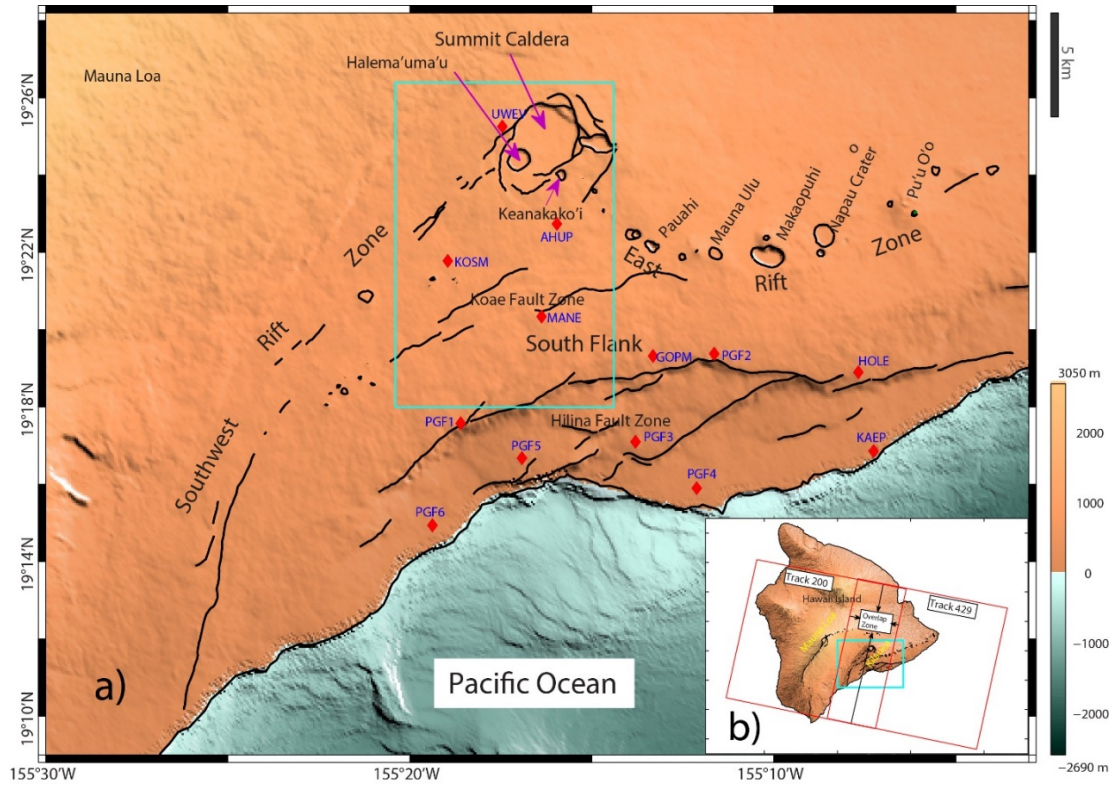


**Figure 2.1.** Map view of Kilauea's summit and rift zones showing major tectonics and volcanic features with topography as background reference. Cyan rectangle defines the horizontal extent of Kilauea's summit used for source modeling in this study. Red diamonds show the locations of GPS stations spanning the time period of InSAR time series and being used for this study. Black lines represent the geological settings (fault traces, craters, calderas, and so on). Inset indicates the relative location of the study area (cyan rectangle) in this paper and the red rectangles represent the frames of two descending SAR tracks (Track 200 and Track 429) explored in this research.

The Pu‘u ‘Ō‘ō–Kupaianaha vents on the ERZ have experienced almost continuous eruptive activities since 1983 and produced nearly half of the lava erupted from Kīlauea in the past 160 years [Heliker and Brantley, 2004]. Subsidence is the predominantly observed deformation pattern at the summit area of Kīlauea, with the exception of three brief inflationary periods associated with vent geometry changes at Pu‘u ‘Ō‘ō during the first 20 years of its eruption history. After late 2003, summit deformation switched from deflation to inflation [Miklius *et al.*, 2005], strongly suggesting a new surge of magma supply into the shallow magma plumbing system [Poland *et al.*, 2012]. Summit inflation culminated in 2007 and was followed by a small fissure eruption in the ERZ, called the Father’s Day event [Poland *et al.*, 2008]. Following this event, the summit deflated until mid-2010.

The south flank of Kīlauea undergoes secular seaward movement, with accompanying quasi-periodic slow slip events on the basal decollement [Brooks *et al.*, 2006; Montgomery-Brown *et al.*, 2009]. On the ERZ, occasional surface deformation occurs due to diking [Cervelli *et al.*, 2002; Montgomery-Brown *et al.*, 2010; Owen *et al.*, 2000b], which is caused by intermittent magmatic activities and long-term seaward movement of Kīlauea’s south flank [Owen *et al.*, 2000a]. The SWRZ has undergone almost continuous subsidence since 1983 with the exception of an inflationary period at the upper part of the SWRZ in 2006 [Myer *et al.*, 2008].

Previous geodetic studies have been focused on the inflation and deflation periods associated with the summit magma reservoir, seaward motion of the south flank, and the ERZ dike intrusions [Baker and Amelung, 2012; Cervelli and Miklius, 2003; Dvorak *et al.*, 1983; Fiske and Kinoshita, 1969; Johnson, 1992; Lockwood *et al.*, 1999; Lundgren *et al.*, 2013; Montgomery-Brown *et al.*, 2010; Owen *et al.*, 1995; Owen *et al.*, 2000b; Poland *et al.*, 2009b; Segall *et al.*, 2006]. The advent of space-based geodetic technologies, such as Interferometric Synthetic Aperture Radar (InSAR) and Global Positioning System (GPS), has significantly enhanced spatial and

temporal resolution of the surface deformation data relevant to the volcanic activity and the associated deformation models used to explain the kinematics of the magmatic systems. To investigate the source geometry and volume change associated with the observed surface deformation data at Kīlauea volcano, various analytical source models have been used [McTigue, 1987; Mogi, 1958; Okada, 1985; Yang *et al.*, 1988]. Cervelli and Miklius [2003] modeled the shallow magma reservoir as a single-point source located no deeper than 3.5 km below the surface, which was constrained by GPS observations. Although this simple model could interpret most of the observed deformation signal, the residual shows another concentrated deformation pattern which is not absorbed in the point source, indicating a more complex magmatic plumbing system underneath the summit. By utilizing InSAR and GPS data, Baker and Amelung [2012] investigated the second-order details of the summit magma chamber, characterized by four separate deformation sources forming an interconnected, top-down, inflation-deflation system. Dike intrusion is another typical active magma process that occasionally happens along the ERZ. The modes of rift intrusion could be passive, due to secular seaward south flank movement or extensional failure of the upper ERZ [Cervelli *et al.*, 2002; Owen *et al.*, 2000b; Shirzaei *et al.*, 2013], or active, marked by increased stress on the ERZ caused by source inflation of Kīlauea's summit [Montgomery-Brown *et al.*, 2010]. To constrain the temporal evolution of the Kīlauea system, including summit magma chamber and rift zones, as well as its coupling with the Mauna Loa system, Shirzaei *et al.* [2013] applied a time-dependent modeling scheme using a combination of the spherical pressurized and rectangular dislocation sources.

Petrological studies also show the geometric complexity of Kīlauea's magmatic plumbing system. Isotopic ratio variation over time for historical lavas erupted at Kīlauea's summit and the coherence between major and trace element whole-rock data indicate a

single spherical magma reservoir beneath Kīlauea’s summit [*Pietruszka and Garvia, 1999a*], with an estimated size of  $\sim 2\text{--}3\text{ km}^3$  [*Pietruszka and Garvia, 1999b*]. However, recent lava chemistry analysis [*Pietruszka et al., 2015*] refined this view of a single magma reservoir. Using Pb isotope ratio analysis, they demonstrated that two magma bodies are beneath the summit, with sizes of  $\sim 0.06\text{--}0.2\text{ km}^3$  and  $\sim 0.1\text{--}0.3\text{ km}^3$  for shallow ( $< 2\text{ km}$ ) and deep ( $2\text{--}4\text{ km}$ ) ones respectively.

Earlier works on the Kīlauea system allow only for constraints to the first-order geometry, strength, interaction, and temporal evolution of the magmatic systems. Therefore, more advanced models of the Kīlauea system need to be provided that can resolve complex magmatic source geometries and their spatiotemporal evolution and interactions. Availability of large sets of space-based surface deformation data at unprecedented spatiotemporal resolution allows for the investigation of the signal associated with subtle magmatic activities at various spatial and temporal scales. Here synthetic aperture radar (SAR) data sets acquired in two overlapping tracks of the Envisat satellite during the period from January 2003 to October 2010 are explored. In order to investigate the source of the summit deformation field, a geometry-free time-dependent inversion, which allows resolving complex magmatic volume changes as well as their spatiotemporal evolutions, is used. In conjunction with seismic and gas data sets, the obtained time-dependent model of volume change distribution is used to investigate the temporally variable relationship between the shallow and deep reservoirs and their connection to the rift zone via stress transferring.

This article is structured as follows: section 2.3 details the methods used in this research, including InSAR time series generation, the time-dependent geometry-free modeling scheme, and principal component analysis (PCA). The data sets and validation are presented in section 2.4, which are followed by modeling results in section 2.5. Applying this

novel time dependent model in the real context of Kīlauea volcano for further discussion is shown in section 2.6. In the last section 2.7, the conclusions inferred from this research will be given.

## 2.3 Methods

To identify the active magmatic reservoirs and their spatiotemporal evolution beneath Kīlauea’s summit, following approach is applied: (1) The multitrack wavelet-based InSAR algorithm is used to generate high spatiotemporal resolution maps of the surface deformation, (2) a time-dependent, geometry-free inversion algorithm is used to investigate the 4-D source of the observed multitemporal surface deformation, and (3) PCA is used to identify the independent components of the deformation source.

### 2.3.1 Multitrack Wavelet-Based InSAR

To measure the time-dependent surface deformation across Kīlauea’s summit, the Wavelet-Based InSAR (WabInSAR) algorithm, a multitemporal SAR interferometric approach [*Shirzaei*, 2013, 2015; *Shirzaei and Bürgmann*, 2013], is used. This approach is detailed and comprehensively validated in earlier publications [*Shirzaei*, 2013, 2015]; however, for the sake of completeness, it is briefly discussed in this section. A large set of SAR images acquired from similar radar-viewing geometries are precisely coregistered to the same master image. WabInSAR generates a large set of interferograms with respect to maximum perpendicular and temporal baselines. The flat earth effect and topography are removed using a reference digital elevation model and satellite ephemeris data [*Franceschetti and Lanari*, 1999]. The algorithm then estimates complex phase noise using wavelet analysis of the interferometric data set. The time series of complex phase noises at each pixel is a

statistically random variable, and a chi-square test is applied to identify elite pixels, i.e., those with less noise [Shirzaei, 2013]. The pixels that pass the test are selected as elite pixels.

WabInSAR then implements a variety of wavelet-based filters for correcting the effects of topography, correlated atmospheric delay [Shirzaei and Bürgmann, 2012], and orbital errors [Shirzaei and Walter, 2011]. Through a reweighted least square approach, WabInSAR inverts the interferometric data set and generates a uniform time series of the line-of-sight (LOS) surface deformation. The effect of temporally uncorrelated atmospheric delay is then removed using a high-pass filter. Maximum spatial and temporal baselines of 500 m and 3 years are chosen to make sure that enough interferograms were generated with acceptable spatial and temporal coherence. To flatten interferograms, a 30 m resolution digital elevation model (DEM) produced by the Shuttle Radar Topography Mission (SRTM) was used. In order to improve the signal-to-noise ratio and enhance phase unwrapping, a multilooking operator to obtain an average pixel size of 40 m is applied. Once two time series of two independent tracks were generated, the multitrack WabInSAR algorithm [Shirzaei, 2015] is used to combine them into a seamless time series of surface deformation over Kīlauea’s summit.

### 2.3.2 Time-Dependent Geometry-Free Source Modeling

The InSAR time series of the surface deformation are used within a time-dependent modeling scheme [Shirzaei and Walter, 2010] to solve for the 4-D distribution of the magmatic volume changes beneath Kīlauea’s summit. This modeling scheme contains two major steps: (1) A static inversion using regularized, reweighted least squares at every time step as a minimum spatial mean square error estimator; (2) a linear Kalman filter [Grewal and Andrews, 2001] to generate a time series of source volume change as a minimum temporal

mean square error estimator. These two steps are implemented iteratively to obtain the optimum time-dependent source model.

#### 2.3.2.1 Static Source Inversion Using Distributed Point Center of Dilatations

Characterizing the magmatic source volume change distribution responsible for the observed surface deformation at each time step, an inversion scheme, comprised of a 3-D distribution of point center of dilatations (PCD) buried in a homogeneous elastic half-space [Segall, 2010], is employed. A similar method was first used by Vasco *et al.* [1988] for the inversion of leveling data at Long Valley Caldera to estimate the distribution of the source volume changes without any assumption on the initial source geometry. In their approach, surface deformation data are inverted to solve for the distribution of three diagonal components of the strain tensor at depth. Mossop and Segall [1999] applied a similar approach to estimate the volumetric strain at the Geysers geothermal field. Masterlark and Lu [2004] used an array of point sources to solve for the 3-D distribution of the pressure changes underneath volcanoes on the Segum Island, Alaska. Camacho *et al.* [2011] presented a geometry-free modeling scheme that jointly inverts the surface deformation and gravity data to solve for the distribution of pressure changes in a volcanic source zone. Recently, D'Auria *et al.* [2012] used surface InSAR deformation data following Vasco *et al.* [2002] to constrain spatiotemporal distribution of the volumetric strain underneath Campi Flegrei caldera, Italy. Here the volume change distribution of PCDs is solved for. Pressurized spherical sources are not used, because the pressure change in the vicinity of each pressurized source is affected by the stress imparted by the other sources [Pascal *et al.*, 2014] and thus its interpretation “is not well motivated on physical grounds” [Segall, 2010]. However, estimating the volume change distribution as is done here is correct. PCDs are composed of

three orthogonal force couples and they can be superimposed once linear elastic rheology is employed [Segall, 2010]. The presented framework here provides only an analogy to the true physical source. The actual physical process involves more complicated mechanisms, affected by material heterogeneities, nonlinear strain, and magma composition.

To solve for the distribution of the volume changes due to shallow magma activities at Kīlauea, a 3-D array of PCDs at locations  $\{X_i, Y_i, Z_i\}$  with assigned volume changes  $dv_i$  ( $i = 1, 2, \dots, m$ ) is employed. To invert the volume change distribution from LOS surface deformation  $L_j$  ( $j = 1, 2, \dots, n$ ) and assuming  $G_{ji}$  is the Green's function and  $r_j$  is the observation residual, following equation holds:

$$\begin{bmatrix} L_1 \\ \vdots \\ L_n \end{bmatrix} = \begin{bmatrix} G_{11} & \cdots & G_{1m} \\ \vdots & \ddots & \vdots \\ G_{n1} & \cdots & G_{nm} \end{bmatrix} \begin{bmatrix} dv_1 \\ \vdots \\ dv_m \end{bmatrix} + \begin{bmatrix} r_1 \\ \vdots \\ r_n \end{bmatrix}, P = S_0^2 D_{LL}^{-1} \quad (2.1)$$

$$l_{b_i} < dv_i < u_{b_i}$$

where  $m$  and  $n$  are the number of PCDs and observations, respectively.  $G_{ji}$  is Green's function and relates the volume change at  $i$ th PCD to the LOS displacement at the location of  $j$ th observation point. The Green's function of a PCD is explained in the appendix (Text A.1).  $P$  is the diagonal matrix of observation weight which is inversely proportional to the observation variance–covariance matrix ( $D_{LL}$ ) with primary variance factor  $S_0^2$ .  $l_b$  and  $u_b$  are

lower and upper bounds on the unknowns. Set  $L = [L_1 \cdots L_n]^T$ ,  $G = \begin{bmatrix} G_{11} & \cdots & G_{1m} \\ \vdots & \ddots & \vdots \\ G_{n1} & \cdots & G_{nm} \end{bmatrix}$ ,

$dv = [dv_1 \cdots dv_m]^T$ , and  $r = [r_1 \cdots r_n]^T$ , and then equation (2.1) is simplified as

$$L = G dv + r \quad (2.2)$$

and parameter variance–covariance ( $Q_{dvdv}$ ) is given by



$$Q_{dv dv} = (G^T P G)^{-1} \quad (2.3)$$

In order to reduce the roughness of the estimated distribution of volume change in the crust and avoid unrealistic stress heterogeneities, the second-order derivative of the PCD volume changes in 3-D space [Harris and Segall, 1987] is minimized:

$$\lambda D \mathbf{d} \mathbf{v} = 0 \quad (2.4)$$

where  $\lambda$  is the smoothing factor controlling the roughness of parameters and  $D$  is the Laplacian operator (Text A.2). A smoothing factor that balances the roughness of parameter space and the misfit between observed and modeled deformation [Harris and Segall, 1987] is chosen. Additionally, a ramp removing the possible remaining effect due to residual orbital error and reference point selection is solved for jointly.

Here linear elastic rheology is considered, which is a first-order assumption for a magma chamber with a complex rheology [Johnson *et al.*, 2000]. Despite this simplification, such model assumptions still explain deformation data well, though the estimated magma flux might be uncertain. A Poisson's ratio of 0.25 is used for volume change inversion and a Young's modulus of 30 GPa is utilized to estimate stress change in the crust, consistent with the range of 20–75 GPa suggested by earlier works [e.g., Baker and Amelung, 2012; Cayol *et al.*, 2000; Delaney and Denlinger, 1999]. Surface topography is not considered in the inversion, which is justified given the gentle surface relief at Kilauea. Moreover, inversion of InSAR data alone is not affected significantly by the topography [Wicks *et al.*, 2002].

This inversion framework will be applied separately to each time step of the InSAR time series to generate a time series of deformation source parameters that is optimized in the sense of minimum spatial root-mean-square error.

### 2.3.2.2 Linear Kalman Filtering

To reduce the temporal noise associated with the source model obtained in the previous step, a Linear Kalman Filter (LKF) in an iterative manner [*Grewal and Andrews*, 2001; *Kalman*, 1960; *Shirzaei and Walter*, 2010] is applied. The Kalman filter implements a predictor–corrector type estimator to minimize the estimated observation variance–covariance. Implementing LKF assures an optimal estimate of the volume changes at the acquisition times of the SAR images. The general expression is governed by linear dynamics and observation equations:

$$\begin{aligned} x_t &= A_{t-1}x_{t-1} + w_{t-1}, & p(w_t) &\sim N(0, Q_t) \\ z_t &= B_tx_t + v_t, & p(v_t) &\sim N(0, R_t), \quad t = 1, 2, 3 \dots \end{aligned} \quad (2.5)$$

where  $A_t$  is the dynamics equation coefficient relating the state of previous time step to the state of current step,  $w_t$  and  $v_t$  are the process and measurement noise, with Gaussian distribution, respectively,  $Q_t$  and  $R_t$  are the process and measurement noise variances and are estimated as diagonal elements of the parameter variance–covariance matrix (equation (2.3)).  $B_t$  is the measurement equation coefficient relating the current state to the estimated volume change, and  $z_t$  is the measurement vector. The iterative solution for discrete LKF is given by *Grewal and Andrews* [2001]. This iterative procedure is conducted to predict the optimal parameters of the current time step from that of the previous time step. Then observations at the current step are used to refine the predicted parameters for the current time step. This procedure reduces the temporal noise of the estimated parameters and is then applied to reduce temporal noise of the volume change time series for every inverted PCD.

### 2.3.3 Principal Component Analysis

PCA is a classic technique in data analysis for cluster analysis, discriminant analysis, and multiple linear regression [Jolliffe, 2005]. It is used to simplify the data set by reducing its dimensionality but retaining most of the significant information of the original variables in the data. PCA employs a mathematical procedure to transform a set of correlated variables into another set of uncorrelated variables called principal components, which is conducted through minimizing mean root squares to find mutually orthogonal directions in the data with maximum variances. This procedure is mathematically expressed by orthogonal transformations to explain the variance–covariance structure of a high-dimensionality random vector through a few linear combinations of the original component variables. Consider  $p$  original variables ( $p$ -dimensional random vector)  $\alpha = (\alpha_1, \alpha_2, \dots, \alpha_p)$ , and  $k$  ( $k \leq p$ ) principal components of  $\alpha$  are random variables  $M = (m_1, m_2, \dots, m_k)$ , so

$$\begin{aligned} m_1 &= n_{11}\alpha_1 + n_{12}\alpha_2 + \dots + n_{1p}\alpha_p \\ m_2 &= n_{21}\alpha_1 + n_{22}\alpha_2 + \dots + n_{2p}\alpha_p \\ &\vdots \quad \quad \quad \vdots \quad \quad \quad \vdots \quad \quad \quad \vdots \\ m_k &= n_{k1}\alpha_1 + n_{k2}\alpha_2 + \dots + n_{kp}\alpha_p \end{aligned} \tag{2.6}$$

The criteria used to choose coefficients  $n_{ij}$  are (a)  $\|n_i\| = 1$ , and  $Var(m_i)$  is the maximum value, where  $n_i$  is the  $i$ th row of  $n_{ij}$ ; (b)  $Cov(m_q, m_r) = 0$  for all  $q < r$ . Var and Cov mean the variance and covariance of a vector, respectively. This means that the principal components are linear combinations of the original variables, which maximize the variance of the linear combinations and have minimal covariance (correlation) with the previous principal components. Typically, the first few combinations explain most of the variance in the original data. Instead of working with all original variables, PCA is first performed and then only the first few principal components are used in subsequent analysis. In addition, the solution is conformed to find the eigenvalues (or singular values), so in most

cases, singular value decomposition is applied to decompose the original variable vector  $\alpha$ . The ratio of different eigenvalues (or singular values) represents the relative importance of corresponding components. To identify the clusters of PCDs that experience similar spatiotemporal volume changes, PCA is applied and the results are presented in section 2.5.

## 2.4 Surface Deformation Data

InSAR time series in conjunction with GPS data are utilized to explore the surface deformation at Kīlauea’s summit during the period from January 2003 to October 2010. The GPS data are mainly used to validate the InSAR time series and estimate the effect of the decollement slip underneath Kīlauea. Then the thoroughly tested and validated InSAR time series is used to model the 4-D maps of the magmatic system beneath Kīlauea’s summit.

### 2.4.1 GPS Data

Thanks to the Hawaiian Volcano Observatory, Stanford University, and the University of Hawai‘i, a dense continuous GPS observation network has been established at Kīlauea with more than 70 stations. The GPS data are made available through University NAVSTAR Consortium and 39 stations recorded continuous data during the same period as the SAR acquisitions. Only GPS stations for InSAR time series validation, modeling slip on the decollement, and variance–covariance analysis of inversion results are shown in Figure 2.2a. The daily GPS solutions were calculated using the GIPSY/OASIS II software developed at Jet Propulsion Laboratory [Stephen *et al.*, 1996; Zumberge *et al.*, 1997] with a processing strategy of undifferenced ionosphere-free observation in the IGS08 reference frame. The coordinate system for GPS measurement is Earth centric and Earth fixed, which is different than the coordinate system used in InSAR processing. This difference is addressed by correcting the

GPS observations with respect to a stable GPS station on Hawai‘i Island (MKEA), which records 3-D Pacific plate movement.

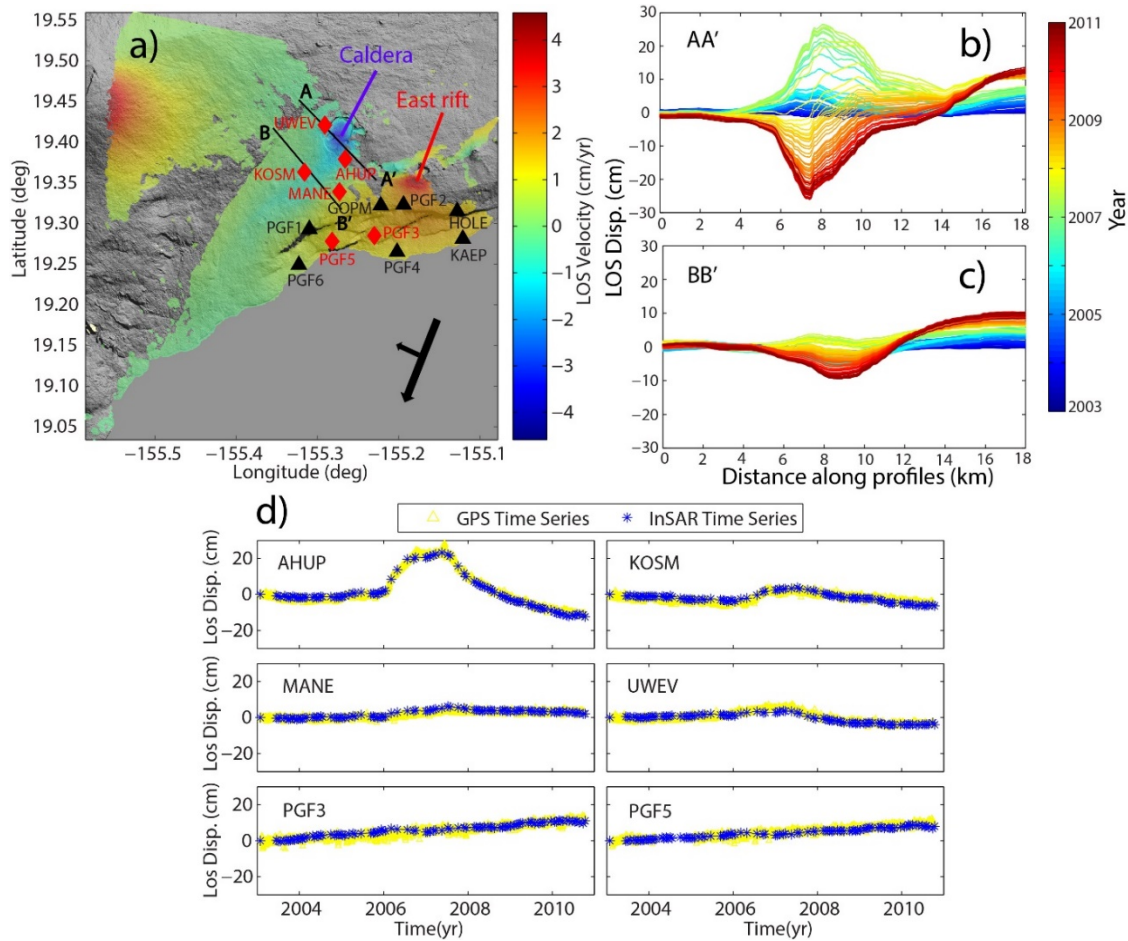


**Figure 2.2.** (a) The long-term LOS surface displacement velocity (cm/yr) calculated from the processed InSAR time series. The convention used in this paper is that positive LOS corresponds to uplift. The time period spans from January 2003 to October 2010. The velocity map is overlaid on a shaded relief image. Red diamonds indicate GPS stations used for InSAR time series validation and black triangles are those used for decollement slip inversion. (b, c) Deformation for all time steps along profiles AA' and BB'. (d) InSAR time series validation. The InSAR (blue stars) and GPS (yellow triangles) displacement time series in Envisat descending LOS direction. Constant velocity of the Pacific Plate movement is removed from GPS data.

#### 2.4.2 InSAR Deformation Time Series

The Envisat advanced SAR images provided by European Space Agency are explored in this paper to constrain the spatiotemporal evolution of Kīlauea's magmatic system. SAR data sets spanning the period from 2003 to 2010 are acquired in descending tracks 200 and

429 (incidence angle =  $23^\circ$  and heading angle =  $192^\circ$ ) and include 54 and 46 images, respectively, with an average sampling rate of 28 days. 650 and 440 interferograms are generated in tracks 200 and 429, respectively, and 180,264 elite pixels collocated in both data sets are identified. Treating these data sets as two independent but temporally overlapping data sets [Shirzaei, 2015], an InSAR time series with high spatiotemporal resolution and accuracy is obtained.

Figure 2.2a shows the obtained long-term LOS velocities. The LOS velocity map displays multiple deformation patterns at Kīlauea's summit. Long-term subsidence is the predominant deformation pattern at Kīlauea's summit caldera and in the middle–upper SWRZ. LOS displacement time series along two profiles are shown in Figures 2.2b and 2.2c. However, the subsidence in the SWRZ is broader and weaker than that of the summit. The ERZ is characterized by a strong signal of uplift along LOS due to rift intrusion south of Makaopuhi Crater and the whole south flank moves seaward as indicated by GPS stations PGF3 and PGF5. Figure 2.2d shows examples of the generated InSAR time series and comparison with GPS observations, which are projected onto the Envisat LOS direction. The InSAR data are in good agreement with GPS data, for both linear and transient signals of surface motion.

The spatiotemporal evolution of the surface deformation on Kīlauea's south flank shows more complicated features. Figure 2.3 shows the spatial distribution of the cumulative LOS displacement during nine different periods from January 2003 to October 2010. The first period 2003/01/27–2004/07/21 (Figure 2.3a) is characterized by weak surface subsidence in the upper SWRZ, uplift east of Halema'uma'u, and seaward motion of the south flank near the Hilina Fault Zone. During the next period 2004/07/21–2005/11/23

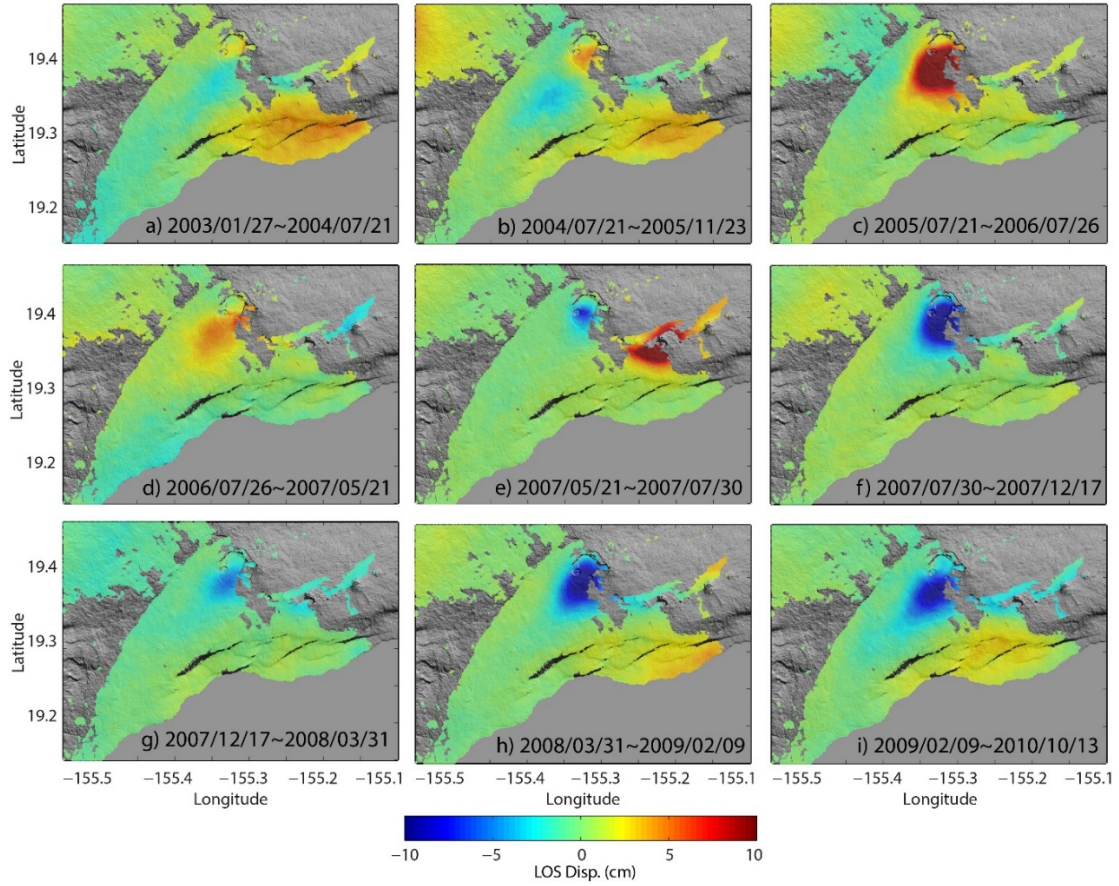


**Figure 2.3.** InSAR time series for LOS displacement during nine periods from 2003/01/27 through 2010/10/13, showing the spatiotemporal evolution of the deformation patterns during this time. Red means surface moves toward satellite (uplift) and blue means movement away from satellite (subsidence). The corresponding time period for each map is labeled.

(Figure 2.3b) subsidence dominates in the SWRZ father away from the caldera and south of Halema'uman'u experiences uplift. In the following period 2005/11/23–2006/07/26 (Figure 2.3c), widely distributed uplift south of the summit caldera becomes the major deformation feature, and subsidence ceases in the upper SWRZ. From 2006/07/26–2007/05/21 (Figure 2.3d), uplift occurred in the upper SWRZ outside Halema'uma'u Crater. The period 2007/05/21–2007/07/30 (Figure 2.3e) is characterized by subsidence east of Halema'uma'u Crater inside the summit caldera and strong rift extension in the ERZ near Makaopuhi Crater following the Father's Day event. During the period 2007/07/30–2007/12/17

(Figure 2.3f), subsidence inside the caldera strengthened and spread with deformation centered on the south rim of the caldera. During the period 2007/12/17–2008/03/31 (Figure 2.3g), subsidence affected the south rim of the caldera. The south rim pattern remained consistent during 2008/03/31–2009/02/09 (Figure 2.3h), except that it became stronger and broader at the south rim of the caldera. During the last period 2009/02/09–2009/10/13 (Figure 2.3i), subsidence decreased in magnitude and area with its center moved slightly southwestward. To understand the causes of these variations, a sophisticated time-dependent modeling scheme is applied, and the results are discussed in the following section 2.5.

## 2.5 Model Results

The modeling scheme presented in section 2.3.2 is implemented and the surface deformation time series that is validated in section 2.4.2 are used to investigate the spatiotemporal evolution of Kilauea’s magmatic system. Prior to inverting the surface deformation data and solving for the volume change distributions as described below, the effects of other sources of deformation, such as slip on the decollement, are removed to isolate the contributions due to localized magmatic activities at the summit. The long-term rate of slip on the decollement is relatively steady at  $11 \pm 1$  cm/year (for details, see appendix Text A.3). This estimate is consistent with that obtained in earlier works [Owen *et al.*, 1995; Owen *et al.*, 2000a]. Then the contribution of the decollement is removed from the LOS deformation time series observed at Kilauea’s summit (Figure A.1). The corrected InSAR surface deformation data are used to apply the time-dependent modeling scheme and investigate the spatiotemporal evolution of the volume changes beneath the caldera. To this end, the model domain is set to be a cuboid, with dimensions of 10 km in the east–west



direction, 16 km in the north–south direction, and 6 km in depth. This cuboid is chosen such that its plane view encompasses deformation at the summit, but it is not affected by the large signal due to the 2007 dike intrusion in the ERZ (Figure 2.1). Given that the summit deformation signal is localized over a few kilometers (Figure 2.2a), it is safe to consider a constraint of zero volume changes at the cuboid edges during the source inversion. In total, 26,697 elite pixels within model domain are used for following inversion. The model domain is discretized into 4095 PCDs, with horizontal spacing of  $0.75 \text{ km} \times 0.75 \text{ km}$  and vertical separation of 0.5 km.

Before using this model set up to solve for the distribution of volume changes beneath the summit area, following aspects on the modeling method are investigated: (1) the model resolution through a 3-D checkerboard test (checkered in three directions), (2) the effect of additional observations, such as GPS, on the uncertainty of model parameters through variance–covariance analysis, and (3) the influence of the observation noise on the model results through bootstrapping.

The 3-D checkerboard test allows analyzing the model resolution, as well as the effect of data gaps, on the model results. Using the model setup detailed above, three scenarios with different source distribution patterns (Figure 2.4) are devised. To this end, PCDs are grouped to form zones of 0 and  $1000 \text{ m}^3$  volume change with dimensions of  $n \times n \times n$  PCDs ( $n = 2, 3, 4$ ) (Figure 2.4). Through forward modeling, the surface LOS deformation associated with each scenario is calculated at the location of the elite pixels identified in section 2.3.1. These scenarios allow evaluating the model and data resolution for resolving various deforming bodies at different depths. The simulated surface LOS deformation is then inverted for the distribution of volume changes associated with each scenario and bounded least squares with regularization is applied to stabilize the matrix inversion (see

section

2.3.2.1). In all

cases, the

model

resolution

decreases with

depth. The

overall

conclusion is

that distinct

zones of

deformation

with

dimension of

$\sim 1$  km or

larger can be resolved accurately at a depth range of 0.5–3.5 km. For sources with larger

dimension ( $\sim 3$  km), the model resolution is still satisfactory at depths greater than 3.5 km.

Next investigation is whether adding sparse GPS observations causes a significant reduction in the variance of inverted volume change distribution. Within the study area, only four GPS stations (i.e., AHUP, UWEV, KOSM, and MANE) provide continuous observations that spans the InSAR observation period. Thus, these GPS stations are used together with InSAR data sets for variance–covariance analysis. Given the linearity of the problem (equation (2.2)), only the locations of the InSAR pixels and GPS stations are

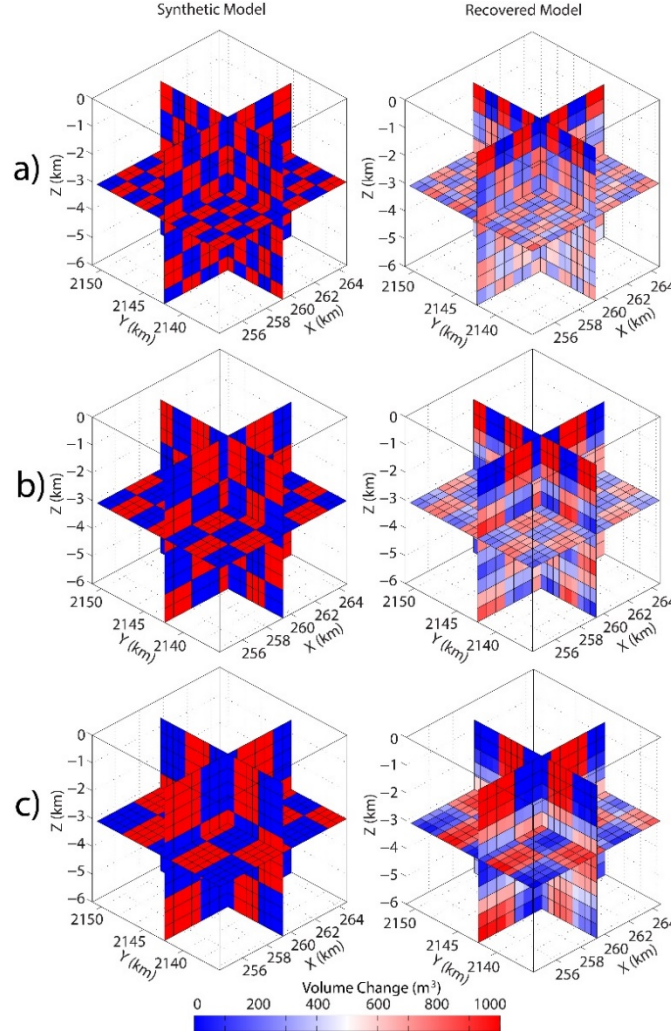


**Figure 2.4.** Tree-dimensional checkerboard test, examining the model resolution and the effect of data gaps on the inverted volume change distribution. Three different model resolutions are investigated using different sizes of checkered grids including (a)  $1.5 \times 1$  km, (b)  $2.25 \times 1.5$  km, and (c)  $3 \times 2$  km (horizontal  $\times$  vertical). Figure 4 (left column) is synthetic models, and Figure 4 (right column) is recovered models.

needed. Since there are many more InSAR pixels compared to four GPS stations, the first task is to estimate the relative weight of GPS data ( $\alpha$ ) using the following relation:

$$Q_{dvdv} = (G_I^T P_I G_I + \alpha G_G^T P_G G_G)^{-1} \quad (2.7)$$

where  $G_I$  and  $G_G$  are design matrices for InSAR and GPS data following equation (2.2) and optimum  $\alpha$  is the one that minimized the trace of  $Q_{dvdv}$ , namely yielding the least variance–covariance for the volume change distribution. Adding GPS data causes very little reduction in variance at every given  $\alpha$  (Figure A.2a). This is better shown in the 3-D view of the variance distribution for the case of the InSAR only inversion, InSAR and GPS inversion, and their difference (Figures A.2b–A.2d). Using  $\alpha = 2200$  which indicates GPS and InSAR data have same relative weight during inversion (Figure A.2c), the improvement is negligible. Therefore, in the presented inversion scheme, the GPS data do not provide a noticeable improvement. To avoid the complexities such as relative data weighting and variable temporal errors, GPS data are not used for the magmatic source inversion.

The sensitivity of the model results to the observation noise and gap is explored using a bootstrapping approach. The bootstrapping is done using the LOS surface displacement measured between the first and last time steps of the InSAR time series. The inversion is repeated 200 times, and in each iteration a random noise with standard deviation of 5 mm (based on the estimated uncertainty for the InSAR time series) is added to the observations. Sufficiently large numbers of iterations allows generating an ensemble of model parameters that is used for estimating standard deviations of the volume change distribution. The estimated distribution of standard deviations (Figure A.3) indicates that the shallow PCDs are more sensitive to the data gap and noise. Also, given the linearity of the equations, the average uncertainty of the volume change rate is estimated to be  $\sim 50 \text{ m}^3/\text{year}$  (uncertainty of LOS velocity map is  $\sim 1 \text{ mm}/\text{year}$ ).

The smoothing factor introduced in equation (2.4) needs to be estimated before applying the time-dependent modeling. In general, the smoothing factor is a function of the number of surface displacement observations and their variance–covariance. Therefore, it

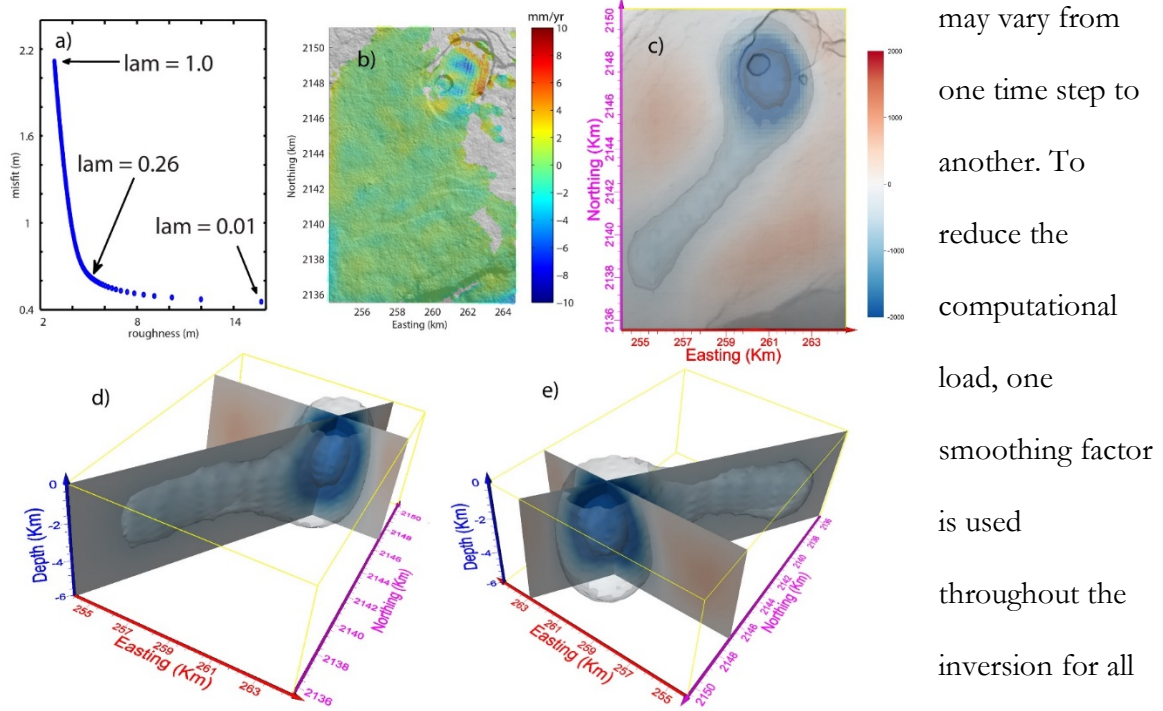


**Figure 2.5.** (a) Trade-off curve. The smoothing factor  $\lambda = 0.26$ , indicating the largest curvature on the trade-off curve, is used for the time-dependent inversion. (b) Rate of residuals averaged over all time steps of inversions. (c) Plan view of the inverted long-term volume change rate at 2.4 km depth. The values of the two isosurfaces are  $-3000 \text{ m}^3/\text{yr}$  (inner one) and  $-540 \text{ m}^3/\text{yr}$  (outer one), respectively. (d, e) The 3-D views of the long-term volume change rate. The isosurfaces are the same as that of Figure 5c. Two vertical profiles are used to show more details of the 3-D volume change distribution. Color bars of Figure 5d and 5e are the same as that in Figure 5c. UTM coordinate system is used for visualization.

may vary from one time step to another. To reduce the computational load, one smoothing factor is used throughout the inversion for all time steps. This value is estimated through the examination of the total surface deformation measured between the first and last time step. The optimal smoothing factor was determined using the trade-off curve method [Jónsson *et al.*, 2002], which shows the relation between model misfit and parameter roughness. The trade-off curve is shown in Figure 2.5a and the optimum smoothing factor of 0.26 is obtained where curvature is at a maximum.

The time-dependent distribution of volume changes underneath Kīlauea’s summit from January 2003 through October 2010 is estimated. Figure 2.5b shows the average rate of the model misfit, which is calculated from model misfits of all time steps (Figure A.5). Overall residuals are smaller than 2 mm/year, except inside the caldera where residuals are larger at some time steps. These larger residuals are possibly due to modification of the SRTM DEM during occasional caldera rim collapses at Halema‘uma‘u, shallow hydrothermal activities or magmatic activities that are not mapped into the model. Temporal data fittings at the Caldera and SWRZ (Figure A.4) as well as spatial data fittings (Figures A.6–A.8) for nine consecutive periods discussed in section 2.4.2 further confirm that the model well explains the observed LOS displacement at the surface both in time and space.

In the following discussion on the model results, the notion “long-term” means the entire time span of this study (2003–2011), “intermediate-term” is periods with length of about half of the entire time span of this study, and “short-term” is six-month time span. In Figures 2.5c–2.5e the 3-D distribution of the long-term volume change rates at Kīlauea’s summit is shown from different perspectives with two isosurfaces of 3000 m<sup>3</sup>/year and 540 m<sup>3</sup>/year, equivalent to ~ 60% and 10% of the largest volume change rate. The red color is associated with an increase in volume (inflation), while the blue color corresponds with a decrease in volume (deflation). In Figure 2.5c, a major zone of deflation is identified at a rate > 3000 m<sup>3</sup>/year underneath and southwest of the Kīlauea caldera. This zone of deflation fades toward the SWRZ, identifying the volume change distribution within the rift zone. The zone of deflation beneath Kīlauea’s summit, to first order, can be approximated using a sphere with radius of 1 km at 2–3 km depth.

Given the non-linear surface deformation, temporally variable behavior is expected in Kīlauea’s magmatic system. Figure 2.6 shows the rate of volume change distributions in the

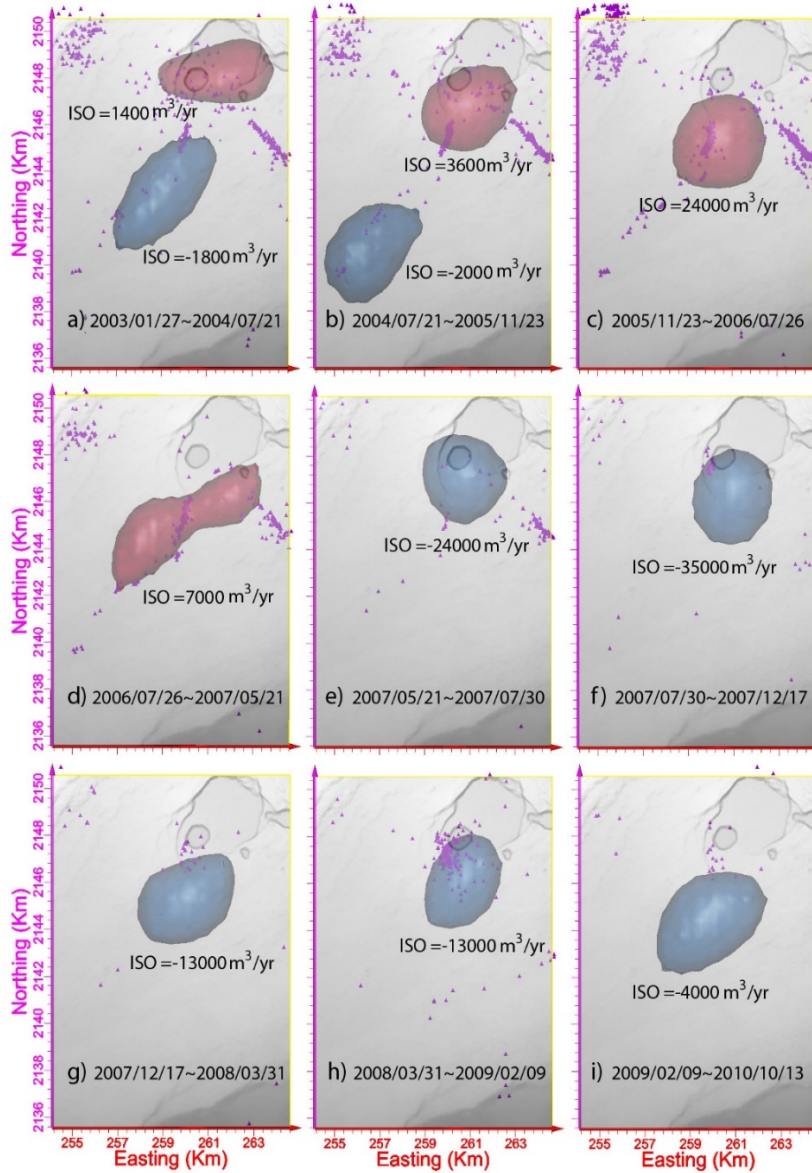


**Figure 2.6.** (a–i) Plane views of the zones of major volume change rate and their spatial evolution at nine consecutive periods. Every zone is characterized by an isosurface that is labeled with its value of volume change rate ( $\text{m}^3/\text{yr}$ ). The choice of isosurface allows for maintaining a similar size for zones of major volume changes throughout the observation period. Negative values indicate volume loss, while positive values correspond with zones of volume gain. Purple dots are the locations of microearthquakes.

form of isosurface plots during nine shorter periods that are identified in Figure 2.3. In each panel, the value of the isosurface is chosen so the zones of major volume change have a relatively similar spatial extent throughout the study period. The first period 2003/01/27–2004/07/21 (Figure 2.6a) is characterized by a zone of deflation in the upper SWRZ at a depth of 2.4 km, and an inflation zone east of Halema‘uma‘u Crater at 2.4 km depth. During the next period 2004/07/21–2005/11/23 (Figure 2.6b) the volume change of the zone of inflation (2.2 km depth) increases southwestward near Halema‘uma‘u Crater, whereas the

zone of deflation (2.4 km depth) is farther away from the caldera along the SWRZ. While the zone of deflation disappears, the zone of inflation (2.5 km depth) continues to grow through the next period 2005/11/23–2006/07/26 (Figure 2.6c), and moves toward the SWRZ. For 2006/07/26–2007/05/21 (Figure 2.6d), the volume change of the inflation zone decreases and splits into two small and connected inflating bodies, with one in the upper SWRZ (centered at 2.6 km depth) and another southeast of Kīlauea caldera (centered at 2.3 km depth). This period leads up to a major rift intrusion in the ERZ, starting on June 17, 2007. During the following period 2007/05/21–2007/07/30 (Figure 2.6e), volume change patterns change from inflation to deflation at Kīlauea caldera, likely in response to the ERZ intrusions. Also within this period, the major zone of deflation is located at the south rim of Kīlauea caldera, at a depth of 2.2 km. Throughout the next periods (2007/07/30–2010/10/13) the zone of deflation persists with slight variations in horizontal location and center depth of 2.2–2.5 km (Figures 2.6f–2.6i).

In order to identify clusters of PCDs that act together and form a quasi-independent magmatic body, the principal component analysis presented in section 2.3.3 is applied. Following PCA and sorting the PCs from greatest to least importance based on the ratio of associated eigenvalues, first three PCs explain about 99% (63.8%, 28.5%, and 6.6%, respectively) of the time-dependent volume change model. Then these PCs are used to decompose the obtained volume changes into three sets of independent clusters. Table 2.1 summarizes the results of this analysis, and Figure 2.7 shows the spatial location and the temporal evolution of the volume changes associated with these clusters. In each panel the isosurfaces and their associated values represent 3-D zones with  $>\sim 50\%$  of the corresponding largest volume change rate. The first PC represents the spatial and temporal



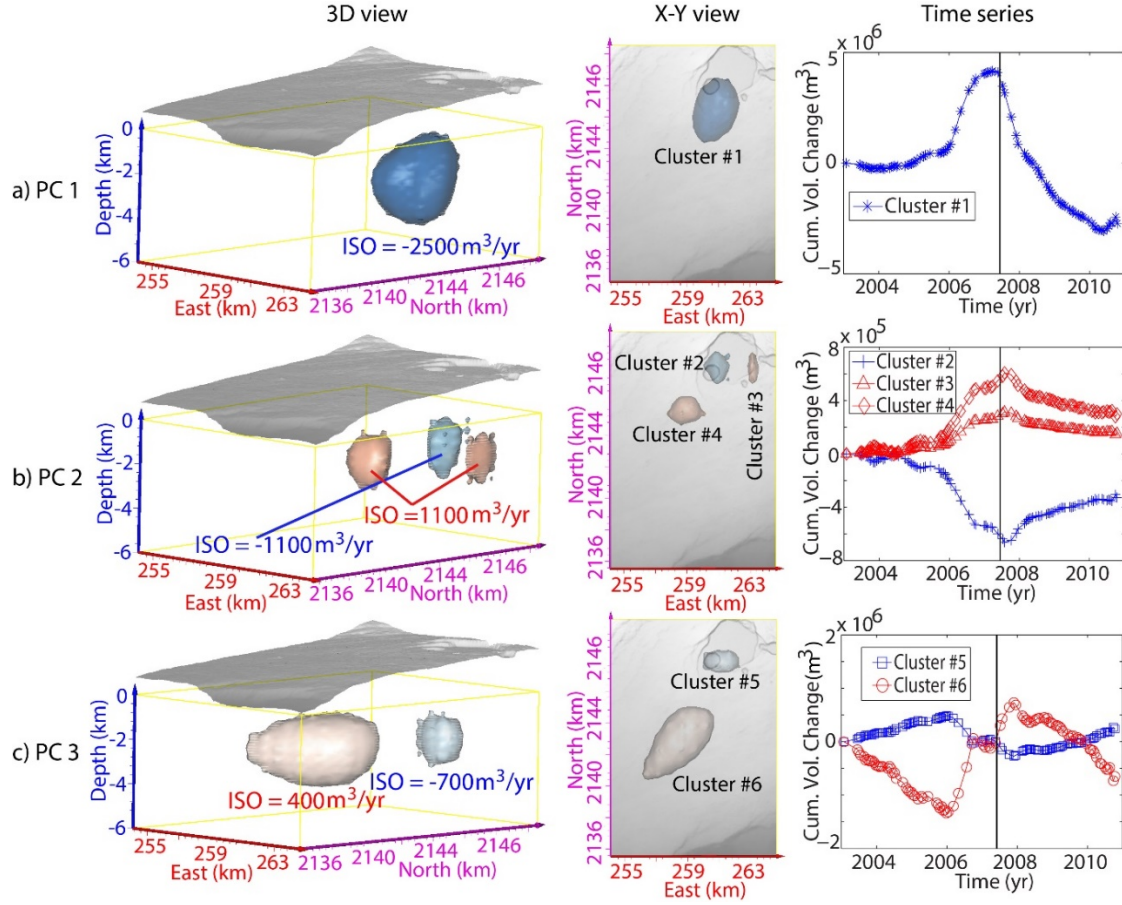


**Figure 2.7.** PCA results of the time-dependent source model of Kilauea's summit plumbing system. In each panel the isosurfaces and their associated values indicates the 3-D zone with  $> \sim 50\%$  of the largest volume change rate. (a) A deflationary PCD cluster identified from the first PC. (b) A deflationary PCD cluster and two inflationary PCD clusters obtained from the second PC. (c) A deflationary and an inflationary PCD cluster identified from the third PC. Figure 7 (first column) shows the 3-D view of each identified clusters; Figure 7 (second column) is the plane view; and Figure 7 (third column) shows the time series of volume change for each cluster, and the vertical lines indicate the Father's Day event. ISO (isosurface) value ( $\text{m}^3/\text{yr}$ ) indicates the value of volume change rate on the enclosing envelope of each cluster.

distribution of the estimated volume change to first order (Figure 2.7a). The isosurface plot of the first PC includes a cluster of deflating PCDs with volume change rates  $> 2500 \text{ m}^3/\text{year}$ , which are located at the south rim of Kilauea caldera at  $\sim 2.4 \text{ km}$  depth. The second and third PCs (Figures 2.7b and 2.7c) represent the spatiotemporal deviations of the volume change distribution from that of the first PC. The second PC identifies a cluster of deflating PCDs as well as two inflating ones. The deflationary cluster is located northeast of the



Halema‘uma‘u Crater with a depth of 1.6 km, and the associated isosurface has a volume change rate  $>1100 \text{ m}^3/\text{year}$ . The two inflationary clusters are located beneath the east rim of Kilauea’s caldera and the upper SWRZ, at depths of 1.9 km and 2.3 km, respectively, and the given isosurface indicates clusters with volume change rates  $>1100 \text{ m}^3/\text{year}$ . The third PC marks inflationary and deflationary clusters. The inflationary cluster is located under the SWRZ with a volume change rate  $>400 \text{ m}^3/\text{year}$  on the isosurface, while the deflationary cluster is located east of Halema‘uma‘u Crater with volume change rate  $>700 \text{ m}^3/\text{year}$  on the isosurface.

**Table 2.1** Summary of the cluster analysis results

PC #	Cluster #	Cluster Depth (km)	Explained Percentage
1	1	2.4	63.8%
2	2	1.6	28.5%
	3	1.9	
	4	2.3	
3	5	2.0	6.6%
	6	2.4	

Figure 2.7 (third column) shows the temporal evolution of the volume changes associated with each cluster. Cluster #1 (southeast of Halema‘uma‘u) experiences slow volume gain prior to 2006, which turns into rapid inflation beginning in 2006 until mid-2007 when the Father’s Day event occurred in the ERZ. Afterward, it deflated and only this cluster regained volume in mid-2010 (Figure 2.7a). Clusters #3 and #4 show similar temporal behavior characterized by volume gain until mid-2007 followed by a slow decay toward the end of the observation period. Cluster #2 located at 1.6 km shows an almost opposite trend to Clusters #3 and #4 (Figure 2.7b). Cluster #5 gains volume until 2006, followed by an episode of volume loss that is reversed immediately after the Father’s Day event. Cluster #6 shows behavior that is opposite to that of Cluster #5. These observations

indicate a complex interaction between components of Kīlauea’s summit magmatic system that is different than the simple top-down relationship suggested in earlier works [e.g., *Baker and Amelung*, 2012].

## 2.6 Discussion

A geometry-free, time-dependent inverse modeling approach, which implements regularized least squares optimization and a linear Kalman filter (LKF), is employed. The usefulness of such a method for constraining the spatiotemporal evolution of deformation sources with complex geometries at Kīlauea is shown. In this section 2.6, some aspects of the presented data, method, and model results are discussed.

### 2.6.1 Distributed PCD Inversion

PCDs consist of three mutually orthogonal double-couple forces and inverting the surface deformation data to solve for these three forces allows for the estimation of the volume change at the center of each PCD. Therefore, their effect can be superimposed analogous to the case of solving for coseismic slip distribution on a fault using a 2-D array of rectangular dislocations. Using a distribution of the PCDs, the volume change inside magma bodies with irregular shapes [*Shirzaei et al.*, 2015] can be solved for. Note that interpreting individual PCDs and their equivalent pressure changes are not physically meaningful and rather the volume change associated with a zone or cluster should be discussed, as presented here.

### 2.6.2 Model Implications for Magma Storage

Understanding the summit reservoir at Kīlauea is of great importance. The magma supplied to Kīlauea first enters the summit reservoirs before subsequent upward and lateral movement to feed the summit and rift eruptions. The time-dependent source model (Figure 2.6) and PCA (Figure 2.7) allow clearly identifying several spatially and temporally independent reservoirs beneath the summit and constrain their dynamics. The summit magmatic system consists of six connected reservoirs with depths between 1 and 3 km where the densities of the surrounding rocks are comparable to that of rising hot magma [Ryan, 1987b]. Both seismic and surface deformation data suggest that the preferable magma storage zone is located in the range of 1–6 km beneath Kīlauea’s summit. Recent works show that magma could be stored at depths less than 2 km as part of Kīlauea’s summit feeding system for the ERZ eruptions [Cervelli and Miklius, 2003; Lundgren *et al.*, 2013].

In the model, the largest reservoir is located south of the caldera, and several other smaller ones are scattered at various locations and depths (Figure 2.7 and Table 2.1). In general, the results agree with many other studies, suggesting that Kīlauea’s summit reservoir comprises multiple active sources with depths varying between 1 and 4 km. Using tilt data, Fiske and Kinoshita [1969] identified an inflation sequence near the summit caldera leading to the 1967–1968 eruption. This sequence is divided into three clusters with depths of 2–3 km, whose locations are northeast of the Halema‘ūma‘u Crater (HMM source), south of the summit caldera, and by the intersection of the SWRZ and Kīlauea caldera. The magmatic source south of the caldera was also identified in earlier studies [Cervelli and Miklius, 2003; Dvorak *et al.*, 1983; Eaton, 1959, 1962; Shirzaei *et al.*, 2013; Yang *et al.*, 1992], all of which suggest a magmatic source comparable in size and location to Cluster #1 obtained from PCA (Table 2.1). A shallow source consistent with Cluster #2 beneath HMM is also

suggested based on modeling of subsidence caused by magma withdrawal to feed rift intrusions and eruptions [Cervelli and Miklius, 2003; Lundgren *et al.*, 2013; Poland *et al.*, 2009b]. The inversion indicates that the HMM source is located at a depth of  $\sim 1.6$  km, which falls in the depth range of 1–2 km suggested by Anderson *et al.* [2015] using large number of deflation-inflation (DI) events. Cervelli and Miklius [2003] estimated a depth of 350 m for HMM source; however, a deeper source depth is favored by the higher-resolution data and more sophisticated inversion scheme. Cluster #3 is located northeast of Keanakāko‘i Crater at a depth of 1.9 km. To constrain the Keanakāko‘i reservoir, Battaglia *et al.* [2003] placed relocated long-period earthquake clusters at the depth of 4 km beneath the summit caldera, and Poland *et al.* [2014] estimate a depth range of 2.0–4.9 km using surface deformation data collected during 2004–2005. Cluster #3 can be interpreted as the reservoir for Keanakāko‘i, but due to the horizontal shift and shallower depth, it can also be considered as a previously unknown reservoir. The resolution test suggested that the estimated depth of 1.9 km for this cluster is robust. Cluster #4 is similar to the magmatic source found by Fiske and Kinoshita [1969] using cluster analysis based on migrating inflation centers and that identified by Baker and Amelung [2012] based on InSAR data. However, the estimated depth of 2.3 km is shallower than the 2.9–4.2 km reported by Baker and Amelung [2012]. Cluster #5 marks a reservoir east of Halema‘uma‘u at a depth of 2 km. Though it overlaps with Cluster #2, its temporal evolution and depth are independent. Thus, it marks a new reservoir, which might have gone unidentified because of its proximity to the HMM reservoir. Myer *et al.* [2008] suggested a shallow magmatic reservoir under the upper SWRZ which is similar to the identified Cluster #6. The estimated depth (2.4 km) of Cluster #6 here falls outside of the depth range (1–2 km) suggested by Myer *et al.* [2008].

### 2.6.3 Model Implications for Magma Supply and Transport

At a given volcano, the eruptive activity, rate of gas emissions, and seismicity are determined by the rate at which magma ascends from depth and supplies the volcano [Dvorak and Dzurisin, 1993].

Estimates of the magma supply rate are a function of two parameters: (1) the volume change beneath the volcano and (2) the long-term volume eruption rate. The discharge rate can be determined using high-

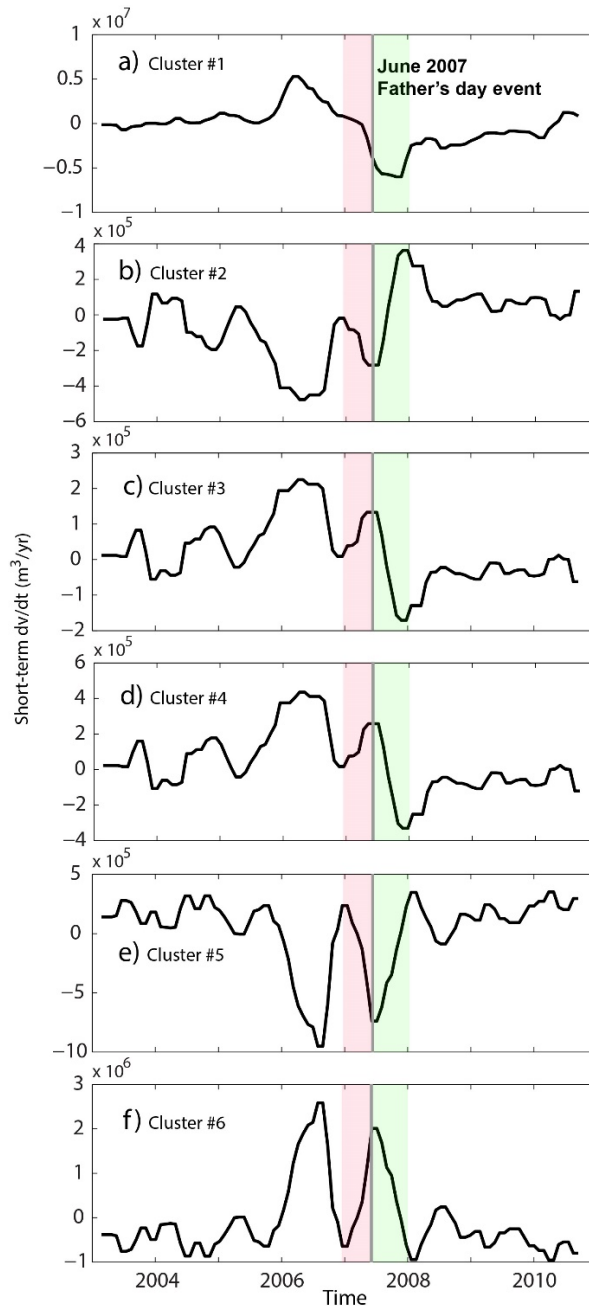


**Figure 2.8.** Estimated magma storage rate (MSR) time series associated with each PCA cluster shown in Figure 7. The rate is calculated using a moving time window of 3 months from the volume change time series. Red and green mark 6 months leading up to and following the Father's Day event, respectively.

resolution DEMs and field mapping [e.g., Poland, 2014] and is an accurate indicator of the supply rate when there is little surface deformation observed at the volcano. Otherwise, the volume changes associated with surface deformation need to be taken into account. Based on different studies, the long-term supply rate to Kilauea is estimated to be  $\sim 0.09 \text{ km}^3/\text{year}$ ,

while its short-, intermediate- and long-term variations range from 0.02 to 0.18 km<sup>3</sup>/year [Dvorak and Dzurisin, 1993; Poland *et al.*, 2014]. The time-dependent model provides a unique opportunity to investigate short- and intermediate-term variations in the magma storage rate (MSR) due to the temporally variable MSR at Kīlauea’s shallow reservoirs. Figure 2.8 shows the estimated short-term MSR time series associated with each PCA cluster. The rates are estimated as the local slope of the volume change time series shown in Figure 2.7. Cluster #1 shows the largest MSR of up to 0.005 km<sup>3</sup>/year, dominating Kīlauea’s shallow reservoir. The MSR is steady near zero prior to mid-2005 followed by a sudden increase in the following year, indicating a new batch of magma has been supplied to the summit reservoir [Poland *et al.*, 2012; Shirzaei *et al.*, 2013]. This period of increased MSR is accompanied by elevated gas emissions, seismicity, and heightened eruption rates at the Pu’u ‘Ō’ō, which also indicates an increased magma supply from the mantle to Kīlauea. A 12-month window spanning the Father’s Day event is explored. The beginning and end of this window are roughly marked by the rapid changes in the surface deformation and MSR that occur immediately preceding and following the Father’s Day event. Following the rapid increase in MSR at Cluster #1 until beginning 2006, MSR declines until the Father’s Day event in June 2007. This apparent decline can be due to migration of magma to other clusters and the rift zone, as well as reconfiguration of the magma body under gravity. Degassing and solidification processes can also contribute to the observed MSR reduction. Nearly 6 months after the event, Cluster #1 starts gaining volume at a rate that is initially high, but the corresponding MSR declines exponentially. Though an order of magnitude smaller, the MSR of other clusters shows a more complicated temporal pattern. In particular, comparing the 6 months leading to and following the Father’s Day event, which are marked in red and green, respectively, shows interesting patterns of MSR. Prior to the Father’s Day event, Clusters #2

and #5 show a decline in MSR similar to that of Cluster #1. In contrast, Clusters #3, #4, and #6, located outside the Halema‘uma‘u area, show an increased MSR. During the ~6 months following the Father’s Day event, when Cluster #1 shows a steady decrease in MSR, Clusters #2 and #5 experience an elevated MSR, while Clusters #3, #4, and #6 decline in their MSR. These observations are sketched in Figure 2.9. As seen prior to the rift eruption, there is a top-down relationship between reservoirs beneath the caldera, together with lateral interaction with off-Halema‘uma‘u reservoirs and rifts. Following an event, the relations are reversed and the fluid flow follows a bottom-up-type relationship beneath HMM. Moreover, the off-Halema‘uma‘u reservoirs lose volume and likely feed the rifts and other reservoirs.

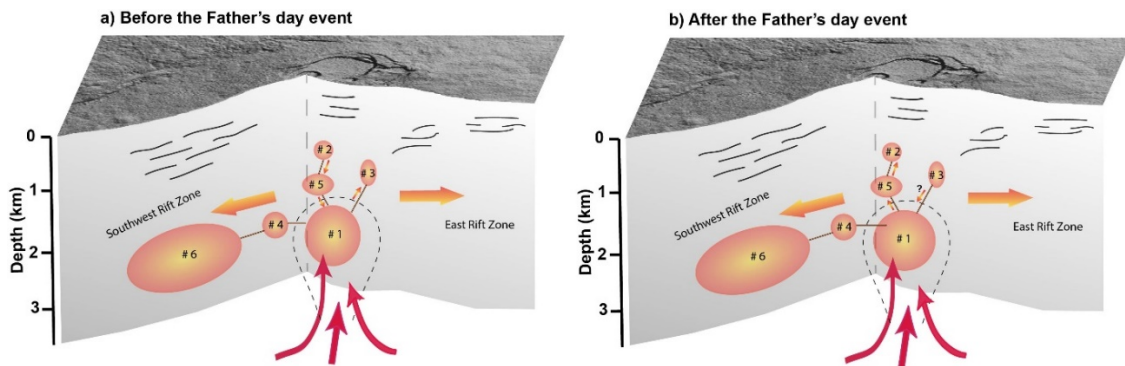


**Figure 2.9.** Sketch showing Kilauea’s magma storage system and mechanism of magma transport and supply (a) prior to and (b) following a major rift intrusion in June 2007. Approximate location of the reservoir (PCA clusters in Figure 7) and the possible direction of the magma transport are shown.

The spatiotemporal link between the magma reservoirs beneath Kilauea’s summit is discussed in previous studies, mostly based on the episodic deformation pattern. *Cervelli and Miklius* [2003] proposed a Γ-shaped model that indicates a single conduit from the south crater reservoir to the Halema‘uma‘u reservoir to the Pu‘u ‘Ō‘ō Crater. A “blocked pipe” between the south crater reservoir and Halema‘uma‘u reservoir was suggested to explain the episodic DI events that happened in the Halema‘uma‘u reservoir. This blockage in magma flow was supported by a hypothesis [*Poland et al.*, 2009a] that involves a process of small-

scale convective overturns within Kilauea's summit shallow magma reservoir system. This process leads the degassed, dense magma to move downward. *Baker and Amelung* [2012] suggested that the changes in shallow magma system only affect one reservoir at a time, and the conduits between different reservoirs are not continuously open. The pressure and stress change could effectively open the conduits. By these speculations, a top-down inflation and deflation model was proposed.

Compared with the earlier works, the modeling results here indicate some differences. Various episodes where the short- and intermediate-term MSR at different clusters show correlated and anticorrelated behaviors are identified. Note that the correlation is interpreted as similarity between volume change time series and does not necessary imply that the two given clusters are connected. To quantify the correlation between volume change time series, three distinct episodes of activities (Figure 2.10) are determined. Figure 2.10a shows the time series of the LOS displacement at Kilauea caldera and in the ERZ. There are major episodes of correlation from 2003 to the beginning of 2006, and anticorrelation following

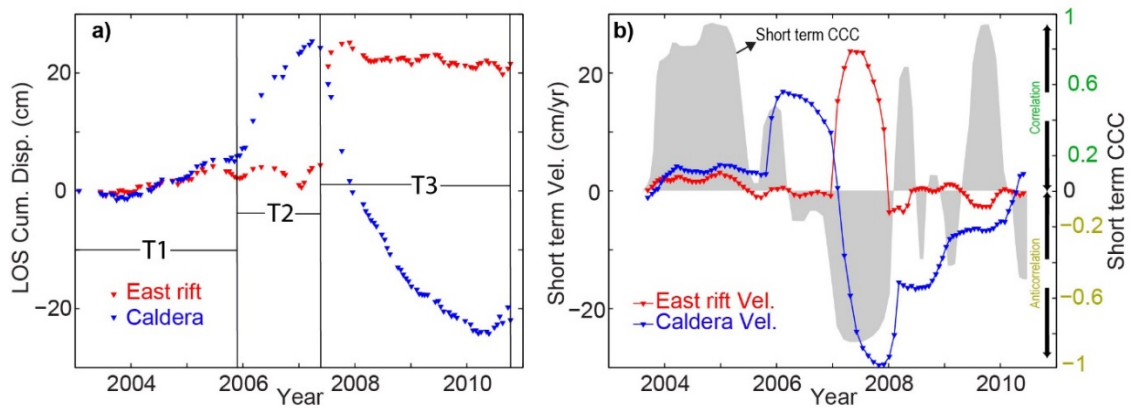


**Figure 2.10.** (a) Time series of surface LOS displacement at the summit caldera and in the ERZ. T1, T2, and T3 are three distinct periods of surface deformation with different LOS velocity. (b) Short-term velocities estimated from surface LOS displacement at the summit caldera and in the ERZ. The window size is 6 months. The gray-shaded diagram shows the short-term cross-correlation coefficient between the caldera and ERZ with window size consistent to that used in velocity estimation. CCC = cross-correlation coefficient.



the Father's Day event. Prior to the Father's Day event, Kīlauea's summit uplifts and shows a positive correlation to the ERZ. Following the Father's Day event, the zones were anticorrelated and rapid rift extension coincided with a rapid collapse of the summit. Afterward, Kīlauea's summit continued to subside until mid-2010 with negligible deformation in the ERZ. However, there are subtler transient periods of correlated behavior. Figure 2.10b shows the short-term linear velocities estimated within a moving 6 month time window, as well as the cross-correlation coefficients between the caldera and rift zone within this moving window. The short-term correlation indicates various episodes of correlated and anticorrelated deformation between the summit and ERZ. Based on Figure 2.10, the time series of the volume changes at all clusters are divided into three periods. Then in each period the intermediate-term correlation coefficient between every two time series and the standard deviation of the short-term correlation (Figure A.10) are calculated. The intermediate-term correlation indicates a similarity between two clusters over a relatively long period of time, and the standard deviation determines how it temporally varies. During the first period (2003/01/27–2005/11/23), Clusters #2 and #6 are correlated with each other. The rest of the clusters correlate mutually and are anticorrelated with Clusters #2 and #6. The most significant standard deviation is observed between Cluster #1 and all others, suggesting that other clusters experience a more temporally variable volume change compared to that of Cluster #1. During the second (2005/11/23–2007/05/21) and third (2007/05/21–2010/10/13) periods, Clusters #2 and #5 are correlated but are anticorrelated with the rest. The standard deviation of short-term correlation between Cluster #1 and Clusters #5 & #6 are higher during the second period, suggesting a more transient behavior of volume changes for clusters #5 & #6. However, during the third period, the standard deviations between Cluster #1 and Clusters #2, #3, & #4 are much smaller than that

between Cluster #1 and Clusters #5 & #6, indicating that Clusters #2, #3, & #4 undergo very tiny transient volume changes over this period. Clusters #1, #3, & #4 are mutually correlated and are anticorrelated with Cluster #2 throughout all three time periods. For the first period, Cluster #2 correlates with Cluster #6 and anticorrelates with Cluster #5. For the following two periods this relation reverses, meaning that Cluster #2 correlates with Cluster #5 and anticorrelates with Cluster #6. This correlation analysis suggests that different clusters are spatially connected, as shown in Figure 2.9.

#### 2.6.4 Other Implications

Earlier works established links between magmatic activity at Kīlauea's summit and seismicity and rift eruptions. The time-dependent source model of Kīlauea's summit presented here can be used to further explain the rift intrusions and seismicity along them. To this end, the concept of stress transferring is used. The normal stress change in the ERZ is calculated using a compression negative convention due to the volume change within the summit reservoir. The distribution of the normal stress rate in the ERZ is shown in Figures 2.11a–2.11c for three time periods, as identified in Figure 2.10a. During the first period (2003/01/27–2005/11/23), when Kīlauea caldera is characterized by a slow rate of volume change (Figure 2.11a), the imparted normal stress in the ERZ is minor. During the second period (2005/11/23–2007/05/21), the maximum inflation rate occurs beneath the caldera (Figure 2.11b), and the normal stress increases significantly across the rift zone, unclamping the ERZ. The increased normal stress culminates during the Father's Day event in June 2007 and then begins to diminish toward end of the observation period. During the third period (2007/05/21–2010/10/13), the rate of volume change beneath the caldera is negative (Figure 2.11c). Consequently, the imparted normal stress is negative, and thus it helps to

clamp the rift zone and possibly stop the intrusion. Figure 2.11d shows the temporal evolution of normal stress history on the ERZ as well as the cumulative volume change beneath Kīlauea caldera where positive values of stress indicate unclamping of the rift zone.

During the process of magma intrusion to rift zones, elevated number of microearthquakes is observed along the path of magma flow. The model suggests the link

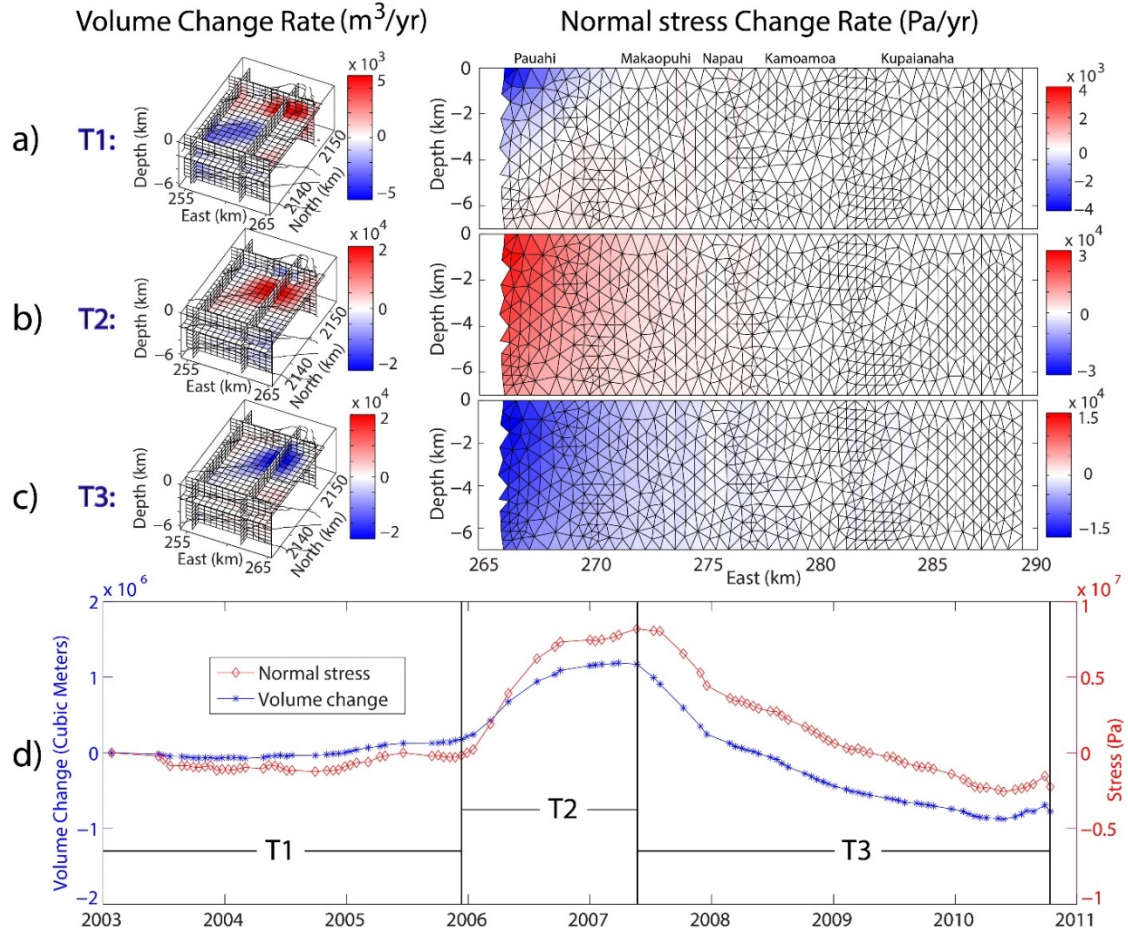


**Figure 2.11.** (a–c) Volume change rate distribution and associated normal stress rate distribution on the ERZ for three time periods (T1, T2, and T3 as seen in Figure 10a). For volume change rate: blue, deflation; red, inflation. For stress rate distribution: blue, clamping; red, unclamping. (d) The time series of source volume change and normal stress on the ERZ.

between seismicity and magmatic activity at the summit reservoir. The catalog of relocated earthquakes at Kīlauea used here is provided by *Lin et al.* [2014], spanning a period of from 1992 to 2009 and including 25,705 events. The earthquakes that occurred near the summit

during the period covered by the InSAR observations are selected. Two distinct periods of inflation (2003/01/27–2007/05/21) and deflation (2007/05/21–2010/10/13) are considered according to the surface deformation data and the ERZ and SWRZ geometries are used as receiver faults. The Coulomb failure stress change ( $\Delta CFS$ ) [King *et al.*, 1994] in the crust is estimated using the estimated volume change distribution at each time step.

$\Delta CFS = \Delta\tau - \mu\Delta\sigma_n$ , where  $\Delta\tau$  is the shear stress change,  $\mu$  is the frictional coefficient, and  $\Delta\sigma_n$  is the normal stress change. A friction coefficient of 0.4 is used. The estimated  $\Delta CFS$  and the distribution of earthquakes are shown in Figure 2.12. For the inflation period (Figures 2.12a and 2.12b), most earthquakes along the SWRZ and ERZ receive

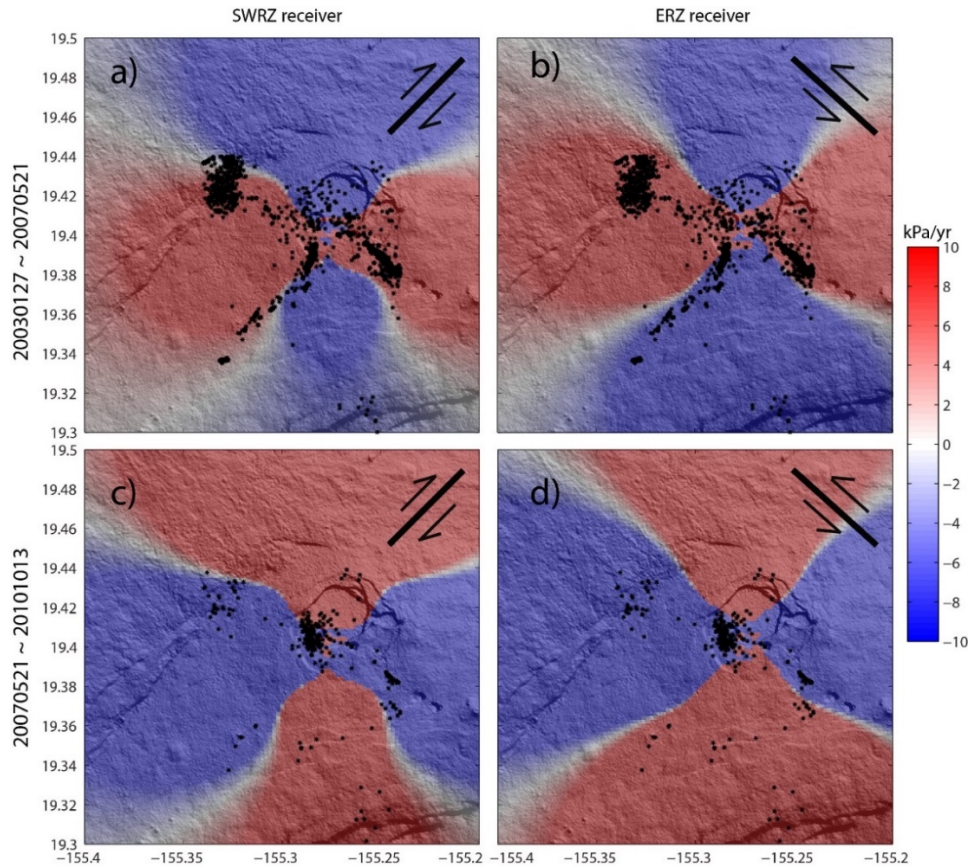


**Figure 2.12.** Coulomb stress change rate distributions for two preferred fault geometries, during two periods. (a) Inflation period and SWRZ receiver. (b) Inflation period and ERZ receiver. (c) Deflation period and SWRZ receiver. (d) Deflation period and ERZ receiver. Dips for both receiver faults are set to be 90 °. Black dots are microearthquakes.

positive  $\Delta CFS$ , suggesting that magmatic activity enhanced the occurrence of earthquakes. However, during the deflation period (Figures 2.12c and 2.12d), most earthquakes were located within zones of negative  $\Delta CFS$ , which suggests they are not triggered by magmatic activities. These earthquakes are located within a narrow zone near Halema‘uma‘u, at a depth range from 0 to 2 km and occurred during 2008–2009 (Figure 2.6h). These earthquakes are likely to be associated with the summit eruption. One possible explanation is that volume loss at the reservoir following the Father’s Day event resulted in magma degassing, which in turn opened the Halema‘uma‘u Crater in 2008, causing the summit eruption.

## 2.7 Conclusions

A novel geometry-free time-dependent modeling scheme is proposed to invert InSAR deformation data for the magmatic source beneath Kīlauea’s summit during 2003–2010. The modeling scheme considers a 3-D array of PCDs and solves for the time series of the distributed volume change at the center of PCDs. Application of principal component analysis to this time-dependent model identifies six independent zones of magmatic activities. Temporal analysis of the volume changes for these reservoirs indicates a more complex relation throughout Kīlauea’s summit reservoir. The data and model results enhance the understanding of magma storage, transport, and supply at Kīlauea’s summit and quantify the relation between magmatic activities at the summit to the rift eruption and seismicity.

## CHAPTER 3

### 3-D MODELING OF IRREGULAR VOLCANIC SOURCES USING SPARSITY-PROMOTING INVERSIONS OF GEODETIC DATA AND BOUNDARY ELEMENT METHOD

The work presented in this chapter has been published as: Zhai, G., and Shirzaei, M. (2017), 3-D Modeling of Irregular Volcanic Sources Using Sparsity-Promoting Inversions of Geodetic Data and Boundary Element Method. *Journal of Geophysical Research: Solid Earth* **122**, 10,515-10,537, doi: 10.1002/2017JB014991.

#### 3.1 Abstract

Geodetic observations of surface deformation associated with volcanic activities can be used to constrain volcanic source parameters and their kinematics. Simple analytical models, such as point and spherical sources, are widely used to model deformation data. The inherent nature of oversimplified model geometries makes them unable to explain fine details of surface deformation. Current nonparametric, geometry-free inversion approaches resolve the distributed volume change, assuming it varies smoothly in space, which may detect artificial volume change outside magmatic source regions. To obtain a physically meaningful representation of an irregular volcanic source, a new sparsity-promoting modeling scheme is devised assuming active magma bodies are well-localized melt accumulations, namely, outliers in the background crust. First, surface deformation data are inverted using a hybrid L1- and L2-norm regularization scheme to solve for sparse volume change distributions. Next, a boundary element method is implemented to solve for the displacement discontinuity distribution of the reservoir, which satisfies a uniform pressure

boundary condition. The inversion approach is thoroughly validated using benchmark and synthetic tests, of which the results show that source dimension, depth, and shape can be recovered appropriately. This modeling scheme is applied to deformation observed at Kilauea summit for periods of uplift and subsidence leading to and following the 2007 Father's Day event. The magmatic source geometries for these periods are statistically distinct, which may be an indicator that magma is released from isolated compartments due to large differential pressure leading to the rift intrusion.

### 3.2 Introduction

Repeated intrusions and emplacements of magma underneath active volcanoes lead to the formation of a magma chamber [Fiske and Kinoshita, 1969]. Acting as a melt repository, its shape evolves gradually through internal mechanical–chemical processes and interactions with crustal host rocks [Dufek *et al.*, 2013; Gudmundsson, 1990]. Although the shape of a shallow magma chamber cannot be highly irregular based on thermal and mechanical stability considerations [Gudmundsson, 1990], its actual shape, size, and temporal evolution are not entirely known [Marsh, 2015]. Except for small lens-shaped magma chambers that are mostly molten during their early stages, the majority of magma chambers is partially molten with low melt fractions and composed mostly of crystal-rich mushes in a suprasolidus state [Marsh, 1981]. The widely used analytical models of the magma chamber, however, assume that the chamber is entirely molten with uniform internal pressure [e.g., Davis, 1986; Mogi, 1958; Yang *et al.*, 1988]. Moreover, the excess pressure in magmatic bodies inferred from these analytical models can be orders of magnitude larger than the solid host rock tensile strength of <10 MPa even when the source dimension is well constrained independently [Beauducel *et al.*, 2004; Gudmundsson, 2008]. Owing to their symmetric shape and uniform

internal pressure, such models predict a symmetric stress field, in contrast to indirect observations of a heterogeneous stress field adjacent to magma chambers from surface fissure orientations and fracture patterns [*Chadwick and Dieterich*, 1995; *Gudmundsson*, 2008]. Therefore, the ability to constrain a realistic shape of a magma chamber and its evolution in time and space improves the estimates of the stress field. This leads to better forecast models predicting the time and location of chamber rupture, dike intrusions, volcanic eruptions, and caldera formations [*Gudmundsson*, 2008].

Most processes associated with magma chambers can only be studied indirectly using geodetic and geophysical methods. While seismic tomography has been widely used to measure heterogeneous properties of magmatic plumbing systems, due to low spatial resolution [e.g., ray coverage; *Lees*, 2007], its application for studying shallow magma chambers is limited. Moreover, seismic imaging does not constrain excess pressure of the magma chamber. On the other hand, geodetic measurements of surface deformation with high spatiotemporal resolution may provide crucial information to illuminate the geometries and internal processes of shallow magmatic systems.

Figure 3.1 sketches a simple magmatic system that deforms as a result of inflation and deflation of a magmatic reservoir. Due to the scarcity of direct observations of volcanic processes responsible for surface deformation at depth, mathematical models provide the linkage between surface deformation and the inaccessible source [*Lisowski*, 2007]. Following the first application of a point dilatational source to interpret surface deformation at Kilauea [*Mogi*, 1958], many other analytical models have been proposed to explain observations of spatial and temporal surface deformation at volcanos [*Bonaccorso and Davis*, 1999; *Davis*, 1983, 1986; *Fialko et al.*, 2001; *McTigue*, 1987; *Okada*, 1992; *Yang and Davis*, 1986; *Yang et al.*, 1988]. Typical analytical models can often explain the first-order surface deformation pattern and



allow for constraining the average depth of the magma chamber. These models fail to explain the high-order complexities of surface deformation, primarily due to oversimplification of the model geometry. Numerical modeling approaches, such as finite element methods (FEMs), are capable of accounting for arbitrary chamber shape and size [Ronchin *et al.*, 2013]. These models consider 3-D heterogeneous medium properties and irregular surface relief [Trasatti *et al.*, 2003], but in most current applications, they assume a fixed geometry provided by prior simple analytical solutions [Bonaccorso *et al.*, 2005; Masterlark *et al.*, 2012; Trasatti *et al.*, 2005]. In addition, using FEM to invert for model geometry is computationally expensive, as it requires iteratively remeshing the model space and numerically evaluating stress tensors [Masterlark *et al.*, 2012]. This limitation could be resolved by incorporating a mesh-independent deformation source into FEM [Charvo and del Sastre, 2014], yet this method relies on *a priori* source shape to resolve source geometrical parameters and strength.

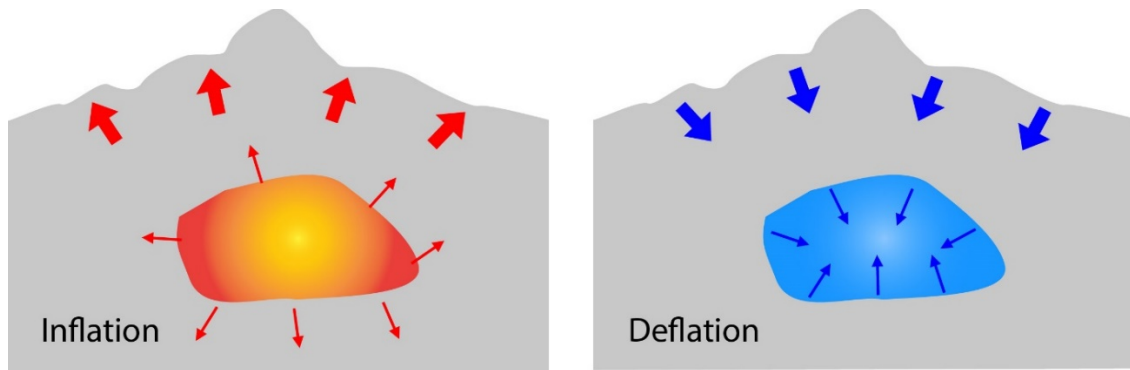


**Figure 3.1.** Schematics showing a simple volcanic system with (left) inflation and (right) deflation behaviors.

Magma chambers also contain chemically distinct, partially molten melts or crystal mushes, which leads to the formation of porous rocks and isolated magma compartments with nonuniform pressure distribution [De Natale and Pingue, 1992, 1996; De Natale *et al.*, 1991; Gudmundsson, 2012]. Yet again, analytical models do not account for these complexities.

To overcome these limitations, some researchers consider a combination of elementary sources to model deformation data to account for chamber heterogeneities as well as investigate chamber shape irregularity without assuming *a priori* source geometry. *Vasco et al.* [1988] divided the source region into three-dimensional cells and used a linear inversion of surface deformation data at Long Valley to model the 3-D distribution of volumetric strain. They identified zones of high volumetric strain consistent with results from seismic imaging. *Mossop and Segall* [1999] used a similar approach to explain leveling and GPS data at the Geyser geothermal field in northern California. *Masterlark and Lu* [2004] extended the concept of the three-dimensional source array and attempted to identify source clusters for Seguin Island. *D'Auria et al.* [2012] investigated 4-D volcanic source beneath Campi Flegrei caldera through inversion of InSAR to map volumetric strain distribution. *Zhai and Shirzaei* [2016] investigated the Kilauea volcano magmatic system using a time-dependent modeling scheme combined with volume change distribution inversion. The strategy of combining 3-D source array inversion with FEM-based numerical models is a challenge to acquire an amorphous source distribution due to the significant computing load required for remeshing the medium for each source. However, remeshing can be avoided by using an array of cubic elements as a static, unchangeable mesh [*Ronchin*, 2015; *Trasatti et al.*, 2008].

Although geometry-free modeling schemes are successful at constraining distributed volumetric strain and illuminating zones of deformation, these models fail to (1) resolve the actual shape and size of the source, (2) constrain the average excess pressure of the magmatic source, and (3) fulfill the uniform pressure boundary condition [*Segall*, 2010].

Here a nonparametric, geometry-free kinematic inverse modeling scheme is proposed. The deformation source comprises distributed point centers of dilatations (PCDs; see section 3.3.1). A nonparametric modeling method relates surface deformation to model

parameters through superposition of elementary sources. A sparsity-promoting inversion scheme is used to image the magmatic source's irregular geometry. For such models of the magmatic body to also fulfill the uniform pressure boundary condition, distributed force dipoles are needed. Otherwise, the resolved excess pressure is nonphysical. Thus, to fulfill the required boundary conditions, the source geometry fixed by implementing the sparsity-promoting inversion is used and a boundary element method (BEM) is applied. The displacement discontinuity distribution on the surface of the chamber and its internal excess pressure are solved for, considering no shear traction on the surface of the chamber and that tensile stress is equal to the excess pressure. This method is validated through benchmark and synthetic tests and then applied to two episodes of deformation at Kilauea volcano, including the uplift period from December 2005 to May 2007 and the subsidence period from May 2007 to May 2010.

### 3.3 Method

#### 3.3.1 Distributed PCDs as Volcanic Deformation Source

In this section, the formula of the forward model, which relates volcanic surface deformation to its source that comprises distributed PCDs characterized by volume changes, is first derived. This forward model is benchmarked through comparison with independent volcanic deformation models.

##### 3.3.1.1 Surface Deformation Due to Volume Change Distribution

Relating the volume change at depth to the surface deformation, a volume integral derived from Volterra's formula [Vasco *et al.*, 1988] is used. Assuming linear elasticity and finite volume of fluid source, the relationship between stress-free volumetric strain  $\theta^T(\mathbf{\xi})$  at

3-D location  $\boldsymbol{\xi}$  inside a finite source with volume of  $V$  and surface deformation  $u_i(\boldsymbol{x})$  in the  $i$ th direction at surface location  $\boldsymbol{x}$  is given by

$$u_i(\boldsymbol{x}) = \int_V (\boldsymbol{\xi} \in V) \theta^T(\boldsymbol{\xi}) k_i(\boldsymbol{x}, \boldsymbol{\xi}) dV, \quad i = 1, 2, 3 \quad (3.1)$$

where  $k_i(\boldsymbol{x}, \boldsymbol{\xi})$  is the directional Green's function in half space [Maruyama, 1964; Vasco et al., 1988]:

$$k_i(\boldsymbol{x}, \boldsymbol{\xi}) = \frac{1+v}{3\pi} S \quad (3.2)$$

$$S = \frac{x_i - \xi_i}{((x_1 - \xi_1)^2 + (x_2 - \xi_2)^2 + (x_3 - \xi_3)^2)^{\frac{3}{2}}}$$

where  $v$  is Poisson's ratio. Note that this Green's function is under stress-free condition and a scale factor is needed to describe volumetric strain under stressed condition (e.g., confinement from surroundings). The scale factor can be determined using the relation between stress-free ( $\epsilon^T$ ) versus stressed ( $\epsilon$ ) dilatational strains of the finite source [Eshelby, 1957]. This relationship is given by Rudnicki [2002] under the condition that the diameter of reservoir is much smaller than its depth;

$$\epsilon(\boldsymbol{X}) = -\frac{1}{4\pi} \frac{1+v}{3(1-v)} \epsilon^T \Delta q \quad (3.3)$$

$$q = \int_V \frac{1}{r} dV$$

where  $\Delta$  is a Laplacian operator,  $q$  is the ordinary Newtonian potential for unit density filling the finite source volume, and  $r$  is the distance between observation point  $\boldsymbol{X}$  in medium and differential volume  $dV$ . Here  $\boldsymbol{X}$  should be located inside  $V$  if one wants to calculate the strain state of the finite source, then  $\Delta q = -4\pi$  based on Poisson's equation [Hofmann-Wellenbof and Moritz, 2005]. Thus,

$$\frac{\epsilon}{\epsilon^T} = \frac{1 + \nu}{3(1 - \nu)} \quad (3.4)$$

This factor is shape-independent when the diameter of the reservoir is much smaller than its depth, which means the reservoir is equivalent to an isotropic point source. Combining equations (3.1) and (3.4), stress-free volumetric strain is replaced with the stressed version ( $\theta$ ):

$$u_i(\mathbf{x}) = \int_V \theta(\boldsymbol{\xi}) K_i(\mathbf{x}, \boldsymbol{\xi}) dV \quad (3.5)$$

where  $K_i(\mathbf{x}, \boldsymbol{\xi}) = k_i(\mathbf{x}, \boldsymbol{\xi}) \frac{3(1-\nu)}{1+\nu} = \frac{1-\nu}{\pi} S$ . This Green's function under stressed conditions is identical to that of *Mossop and Segall* [1999]. Equation (3.5) indicates that the surface deformation due to an arbitrary-shaped source is an integration of volumetric strain scaled with stressed Green's function over the volume of the finite source. The stressed condition can be accounted for by applying a similar type of scaling factor to the Green's function presented in other studies, which can also be used for calculating source volume change without altering source shape [*Lu et al.*, 2002; *Masterlark and Lu*, 2004; *Vasco et al.*, 2007; *Vasco et al.*, 2002].

Next step is to divide  $V$  into  $n$  volume cells  $V_m$  ( $m = 1, 2, \dots, n$ ). Assuming uniform volumetric strain  $\theta_m$  within each volume cell, equation (3.5) can be rewritten as

$$\begin{aligned} u_i(\mathbf{x}) &= \sum_{m=1}^n \theta_m \int_{V_m} K_i(\mathbf{x}, \boldsymbol{\xi}) dV_m \\ &= \sum_{m=1}^n \theta_m K_i(\mathbf{x}, \boldsymbol{\xi}_m) V_m \\ &= \sum_{m=1}^n \Delta V_m K_i(\mathbf{x}, \boldsymbol{\xi}_m) \end{aligned} \quad (3.6)$$

where  $\int_{V_m} K_i(\mathbf{x}, \boldsymbol{\xi}) dV_m = K_i(\mathbf{x}, \boldsymbol{\xi}_m) V_m$  and  $\boldsymbol{\xi}_m$  is the center location of the  $m$ th cell. This is justified considering that every cell is small enough and equivalent to an isotropic point source. Also, using a FEM simulation, *Ronchin* [2015] showed that a cell half the size of its depth is equivalent to an isotropic point source at the cell center with error  $\sim 2\%$  in predicted InSAR line of sight (LOS) displacement.  $\Delta V_m = \theta_m V_m$  is the volume change of the  $m$ th source cell under stressed conditions. Equation (3.6) indicates that a finite reservoir with an arbitrary shape can be approximated by a superposition of spatially distributed PCDs. Note that equation (3.6) neither requires a constant pressure boundary condition on the surface of a chamber nor satisfies this condition [*Segall*, 2010].

### 3.3.1.2 Benchmark Test

To numerically test the validity and applicability of the proposed forward model (equation (3.6)), several benchmark tests are implemented as a reference, considering solution of pressurized prolate spheroid [*Yang et al.*, 1988] widely used for modeling volcanic deformation [e.g., *Lundgren et al.*, 2015; *Tiampo et al.*, 2000] and numerical solution of pressurized oblate spheroid obtained from BEM. Four different prolate spheroids are tested with fixed vertical semiaxes of 3 km and horizontal semiaxis of 0.5 km, 1 km, 1.5 km, and 3 km, and two different oblate spheroids with fixed horizontal semiaxis of 3 km and vertical semiaxis of 1.5 km and 0.5 km. The uniform pressure on the surface of each spheroid is 8 MPa, and the depth to the center of each spheroid is 6 km. The shear modulus and Poisson ratio of the elastic half-space medium are 20 GPa and 0.25, respectively. For the purpose of comparison, the total (stress-free) volume change associated with the spheroid and the equivalent distribution of PCDs are identical. The volume change of a prolate spheroid is calculated using transformation strain after *Eshelby* [1957] and volume–pressure relationship

[Segall, 2010]. Due to the inherent nonuniqueness of the volume change distribution estimated using PCD arrays, the PCD distribution that best fits the prolate spheroid results in terms of least-squares is considered to be the optimal representation of the prolate spheroid. For the case of an elongated spheroid with an aspect ratio of 6 (Figure 3.2a), the agreement between surface displacement associated reference model and that of PCDs is

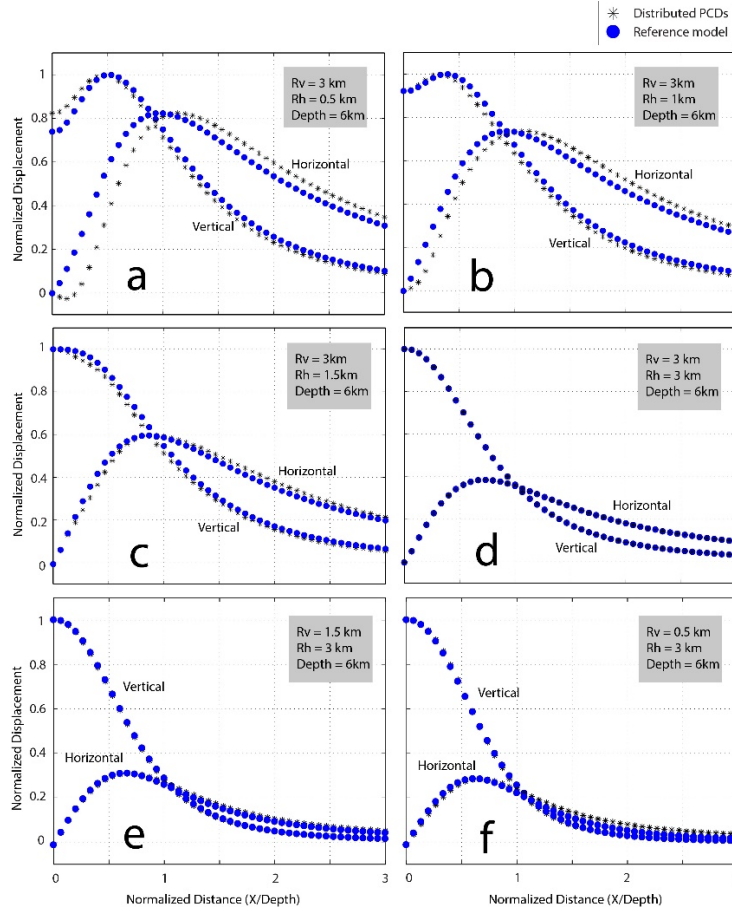


**Figure 3.2.** Benchmark tests for prolate and oblate spheroid sources. (a–d) Comparison between displacements associated with a prolate spheroid [Yang *et al.*, 1988] with aspect ratios of (a) 6.0, (b) 3.0, (c) 1.5, (d) 1.0, and the equivalent model comprising distributed PCDs. (e, f) Comparison between displacements associated with an oblate spheroid obtained from BEM with aspect ratios of (e) 2.0 and (f) 6.0, and the equivalent model comprising distributed PCDs. All prolate and oblate spheroids have a fixed depth of 6 km and uniform pressure of 8 MPa.

fair, although the distributed PCDs overestimate vertical and underestimate horizontal displacements in the near field. As for the prolate with aspect ratios of 1–3 (Figures 3.2b–3.2d) and oblate spheroids with aspect ratios of 2 and 6 (Figures 3.2e and 3.2f), the agreement between results from distributed PCDs and that of the reference model is satisfactory. The benchmark tests indicate that the smaller the aspect ratio of the volcanic source, the better the performance of distributed PCDs to represent surface displacement

field. It also highlights that this modeling approach shall not be used for interpreting deformation associated with conduits.

### 3.3.2 Magmatic Deformation Source Modeling

Although distributed point sources show great success in modeling volcanic processes [D'Auria *et al.*, 2012; Masterlark and Lu, 2004; Mossop and Segall, 1999; Ronchin, 2015; Trasatti *et al.*, 2008; Vasco *et al.*, 2007; Vasco *et al.*, 1988; Vasco *et al.*, 2002; Zhai and Shirzaei, 2016], they provide very limited information about the physics of a magma chamber as a finite body with an irregular shape. For instance, the volume change associated with distributed point sources does not correspond to a uniform pressure boundary condition, which is required for a finite source [Segall, 2010]. To overcome this limitation and obtain a finite source with irregular shape that satisfies the boundary conditions, a modeling scheme that consists of two main steps is proposed: (1) Constrain the geometry of the magmatic source through a sparsity-promoting inversion of surface deformation data and (2) apply BEM to estimate the displacement discontinuity distribution and associated pressure change on a closed surface approximating the circumference of the model geometry fixed in the previous stage.

#### 3.3.2.1 Sparsity-Promoting Inversion for Source Geometry

##### 3.3.2.1.1 Formulating Problem with Sparse Constraint

Following Zhai and Shirzaei [2016] and discretizing the 3-D medium into cubical cells with center coordinates of  $\{X_i, Y_i, Z_i\}$ , PCDs are assigned with volume changes of

$\mathbf{dv} = [dv_1, \dots, dv_i, \dots, dv_m]^T$ ,  $i = 1, \dots, m$  to each cell center, where  $m$  is the number of

parameters. The relation between volume change distribution  $\mathbf{dv}$  and surface LOS

deformation  $L = [L_1 \cdots L_j \cdots L_l]^T$ ,  $j = 1, \dots, l$  is formularized as



$$L = G\mathbf{d}\mathbf{v} + \mathbf{e} \quad (3.7)$$

where  $l$  is the number of observations and  $\mathbf{e}$  is the vector of observation residuals. Within  $G$ , the matrix of Green's function, also commonly called the design matrix, each component on row  $i$  and column  $j$  relates the  $i$ th source cell to the corresponding LOS deformation at the  $j$ th observation point on surface and is computed using equation (3.6) and a unit range vector of the SAR satellite.

Equation (3.7) is often solved by minimizing  $\|L - G\mathbf{d}\mathbf{v}\|_2^2$ , which requires a full ranked design matrix  $G$ . Given that such design matrices are often poorly conditioned, namely, rank is less than the number of unknowns [Bjerhammar, 1973], to obtain a unique and robust solution, a penalty term  $p(\mathbf{d}\mathbf{v})$  is introduced, which makes the solution feasible [Smith and Coit, 1997]. Thus, the revised form of the objective function is

$$\arg \min_{\mathbf{d}\mathbf{v}} \|L - G\mathbf{d}\mathbf{v}\|_2^2 + p(\mathbf{d}\mathbf{v}) \quad (3.8)$$

Tikhonov regularization presented by  $\lambda^2 \|\Gamma \mathbf{d}\mathbf{v}\|_2^2$  is a popular penalty term [Tikhonov and Arsenin, 1977].  $\lambda^2$  controls amount of penalty. Depending on the purpose of regularization,  $\Gamma$  can be an identity matrix, gradient operator, or Laplacian operator, respectively, to acquire minimally perturbed, flat (or zero gradient), and smooth solutions. An efficient way to solve Tikhonov regularization is through the data augmentation approach [Golub and Van Loan, 2012]. Incorporating the penalty term, equation (3.8) is equivalent to solving the following least-squares problem:

$$L_a = G_a \mathbf{d}\mathbf{v} + \mathbf{E} \quad (3.9)$$

where  $L_a = [L, 0]^T$  and  $G_a = [G, \lambda\Gamma]^T$  are the augmented observation vector and the design matrix, respectively, and  $\mathbf{E} = [\mathbf{e}, 0]^T$  is the observation residuals. The regularized

solution of equation (3.9) is given by  $(G_a^T G_a)^{-1} G_a^T L_a$ . As shown in Figure 3.3a, all components in the solution are nonzero for L2-norm penalty problem.

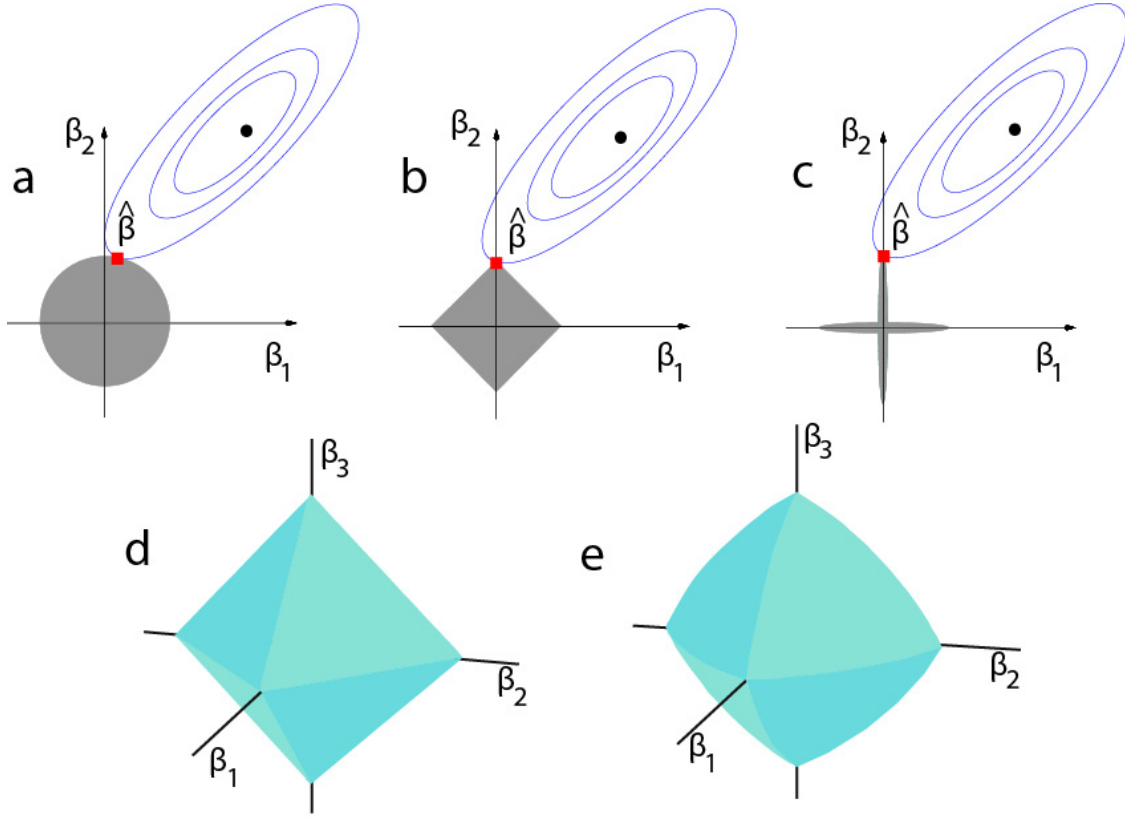


**Figure 3.3.** (a–c) Comparison of L2-, L1-, and L0-norm minimization in the two-dimensional (x, y) plane. The solid gray areas are the constraint regions. The blue ellipses are the contours of the residual sum of squares function. The constrained solution is defined by the red square ( $\hat{\beta}$ ) at the intersection of the blue ellipse and the gray area. The black point depicts the least squares solution without constraint. The L1-norm minimization generally produces a sparse solution similar to L0-norm minimization. In this 2-D case, one of the components is exactly zero. (d, e) The (e) elastic-net ball with  $\lambda^2/\alpha = 0.5$ , compared to the (d) L-1 ball. The curved surface (Figure 3e) encourages a grouping effect on strongly correlated variables.

In addition to the L2-norm penalty term, some other norms can be used to serve particular purposes. For instance, at active volcanos, the zone of molten rock is often well localized, and the geometrical and physical properties are distinct compared with host rock. Thus, it is reasonable to seek an optimum solution to equation (3.7) that fulfills some

sparsity criterion, namely, only a small fraction of parameter vector is nonzero. One effective penalty term to obtain a sparse solution is  $p(\mathbf{d}\mathbf{v}) = \alpha \|\mathbf{d}\mathbf{v}\|_0$ , where  $\alpha$  is the penalty factor controlling the degree of sparsity. An L0-norm optimization problem (Figure 3.3c) is nonconvex and is computationally expensive by an order  $2^m$ , which is impractical when the number of unknowns is large (e.g.,  $m > 20$ ). Alternatively, one can use an L1-norm penalty term (Figure 3.3b) [Figueiredo et al., 2007], which approximates properties of the L0 solutions [Donoho, 2006a; Donoho, 2006b]. The broad applications of L1-norm based sparsity-promoting optimization include data compression [Candes and Tao, 2006], digital image processing for object recognition [Mutch and Lowe, 2006], digital signal processing for source localization with sensor array [Malioutov et al., 2005], medical imaging [Lustig et al., 2007; Winters et al., 2010], and geophysical inversions [Charl  ty et al., 2013; Evans et al., 2015; Evans and Meade, 2012; Gholami and Siabkoobi, 2010; Yao et al., 2011; Yao et al., 2013]. The penalty term associated with L1-norm regularization is of the form  $p(\mathbf{d}\mathbf{v}) = \alpha \|\mathbf{d}\mathbf{v}\|_1$ ; thus, the objective function in equation (3.8) is revised as

$$\arg \min_{\mathbf{d}\mathbf{v}} \|L - G\mathbf{d}\mathbf{v}\|_2^2 + \alpha \|\mathbf{d}\mathbf{v}\|_1 \quad (3.10)$$

Minimization using an L1 penalty term is successfully used to recover sparse solutions; however, when parameters are strongly correlated, it may fail to find the optimum sparse solution, namely, the solution may become overly sparse [Zou and Hastie, 2005]. Figures 3.3b and 3.3d show that for an L1 penalty problem, the optimal model has only one nonzero component in the vector of model variables. This is because minimization with the L1 penalty always seeks the sparsest solution. To overcome this limitation, a combination of L1 and L2 penalty terms, so-called elastic net [Zou and Hastie, 2005], is commonly used:

$$\arg \min_{\mathbf{d}\mathbf{v}} \|L - G\mathbf{d}\mathbf{v}\|_2^2 + \lambda^2 \|\Gamma \mathbf{d}\mathbf{v}\|_2^2 + \alpha \|\mathbf{d}\mathbf{v}\|_1 \quad (3.11)$$

where  $\Gamma$  is defined as Laplacian operator that is calculated using the finite-difference approximation [Zhai and Shirzaei, 2016]. The great advantage of minimization with mixed penalty regularization is that (1) the solution space is strictly convex, in contrast to that of minimization using only an L1 penalty term and (2) it encourages a grouping effect, where strongly correlated variables tend to be in or out of the model together. The elastic net allows for selecting groups of correlated variables (Figure 3.3e), required by the L2-norm penalty term while remaining sparse as dictated by the L1-norm penalty term. It can be transformed to an equivalent minimization problem using L1 penalty term using the notation of equation (3.9):

$$\arg \min_{\mathbf{dv}} \|\mathbf{L}_a - \mathbf{G}_a \mathbf{dv}\|_2^2 + \alpha \|\mathbf{dv}\|_1 \quad (3.12)$$

The objective function in equation (3.12) is known as Least Absolute Shrinkage and Selection Operator and is also presented in the following form [Tibshirani, 1996]:

$$\arg \min_{\mathbf{dv}} \|\mathbf{L}_a - \mathbf{G}_a \mathbf{dv}\|_2^2, \text{subject to } \|\mathbf{dv}\|_1 \leq \tau \quad (3.13)$$

Equations (3.12) and (3.13) are equivalent and the solutions coincide when parameters  $\alpha$  and  $\tau$  are appropriately chosen [Van Den Berg and Friedlander, 2008]; however, implementing equation (3.13) is more straightforward [Evans and Meade, 2012; Van Den Berg and Friedlander, 2008].

In equation (3.13), the tuning parameter  $\tau$  can be approximated based on observed surface deformation data. Assuming an elastic medium, the total volume change underneath the surface is not model-dependent and is only a function of surface deformation [D'Auria et al., 2012]. Geertsma [1973] uses nuclei theory to show that total volume change observed at the Earth's surface is  $2(1 - \nu)$  times the volume change in a subsurface reservoir, which is consistent to more recent results [Walsh, 2002]. The expression of total volume change

beneath the surface based on InSAR observation is given by *Shirzaei et al.* [2015]. Assuming monotonic surface deformation, the only meaningful solutions are those of which volume changes are pervasively positive or negative [De Natale and Pingue, 1992]. Thus, the total volume change can be estimated by

$$\|\mathbf{dv}\|_1 = \left| \sum_{i=1}^m dv_i \right| = V_c, V_c = \left| \frac{\iint_{R^2} L \, dx dy}{2(1-v)c_z} \right| \quad (3.14)$$

where  $L$  is LOS displacement,  $v$  is the Poisson's ratio with value set to be 0.25, and  $c_z$  is the vertical component of the unit range vector of the SAR satellite ( $\sim 0.92$  for Envisat). Due to incompleteness of observed surface deformation and data noise, the calculated  $V_c$  from equation (3.14) may not be accurate, yet it serves an excellent starting point. Thus, using a Pareto curve [Hennenfent et al., 2008; Van Den Berg and Friedlander, 2008] to find the best  $\tau$  yielding optimal solution of equation (3.13), the possible value of  $\tau$  within the following range is systematically examined:

$$(1 - \varepsilon)V_c \leq \tau \leq (1 + \varepsilon)V_c \quad (3.15)$$

where  $\varepsilon$  is a value between 0 and 1. The tests indicate that this range is wide enough to identify optimum  $\tau$  in most cases.

### 3.3.2.1.2 Refining the Source Sparsity

Although by including an L2-norm penalty factor, a grouping effect is produced, namely, it eliminates oversparse solutions, various selections of  $\lambda$  may result in artifacts (small but nonzero values) in the sparse solution [Zou and Hastie, 2005]. To mitigate this effect, a statistical framework is implemented to eliminate insignificant elements of the solution vector, enhancing model sparsity while still explaining the observed surface

deformation. Assuming  $\widehat{\mathbf{d}\mathbf{v}}$  is the vector of optimum volume change distribution obtained from equation (3.13), then

$$\hat{\mathbf{L}} = \mathbf{G}\widehat{\mathbf{d}\mathbf{v}} \quad (3.16)$$

where  $\hat{\mathbf{L}}$  is the predicted surface LOS displacement. By removing insignificant elements (i.e., setting them to be zero) in  $\widehat{\mathbf{d}\mathbf{v}}$ , the updated vector of volume changes  $\widehat{\mathbf{d}\mathbf{v}}'$  and associated predicted observation  $\hat{\mathbf{L}}'$  are obtained. Defining the residual vector  $\mathbf{r} = \hat{\mathbf{L}} - \hat{\mathbf{L}}'$  and assuming a normally distributed error, the variables  $\frac{r_i}{\sigma}$ ,  $i = 1, \dots, m$ , follow a standard normal distribution  $N(0,1)$ , where  $\sigma$  is the standard deviation of residuals, a function of observation error and distribution and model setup.  $\frac{\mathbf{r}^T \mathbf{r}}{\sigma^2}$  follows a chi-square distribution ( $\chi^2$ ) with  $n - m$  degrees of freedom. By specifying a significance level of  $\vartheta$ , the confidence interval of  $\mathbf{r}^T \mathbf{r}$  is given by

$$0 < \mathbf{r}^T \mathbf{r} < \sigma^2 \chi_{n-m, 1-\vartheta}^2 \quad (3.17)$$

The elements in vector  $\widehat{\mathbf{d}\mathbf{v}}$  with absolute value close to zero are likely to be artifacts and thus are set to zero. The goal is to eliminate as many as possible insignificant elements, while maintaining that the residual vector satisfies equation (3.17).

Implementing this statistical framework to identify insignificant PCDs may introduce some errors because the solution  $\widehat{\mathbf{d}\mathbf{v}}$  is an approximation of the optimum solution without knowing the true sparse model. Therefore, an approach that iterates between estimating  $\widehat{\mathbf{d}\mathbf{v}}$  through penalized least squares and refining the model sparsity through a statistical test is proposed. Thus, the algorithm with  $k$  iterations is designed as follows:

1. When  $k = 0$ , obtain the initial solution  $\widehat{\mathbf{d}\mathbf{v}}^{(k)}$  using equation (3.13) and identify subset of insignificant elements,  $\mathbf{S}_{d\mathbf{v}}^{(k)}$ , using the statistical test provided in equation (3.17).

2. When  $k > 0$ , solve the sparsity-constrained subject to

$$\widehat{\mathbf{d}\mathbf{v}}^{(k)} = \arg \min_{\mathbf{d}\mathbf{v}} \|\mathbf{L}_a - \mathbf{G}_a \mathbf{d}\mathbf{v}\|_2^2, \text{ subject to } \|\mathbf{d}\mathbf{v}\|_1 \leq \tau, \mathbf{S}_{\mathbf{d}\mathbf{v}}^{(k-1)} = 0 \quad (3.18)$$

The iterations stop once  $\mathbf{S}_{\mathbf{d}\mathbf{v}}$  reaches the steady state, namely, the number of insignificant PCDs remains constant with an increasing number of iterations, or  $k$  reaches a specified maximum number of iterations  $k_{max}$ .

### 3.3.2.2 Solving for Source Strength and Displacement Discontinuity Distribution

A hybrid L1- and L2-norm regularization approach for inverting deformation data allows for constraining a sparse model composed of the 3-D location, size, and irregular geometry of the volcanic source. The irregular surface surrounding this sparse model can also be used to develop a mesh with triangular elements [Beauducel *et al.*, 2004; Maerten *et al.*, 2005]. This mesh represents the magma chamber as a closed surface, which can be used to solve for the displacement discontinuity distribution to investigate the associated chamber evolution assuming that the chamber surface is only affected by tensile tractions. The triangular patches are assumed to be embedded in an elastic, isotropic, and homogeneous half-space medium with zero tractions on the free surface and shear modulus and Poisson's ratio of 20 GPa and 0.25, respectively. To solve for the displacement discontinuity distribution on the surface of the magma chamber, a BEM, which relates displacement discontinuities to the boundary conditions on the surface of the magma chamber through the coefficient matrix  $\mathbf{A}$  [Liu *et al.*, 2011; Thomas, 1993], is implemented. More extensive readings on this topic are referred to Gaul *et al.* [2003] and Liu [2009]. The coefficient matrix is a function of source geometry and mechanical properties of the medium. The boundary conditions include tensile traction equals a uniform pressure  $p$  and shear tractions vanish on

each triangular patch. Thus, the primary unknown is  $\mathbf{p}$ . However, due to approximation errors, the source geometry determined in sparsity-promoting inversion may not be accurate enough. Therefore, a scaling factor  $\delta$  and three rigid shift parameters  $x_0$ ,  $y_0$ , and,  $z_0$ , which allow expanding/shrinking and translating the magmatic body, are additionally considered. Given the triangular mesh  $\Gamma$ , the system of equations to be solved is

$$\mathbf{T}(\mathbf{p}) = \mathbf{A}(\Gamma, \mu, \nu, \delta, x_0, y_0, z_0) \mathbf{s} \quad (3.19)$$

where  $\mathbf{s}$  is the vector of displacement discontinuities including the tensile, strike, and dip components of all triangles.  $\mathbf{T}$  is the traction vector containing only tensile tractions at each triangle, which equals to pressure change  $\mathbf{p}$ .  $\mu$  and  $\nu$  are shear modulus and Poisson's ratio, respectively.

In addition, to relate the displacement discontinuities to surface deformation, a solution of triangular dislocations [Nikkhoo and Walter, 2015] is applied:

$$\mathbf{L} = \mathbf{B}(\Gamma, \nu, \delta, x_0, y_0, z_0) \mathbf{s} \quad (3.20)$$

where  $\mathbf{B}$  is the design matrix containing Green's functions, which relates displacement discontinuities on triangular patches to surface deformation projected onto the SAR satellite LOS direction using a unit range vector.  $\mathbf{L}$  is the observed LOS surface displacement.

Equations (3.19) and (3.20) together form a system of nonlinear inverse problem with five unknowns of  $\delta$ ,  $x_0$ ,  $y_0$ ,  $z_0$ , and  $\mathbf{p}$ , which can be solved using a nonlinear optimization method [Shirzaei and Walter, 2009]. To account for residual errors due to satellite orbit and clock inaccuracy, the best-fitting plane is also solved for.



### 3.4 Algorithm Learning and Synthetic Test

Here the robustness of the presented approach for modeling irregular volcanic sources is investigated. Given the difficulty of linearizing a sparsity-constrained inversion problem, an analytical solution is unavailable, and using a conventional resolution matrix to assess posterior errors is not feasible [Franklin, 1970; Menke, 1984]. Therefore, several synthetic tests are performed. The checkerboard test is a widely used synthetic model to test the performance of an inversion method, which is highly dependent on the pattern of the model expected to retrieve [Lévéque et al., 1993]. Given that the presented inversion scheme is designed to recover sparse models, the synthetic sources for simulating observation should be sparse. Therefore, several complex sparse volcanic sources are simulated, and through forward modeling, the associated surface deformation is calculated. This synthetic surface deformation will then be inverted to solve for simulated volcanic sources.

Five synthetic sources with 3-D geometries are considered, including a sphere, prolate ellipsoid, torus, and vertical and horizontal L shaped chambers (Figure 3.5), and generate the associated LOS deformation fields at a resolution of 50 m. To invert the simulated observations and recover the synthetic sources using the approach presented in section 3.3.2.1, the model medium is discretized into cubic cells of 0.1 km dimension with a PCD at the center of the cell. Moreover, before implementing the inversion, the parameters of the inversion approach, which includes a smoothing factor  $\lambda$ , tuning parameter  $\tau$ , standard deviation  $\sigma$ , and iteration number  $k$ , need to be set up. To this end, the inversion problem can be viewed as a mapping operator that projects observation  $\mathbf{L}$  onto the parameter space  $\mathbf{dv}$  [Alpaydin, 2014]. This mapping operator,  $f(\cdot)$ , returns the optimum solution of the regularized inversion and has a generalized form of

$$d\mathbf{v} = f(L|\lambda, \tau, \sigma, k) \quad (3.21)$$

where the tuning parameter  $\tau$  can be determined using a Pareto curve [Hennenfent *et al.*, 2008; Van Den Berg and Friedlander, 2008]. Considering the purpose of a synthetic test, the value of  $\tau$  is initialized with the absolute value of volume change associated with each synthetic model. The Laplacian operator,  $\Gamma$ , designed in the presented approach is used to stabilize the inversion and enforce the grouping effect on model variables, and smoothing factor  $\lambda$  is selected from an interval  $[0, 1]$ . To refine the model sparsity, a confidence level of 5% for  $\vartheta$  is considered. The standard deviation of residuals,  $\sigma$ , can be estimated through rigorous analysis of error variance–covariance propagation at each iteration  $k$ . However, a value between 1 and 10% of the largest surface deformation yields reasonable results based on many tests.

Here an iterative algorithm is implemented to identify optimum values of the hyperparameters (so-called algorithm learning in Figure 3.4a). However, to reduce the computation time, these parameters for one source is estimated and then investigation is made to explore if these parameters can be directly used to recover other synthetic sources. To this end, a spherical source is used as the reference and a standard Monte Carlo search algorithm is applied to systematically examine the different combinations of hyperparameters. It is found that  $\lambda = 10^{-4}$ ,  $kmax = 5$ , and  $\sigma$  being 5% of the largest surface deformation provide the best estimates of the reference source (Figure 3.5a). In the following steps, the same hyperparameters are used to recover deformation sources associated with a prolate ellipsoid, vertical L shape, horizontal L shape, and torus. There is good agreement between synthetic and recovered sources (Figures 3.5b–3.5e), and the model fit to simulated observations is reasonable (Figure B.1 in the appendix).

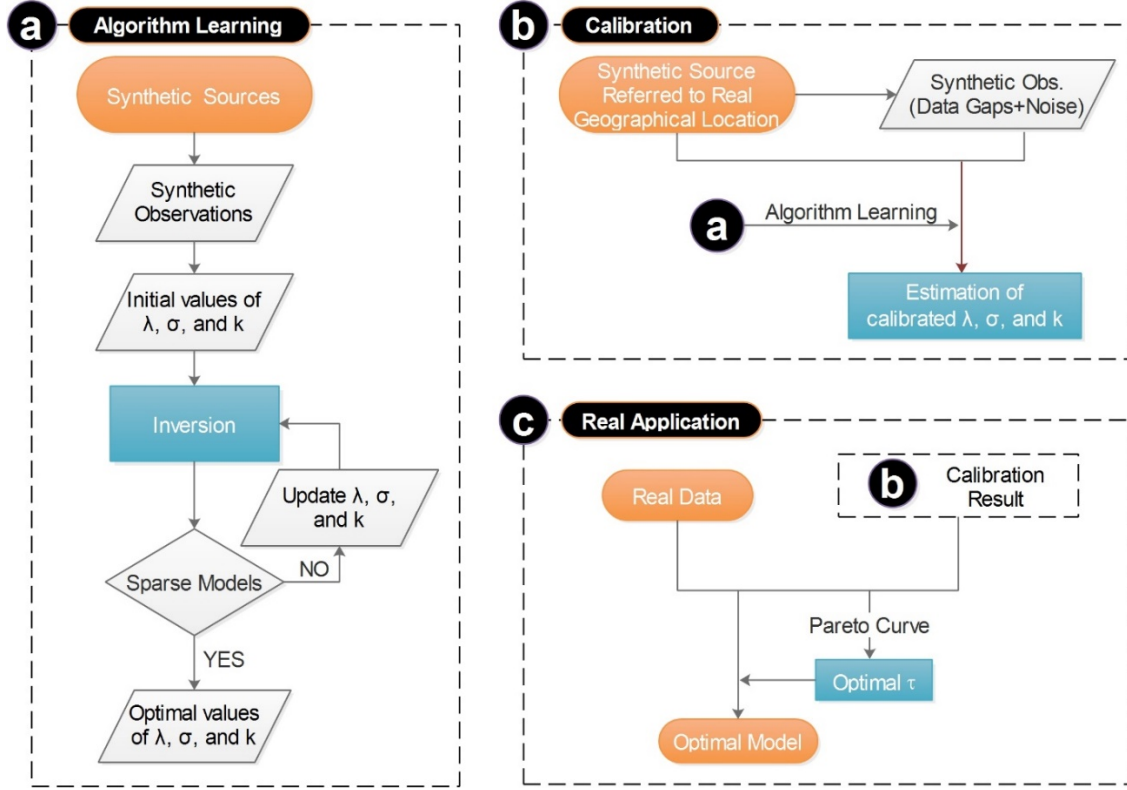


**Figure 3.4.** Workflow chart. Three modules are designed to implement the sparsity-promoting algorithm. Module (a): Using synthetic sources to learn the algorithm and show the performance of the inversion method. Module (b): Using a synthetic source referred to the real geographical location to calibrate the hyperparameters associated in the algorithm for inversion of the real data set. Module (c): Applying the calibrated hyperparameters and inversion method to real data.

To further investigate the effect of data noise on inversion results, the synthetic tests are repeated using the sphere and vertical L shaped geometries, which were the most challenging in previous tests, and 5% colored noise is added to the corresponding simulated InSAR LOS deformation. Considering real case studies of InSAR observation (discussed later) and the precision of multitemporal processing ( $\sim 5$  mm for displacement; *Shirzaei et al.*, 2015), 5% colored noise is chosen here to serve as lower bound to evaluate the performance of the inversion method. The optimal hyperparameters  $\lambda$ ,  $kmax$ , and  $\sigma$  are found to be 0.3,

6, and 5% of largest deformation, respectively. Despite noisy observations, the source sizes and shapes are well recovered compared with the synthetic geometries (Figure 3.6), and the model fit to simulated data is satisfactory (Figure B.2). Based on these synthetic tests, it is concluded that hyperparameters are geometry-independent, as long as the model resolution remains similar and the same hyperparameters can be used to recover sources of different geometries. Also, observation noise affects the results, yet the effect remains in the acceptable range, as long as the majority of systematic errors are removed through proper filtering techniques.

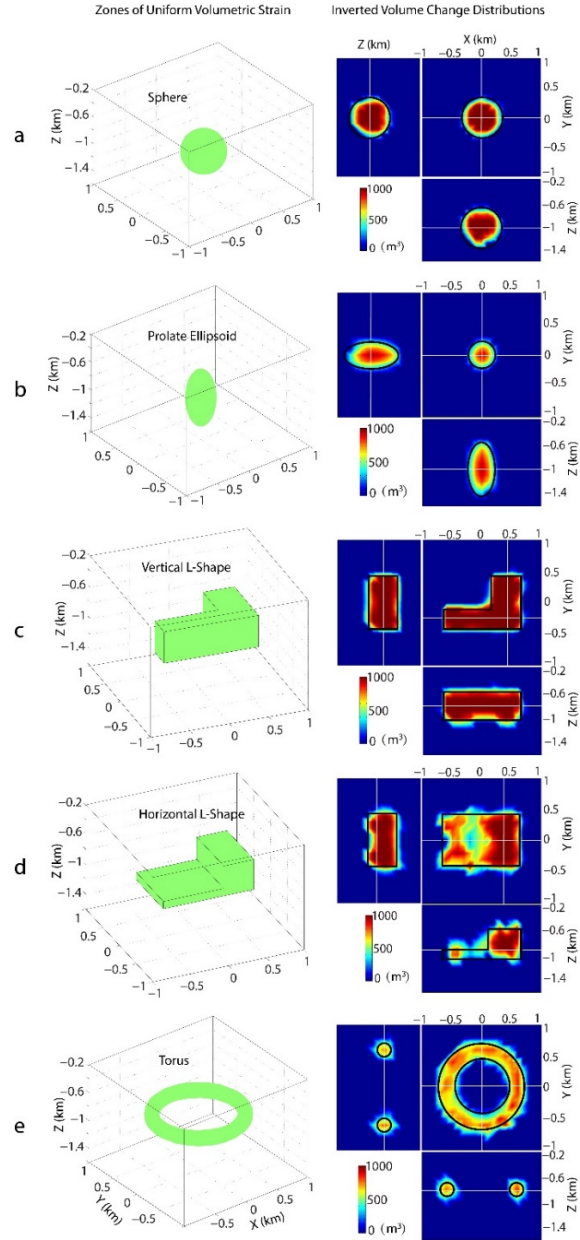


**Figure 3.5.** Algorithm learning using synthetic tests with five different shapes: (a) sphere, (b) prolate ellipsoid, (c) vertical L shape, (d) horizontal L shape, and (e) torus. (left panel) Zones of uniform volumetric strain. (right panel) Inverted volume change distribution. The model domain has dimensions of  $(-1, 1)$  km in east,  $(-1, 1)$  km in north, and  $(0.2, 1.6)$  km in depth. White lines mark the cross sections. Black circles and polygons show corresponding spatial extensions of synthetic

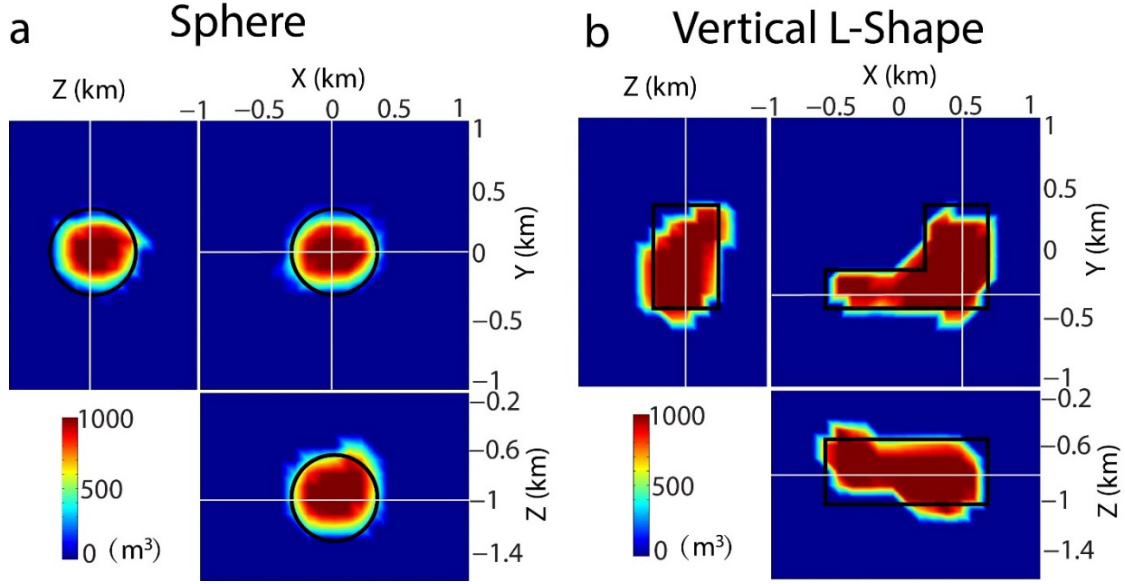


**Figure 3.6.** Synthetic tests considering data noise in the simulated LOS deformation using a sphere and vertical L shape in Figure 4. (a) Inverted volume change distributions for sphere. (b) Inverted volume change distributions for vertical L shape. White lines mark the cross sections. Black circles and polygons show corresponding spatial extensions of the synthetic sphere and vertical L shape sources.

### 3.5 Application to Kilauea Volcano

Kilauea on Hawaii Island is one of the most active volcanoes around the world, acting as a natural laboratory for investigating subsurface volcanic processes associated with basaltic magmatism due to its high frequency of magmatic intrusions and eruptions. The volcanic tectonics of Kilauea are characterized by a 5 km wide summit caldera from which two rifts originate to the southwest and east, forming narrow boundaries between the northern stable sector of the Kilauea edifice and the mobile southern flank situated on a subhorizontal fault system [Cayol *et al.*, 2000]. Magma rising from a deep source [Gonnermann *et al.*, 2012; Wright and Klein, 2006] is thought to be stored in a shallow magma reservoir [Baker and Amelung, 2012; Cervelli and Miklius, 2003; Delaney *et al.*, 1990]. The shallow magma reservoir is a key element of Kilauea's plumbing system [Eaton and Murata, 1960], which acts as a waypoint to feed rift zone intrusions [Montgomery-Brown *et al.*, 2010] and sustain summit eruptions [Carbone *et al.*, 2013].

Kilauea hosts a long history of documented unrest. Eruptive activity was concentrated at the summit caldera until 1955 when eruptions became more common in the east rift zone. Notable eruptive episodes did occur from 1972 to 1974 [*Lockwood et al.*, 1999] and from 1981 to 1983 [*Klein et al.*, 1987] at the summit caldera. For the next 20 years, subsidence was the predominantly observed deformation pattern at the summit area of Kilauea. Simultaneously, the Pu'u O'o–Kupaianaha vents on the east rift zone experienced almost continuous eruptive activities. Starting in late 2003, the summit deformation mode switched from deflation to inflation [*Miklius et al.*, 2005] due to a new surge of magma supply into shallow magma plumbing system [*Poland et al.*, 2012]. The summit inflation culminated in 2007, followed immediately by a small fissure eruption on the east rift zone (called the Father's Day event) and by a summit eruption in Halemaumau crater in 2008 [*Patrick et al.*, 2013]. After the inflation period, the summit deflated from 2007 until mid-2010, followed by reinflation [*Lundgren et al.*, 2013].

Previous geophysical and geochemical investigations including ground deformation, seismicity, gravity, and isotopes mainly focused on different centers of inflation and deflation associated with the Kilauea summit shallow reservoir [*Baker and Amelung*, 2012; *Battaglia et al.*, 2003; *Cervelli and Miklius*, 2003; *Fiske and Kinoshita*, 1969; *Johnson et al.*, 2010; *Lundgren et al.*, 2013; *Pietruszka et al.*, 2015; *Yang et al.*, 1992]. The diversity of the source locations from those results likely suggests complex magmatic reservoirs with irregular geometry beneath Kilauea summit, given that different parts of a magma reservoir are active during distinct time periods [*Gudmundsson*, 2012]. In order to investigate the source geometry, the presented sparsity-promoting inversion approach is applied to InSAR LOS deformation observed at Kilauea's summit for two periods: 2005–2007 and 2007–2010. After determining source geometry, the surface deformation is inverted to solve for the tensile displacement

discontinuity distribution on the periphery of the constrained source to examine the details of the kinematics of the magma chamber. The results from this modeling method provide additional insights into the dynamics of Kilauea's summit reservoir.

### 3.5.1 Data Sets

The time series of surface deformation at the Kilauea volcano is generated using an advanced multitemporal InSAR algorithm [Shirzaei, 2013; Shirzaei and Bürgmann, 2013; Shirzaei *et al.*, 2013] for the period 2003–2010. The SAR data set includes 100 images and 38 images acquired in descending (track 200 and 429) and ascending (track 93) orbit of the Envisat satellite. The details of processing and validation are provided in [Zhai and Shirzaei, 2016]. The effect of mobile southern flank on the surface deformation of both viewing geometries is corrected using a long-term decollement slip model. The LOS velocity map and the time series of the displacement field at a selected point inside the summit area for descending orbit are shown in Figure 3.7. To implement the modeling scheme, two periods with rapid changes in the pattern of observed surface deformation are selected (Figure 3.7b), including the inflation period from December 2005 to May 2007 leading to the Father's Day eastern rift intrusion in July 2007 and the deflation period from May 2007 to May 2010 following the event. The inflation period accumulated up to 25 cm and 23 cm of uplift in descending and ascending viewing geometries, respectively, south of the Kilauea caldera (Figure B.4), whereas during the deflation period, the location of maximum subsidence of 43 cm and 46 cm in descending and ascending viewing geometries, respectively, is at the southern rim of the caldera (Figure B.5). The different patterns of deformation distribution may reflect source geometrical complexities during the corresponding periods.

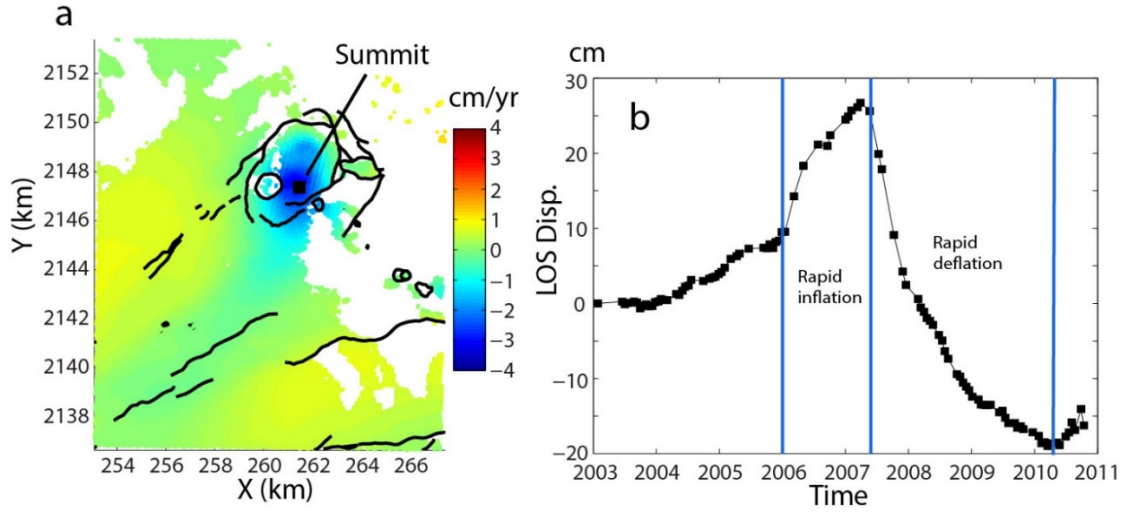


**Figure 3.7.** Descending InSAR processing result at Kilauea. (a) Velocity map of surface deformation along the LOS direction at the summit area. The effect of slip on decollement is removed from the InSAR time series. (b) Time series of LOS deformation for a selected point at the summit area. Rapid inflation and deflation periods are investigated.

### 3.5.2 Inversion Parameter Setup

To apply the presented inversion scheme to Kilauea deformation data, hyperparameters  $\lambda$ ,  $\sigma$ , and  $k$  (Figure 3.4b) are first needed to be calibrated. As noted earlier, hyperparameters are a function of the model resolution and observation quality but not a function of source geometry. Therefore, a synthetic model is used to estimate optimal hyperparameters based upon the actual model setup and observation locations at Kilauea. The model domain is set to be a cuboid, with dimensions of  $\sim 14$  km in east,  $\sim 17$  km in north, and 6 km in depth, which is discretized into 6,615 PCDs, with spacing of 0.8 km, 0.8 km, and 0.4 km in respective directions. The effect of data gaps is considered and the actual distribution of InSAR surface deformation data in descending orbit, as shown in Figure 3.7a, are used. Using this model domain and observation locations, surface deformation (Figure 3.8a) associated with a spherical zone of uniform volumetric strain with radius of 1.2 km and center depth of 3 km (informed based upon previous studies) is simulated. To mimic a realistic scenario, a colored noise with a standard deviation of 5 mm (Figure B.3), obtained



from comparing InSAR time series with independent observations [Shirzaei, 2015], is added. Implementing the iterated approach shown in Figure 3.4a, different combinations of hyperparameters are examined with variations of  $\lambda$  between 0 and 1,  $\sigma$  between 1% and 10% of largest deformation, and  $k$  between 1 and 20. The optimum parameters of  $\lambda$ ,  $\sigma$ , and  $k$  are 0.2, 5%, and 8, respectively. Using these hyperparameters, the synthetic surface deformation is inverted to solve for distribution of volume change (Figure 3.8b). Model prediction and residuals are shown in Figures 3.8c and 3.8d. The other complex source geometries are also successfully constrained using these hyperparameters, given the same model resolution, observation distribution, and data noise at Kilauea. Therefore, these optimum values will be used to inform the optimization algorithm (Figure 3.4c) for inverting actual surface deformation observations during both uplift and subsidence periods at Kilauea.

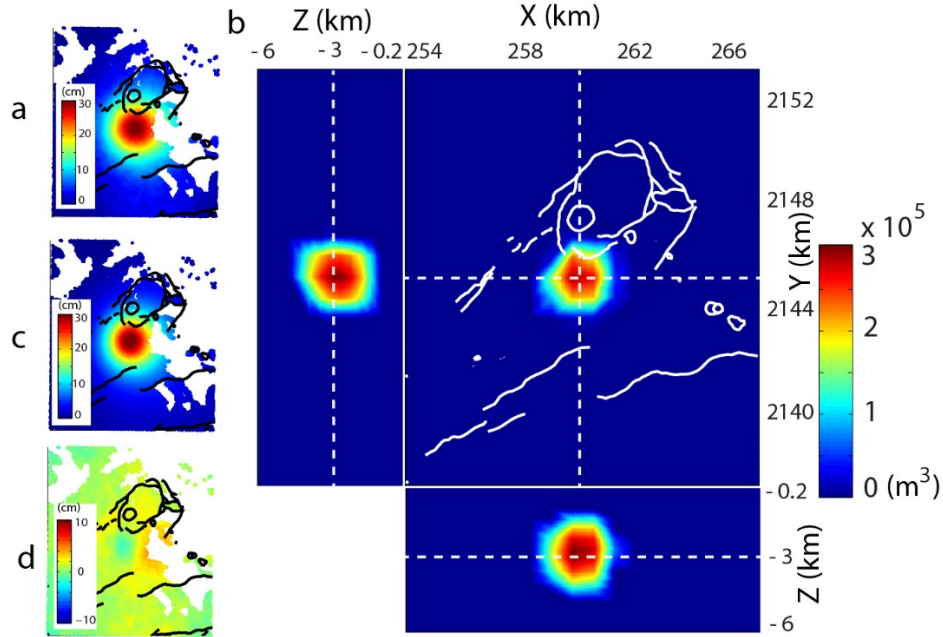


**Figure 3.8.** Result of calibration test referred to Kilauea summit area using a synthetic spherical zone of uniform volumetric strain as the deformation source with a center depth of 3 km and radius of 1.2 km. (a) Simulated surface deformation from the synthetic spherical source. Colored noise is considered. (b) The inverted volume change distribution. (c) The predicted surface deformation from the inverted sparse model in Figure 8b. (d) Misfit of surface deformation (Figure 8a–8c).

### 3.5.3 Model Result

Using the optimized  $\lambda$ ,  $\sigma$ , and  $k$ , the initial value of tuning parameter  $\tau$  for uplift and subsidence periods is set up using equation (3.14), which is optimized with a Pareto curve [Charl  y *et al.*, 2013; Hennenfent *et al.*, 2008; Van Den Berg and Friedlander, 2008]. A Pareto curve relates chi-square of misfit to the L1-norm of parameters, and the optimum value of  $\tau$  corresponds to the location of maximum curvature on it. The Pareto curve is constructed by investigating values adjacent to those obtained from equation (3.14), controlled by the nondimensional parameter  $\epsilon$  in equation (3.15). The choice of  $\epsilon$  depends on the characteristics of surface deformation, such as data noise, coverage, gaps, and spatial resolution. For the case study,  $\epsilon = 0.3$  is an appropriate choice to acquire a typical Pareto curve, as discussed below.

#### 3.5.3.1 Uplift Period

Figure 3.9a shows the Pareto curve and the optimum value of  $1.17 \times 10^7 \text{ m}^3$  for tuning parameter  $\tau$ . Using the optimum hyperparameters, the inversion algorithm is implemented to find the sparse model of an inflating magmatic source constrained by uplift data. Figure 3.9b shows the pattern of inverted sparse volume change distribution along three profiles. The optimum model includes a concentrated zone of volume distribution south of the summit caldera. The plan view shows that the body is pear-shaped with a tail stretching to the upper seismic southwest rift zone. The observed and predicted LOS displacements for both descending and ascending viewing geometries indicate good fits to the data (Figure B.4). A slightly larger residual for the ascending data set can be due to the orbit of satellite being perpendicular to the southwest rift zone, which degrades sensitivity of ascending measurements to the rift-perpendicular displacements. Once the geometry and location of



cm and 2.1 cm for descending and ascending data sets, respectively. The optimum pressure change is 4.6 MPa inside the magmatic body. The magnitude of strike and dip components are average less than 10% of the tensile component and are not discussed further. The obtained tensile displacement discontinuity distribution on the triangular mesh is shown in Figure 3.10a. It indicates that the magma body expands vertically at the top and bottom with negligible expansion on its sides. The greatest openings happen at the top of the magma body.

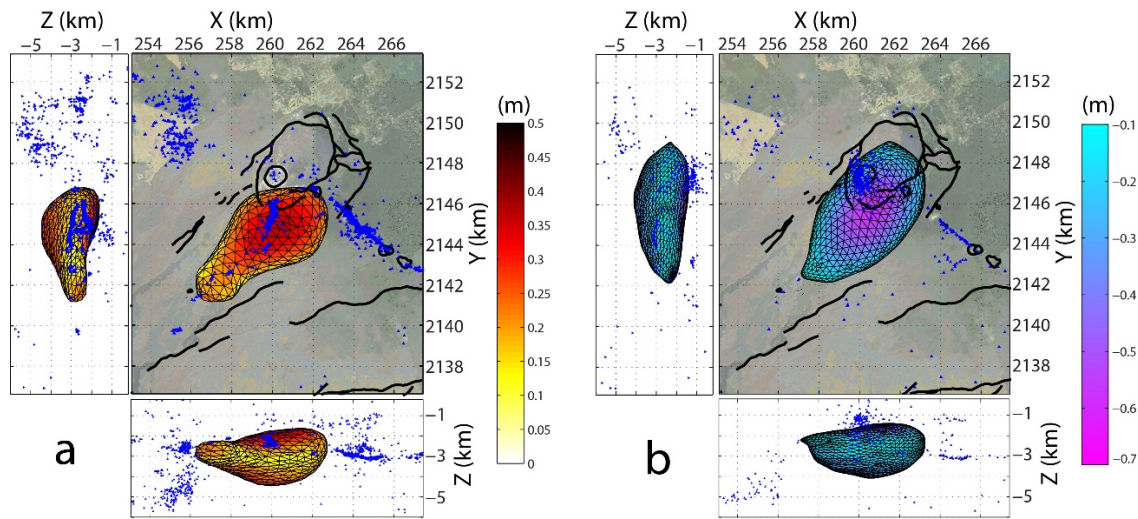


**Figure 3.10.** Tensile slip models from BEM modeling for (a) inflation and (b) deflation periods in side views. The shapes are generated to approximate the inverted sparse distribution of volume change associated with each time period. Blue triangles are seismicity during the corresponding time periods.

### 3.5.3.2 Subsidence Period

For the subsidence period, the Pareto curve (Figure 3.9c) indicates an optimal tuning parameter of  $1.44 \times 10^7 \text{ m}^3$ . The inversion result of the volume change distribution is shown in Figure 3.9d, which comprises a magmatic body of  $\sim 37.3 \text{ km}^3$  volume. The data fit shown in Figure B.5 presents a satisfactory agreement between observed and modeled displacement fields. Profiles show that the constrained body is a NE–SW oriented, horizontal, prolate ellipsoid extending from inside the caldera to the upper seismic southwest rift zone. The

tensile displacement discontinuity distribution from BEM modeling is shown in Figure 3.10b and the optimum pressure change is  $-3.9$  MPa. The optimal model has a RMSE of 2.7 cm and 3.1 cm for descending and ascending data sets, respectively (Figure B.7). The tensile displacement discontinuity model shows that closings happen at top and bottom of the body with weak behavior along the sides.

### 3.6 Discussion

A two-step volcanic source modeling scheme that allows imposing a realistic pressure boundary condition on an irregularly shaped magmatic body constrained based on the geodetic observations is proposed. The first optional step is to apply an iterative sparsity-promoting inversion approach to image irregular volcanic reservoirs based on ground deformation data. This step is optional as one can instead use the source geometry constrained using any other methods such as seismic tomography. Applying the method, the algorithm hyperparameters are optimized using synthetic tests through an algorithm learning procedure. The majority of hyperparameters including the smoothing factor, residuals standard deviation, and iteration number are geometry-independent and only depend on model resolution and distribution of surface deformation data. This allows for optimizing hyperparameters through a limited number of synthetic tests and then using them for a wide range of modeling exercises, as long as the model setup and observation distribution remain unchanged. Once the irregular geometry of the magmatic source is constrained in the first step (or obtained using other methods), in the second step a boundary element method is applied to impose physical boundary conditions and solve for the uniform pressure inside the reservoir. The entire procedure is thoroughly validated using several synthetic examples and then applied to two episodes of rapid inflation and follow up deflation at Kilauea

volcano. To investigate real data sets, a similar concept is used and an additional calibration step is applied to identify hyperparameters relevant to the model set up (dimension and resolution) and distribution of deformation data.

### 3.6.1 Advances and Limitations of Two-Step Modeling

The presented inversion method can resolve the shape, size, and location of the magmatic source associated with zones of volume change underneath volcanoes. However, like other inversion methods its success depends on the quality and coverage of the surface deformation data as well as the resolution that is allowed by the model for solving details of the source geometry. The synthetic tests and real case studies, however, indicate several advantages of the proposed method compared to other volcanic source inversion techniques. For example, a source like a torus (or magma tube) is extremely hard to be resolved using conventional inversion approaches. While the inversion method can successfully resolve such geometries (Figure 3.5e). A major limitation of the PCD inversion is its inability to reconstruct deformation associated with a dike. That is because a magma overpressure within a dike can be approximated by a distribution of force couples perpendicular to the dike surface, while PCD includes three mutually orthogonal double forces. Although sill (horizontal dike) also consists of single double force, since the majority of the signal is vertical, the reconstruction of the associated signal using PCD is satisfactory, provided that the sill radius-to-depth ratio is sufficiently small. However, in most cases, dike sources can be identified by their distinct surface deformation pattern, and thus, the geometry can be constrained using a standard inversion technique, which can be used as an input to the next inversion step. Once the geometry is constrained, a BEM approach is applied to impose a realistic pressure condition and solve for uniform pressure inside the

magmatic body. Thus, in contrast to the analytical models [e.g., *Davis*, 1986; *McTigue*, 1987; *Mogi*, 1958], the presented approach allows for constraining the actual shape and dimension of the source.

Recently, major advances were made in investigating the physics of volcanic sources [*Anderson and Poland*, 2016; *Anderson and Segall*, 2011]. Yet one major disadvantage of these physics-based volcano source modeling techniques is the reliance on simple analytical models. This limitation can be overcome by combining the physics-based inversion methods with the approach presented here.

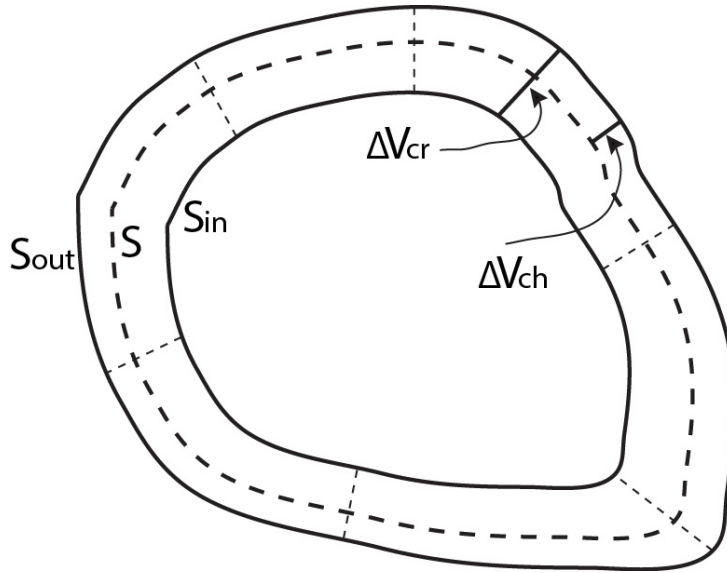


**Figure 3.11.** Schematic of magmatic source volume change represented as an enclosed tensile crack. The dashed line indicates the surface of the magma chamber. The inner wall of the crack moves from S to S<sub>in</sub>. The outer wall of the crack moves from S to S<sub>out</sub>. The volume change of crack  $\Delta V_{cr}$  is the sum of volume change caused by the inner wall and outer wall movements. The magma chamber volume change  $\Delta V_{ch}$  is caused by the movement of the outer wall.

### 3.6.2 Implications for Volcanic Source Volume Change

Volume change within a magma body is regarded as the cause of surface deformation and seismic signals. First order analytical models of magma chamber with simple geometries [e.g., *Davis*, 1986; *McTigue*, 1987; *Mogi*, 1958] are widely applied to investigate surface deformation at volcanoes and constrain the subsurface volume change. However, for more complex source geometries, closed mathematical expressions are not available. An alternative

method was presented to model irregular volcanic sources through a two-step procedure, which has the ability to constrain the irregular source geometry as an enclosed crack of dislocation satisfying a uniform pressure boundary condition. The source volume change can be estimated using a distribution of tensile crack openings and the surface area of the source. Although the surface observation is well explained, interpreting the estimated volume change is not trivial. *Müller* [2001] notices two different formulas for calculating seismic moment ( $M$ ) of an isotropic spherical/point source,  $M = (\lambda + 2\mu)\Delta V_{ch}$  and  $M = (\lambda + 2\mu/3)\Delta V_{cr}$ , where  $\lambda$  and  $\mu$  are the Lamé parameters and  $\Delta V$  is volume change. The volume change,  $\Delta V$ , in each formulation has different physical meanings, representing either the chamber mechanical volume change ( $\Delta V_{ch}$ ) or crack volume change ( $\Delta V_{cr}$ ), respectively (Figure 3.11). Crack volume change  $\Delta V_{cr}$  is the total volume change that resulted from a crack surface moving inward and outward. Volume change defined using a crack dislocation model corresponds to stress-free volume change [*Eshelby*, 1957] and provides the exact source moment [*Müller*, 2001]. However, mechanical chamber volume change  $\Delta V_{ch}$ , namely, the actual change in the source volume under confining pressure, is defined by the chamber surface moving outward, which is smaller than the crack volume change. This is due to the fact that filling a crack requires no additional moment to push away surrounding medium when the crack is thin [*Wielandt*, 2003]. The transformation from  $\Delta V_{cr}$  to  $\Delta V_{ch}$  is dependent on the shape of magma body. For isotropic sources, such as point source (the dimension is small enough) and spherical source, the relation between  $\Delta V_{cr}$  and  $\Delta V_{sph}$  is identical to equation (3.4):

$$\frac{\Delta V_{cr}}{\Delta V_{sph}} = \frac{\lambda + 2\mu}{\lambda + 2\mu/3} = \frac{3(1 - \nu)}{1 + \nu} \quad (3.22)$$



where  $\lambda$  and  $\mu$  are Lamé constants.  $\Delta V_{sph}$  is the volume change of a spherical chamber. For a source with the geometry of a prolate ellipsoid, the chamber volume change  $\Delta V_{pro}$  lies between  $\Delta V_{cr}$  and  $\Delta V_{sph}$ , but closer to  $\Delta V_{sph}$ , as concluded by *Müller* [2001] using a cylinder approximation of a prolate ellipsoid. Thus, for a geometry-free volcanic source, the actual chamber volume change ( $\Delta V_{ch}$ ) is within the range determined by  $\Delta V_{cr}$  as the upper bound and the equivalent volume change of a best approximating sphere as the lower bound [*Amoruso and Crescentini*, 2009]. In practical applications, if the source shape is close neither to a crack with tensile components nor to an isotropic inflation/deflation source, a range of volume changes should be estimated. The lower limit  $\Delta V_{sph}$  is readily calculated using upper limit  $\Delta V_{cr}$  (equation (3.22)), then following inequality holds:

$$\Delta V_{cr} \frac{1 + \nu}{3(1 - \nu)} \leq \Delta V_{ch} \leq \Delta V_{cr} \quad (3.23)$$

On the other hand and given the magma chamber compressibility,  $\beta_{ch}$ , which is dependent on shape and depth of magma chamber and host rock rigidity ( $\beta_{hr}$ ; *Amoruso and Crescentini*, 2009; *Rivalta and Segall*, 2008; *Segall et al.*, 2001), the exact value of  $\Delta V_{ch}$  can be calculated (Text B.1):

$$\Delta V_{ch} = \frac{\Delta V_{cr}}{(1 + \beta_{hr}/\beta_{ch})} \quad (3.24)$$

The compressibility of a chamber with a complex geometry can be numerically computed using a finite element method [*Anderson and Segall*, 2011]. However, the chamber compressibility can be constrained by applying its definition when pressure change  $p$  is known:

$$\frac{\Delta V_{ch}}{V} = p\beta_{ch} \quad (3.25)$$

where  $V$  is the source volume. Combining equations (3.24) and (3.25), then

$$\beta_{ch} = \frac{\Delta V_{cr}}{VP} - \beta_{hr} \quad (3.26)$$

$$\Delta V_{ch} = \Delta V_{cr} - Vp\beta_{hr} \quad (3.27)$$

At Kilauea, the appropriate value of shear modulus for the host rock is 5–25 GPa [Johnson *et al.*, 2000]. Here a value of 20 GPa is used, which is consistent with laboratory experiments using intact samples [Ryan, 1987a]. In the case studies, the crack volume changes are  $1.29 \times 10^7 \text{ m}^3$  and  $1.76 \times 10^7 \text{ m}^3$  for the uplift and subsidence periods, respectively. From equation (3.23), the chamber volume change for the uplift period is between  $0.72 \times 10^7 \text{ m}^3$  and  $1.29 \times 10^7 \text{ m}^3$ , while the range of chamber volume change for the subsidence period is between  $0.98 \times 10^7 \text{ m}^3$  and  $1.76 \times 10^7 \text{ m}^3$ . Moreover, given equations (3.26) and (3.27), the exact values of estimated chamber volume changes for both periods are  $0.89 \times 10^7 \text{ m}^3$  and  $1.32 \times 10^7 \text{ m}^3$ , respectively. The chamber compressibilities for both periods are  $0.66 \times 10^{-10} \text{ Pa}^{-1}$  and  $0.91 \times 10^{-10} \text{ Pa}^{-1}$ , respectively.

### 3.6.3 Implications for Reservoir Storage Change

In complex volcanic settings, such as Kilauea, where the magma chamber is coupled with the rift system [Segall *et al.*, 2001], the typical movement of magma to the rift zone is accompanied by dike intrusion [e.g., Lundgren *et al.*, 2013; Montgomery-Brown *et al.*, 2010]. Investigating the link between reservoir and rift requires implementing mass balance analysis, constraining magma volume rather than chamber or crack volume. Thus, realistic estimates of reservoir magma storage change are of great importance.

For volcanoes storing large amounts of magma in a reservoir, magma compression due to slight pressure variations in the chamber from magma intrusions can amount to a

significant net volume change of stored magma. A parcel of magma ( $\Delta V_{magma}$ ) intruded into a chamber is accommodated by both expansion of magma chamber ( $\Delta V_{ch}$ ) and compression of stored magma ( $\Delta V_{compression}$ ; *Johnson et al.*, 2000):

$$\Delta V_{magma} = \Delta V_{ch} + \Delta V_{compression} \quad (3.28)$$

$\Delta V_{compression}$  is a function of chamber volume  $V$ , compressibility of magma  $\beta_{magma}$ , and chamber pressure change  $p$ :

$$\frac{\Delta V_{compression}}{V} = p\beta_{magma} \quad (3.29)$$

Then, considering equations (3.24), (3.25), (3.28), and (3.29), following equation is derived:

$$\Delta V_{magma} = \Delta V_{ch}(1 + \beta_{magma}/\beta_{ch}) = \Delta V_{cr} \frac{1 + \beta_{magma}/\beta_{ch}}{1 + \beta_{hr}/\beta_{ch}} \quad (3.30)$$

Applying equations (3.26) and (3.27), then

$$\Delta V_{magma} = \Delta V_{cr} + Vp(\beta_{magma} - \beta_{hr}) \quad (3.31)$$

Compressibility of degassed basalt at crustal depths is  $0.4 - 2 \times 10^{-10} Pa^{-1}$  and the acceptable value for Kilauea basalt is  $0.59 - 0.87 \times 10^{-10} Pa^{-1}$  based on measurements of magma bulk modulus for gas-poor Kilauea olivine tholeiite [*Fujii and Kushiro*, 1977]. Then the magma volume change can be estimated using equation (3.31). For uplift and subsidence periods, the ranges of magma volume change are  $1.68 - 2.05 \times 10^7 m^3$  and  $2.18 - 2.59 \times 10^7 m^3$ , respectively. Note that the calculated magma volume change is at the depth of the magmatic reservoir. The effect of the depth difference on the estimation of magma volume change should be accounted for to transform it to a different depth level [*Rivalta and Segall*, 2008].

### 3.6.4 Implications for Evolution of Kilauea Magma Chamber

The presented modeling approach is used to investigate the source of the rapid uplift period leading to the 2007 Father's Day east rift intrusion and the following subsidence period at Kilauea volcano. The resolved complex model geometries and concurrent seismicity [Lin *et al.*, 2014] are presented in Figure 3.10. The volume of the source associated with the  $\sim 1.5$ -year uplift period is  $\sim 29.1 \text{ km}^3$ , while that of the  $\sim 3$ -year subsidence period is  $\sim 37.3 \text{ km}^3$ . The source of the subsidence episode is also slightly shallower, extending roughly from 1 km to 4 km depth. Visual inspection suggests that the source geometry of the subsidence period is different from that of the uplift period. Note that data uncertainties and model deficiencies may have a significant impact on model results. For instance, the effect of surface topography and heterogeneities of the elastic medium [Montgomery-Brown *et al.*, 2009], which can bias the inversion results and lead to the inaccurate distribution of PCDs, are not accounted for. Yet, such errors are systematic in nature with the direction of bias remaining identical for both episodes. Therefore, the medium heterogeneities and surface topography cannot be a reason for the apparent difference between geometries, unless they also vary from one episode to another, which is implausible. Thus, the difference might be due to observation error, which is random in nature, namely, it changes from one episode to another. There are several standard statistical tests to investigate the impact of observation errors [Meyer, 1970]. Here, to investigate if the apparent difference is statistically significant, the model geometry of the uplift period is used as input for the BEM modeling of deformation data during the subsidence period and the displacement discontinuity distribution and associated pressure change are solved for. In this case, the optimal pressure change is  $-7.4 \text{ MPa}$  and RMSEs of the model fits to the observed descending and ascending deformation are 4.5 cm and 4.5 cm, which are 66% and 45% worse, respectively. An  $F$  test

indicates that at 99% confidence level, the complex geometries resolved for the uplift and subsidence periods are distinct. Note that although the difference is significant and beyond the observation error, it is not to suggest that two independent source models are present, but the evidence suggests that during these periods, different parts of the same magmatic body were activated.

Geodetic observations and models suggest that during the 2007 Kilauea east rift intrusion, magma is transported directly from the reservoir beneath the caldera to the rift zone [Montgomery-Brown *et al.*, 2011]. During this eruption, magma is likely mobilized from crystal mush toward the rift zone, where magma has higher melt fraction. Moreover, during large eruptions, like the 2007 Father's Day event, due to a rapid drop in differential pressure, magma is likely transported to the dike from isolated compartments [Gudmundsson, 2012, 2016]. Compartments with different pore fluid pressures are well known in many hydrocarbon reservoirs [Deming, 2002; Economides and Nolte, 2000; Satter *et al.*, 2008]. Although their origin and role in the volcanic process have been debated, it is suggested that the observed change in source shape from uplift to the subsidence episode is due to transported magma to the rift zone from isolated compartments under significant differential pressure. These compartments are linked to structural boundaries (e.g., faults) and pressure seals [Deming, 2002] and are possibly one of the reasons why the composition of the material varies during eruptions [Gudmundsson, 2012]. At Kilauea, however, the composition of erupted materials and thus the style of eruption are linked to the geochemistry of the primary melts formed far below the volcano in the mantle [Sides *et al.*, 2014], and the existence and role of the magma chamber compartment at Kilauea are yet to be investigated.

The difference between source geometries from uplift to subsidence period can also be explained by alteration of the local stress field due to rift intrusion. The shape of the magma

chamber is a function of tectonic stress, magmatic pressure, surrounding rock properties and long-term equilibrium conditions [e.g., *Gudmundsson*, 2012; *Marsh*, 1989]. Rift opening and dike intrusions are capable of altering local stress at the summit magma reservoir, which in turn controls the shape of the magma chamber.

### 3.7 Conclusion

A finite reservoir with an arbitrary shape as the deformation source can be approximated by a superposition of spatially distributed PCDs. A new sparsity-promoting inversion scheme is proposed to image complex volcanic source geometries using geodetic observations such as InSAR deformation data. This inversion method applies hybrid L1- and L2-norm regularization on volume change distribution in an iterative manner. The main assumption is that the model sought is sparse, namely, only small numbers of model parameters are nonzero. Through synthetic tests, it is shown that this inversion method is able to recover the shape, location, and depth of a zone of volume change with complex geometry and sharp edges. Representing the complex source geometry using a triangular mesh of dislocations, a BEM modeling scheme is applied to solve for the distributed displacement discontinuities on the surface of the finite magma chamber and associated pressure change under uniform pressure boundary conditions.

Results of applying this method to InSAR surface deformation observed at Kilauea for rapid uplift and subsidence indicate that the geometries and depths of the summit magma reservoir vary from one period to another, implying short-term (a timescale less than several years) evolution of the magma chamber. The models of displacement discontinuities reveal that inflation and deflation mainly occur at the top and bottom of the magma chamber with negligible expansion on the sides. The magnitudes of pressure changes for the two periods

are comparable. This new model revises kinematics of the Kilauea summit plumbing system and is valuable for understanding associated physical processes.

## Part II

### Induced Seismicity



## CHAPTER 4

### FLUID INJECTION AND TIME-DEPENDENT SEISMIC HAZARD IN THE BARNETT SHALE, TEXAS

The work presented in this chapter has been published as: Zhai, G., and Shirzaei, M. (2018). Fluid injection and time-dependent seismic hazard in the Barnett Shale, Texas. *Geophysical Research Letters*, 45. <https://doi.org/10.1029/2018GL077696>.

#### 4.1 Abstract

The Barnett Shale in Texas has experienced an increase in seismicity since 2008, coinciding with high-volume deep fluid injection. Despite the spatial proximity, the lack of a first-order correlation between seismic records and the total volume of injected fluid requires more comprehensive geomechanical analysis, which accounts for local hydrogeology. Using time-varying injections at 96 wells and employing a coupled linear poroelastic model, the spatiotemporal evolution of pore pressure and poroelastic stresses during 2007–2015 is simulated. The overall contribution of poroelastic stresses to Coulomb failure stress change is  $\sim 10\%$  of that of pore pressure; however, both can explain the spatiotemporal distribution of earthquakes. A seismicity rate model is used to calculate earthquake magnitude exceedance probability due to stress changes. The obtained time-dependent seismic hazard is heterogeneous in space and time. Decreasing injection rates does not necessarily reduce probabilities immediately.

## 4.2 Introduction

A variety of human activities, such as water impoundment, underground mining, geological carbon sequestration, hydraulic stimulation of enhanced geothermal system, and fluid injection/extraction associated with oil and gas exploitation, can induce earthquakes [Ellsworth, 2013; Grigoli *et al.*, 2017; Rubinstein and Mahani, 2015]. The recent increase of seismicity in the central and eastern United States is suggested to be induced by deep injection of coproduced brine into the subsurface [Ellsworth, 2013]. Most of the increased seismic events are found in the proximity of injection wells preceded by high-volume injections [e.g., Frohlich, 2012; Horton, 2012; Keranen *et al.*, 2013; Kim, 2013; Rubinstein *et al.*, 2014]. The process of inducing seismicity through injection is well known since the Denver earthquakes triggered at the Rocky Mountain Arsenal [Healy *et al.*, 1968] and the experiments in Rangely earthquake control [Raleigh *et al.*, 1976]. However, distinguishing them from natural earthquakes is not straightforward due to poor constraints on local hydrogeology, the background stress field, and the initial pore pressure [Ellsworth, 2013; Grigoli *et al.*, 2017], which can be resolved using structural geology analysis [Magnani *et al.*, 2017].

There are numerous mechanisms impacting the process of injection-induced seismicity, including direct increase of pore pressure reducing effective normal stress through fluid diffusion [Healy *et al.*, 1968; Hubbert and Rubey, 1959], stress perturbation in the medium due to poroelastic stress changes [Barbour *et al.*, 2017; Deng *et al.*, 2016; Segall and Lu, 2015], interaction with induced seismic [Sumy *et al.*, 2014] or aseismic [Guglielmi *et al.*, 2015] slips, thermoelastic response caused by temperature difference of injected fluid and host rocks [Majer *et al.*, 2007], modifying velocity-strengthening frictional properties into velocity-neutral due to increased pore pressure [Scuderi and Collettini, 2016], and reducing rock frictional strength due to geochemical alteration of fracture surfaces [Majer *et al.*, 2007]. Most studies

addressing the correlation between injection and nearby seismicity either are qualitative [Ake *et al.*, 2005; Frohlich, 2012] or quantify pore pressure using uncoupled groundwater flow equations [Hornbach *et al.*, 2015; Keranen *et al.*, 2014]. Recent studies consider coupling between pore pressure and matrix deformation to investigate the relationship between injection and earthquakes [Deng *et al.*, 2016; Fan *et al.*, 2016; Segall and Lu, 2015; Shirzaei *et al.*, 2016]. This relationship is a function of injection rate, local hydrogeology, initial pore pressure and background stress state, fault orientation and permeability, and frictional properties [Chang and Segall, 2016; Fan *et al.*, 2016]. Moreover, a delay of months to years is often observed between injection and seismicity, which stems from a low initial pore pressure [Keranen *et al.*, 2013], low rate of fluid diffusion [Keranen *et al.*, 2014], transient fluid flow [Norbeck and Horne, 2016], unsuitable fault orientation, and low background stress. Also, varying injection rates can result in transient and possibly large changes in poroelastic stress and pore pressure rate [Barbour *et al.*, 2017; Segall and Lu, 2015].

The seismic hazard associated with fluid injection is estimated using a reconstructed Gutenberg-Richter law adapted for induced events [Shapiro *et al.*, 2013]. This law predicts a probability decrease for large earthquakes immediately after an injection rate decline [Langenbruch and Zoback, 2016], which is in contrast with the not uncommon observation of large earthquakes occurring after injection shut-in [Horton, 2012; Kim, 2013]. This is likely because the reconstructed Gutenberg-Richter law is obtained assuming nondecreasing injection rates and is applicable for earthquake magnitudes less than 2.0 [Shapiro, 2015], ignoring time-dependent fluid diffusion and mechanisms of earthquake nucleation. Thus, a comprehensive analysis requires incorporating the rate-and-state friction law into geomechanical modeling [Dieterich *et al.*, 2015; McClure and Horne, 2011; Segall and Lu, 2015]. In this approach, the seismicity rate is expressed as a function of space and time,

hydrogeological properties, fault geometries, and injection rates. Furthermore, the seismicity rate model acts as an input for the calculation of spatiotemporal earthquake probability, which is important for seismic hazard forecasting.

The Barnett Shale in Texas experienced a dramatic increase in seismicity since 2008, when large-volume coproduced waste fluid was injected into the subsurface. Three major earthquake sequences (Dallas-Fort Worth [DFW] Airport earthquakes, Cleburne earthquakes, and Azle earthquakes) occurred in this area suggesting a causal link between injection and increased seismicity [Froblich *et al.*, 2011; Hornbach *et al.*, 2015; Justinic *et al.*, 2013]. A coupled poroelastic model is used to simulate the spatiotemporal evolution of pore pressure and poroelastic stresses at the basin-wide scale considering high-volume time-varying injections. The model results combined with geomechanical analysis and seismicity rate theory are used for the evaluation of potential fault activation and estimation of time-dependent seismic hazard.

#### 4.3 Seismic and Injection Data Sets

The seismic data are obtained from the Advanced National Seismic System composite earthquake catalog (ComCat), which contains 203  $M \geq 2.0$  earthquakes from 2008 to 2015 (Figure 4.1 and Table C.3). It is notable that only three earthquakes are recorded in the study area during 1990–2007. Most of the earthquakes are located 5 km deep in the Precambrian crystalline basement overlaid by the Ellenburger formation. In addition, 67 earthquakes located by Froblich [2012] from 2009 through 2011 are compiled (Table C.4). Many of these events are absent from ComCat owing to the recording from a local monitoring network used by Froblich [2012]. These events have also a fixed 5 km depths. Cumulative numbers of earthquakes for both ComCat and Froblich catalogues are shown in Figure C.13.

Injection data are provided by Texas Railroad Commission for 96 injection wells within the Barnett Shale for the period 2007–2015, given injection shut-in in December 2015 (Figure 4.1 and Table C.2). The annual total injection volume increases from  $\sim 1.8 \times 10^7 \text{ m}^3/\text{year}$  to  $\sim 3.6 \times 10^7 \text{ m}^3/\text{year}$  during 2007–2011 and then decreases to  $\sim 1.7 \times 10^7 \text{ m}^3/\text{year}$  in 2015 (Figure C.1). The injection rate for individual wells has

strong temporal variability (Figures 4.1b and 4.1c). Most wells inject into the Ellenburger formation, except a few that dispose into shallower zones (Table C.2). Each well has an

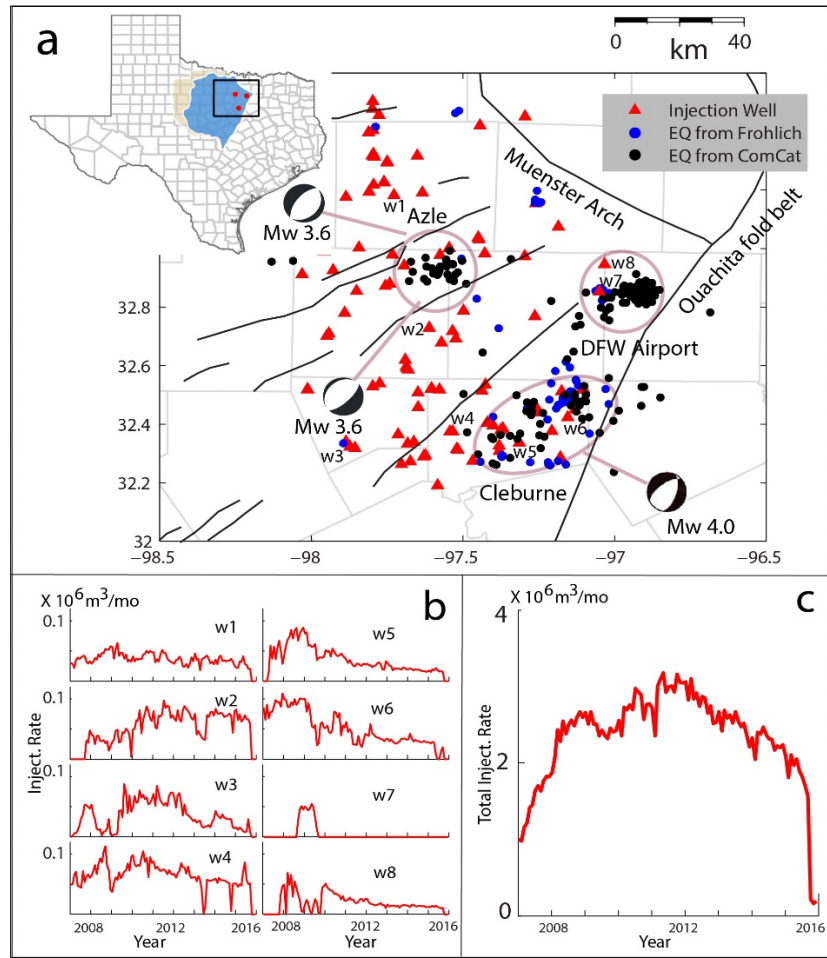


**Figure 4.1.** The Barnett Shale injection and seismic data for the period 2007–2015. (a) Spatial distribution of 96 injection wells (filled triangles) and earthquakes including earthquakes compiled by *Frohlich* [2012] in blue filled circles and that from ComCat in black filled circles. Major regional subsurface faults (black lines) and earthquake focal mechanisms are provided by from *Hornbach et al.* [2015] and U.S. Geological Survey National Earthquake Information Center. The inset shows the study area, and three red dots are center locations of three earthquake sequences at DFW airport, Cleburne, and Azle. Two shaded areas within inset are the Fort Worth basin (grey) and Barnett Shale (blue). (b) Examples of monthly injection rate time series for eight selected wells, whose locations are shown in panel (a). (c) Time series of total injection rate aggregated over all 96 wells.

upper limit on the daily injection volume based on the well's individual permit. The maximum upper limit is 35,000 BBLS/day ( $\sim 5565 \text{ m}^3/\text{day}$ ; Table C.2). Although these wells are injecting into an area adjacent to seismic faults (Figure 4.1), the overall correlation between the total volume or rate of injected fluid and seismicity rate is poor (Figure C.1). This suggests a higher-order relationship between injection and seismicity, enhanced by heterogeneous background stress and local hydrogeology of the relatively large study area.

#### 4.4 Method

A coupled poroelastic model is employed to calculate the spatial and temporal evolution of poroelastic stresses and pore pressure due to fluid injections in the Barnett Shale. Note that the pore pressure estimate through poroelastic modeling is different from wellhead pressure. The wellhead pressure is the pressure at which fluid is injected into the formation matrix, while the term “pore pressure” refers to the change in formation pressure due to the process of fluid diffusion. The governing equations relating the deformation field  $\mathbf{u}$  and pore pressure  $p$ , both of which are a function of location  $\mathbf{x}$  and time  $t$ , are given [Cheng, 2016; Wang and Kümpel, 2003]

$$G\nabla \cdot \nabla \mathbf{u} + \frac{G}{1-2\nu} \nabla(\nabla \cdot \mathbf{u}) - \alpha \nabla p = \mathbf{f}(\mathbf{x}, t) \quad (4.1)$$

$$\frac{1}{Q} \frac{\partial p}{\partial t} + \alpha \frac{\partial(\nabla \cdot \mathbf{u})}{\partial t} - \nabla \cdot (\chi \nabla p) = q(\mathbf{x}, t) \quad (4.2)$$

where  $\nabla$  is the gradient operator and  $\nabla \cdot$  is the divergence operator,  $G$  is the shear modulus,  $\nu$  is the drained Poisson ratio,  $\alpha$  is the Biot effective stress coefficient (the change in fluid volume per unit volumetric change in medium under drained condition),  $Q$  is the Biot modulus,  $\chi$  is the mobility coefficient defined by the ratio of intrinsic permeability and dynamic fluid viscosity,  $\mathbf{f}$  is the body force per unit bulk volume acting on solid medium,

and  $q$  is the volumetric fluid injection rate per unit bulk volume. To characterize a linear poroelastic medium, five independent parameters are needed, including  $G$ ,  $\nu$ , undrained Poisson ratio  $\nu_u$ , hydraulic diffusivity  $D$  (the ratio of hydraulic conductivity and specific storage), and Skempton coefficient  $B$  (the change in pore pressure per unit change in confining pressure under undrained conditions). Parameters  $\alpha$ ,  $\chi$ , and  $Q$  can be uniquely determined using these five parameters [Wang and Kümpel, 2003]. Equations (4.1) and (4.2) are solved by imposing boundary conditions of zero traction and excess pore pressure at the half-space surface [Fan *et al.*, 2016].

The poroelastic model informed by injection and hydrogeological data provides the spatiotemporal distribution of elastic stress tensor derived from  $\mathbf{u}$ ,  $\Delta \mathbf{S}(\mathbf{x}, t)$  and pore pressure change,  $\Delta p(\mathbf{x}, t)$ . Defining the fault orientations and the coefficient of friction  $\mu$ , the shear stress  $\Delta \tau_s(\mathbf{x}, t)$  and normal stress  $\Delta \sigma(\mathbf{x}, t)$  (positive for unclamping) are calculated; thus, the Coulomb failure stress (CFS) change  $\Delta \tau(\mathbf{x}, t)$  is given by

$$\Delta \tau = \Delta \tau_s + \mu(\Delta \sigma + \Delta p) = (\Delta \tau_s + \mu \Delta \sigma) + \mu \Delta p \quad (4.3)$$

Dieterich [1994] developed a framework describing the evolution of seismicity rate as a function of background seismicity rate and CFS change. A simplified version was given by Segall and Lu [2015] relating the relative seismicity rate  $R(\mathbf{x}, t)$  (rate of seismicity relative to the background seismicity rate) to the Coulomb stressing rate  $\dot{\tau}(\mathbf{x}, t)$ :

$$\frac{dR(\mathbf{x}, t)}{dt} = \frac{R(\mathbf{x}, t)\dot{\tau}_0}{A\bar{\sigma}} \left( \frac{\dot{\tau}(\mathbf{x}, t)}{\dot{\tau}_0} - R(\mathbf{x}, t) \right) \quad (4.4)$$

where  $\dot{\tau}_0$  is the background stressing rate,  $A$  is a constitutive parameter in the rate-and-state friction law,  $\bar{\sigma}$  is the background effective normal stress, and  $\frac{A\bar{\sigma}}{\dot{\tau}_0}$  is the characteristic relaxation time. Table C.1 gives the typical values for  $A$  [Segall and Lu, 2015]. The value of

$10^{-5}$  MPa/year is used for background stressing rate  $\dot{\tau}_0$ , which is obtained based on a geodetic study of the strain rate of the Northern American plate [Calais *et al.*, 2006].  $\bar{\sigma}$  is 35 MPa at the bottom of the Ellenburger formation, considering a normal stress gradient of 10 MPa/km along depth for high-dip angle faults.

Assuming an inhomogeneous Poisson process for earthquake occurrence, the probability of at least one event larger than  $M$  in time interval  $[t_1, t_2]$  at location  $\mathbf{x}$  is

$$P_{\geq M}(t_1, t_2, \mathbf{x}) = 1 - \exp[-N_{\geq M}(t_1, t_2, \mathbf{x})] \quad (4.5)$$

where  $N_{\geq M}(t_1, t_2, \mathbf{x})$  is the expected number of  $\geq M$  earthquakes during  $[t_1, t_2]$  at  $\mathbf{x}$ . From equation (4.4) and assuming a constant background seismicity rate,  $r_{\geq M}(\mathbf{x})$  at  $\mathbf{x}$ , the number of earthquakes is

$$N_{\geq M}(t_1, t_2, \mathbf{x}) = \int_{t_1}^{t_2} r_{\geq M}(\mathbf{x}) R(\mathbf{x}, t) dt \quad (4.6)$$

where  $r_{\geq M}(\mathbf{x}) * R(\mathbf{x}, t)$  defines the earthquake rate after stress perturbation for earthquake magnitude larger than  $M$  at location  $\mathbf{x}$  and time  $t$ .  $r_{\geq M}(\mathbf{x})$  is given using Gutenberg-Richter frequency-magnitude relationship and is scaled with grid size  $s(\mathbf{x})$  at  $\mathbf{x}$ :

$$r_{\geq M}(\mathbf{x}) = \frac{s(\mathbf{x})}{S} k 10^{-bM} \quad (4.7)$$

where  $k$  is the background earthquake rate of magnitude  $\geq 0$ , describing the productivity level in the whole study region with size  $S$ .  $b$  is the slope of frequency-magnitude relationship, characterizing the earthquake size distribution. Considering the spatial proximity of the study area to Oklahoma, the  $b$ -value determined using Oklahoma catalog is taken as a reference (Table C.1) [Langenbruch and Zoback, 2016]. Also, using the historical earthquakes of  $M > 2.0$  within the study area [Table C.3; Froblich *et al.*, 2016; Gono, 2015],  $k$  value roughly equals to  $10^{1.3}$ /year (Table C.1). The absolute values of seismicity rate and



earthquake probability are sensitive to  $k$  and  $b$ , while the relative values are weakly dependent on them.

#### 4.5 Hydrogeological Background and Model Setup

The availability of hydrogeological data following *Hornbach et al.* [2016] (Text C.1 and Figure C.2A) and the depths of injected fluid allow identifying five layers (Figure C.2B), characterizing the geomechanical properties of the poroelastic medium (Text C.2 and Figure C.2C). The main injection layer of the dolomitic Ellenburger formation has a basin-wide depth range of 2,200–3,500 m with an average thickness of 1,300 m in the model [*Montgomery et al.*, 2005; *Pollastro et al.*, 2007; *Zhao et al.*, 2007]. The 100-m-thick Barnett Shale formation acts as a sealing layer atop the Ellenburger formation. The granite basement below 3.5 km is thought to be fractured and hydraulically connected to the Ellenburger formation [*Ewing*, 1990], hosting most of the observed seismicity. The Ellenburger formation is believed to comprise very low permeability rocks [*Gale and Gomez*, 2007]. The overall stress state in the Barnett Shale is consistent with normal faulting regime [*Snee and Zoback*, 2016] where high-dip-angle faults are oriented along the northeast (Figure 4.1). The Cleburne and Azle earthquake sequences involve dip-slip focal mechanism. The focal mechanism of the DFW Airport sequence is not determined but is perceived to be similar to that of the Cleburne and Azle sequences [*Frohlich et al.*, 2011]. The optimal receiver fault geometry used for calculating CFS change is summarized in Table C.1 [*Hornbach et al.*, 2015; *Scales et al.*, 2017; *Snee and Zoback*, 2016].

## 4.6 Result

Using time-varying injected volumes at 96 wells with injection shut-in in December 2015, the evolution of pore pressure and poroelastic stresses is simulated in the study area (Text C.3 and Figure C.3). Figure 4.2 shows snapshots of the temporal evolution of pore pressure scaled by the frictional coefficient with a value of 0.6, as well as CFS change due to poroelastic stresses at the bottom of the Ellenburger formation (3.5 km). Note that Figure 4.2 is divided into two blocks, demonstrating the evolution of parameters prior to and after the assumed injection shut-in in December 2015. Therefore, all model validations are performed only using the block associated with the preshut-in period. The overall effect of pore pressure (maximum of 3.5 MPa) is an order of magnitude larger than that of poroelastic stresses, which is consistent with *Chang and Segall* [2016].

Visual inspection suggests that the location and timing of the seismicity correspond to zones of increased pore pressure, poroelastic stress, and total CFS change, although the values for DFW Airport sequence appear to be small (Figure 4.2). The calculated pore pressure following injection shut-in shows a slow decay, consistent with *Shirzaei et al.* [2016]. Also, simulated time-dependent seismicity rates correlate with the location and timing of observed seismicity, but the values for the DFW Airport sequence also appear to be small (Figure 4.2). Interestingly, although the simulated seismicity rate adjacent to the wells has already dropped following injection shut-in, at further distances, the seismicity rate remains high and then gradually decays.

Given the spatiotemporally variable injections, the patterns and values of CFS change, stressing rate, and time-dependent seismicity rate are different at the locations of seismic swarms (Figures 4.3a–4.3c). Three regions of 20-km radial distance from a swarm center are

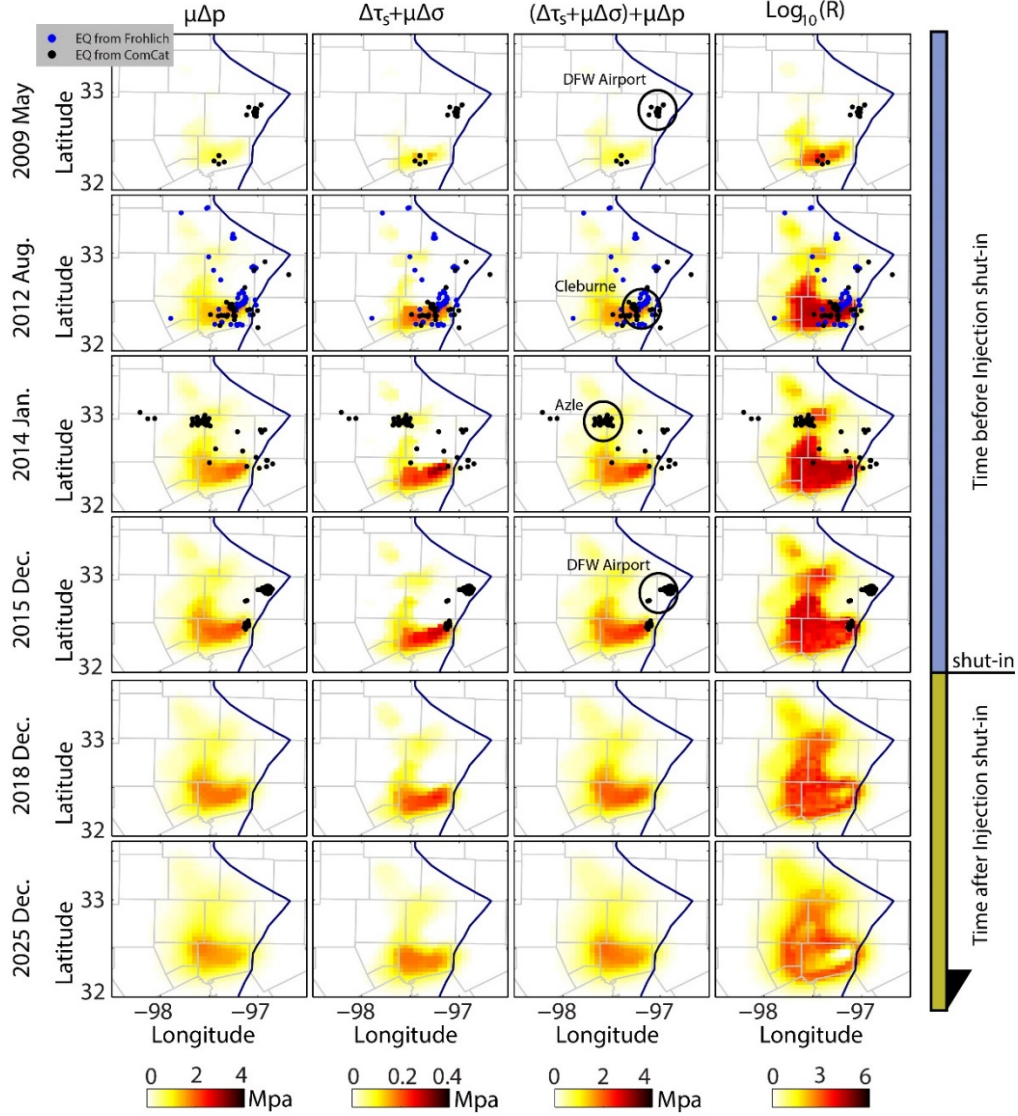


**Figure 4.2.** Comprises two blocks associated with preinjection and postinjection shut-in on December 2015 and shown are snapshots of the distribution of the modeled cumulative  $\mu\Delta p$ ,  $\Delta\tau_s + \mu\Delta\sigma$ ,  $(\Delta\tau_s + \mu\Delta\sigma) + \mu\Delta p$ , and  $\text{Log}_{10}(R)$  at different times, corresponding with the end of each earthquake sequences, the end of injection operation, and two postinjection epochs. Incremental occurrences of earthquakes from *Frohlich* [2012] (blue dots) and ComCat (black dots) catalogues are shown for the preinjection shut-in period. Note the different magnitudes of pore pressure and poroelastic stress. Zones defined for earthquake sequences of DFW Airport, Cleburne, and Azle are marked by black circles. Here  $\mu\Delta p$  is the CFS change due to pore pressure change, scaled by the coefficient of friction;  $\Delta\tau_s + \mu\Delta\sigma$  is the CFS change due to poroelastic stress change;  $(\Delta\tau_s + \mu\Delta\sigma) + \mu\Delta p$  is the total CFS change; and  $\text{Log}_{10}(R)$  is the logarithm of seismicity rate.

defined to identify areas affected by the earthquake sequences (Figure 4.2). For each area, the time series of CFS change, stressing rate, and seismicity rate are spatially averaged (Figure

4.3). For DFW Airport, both CFS change and seismicity rate increase with time and they continue to increase beyond injection shut-in. The seismicity rate at Cleburne increases until 2011, then decays to the background level, although the CFS change only gradually decreases after 2015. At Azle, both values increase until 2015, after which the CFS change reaches a persistent high value, while the seismicity rate decreases toward the background value. Figure 4.3d shows similar parameters as shown in Figures 4.3a–4.3c, but now calculation is done for

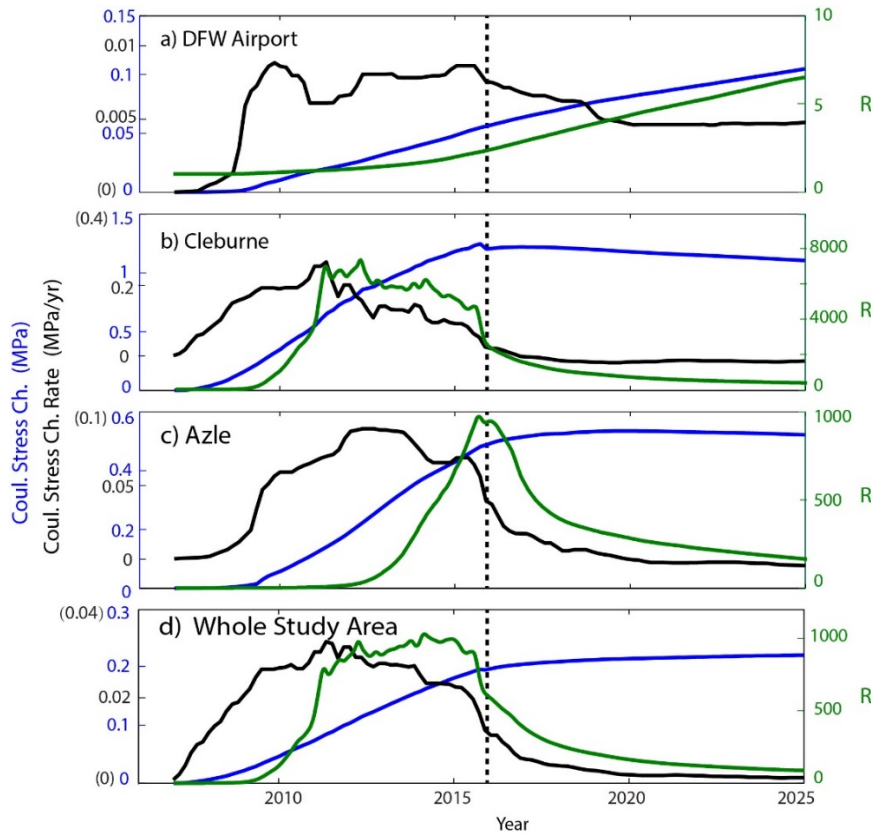


**Figure 4.3.** Modeled time series of spatially average total CFS change (blue), Coulomb stressing rate (black), and relative seismicity rate (green) for zones of (a) DFW Airport, (b) Cleburne, (c) Azle, and (d) the whole study area. The vertical dashed lines show the timing of injection shut-in. The Coulomb stressing rate is smoothed using six-month moving average window.

the whole study area. During period 2011–2015, the average CFS change increases and the seismicity rate reaches a steady state. Afterward, the seismicity rate gradually drops, but the average CFS change remains almost constant near its high value. The impact of various  $A$  values and background stressing rates on the estimated seismicity rate is further tested for the whole study area (Figure C.14). As seen, various combinations result in very different seismicity rate pattern. However, the preferred set of parameters (Table C.1) yields an

earthquake magnitude exceedance probability (discussed below) that is most consistent with the observed seismicity. Nevertheless, due to the poor quality of seismic data and incompleteness of catalog, performing comprehensive quantitative validation of seismicity rate model is not possible.

The simulated earthquake magnitude exceedance probability is a function of time and location (equation (4.5)). The local earthquake probability is sensitive to the seismicity rate (or Coulomb stressing rate), as indicated by the relative earthquake probability distribution (Figures 4.2 and C.4). Through spatial integration, the annual magnitude exceedance probability is estimated for different zones (Figure 4.4) same as those investigated in Figure 4.3. In the vicinity of the DFW Airport sequence, the exceedance probability continues to increase over time (Figure 4.4a), as does the seismicity rate (Figure 4.3a). However, the magnitude of probability increase is less than 6% for magnitude  $\geq 2.0$ . For Cleburne, the annual exceedance probability culminates during years 2011–2014 with a maximum of  $\sim 40\%$  for magnitude  $\geq 4.0$  and then decreases. The probability for magnitude  $\geq 4.0$  is  $\sim 30\%$  in Cleburne in 2015 when the Venus magnitude 4.0 event occurred. In contrast, Azle peaks in 2015, followed by a decaying period. During 2015, the exceedance probability for magnitude  $\geq 4.0$  is  $\sim 8\%$ . The magnitude exceedance probability is also evaluated for the whole study area (Figure 4.4d). Three distinct episodes for the annual probability change are identified including an increasing period from 2007 to 2011, a steady episode of 2011–2015, and a decaying period following 2015. The steady episode has a yearly probability of  $\sim 60\%$  for magnitude  $\geq 4.0$ .

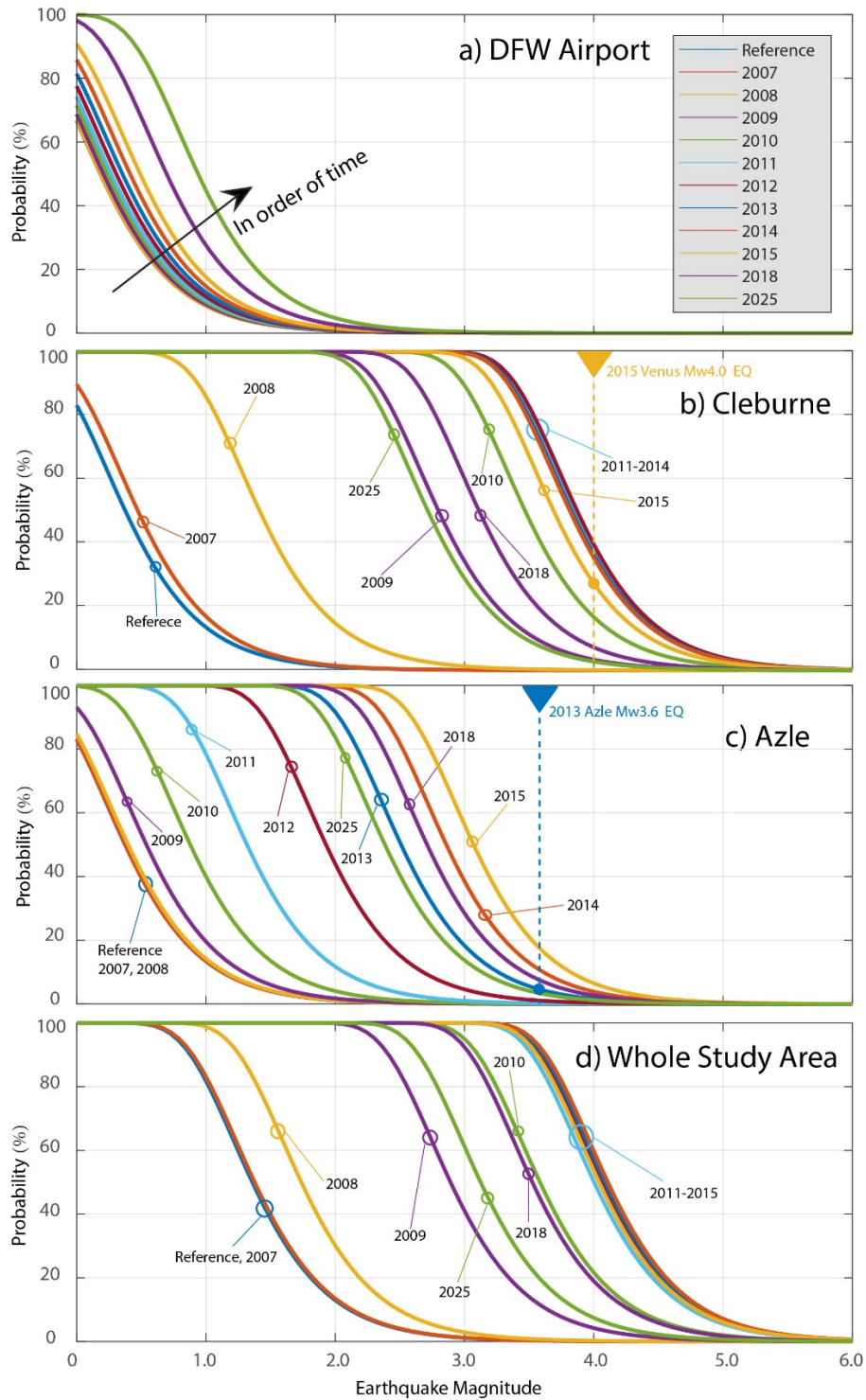


**Figure 4.4.** Annual earthquake magnitude exceedance probabilities for (a) DFW Airport, (b) Cleburne, (c) Azle, and (d) the whole study area for different years. The vertical dashed lines indicate the largest magnitudes of earthquakes occurred in Cleburne and Azle, color-coded with the associated year.

#### 4.7 Discussion and Summary

The linear poroelastic model is characterized by five layers in half space, and each layer is assumed to be homogeneous, isotropic, and porous. However, this is an idealized description of an inherently complex medium. In the Barnett Shale, the Ellenburger formation and underlying basement are fractured [Ewing, 1990], enhancing permeability. The existence of paleokarst may also increase permeability. Using the upper value of  $0.7 \text{ m}^2/\text{s}$  for hydraulic diffusivity [Hornbach *et al.*, 2015], new poroelastic, seismicity rate, and earthquake probability models are obtained (Figures C.5 and C.6). As seen, increasing the hydraulic diffusivity results in pore pressure and seismicity rates with broader spatial distribution, although the maximum magnitudes are reduced (Figures C.3 and C.5). This leads to the reduction of annual exceedance probability for  $M \geq 4.0$  earthquakes from 60% to 40% for the whole area. It also modifies the temporal pattern of annual earthquake probabilities (Figures 4.4d and C.6). Moreover, well logs and seismic imaging show that subsurface architectures are not perfect layers with equal thicknesses, which can alter fluid diffusion. Investigating such effect on earthquake probability is a subject of future studies. The interaction between permeability and pore pressure may alter the estimated stress changes because permeability is pressure dependent, but this effect likely has a secondary impact on the results compared with other model uncertainties.

Although most earthquakes occur in zones of increased CFS change or predicted high seismicity rates, there are zones subject to elevated CFS change lacking elevated seismicity. This may be attributed to heterogeneous background tectonic stresses or initial pore pressures, the absence of faults, and/or heterogeneous fault orientations. Due to the low permeability of the injection layer, the prediction of CFS change after injection shut-in exhibits a slowly decaying pattern (Figures 4.2 and 4.3). The large postinjection CFS change

may expedite earthquake occurrence (e.g., clock advance in the context of the earthquake cycle), which could have a longer-lasting effect on earthquake probability. However, the calculation of this effect requires detailed knowledge of the earthquake cycle for a preexisting fault, which is unavailable. Also, the seismicity rate model presented here (equation (4.4)) only predicts rupture nucleation rate and does not account for the effect of interactions between adjacent ruptures [Segall and Lu, 2015]. Future work needs to be done to overcome this limitation.

The model depicts an outward propagating seismicity front after injection shut-in following December 2015 (Figures 4.2 and C.3), where fluid continues to propagate and transiently changes the stress state [Segall and Lu, 2015]. Following shut-in, the seismicity rate within the zone of high-rate injections (near-field) drops faster than that of outside (far-field). During injection, both pore pressure and poroelastic stresses contribute to the CFS change. After injection shut-in, the pore pressure in the near-field decreases faster; however, due to the process of fluid diffusion, the pore pressure declining rate decreases in the far-field. Also, note that following injection shut-in, poroelastic stresses decrease but their contribution to the total CFS change is too small to make a noticeable impact.

The maps of CFS change indicate that different amounts of stress change are needed to trigger an earthquake sequence at different locations (Figures 4.3a–4.3c and C.13). For DFW Airport, the earthquake sequence starts almost at the beginning of injection with CFS increase of  $\sim 0.005$  MPa. This indicates either the faults in this area were critically stressed prior to injection, the isotropic poroelastic model is overly simplified, or a combination of both. Also, the possibility that the DFW Airport sequence is of natural origin cannot be ruled out. At Cleburne and Azle, the required CFS change for the first events to occur is 0.35–0.4 MPa. In late 2015 another earthquake sequence occurred near DFW Airport,



accompanied by a continuous increase of CFS change (Figures 4.2 and 4.3a). The timing of the earthquake sequences shows that they occur once CFS change increases by 0.05 MPa. Examining the spatiotemporal evolution of earthquakes recorded by ComCat, two other earthquake sequences occurred in the Cleburne zone [e.g., *Gono*, 2015], which are noted as sharp increases in cumulative earthquake count (Figure C.13). This suggests a recurring pattern for seismic swarms following CFS change of 0.45–0.5 MPa (Figure 4.3b). However, the Azle earthquake record is too sparse to allow such an examination.

Regional estimates of time-dependent earthquake probability caused by stress field perturbation due to fluid injection are obtained. The results highlight the importance of the stressing rate for earthquake probability change, which can be orders of magnitude above the background probability (Figure C.4). The key to probability calculation is predicting the seismicity rate dependent on the injection-induced stress history (Figures 4.3 and 4.4). The average CFS change increases linearly from 2011–2015, corresponding with a steady stressing rate (Figure 4.3d). Accordingly, the annual magnitude exceedance probability almost remains unchanged during the same period (Figure 4.4d). After 2015, the average CFS change reaches a steady state accompanied by a period of decaying seismicity rate and decreasing annual magnitude exceedance probability (Figures 4.3d and 4.4d). This implies that after injection shut-in, the earthquake probability reduces due to a rapid decrease of CFS change. However, during a period of decreasing injection rate from 2011 through 2015 (Figure 4.1c), the stressing rate and earthquake probability do not decrease immediately. This is because the time-dependent poroelastic process positively contributes to the stressing rate. This is opposite to the direct effect of a declining injection rate on the CFS change. These results demonstrate that the change in injection-induced earthquake probability is highly

time-dependent because of the temporally variable nature of the poroelastic process and injection rate.

In addition to fluid injection, brine is possibly produced, especially at Azle, from the Ellenburger formation along with hydraulic fracturing [*Hornbach et al.*, 2015]. This volume of extracted fluid may change the pore pressure within the formation, revising the total CFS change. To investigate this effect, the data from *Hornbach et al.* [2015] for 120 production wells at Azle are used (Figure C.7) and the associated CFS change due to production volume is evaluated (Text C.4 and Figures C.8–C.12). The impacts of brine production on stress change and seismicity rate at Azle are negligible. However, the data set of production wells is not complete, and the true impact of fluid extraction may be much larger. This highlights the need for new regulations to require operators to release production data in a timely fashion.

## CHAPTER 5

### PHYSICS-BASED INDUCED EARTHQUAKE FORECASTING IN OKLAHOMA

The work presented in this chapter has been submitted to a journal for publication.

#### 5.1 Abstract

Models that unequivocally link probability of induced earthquakes with volume of wastewater injection are scarce. Here, it is shown that physics-based models of fluid diffusion and seismicity rate are capable of predicting the time and magnitude of the induced earthquakes. Using reported injection data and a poroelastic model combined with a rate/state-friction law, the changes in crustal stress and seismicity rate in Oklahoma were computed. The magnitude-time distribution of the observed M3+ earthquakes for the period 2008 – 2017 is accurately reproducible. Also, the injection rate reduction in 2016 mitigates the exceedance probability of M5.0 by 22% in Western Oklahoma, but it does not affect that of Central Oklahoma. After injection shut-in in April 2017, the earthquake exceedance probability will approach its historical background level by 2025. The increased fluid pressure at pre-stressed faults is the main driver of the induced earthquakes in Oklahoma.

#### 5.2 Introduction

The recent increase in the number of earthquakes in the central and eastern United States since 2008 is attributed to massive deep subsurface injection of saltwater [Ellsworth, 2013; Keranen *et al.*, 2014; Shirzaei *et al.*, 2016; Weingarten *et al.*, 2015]. The spatial proximity of the seismicity to the injection wells and the fact that many of these events are preceded by

months to years of high volume fluid injection suggest a link between the observed seismicity and injection [Froblich, 2012; Horton, 2012; Kim, 2013; Rubinstein *et al.*, 2014]. The elevated rate of seismicity and chance of damaging earthquakes cause broad societal concerns among the public and regulators [Ellsworth, 2013]. Despite significant efforts in improving the monitoring capability for detecting induced seismicity [Froblich, 2012] and understanding the underlying mechanism [Healy *et al.*, 1968; Majer *et al.*, 2007; Segall and Lu, 2015; Shirzaei *et al.*, 2016], there have been very limited efforts with modest success to quantify the associated time-varying seismic hazard [Langenbruch and Zoback, 2016; Norbeck and Rubinstein, 2018; Petersen *et al.*, 2016].

Since 2008, central and northern Oklahoma have experienced a 900-fold increase in seismicity (Figures 5.1 and D.1), including four major events of 2011-11-09 Mw5.7 Prague, 2016-02-13 Mw5.1 Fairview, 2016-09-03 Mw5.8 Pawnee, and 2016-11-07 Mw 5.0 Cushing [Yeck *et al.*, 2017]. In response to the seismicity surge during 2015 and to mitigate hazards, regulators reduced the total volume of disposed brine within areas of elevated seismicity in 2016 to less than 40% of the 2014 total volume [OCC, 2016]. In spite of injection reduction, seismic moment release soared within the injection regulation zones, culminating in several major events in late 2016 such as the Pawnee and Cushing earthquakes. This indicates the relation between fluid injection and associated induced seismic hazard is complex, a likely reason for the limited success of current induced earthquake forecasting models [Langenbruch and Zoback, 2016].

Overall earthquake hazard is proportional to seismicity rate [Petersen *et al.*, 2016], which is determined by changes in crustal stress field [Dieterich, 1994]. As fluid is injected into the target formations and diffuses away, the stress field is perturbed [Cheng, 2016; Segall and Lu, 2015], reducing the shear strength of pre-stressed faults and promoting their slip [Fan *et al.*,

2016; *Shirzaei et al.*, 2016]. Moreover, the maximum magnitude of injection-induced events is controlled by several factors including total injected volume, regional tectonics, and local hydrogeology [*Holland*, 2013; *McGarr*, 2014; *Pei et al.*, 2018; *van der Elst et al.*, 2016]. The total seismic moment is correlated with both injection volume and basement depth [*Hincks et al.*, 2018]. We also suggest that the occurrence of moderate to large magnitude induced earthquakes is determined by background tectonic stress and basement fault structures [*Pei et al.*, 2018]. This body of evidence highlights that a successful forecasting model requires full integration of the physics governing the processes of fluid diffusion in a poroelastic medium and induced earthquake nucleation [*Zhai and Shirzaei*, 2018].

### 5.3 Data

#### 5.3.1 Well Injections

The monthly injection volumes at 867 high-volume wells spanning from January-1995 to April-2017 were obtained from the Oklahoma Corporation Commission (Figure 5.1). Most of the active wells are located in the seismically active north-central zone [*Langenbruch and Zoback*, 2016]. The analysis was restricted to the wells injecting into the Arbuckle formation. The information (e.g., coordinates, depth, and injection records) associated with each well were also visually inspected and those with incorrect or unreasonable (e.g., extremely large monthly injection volume) values were discarded. This provides us with 715 wells within north-central Oklahoma, and their records are reliable. Shown in Figure D.1, the total monthly injection time series is comparable with published work [*Langenbruch and Zoback*, 2016].

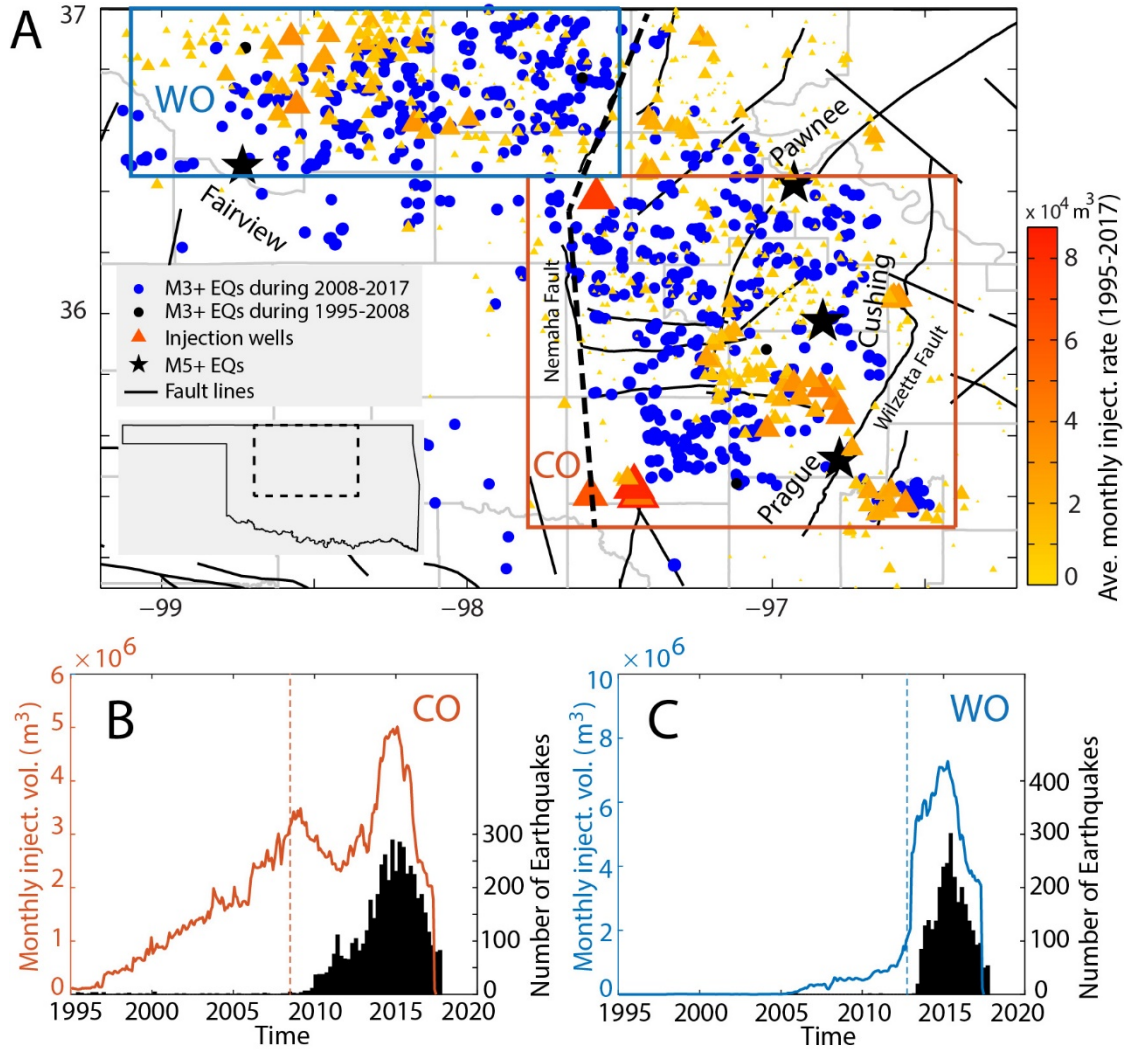


**Figure 5.1.** Fluid injection and seismicity in Oklahoma from 1995-2017. (A) Map showing the locations of M3+ earthquakes after declustering and Arbuckle wastewater disposal wells. Blue circles are recent earthquakes during 2008-2017 and black circles indicate the historical earthquakes before 2008. Red triangles represent the injection wells colored and scaled according to average monthly injection rate. The four M5+ earthquakes are shown as black stars. Black lines are mapped faults [Marsh and Holland, 2016]. Black dashed line is the Nemaha Fault Zone and Uplift dividing CO (red rectangle) and WO (blue rectangle). The inset shows the location of the study region (black dashed rectangle). (B) Time series of total monthly injection volume (red) and a histogram of all recorded seismicity (black) after declustering in CO. (C) Time series of total monthly injection volume (blue) and a histogram of all recorded seismicity (black) after declustering in WO.

### 5.3.2 Seismicity

The Oklahoma Geological Survey compiled the earthquake catalog used here. The seismic moment released in both central Oklahoma (CO) and west Oklahoma (WO) was dominated by the M3+ earthquakes that mostly nucleated either within the Arbuckle group or the upper few kilometers of the crystalline basement [Keranen *et al.*, 2014; Langenbruch and Zoback, 2016]. In CO, although the fluid injection commenced in 1995 and increased over time, the seismicity began only in 2008 and peaked in 2015 (Figure 5.1B). In WO, injection began in 2005, but the sharp increase in seismicity occurred in 2013, coinciding with a rapid rise of fluid injection rate (Figure 5.1C).

## 5.4 Method

### 5.4.1 Declustering the Seismic Catalog

Generally, recorded seismicity catalogs consist of earthquakes that are independent and earthquakes that interact with and depend on others, such as foreshocks and aftershocks. To remove the foreshocks and aftershocks, the declustering algorithm of Reasenber *et al.* [1985] is used. This approach is widely used to eliminate the dependent earthquakes that form earthquake clusters. It relies on the definition of spatial and temporal interaction zones. The spatial radial extent of interaction zone is defined by  $d \text{ (km)} = 10^{0.4M_0 - 1.943 + k}$ , where  $M_0$  is the earthquake magnitude;  $k = 1$  for the distance to the largest earthquake and  $k = 0$  for the distance to the last event. The temporal extension of the interaction zone is defined based on Omori's law. All linked events form a cluster and the largest earthquake is defined as the mainshock.

To decluster the seismicity catalog, the parameters associated with the algorithm [Reasenber *et al.*, 1985] should be set up. Since the successful application of this method to detect

foreshocks and aftershocks [Reasenber, 1985], it is a common exercise to utilize the standard parameters values obtained by *Schorlemmer and Gerstenberger* [2007] through a Monte Carlo simulation. However, among those parameters, attention should be paid to  $\tau_{min}$  and  $\tau_{max}$ , the minimum and maximum look-ahead time of observing the next earthquake at a certain probability  $p$ , because the behavior of Omori's law is related to the site-dependent tectonic setting [Dieterich, 1994]. In Oklahoma,  $\tau_{min}$  and  $\tau_{max}$  can be estimated through earthquake sequence analysis from four M5+ earthquakes (2011-11-09 Mw 5.7 Prague Earthquake, 2016-02-13 Mw 5.1 Fairview Earthquake, 2016-09-03 Mw 5.8 Pawnee Earthquake, 2016-11-07 Mw 5.0 Cushing Earthquake), which provide a value of 1 day for  $\tau_{min}$  and 30 days for  $\tau_{max}$  [Yeck *et al.*, 2017]. For probability  $p$ , the standard value of 95% is used. Moreover, an average location uncertainty of 1.5 km for earthquake epicenter and 2.0 km for earthquake depth is obtained based on the seismic catalog. Focusing on the mainshocks, the dependent earthquakes were removed and the events directly linked to deep fluid injection were identified using the declustering scheme. Finally, the number of M3+ earthquakes was reduced by 60% (Figures D.2 and D.3).

#### 5.4.2 Poroelastic Modeling

A coupled poroelastic model is employed to calculate the spatial and temporal evolution of poroelastic stresses and pore pressure due to fluid injections. The theory of poroelasticity accounts for the coupling between deformation of the porous medium and evolution of the pore fluid pressure. This means a change of pore pressure can deform rocks and vice versa. The full governing equations of linear poroelasticity contain the Navier-Cauchy equation which is derived by substituting poroelastic constitutional equations into the equilibrium equation and the diffusion equation which is obtained by combining Darcy's



law and the Continuity equation [Cheng, 2016]. More details are reported in Zhai and Shirzaei [2018].

The subsurface geological structure in Oklahoma is complex, owing to its long and complex magmatic and tectonic history [Johnson, 2008]. The central seismically active Oklahoma (CO) is located between the south-north trending Nemaha fault system and the eastern Wilzetta fault system. The Nemaha uplift acts as a boundary separating the western seismically active Oklahoma (WO) from CO (Figure 5.1). Most of the industry co-produced saltwater was injected into deep un-pressured and permeable carbonate/sandstone Arbuckle formation, which overlies the Precambrian crystalline granite basement [Faith *et al.*, 2010]. The average thickness of the Arbuckle formation is  $\sim 1000$  m [Keranen *et al.*, 2013]. Resting on the Arbuckle formation, there are formations including the Post-Simpson Mississippian shale, the Devonian shale, and the Upper Ordovician shale. Atop the Mississippian shales are Pennsylvania and Permian sandstones. The stratigraphic columns are summarized in Figure D.4.

A recent study shows that induced seismicity is strongly correlated with the relative distance ( $D_{rela}$ ) between injection depth and basement depth [Hincks *et al.*, 2018]. Based on penetrating-basement well log information, the top of the granite basement is not a planar surface. The basement depth increases from east to west with a range of 1000 – 3000 m. Injection well depth also reflects this trend, suggesting that the injection bottoms in the Arbuckle formation are very close to the basement (Figure D.5). Using the records of wells drilled into the crystalline basement [Campbell and Weber, 2006], the basement depth was estimated using a polynomial curve fitting (Figure D.6), which is then used to approximate  $D_{rela}$  at the locations of injection wells (Figure D.7). The lithostratigraphic columns were simplified by considering four horizontal layers shown in Figure D.8.

To characterize the poroelastic medium, the shear modulus  $G$ , Poisson ratio  $\nu$ , undrained Poisson ratio  $\nu_u$ , hydraulic diffusivity  $D$ , and Skempton coefficient  $B$  are needed. The Poisson ratio can be determined using the ratio of P and S wave velocities [Christensen, 1996]:

$$\nu = \frac{1}{2} \left( 1 - \frac{1}{(v_p/v_s)^2 - 1} \right) \quad (5.1)$$

Tomographic imaging shows that the average values of  $v_p/v_s$  at different depths ( $< 15$  km) are in the range of 1.71 - 1.74 [Chen, 2016], which corresponds to a value roughly equal to 0.25 for Poisson ratio. Another important hydrogeological parameter is the hydraulic diffusivity  $D$  within Arbuckle formation. Analysis of seismicity migration pattern and local hydrogeology provide a diffusivity range of 0.5 – 4.5 m<sup>2</sup>/s [Goebel *et al.*, 2017; Keranen *et al.*, 2014]. Distinct geological signatures indicate obvious differences between hydrogeology in WO and CO [Shah and Keller, 2017]. Also, the Earth tide strain analysis at several different saltwater disposal wells suggests larger hydraulic diffusivity in WO and smaller hydraulic diffusivity in CO [Perilla-Castillo, 2017]. Earthquake migration towards Kansas as far as 90 km away from the initial swarm locations near high-volume injections within WO is an indicator for relatively large hydraulic diffusivity of the formation in WO [Peterie *et al.*, 2018]. Accounting for these hydrogeological differences, different diffusivity values of 1.5 m<sup>2</sup>/s and 4.0 m<sup>2</sup>/s for CO and WO, respectively, were used. As seen in Figure 5.3 (discussed later), the model setup using these values provides the best fit to the observations in CO and WO. Figure D.9 lists the optimal values of the model parameters. Other values of hydraulic diffusivity were further tested, including 1.0 m<sup>2</sup>/s and 2.0 m<sup>2</sup>/s for CO, and 2.0 m<sup>2</sup>/s and 6.0 m<sup>2</sup>/s for WO and found that fit to the data did not improve and got worse in some cases.

The hydraulic diffusivities of basement and shale formations were assumed to be several orders of magnitude smaller than that of the Arbuckle formation [Hornbach *et al.*, 2016].

Once the Earth model is obtained, the method of Wang and Kümpel [2003] is applied to simulate the spatial and temporal evolution of poroelastic stresses and pore pressure due to time series of monthly injected volumes in a layered poroelastic half-space. This method uses a spectral element method and calculates time-dependent axisymmetric pore pressure and poroelastic strain tensor in a 3D cylindrical coordinate system. For each well, a radial domain of 100 km with 50 radial samples and a time span of 35 years between 1995 and 2030 with 280 temporal samples were defined for simulating the output. To reduce the computation load, only the results at the bottom of Arbuckle formation were output. Then a tensor transformation was applied to compute the strain tensor in a Cartesian coordinate system. Afterward, the pore pressure and transformed poroelastic strain associated with each well were resampled on a grid of 5.5 by 3.5 degrees with a cell size of 0.025 by 0.025 degrees in longitude and latitude directions, respectively.

#### 5.4.3 Seismicity Rate Modeling

The poroelastic model provides the spatiotemporal distribution of the elastic stress tensor ( $\Delta \mathbf{S}$ ) derived from  $\mathbf{u}$ , and pore pressure change ( $\Delta p$ ). This information allows us to calculate the spatial and temporal distribution of the Coulomb Failure Stress (CFS) change  $\Delta \tau(\mathbf{x}, t)$ , which is obtained from contributions of pore pressure and poroelastic stresses once the fault geometry and frictional coefficient are defined [Zhai and Shirzaei, 2018].

Both laboratory experiments and rate-and-state friction laws predict that a small change in shear or normal stresses may cause a large change in fault slip rate. Dieterich [1994] developed a framework describing the evolution of seismicity rate as a function of

background seismicity rate and CFS change. A simplified version was given by *Segall and Lu* [2015] relating the relative seismicity rate  $R(\mathbf{x}, t)$  (rate of seismicity relative to the background seismicity rate) to the Coulomb Failure Stress rate  $\dot{\tau}(\mathbf{x}, t)$ . However, the inherent assumption associated with the *Dieterich* [1994] model is that the background stress is sufficiently high relative to the shear resistance and a nonzero background stressing rate leads to a nonzero background seismicity rate. Given that the Arbuckle formation is naturally under-pressured [*Keranen et al.*, 2013; *Murray and Holland*, 2014], an amount of fluid is initially needed to compensate the pressure deficit before the seismicity rate increases. Thus, to solve for the seismicity rate associated with the imparted Coulomb Failure Stress rate, a critical time  $t_{crit}$  (when the seismicity rate starts to deviate from its background value) is considered:

$$\begin{aligned} \frac{dR(\mathbf{x}, t)}{dt} &= \frac{R(\mathbf{x}, t)\dot{\tau}_0}{A\bar{\sigma}} \left( \frac{\dot{\tau}(\mathbf{x}, t)}{\dot{\tau}_0} - R(\mathbf{x}, t) \right), t \geq t_{crit} \\ \frac{dR(\mathbf{x}, t)}{dt} &= \frac{R(\mathbf{x}, t)\dot{\tau}_0}{A\bar{\sigma}} (1 - R(\mathbf{x}, t)), t < t_{crit} \end{aligned} \quad (5.2)$$

where,  $\dot{\tau}_0$  is the background stressing rate,  $A$  is a constitutive parameter in the rate-and-state friction law,  $\bar{\sigma}$  is the background effective normal stress,  $\frac{A\bar{\sigma}}{\dot{\tau}_0}$  is the characteristic relaxation time.

Calculating CFS change, the geometry of receiver faults should be determined. *In Situ* stress analysis shows that the stress directions are remarkably uniform in north-central Oklahoma with maximum horizontal stress oriented to  $85^\circ \pm 5^\circ$  (referred to North direction), which predicts northeast and southeast trending strike-slip faults, consistent with mapped active fault geometries [*Alt and Zoback*, 2016]. Statistical analysis of earthquake focal mechanisms indicates two optimal fault strikes of  $40^\circ$ - $60^\circ$  and  $130^\circ$ - $150^\circ$ , with most

earthquakes occurring on faults elongated in the northeast direction [Holland, 2013]. Thus, the geometrical parameters of an optimal receiver fault were set to be a strike of  $50^\circ$ , a dip of  $90^\circ$ , and a rake of  $180^\circ$ .

To solve for seismicity rate evolution using equation (5.2), the critical time  $t_{crit}$  for CO and WO zones are identified first. Figures 5.1B and 5.1C show the time series of total monthly injection volume versus earthquake histogram for both zones, suggesting a critical time of 2008 for CO and 2013 for WO. To set up the seismicity rate model parameters, a typical value of 0.003 for  $A$  was used [Segall and Lu, 2015]. A value of  $10^{-5}$  MPa/year is considered for the background stressing rate  $\dot{\tau}_0$ , which was obtained based on geodetic studies of the strain rate across the Northern American plate [Calais *et al.*, 2006].  $\bar{\sigma}$  was 22 MPa at the bottom of the Arbuckle formation, considering a normal stress gradient of 10 MPa/km along depth.

## 5.5 Result and Discussion

Using the Earth model and time series of injected fluid volume, the spatiotemporal evolution of the pore pressure and poroelastic stresses in the crust were solved for [Shirzaei *et al.*, 2016; Zhai and Shirzaei, 2018] (Figures D.10 and D.11). Based on the resolved spatiotemporal distribution of pressure and stress changes, the Coulomb Failure Stress (CFS) was calculated on a fault with the strike, dip and rake angles of  $50^\circ$ ,  $90^\circ$ , and  $180^\circ$ , respectively, assuming a frictional coefficient of 0.6 (Figures 5.2, D.10 and D.11). Changes in pore pressure control the spatial and temporal patterns of CFS change. The temporal evolutions of averaged CFS rates for both CO and WO regions have a nonlinear pattern. Two peaks characterize the time series of CFS rate at the end of 2008 and 2014 in CO region and an extended period of elevation occurs during 2013 – 2015 in the WO area

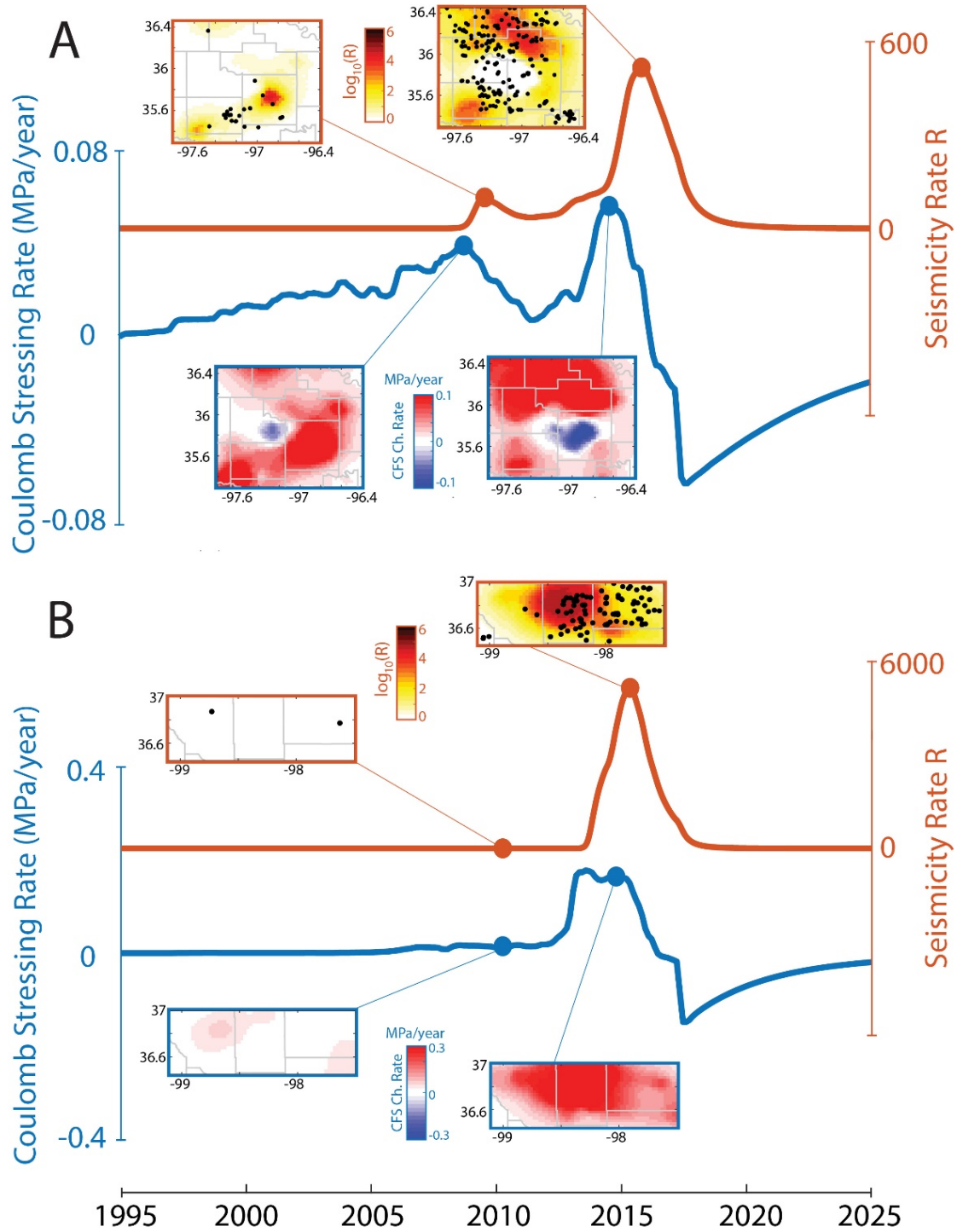


**Figure 5.2.** Simulated time series of average coulomb stressing rate and seismicity rate in (A) CO and (B) WO. Blue and red curves are the time series of average coulomb stressing rate and seismicity rate, respectively. Two snapshots of spatial distributions of CFS change rate and logarithmic seismicity rate are also shown for each study area. Black circles are the incremental M3+ seismicity either from the beginning of the observation period in 1995 or the timing of the previous snapshot.

(Figure 5.2), consistent with the temporally variable injected volumes (Figures 5.1B, C).

Following injection shut-in, the predicted pore pressure, poroelastic stress, and CFS change have decaying patterns (Figures 5.2, D.10 and D.11).

Assuming a background stressing rate of  $10^{-5}$  MPa/year [Calais *et al.*, 2006], a rate- and state-dependent seismicity rate model [Dieterich, 1994; Segall and Lu, 2015; Zhai and Shirzaei, 2018] was applied to simulate the change in earthquake count relative to the background seismicity, as a result of imparted CFS change. Such model is applicable if fault systems are critically stressed before injection. It is perceived that Arbuckle group, where most injection occurred, is naturally under-pressured throughout most of the midcontinent [Keranen *et al.*, 2013; Murray and Holland, 2014]. Thus, at the early stage of injection, the fluid was used to compensate the pressure deficit, and only when a state of pressure equilibrium reached the excess pressure might propagate into the basement, triggering the seismicity. This hypothesis is consistent with the observations that elevated seismicity in CO and WO regions began  $\sim 13$  and  $\sim 8$  years after injection commencement, respectively (Figures 5.1B, C). Accounting for these delays and informed by the time series of CFS rate, the temporal evolution of relative seismicity rates in CO and WO were solved for (Figure 5.2, D.10 and D.11). In 2015, both time series of seismicity rates are characterized by a major peak, while that of CO shows an additional smaller peak in 2010. The snapshots of the spatial distribution of modeled seismicity rate show outward propagating seismicity fronts after injection shut-in at some high-volume wells. This is consistent with the notion that fluid diffuses until pressure equilibrium is reached and until then it transiently changes the stress state in the medium and induces earthquakes. Notably, the locations of observed seismicity are either collocated with the zones of predicted increased seismicity rate or close to its front. The sensitivity tests also

show that seismicity rate weakly depends on the assumed orientation of fault system in Oklahoma (Figure D.12).

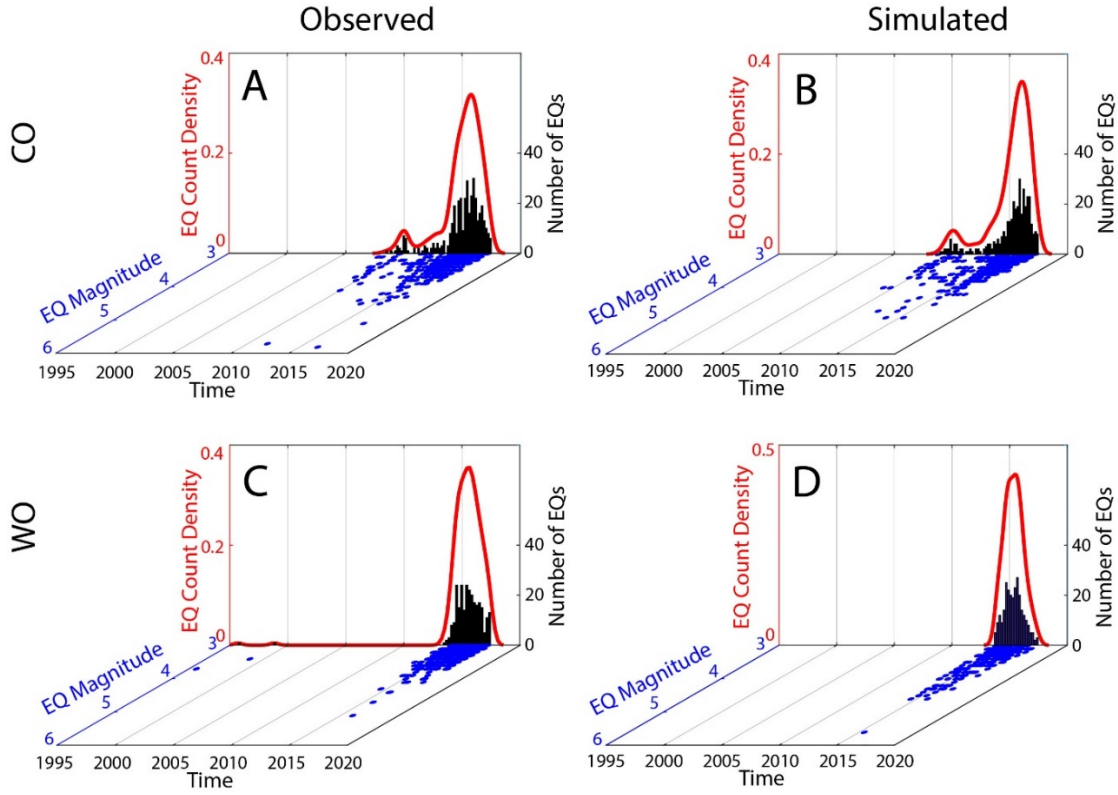


**Figure 5.3.** Observed and predicted M3+ earthquakes in CO and WO through the physics-based approach. (A, B) Observed (left) and simulated (right) earthquake magnitude-time distribution (blue dot) and the associated earthquake count density (black and red) for M3+ earthquakes in CO. (C, D) Observed (left) and simulated (right) earthquake magnitude-time distribution (blue dots) and the associated earthquake count density (black and red) for M3+ earthquakes in WO.

Next the Gutenberg-Richter (GR) frequency-magnitude relationship for the recorded seismicity before seismicity increase was evaluated in CO and WO regions (Text D.1 and Figures D.13-D.15). The background seismicity rate of  $M \geq 0$  (so-called  $k$ -value) are  $\sim 10^{2.71}$  and  $\sim 10^{1.7}$  for the two regions, respectively, with the same  $b$ -value of 1.09. Availability of GR parameters that characterize the seismicity rate before injection and the relative seismicity rate change obtained through poroelastic modeling allow estimating the probability density function of absolute seismicity rate change as a function of earthquake



magnitude and time (Text D.2). Estimating the probability density function of given earthquake magnitudes (e.g., M3+) at any time interval, the magnitude-time space can be discretized and randomly sampled through iterations (Text D.2 and Figure 5.3). In CO, two peaks of increased seismicity rate and earthquake magnitude are accurately recovered in 2010 and 2015. In WO, both predicted and observed earthquake magnitude-time distribution are characterized by a single peak in 2015. In both zones, the predicted numbers of M3+ earthquakes are comparable to that of observed seismicity. However, In CO the largest predicted event is slightly smaller than that observed, suggesting some of the largest events may not be purely induced. The annual earthquake magnitude exceedance probabilities in CO and WO were further estimated (Text D.3 and Figure 5.4). The annual probability for exceeding M5 increases with time till 2015, from <1% in 2008 to 43% in 2015 for CO and from <1% in 2012 to 45% in 2015 for WO. Due to the mandated injected volume reduction in 2016, the model predicts a significant decrease in the probability of exceeding M5 (down to 23%) in WO. However, the decrease of probability is negligible in 2016 for CO. The reason for different responses to injected volume reduction is that the earthquake exceedance probability is highly time-dependent because of the temporally variable nature of diffusion process. In WO, the injection volume reduction is more significant than that of CO. Also, the Earth model in WO is characterized by a larger hydraulic diffusivity, which results in a more rapid diffusion of fluid and decrease in seismicity rate and exceedance probability.

The model predicts a probability of ~10% to exceed M5.8 during 2016 in CO where an M5.8 Pawnee earthquake occurred in September 2016. Injection-induced seismicity follows GR relationship which generally holds for the distributed events. The major limitation in applying this law is estimating the maximum earthquake that can be hosted by the local faults

because the linear relationship associated with GR law may not capture the background magnitude statistics of the rare large-size earthquakes. However, the model provides a lower bound on the probability to exceed M5.8, consistent with the suggestion that following injection operations b-value decreases [Bachmann *et al.*, 2011].

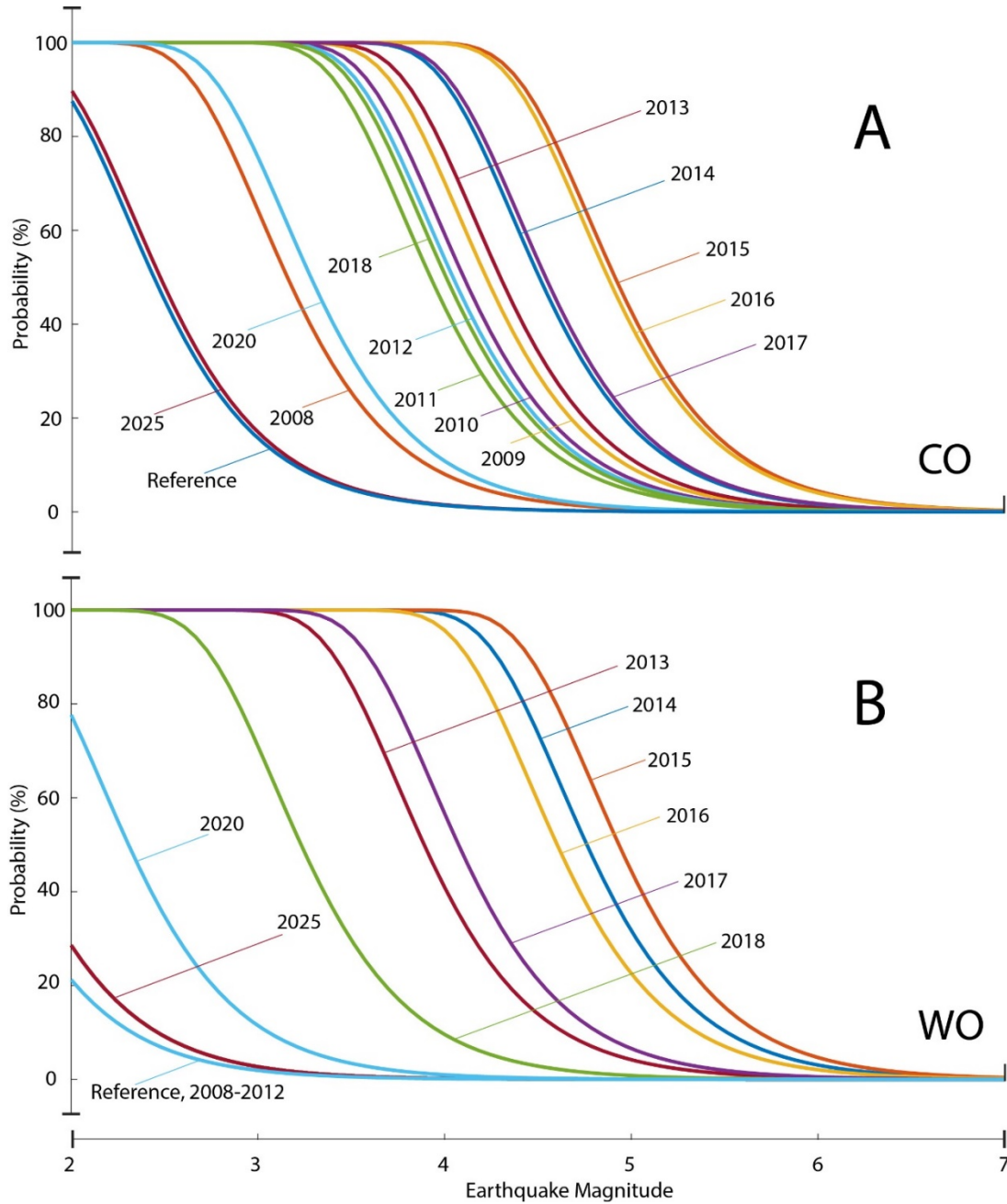


**Figure 5.4.** Annual earthquake magnitude exceedance probabilities in (A) CO and (B) WO.

Assuming a hypothetical injection shut-in in 2017 April, the probabilities within both CO and WO continue to decrease, as expected from postinjection decaying patterns of both pore pressure and seismicity rate, and approach to background tectonic level only in 2025. This indicates that the probability of large earthquakes may not decrease immediately following injection shut-in, primarily due to time-dependent nature of fluid diffusion, which takes some time to reach the earthquake epicenters [Barbour *et al.*, 2017; Keranen *et al.*, 2013; Norbeck and Horne, 2016; Shirzaei *et al.*, 2016]. Factors affecting the delay include injection rate, background stress condition, and local hydrogeology.

## 5.6 Conclusion

Assessing the time-varying seismic hazard due to fluid injection is critically important. Successful effort to forecast fault activation requires accurate quantification of the physics governing the evolution of crustal stresses and seismicity rate [Ellsworth, 2013; McClure and Horne, 2011; Zhai and Shirzaei, 2018]. Despite the improvements in seismic monitoring capacity and the resulting decrease in the magnitude detection threshold [Deichmann and Giardini, 2009; Kim, 2013], estimates of induced earthquake probability remain elusive due to insufficient models incapable of accounting for the complexities of the physical mechanisms. This work highlights the critical role of fluid diffusion in a poroelastic medium to understand the temporal evolution of induced seismic hazard. Also, continuously updated information about the probability of a future earthquake is essential for successful operational earthquake forecasting. Thus, the ability to link the evolution of pore fluid pressure change to seismicity rate change presents a proactive approach to quantifying the seismic hazard associated with fluid injection [Segall and Lu, 2015] and developing frameworks for operational induced earthquake forecasting [Jordan *et al.*, 2011].

## CHAPTER 6

### SUMMARIES AND CONCLUSIONS

In this dissertation, I investigate problems on volcanic and earthquake processes using different observations and developing various methods. Both problems involve mechanical interactions of fluid with solid crust, which are typical processes in the dynamic earth.

In the first part of this dissertation, I develop two different modeling approaches to investigate Kīlauea’s shallow magmatic reservoir.

First, a novel geometry-free time-dependent modeling scheme is used to invert InSAR deformation data for the magmatic source beneath Kīlauea’s summit during 2003–2010. The modeling scheme considers a 3-D array of PCDs and solves for the time series of the distributed volume change at the center of PCDs. Application of principal component analysis to this time-dependent model identifies six independent zones of magmatic activities. Temporal analysis of the volume changes for these reservoirs indicates a more complex relation throughout Kīlauea’s summit reservoir. The data and model results improve the understanding of magma storage, transport, and supply at Kīlauea’s summit and quantify the relation between magmatic activities at the summit to the rift eruption and seismicity.

Second, a new sparsity-promoting inversion scheme is used to image complex volcanic source geometries using geodetic observations such as InSAR deformation data. Benchmark and synthesis tests show that the shape, location, and depth of a zone of volume change with complex geometry can be recovered appropriately. To impose a physically meaningful uniform pressure boundary condition, the boundary element method is applied to solve for the distributed displacement discontinuities on the surface of the finite magma chamber and

associated pressure change. I apply this modeling scheme to InSAR deformation observed at Kilauea summit for periods of rapid uplift and subsidence leading to and following the 2007 Father's Day event. Results indicate that the geometries and depths of the summit magma reservoir vary from one period to another, implying short-term (a timescale less than several years) evolution of the magma chamber. The shallow reservoir inflation and deflation mainly occur at its top and bottom with negligible expansion on its sides. The magnitudes of pressure changes for the two periods are comparable. This new model revises kinematics of the Kilauea summit plumbing system and is valuable for understanding associated physical processes.

Third, for the same Kilauea summit magmatic reservoir, two different sets of models can explain the observations. Time-dependent kinematic modeling allows to identify several deformation centers. A physics-based approach can constrain the shape of zones of irregular magmatic bodies. The deformation centers spatially overlap the resolved irregular magma bodies and thus I propose a new model of the magma chamber that consists of isolated compartments. Although the origin and role of compartments are still in debate, the possible mechanism involves the fact that chambers contain magmas of different compositions with different thermal and mechanical properties. The magmas in a chamber are generally at various stages of solidification and thus at a different temperature and viscosity. Low permeability and different mechanical properties may act as barrier to fluid movement and contribute to the formation of compartments.

In the second part of this dissertation, I use hydrogeological modeling to investigate fluid injection induced seismicity.

I suggest an effective induced earthquake forecasting model, considering a more complex relationship between injection operations and consequent seismicity than other

existing models. To this end, I develop a new physics-based framework to evaluate time-dependent seismic hazard due to fluid injection. In the model, I integrate the mechanisms of earthquake nucleation within a poroelastic medium affected by ambient stress. Firstly, I implement a coupled flow and poroelastic model to simulate the evolution of pore pressure and poroelastic stresses in time and space. Secondly, I use local geology and maps of existing faults to calculate the rate of Coulomb failure stress change. Thirdly, I import the maps of Coulomb stress change rate into a seismicity rate model derived from the rate-and-state friction law. Finally, the estimated seismicity rate changes are used within a probabilistic model to evaluate the time-dependent seismic hazard for each given fault.

I apply this method to the time-varying injections at 96 Ellenberger wells in the Barnett Shale during 2007-2015 and 855 Arbuckle wells in Oklahoma during 1995-2017. In both study areas, earthquake locations correlate well with pore pressure and poroelastic stress, although poroelastic stress is smaller by up to one order of magnitude than pore pressure. Given the good quality of earthquake catalog in Oklahoma, the predicted earthquake magnitude-time distribution based on the modeling results shows excellent fit to observations. These case studies show that the regional induced earthquake timing and magnitude are fully controlled by the process of fluid diffusion in a poroelastic medium and thus it can be successfully forecasted. The obtained time-dependent seismic hazard is spatiotemporally heterogeneous and decreasing the injection rates does not necessarily reduce probabilities immediately, highlighting the important role of hydrological parameters in assessing seismic hazard. The presented framework can be used for operational induced earthquake forecasting and information about the fundamental process understanding, inducing conditions, and probabilistic seismic hazard assessment have tremendous value to the broad society.

## REFERENCES

- Ake, J., K. Mahrer, D. O'Connell, and L. Block (2005), Deep-injection and closely monitored induced seismicity at Paradox Valley, Colorado, *Bulletin of the Seismological Society of America*, 95(2), 664-683.
- Alpaydin, E. (2014), *Introduction to machine learning*, MIT press.
- Alt, R. C., and M. D. Zoback (2016), In situ stress and active faulting in Oklahoma, *Bulletin of the Seismological Society of America*, 107(1), 216-228.
- Amoruso, A., and L. Crescentini (2009), Shape and volume change of pressurized ellipsoidal cavities from deformation and seismic data, *Journal of Geophysical Research: Solid Earth*, 114(B2).
- Anderson, K., and M. P. Poland (2016), Bayesian estimation of magma supply, storage, and eruption rates using a multiphysical volcano model: Kilauea Volcano, 2000–2012, *Earth and Planetary Science Letters*, 447, 161-171, doi:10.1016/j.epsl.2016.04.029.
- Anderson, K., and P. Segall (2011), Physics-based models of ground deformation and extrusion rate at effusively erupting volcanoes, *Journal of Geophysical Research-Solid Earth*, 116, doi:10.1029/2010jb007939.
- Anderson, K. R., M. P. Poland, J. H. Johnson, and A. Miklius (2015), Episodic Deflation–Inflation Events at Kilauea Volcano and Implications for the Shallow Magma System, *Hawaiian Volcanoes: From Source to Surface*, 208, 229.
- Bachmann, C. E., S. Wiemer, J. Woessner, and S. Hainzl (2011), Statistical analysis of the induced Basel 2006 earthquake sequence: introducing a probability-based monitoring approach for Enhanced Geothermal Systems, *Geophysical Journal International*, 186(2), 793-807, doi:10.1111/j.1365-246X.2011.05068.x.
- Baker, S., and F. Amelung (2012), Top-down inflation and deflation at the summit of Kilauea Volcano, Hawai'i observed with InSAR, *Journal of Geophysical Research*, 117(B12), doi:10.1029/2011jb009123.
- Barbour, A. J., J. H. Norbeck, and J. L. Rubinstein (2017), The Effects of Varying Injection Rates in Osage County, Oklahoma, on the 2016 Mw 5.8 Pawnee Earthquake, *Seismological Research Letters*.
- Battaglia, J., J. L. Got, and P. Okubo (2003), Location of long-period events below Kilauea Volcano using seismic amplitudes and accurate relative relocation, *Journal of Geophysical Research: Solid Earth (1978–2012)*, 108(B12).
- Beauducel, F., G. De\_Natale, F. Obrizzo, and F. Pingue (2004), 3-D modelling of Campi Flegrei ground deformations: Role of caldera boundary discontinuities, *Pure and Applied Geophysics*, 161(7), 1305-1327, doi:doi: 10.1007/s00024-004-2506-5.
- Bjerhammar, A. (1973), *Theory of errors and generalized matrix inverse*, 127-128 pp., Elsevier publishing company, Amsterdam.

- Bonaccorso, A., S. Cianetti, C. Giunchi, E. Trasatti, M. Bonafede, and E. Boschi (2005), Analytical and 3-D numerical modelling of Mt. Etna (Italy) volcano inflation, *Geophys. J. Int.*, *163*(2), 852-862, doi:doi: 10.1111/j.1365-246X.2005.02777.x.
- Bonaccorso, A., and P. M. Davis (1999), Models of ground deformation from vertical volcanic conduits with application to eruptions of Mount St. Helens and Mount Etna, *Journal of Geophysical Research*, *104*(B5), 10,531-510,542.
- Borgia, A., P. T. Delaney, and R. P. Denlinger (2000), Spreading volcanoes, *Annual Review of Earth and Planetary Sciences*, *28*, 539-570.
- Brooks, B. A., J. Foster, D. Sandwell, C. J. Wolfe, P. Okubo, M. Poland, and D. Myer (2008), Magmatically Triggered Slow Slip at Kilauea Volcano, Hawaii, *Science*, *321*(5893), 1177.
- Brooks, B. A., J. H. Foster, M. Bevis, L. N. Frazer, C. J. Wolfe, and M. Behn (2006), Periodic slow earthquakes on the flank of Kilauea volcano, Hawaii, *Earth Planet. Sci. Lett.*, *246*, 207-216.
- Calais, E., J. Y. Han, C. DeMets, and J. M. Nocquet (2006), Deformation of the North American plate interior from a decade of continuous GPS measurements, *Journal of Geophysical Research-Solid Earth*, *111*(B6), doi:10.1029/2005jb004253.
- Camacho, A. G., P. J. González, J. Fernández, and G. Berrino (2011), Simultaneous inversion of surface deformation and gravity changes by means of extended bodies with a free geometry: Application to deforming calderas, *Journal of Geophysical Research: Solid Earth* (1978-2012), *116*(B10).
- Campbell, J. A., and J. L. Weber (2006), *Wells drilled to basement in Oklahoma*.
- Candes, E. J., and T. Tao (2006), Near-optimal signal recovery from random projections: Universal encoding strategies?, *IEEE transactions on information theory*, *52*(12), 5406-5425.
- Carbone, D., and M. P. Poland (2012), Gravity fluctuations induced by magma convection at Kilauea Volcano, Hawai'i, *Geology*, *40*(9), 803-806, doi:10.1130/g33060.1.
- Carbone, D., M. P. Poland, M. R. Patrick, and T. R. Orr (2013), Continuous gravity measurements reveal a low-density lava lake at Kilauea Volcano, Hawai'i, *Earth and Planetary Science Letters*, *376*, 178-185, doi:10.1016/j.epsl.2013.06.024.
- Cayol, V., J. H. Dieterich, A. T. Okamura, and A. Miklius (2000), High Magma Storage Rates Before the 1983 Eruption of Kilauea, Hawaii, *Science*, *288*(2343).
- Cervelli, P., and A. Miklius (2003), The shallow magmatic system of Kilauea Volcano, *USGS Professional Paper 1676*, 149-164.
- Cervelli, P., P. Segall, F. Amelung, H. Garbeil, C. Meertens, S. Owen, A. Miklius, and M. Lisowski (2002), The 12 September 1999 Upper East Rift Zone dike intrusion at Kilauea Volcano, Hawaii, *Journal of Geophysical Research-Solid Earth*, *107*(B7), doi:10.1029/2001jb000602.
- Chadwick, W. W., Jr., and J. H. Dieterich (1995), Mechanical modeling of circumferential and radial dike intrusion on Galapagos volcanoes, *J. Volc. Geotherm. Res.*, *66*, 37-52.



- Chang, K. W., and P. Segall (2016), Injection-induced seismicity on basement faults including poroelastic stressing, *Journal of Geophysical Research-Solid Earth*, 121(4), 2708-2726, doi:10.1002/2015jb012561.
- Charco, M., and P. G. del Sastre (2014), Efficient inversion of three-dimensional finite element models of volcano deformation, *Geophysical Journal International*, 196(3), 1441-1454.
- Charl  ty, J., S. Voronin, G. Nolet, I. Loris, F. J. Simons, K. Sigloch, and I. C. Daubechies (2013), Global seismic tomography with sparsity constraints: Comparison with smoothing and damping regularization, *Journal of Geophysical Research: Solid Earth*, 118(9), 4887-4899.
- Chen, C. (2016), *Comprehensive analysis of Oklahoma earthquakes: From earthquake monitoring to 3D tomography and relocation*.
- Cheng, A. H.-D. (2016), *Poroelasticity*, Springer.
- Christensen, N. I. (1996), Poisson's ratio and crustal seismology, *J. Geophys. Res.*, 101, 3139-3156.
- D'Auria, L., F. Giudicepietro, M. Martini, and R. Lanari (2012), The 4D imaging of the source of ground deformation at Campi Flegrei caldera (southern Italy), *Journal of Geophysical Research: Solid Earth (1978–2012)*, 117(B8).
- Davis, P. M. (1983), Surface deformation associated with a dipping hydrofracture, *J. Geophys. Res.*, 88, 5826-5834.
- Davis, P. M. (1986), Surface deformation due to inflation of an arbitrarily oriented triaxial ellipsoidal cavity in an elastic half-space, with reference to Kilauea volcano, Hawaii, *J. Geophys. Res.*, 91, 7429-7438.
- Davis, R. O., and A. P. Selvadurai (1996), *Elasticity and Geomechanics*, Cambridge Univ. Press, Cambridge, xi+201 pp.
- De Natale, G., and F. Pingue (1992), Seismological and geodetic data at Campi Flegrei (Southern Italy): Constraints on volcanological models, in *Volcanic seismology*, edited, pp. 484-502, Springer.
- De Natale, G., and F. Pingue (1996), Ground deformation modeling in volcanic areas, in *Monitoring and Mitigation of Volcano Hazards*, edited, pp. 365-388, Springer.
- De Natale, G., F. Pingue, P. Allard, and A. Zollo (1991), Geophysical and geochemical modelling of the 1982–1984 unrest phenomena at Campi Flegrei caldera (southern Italy), *Journal of Volcanology and Geothermal Research*, 48(1), 199-222.
- Deichmann, N., and D. Giardini (2009), Earthquakes Induced by the Stimulation of an Enhanced Geothermal System below Basel (Switzerland), *Seismological Research Letters*, 80(5), 784-798, doi:10.1785/gssrl.80.5.784.
- Delaney, P. T., and R. P. Denlinger (1999), Stabilization of volcanic flanks by dike intrusion: an example from Kilauea, *Bulletin of Volcanology*, 61(6), 356-362, doi:10.1007/s004450050278.

- Delaney, P. T., R. S. Fiske, A. Miklius, A. T. Okamura, and M. K. Sako (1990), Deep Magma Body beneath the Summit and Rift Zones of Kilauea Volcano, Hawaii, *Science*, 247(4948), 1311-1316, doi:DOI 10.1126/science.247.4948.1311.
- Deming, D. (2002), *Introduction to hydrogeology*, McGraw-Hill College, New York.
- Deng, K., Y. Liu, and R. M. Harrington (2016), Poroelastic stress triggering of the December 2013 Crooked Lake, Alberta, induced seismicity sequence, *Geophysical Research Letters*, 43(16), 8482-8491.
- Denlinger, R. P., and P. Okubo (1995), Structure of the mobile south flank of Kilauea, Volcano, Hawaii, *J. Geophys Res.*(100), 24,499-424,507.
- Dieterich, J. H. (1994), A constitutive law for rate of earthquake production and its application to earthquake clustering, *J. Geophys. Res.*, 99, 2601-2618.
- Dieterich, J. H., K. B. Richards-Dinger, and K. A. Kroll (2015), Modeling Injection-Induced Seismicity with the Physics-Based Earthquake Simulator RSQSim, *Seismological Research Letters*, 86(4), 1102-1109, doi:10.1785/0220150057.
- Donoho, D. L. (2006a), Compressed sensing, *IEEE Transactions on information theory*, 52(4), 1289-1306.
- Donoho, D. L. (2006b), For most large underdetermined systems of equations, the minimal L1-norm near-solution approximates the sparsest near-solution, *Communications on Pure and Applied Mathematics*, 59(7), 907-934.
- Dufek, J., C. Huber, and L. Karlstrom (2013), Magma chamber dynamics and thermodynamics, in *Modeling Volcanic Processes: The Physics and Mathematics of Volcanism*, edited by S. A. Fagents, T. K. P. Gregg and R. M. C. Lopes, pp. 5-31, Cambridge University Press, Cambridge, doi:10.1017/CBO9781139021562.002.
- Duffield, W. A., R. L. Christiansen, R. Y. Koyanagi, and D. W. Peterson (1982), Storage, Migration, and Eruption of Magma at Kilauea Volcano, Hawaii, 1971-1972, *Journal of Volcanology and Geothermal Research*, 13(3-4), 273-307, doi:Doi 10.1016/0377-0273(82)90054-3.
- Dvorak, J., A. Okamura, and J. H. Dieterich (1983), Analysis of surface deformation data, Kilauea Volcano, Hawaii, October 1966 to September 1970, *J. Geophys. Res.*, 88, 9295-9304.
- Dvorak, J. J., and D. Dzurisin (1993), Variations in magma supply rate at Kilauea volcano, Hawaii, *Journal of Geophysical Research: Solid Earth (1978–2012)*, 98(B12), 22255-22268.
- Dzurisin, D. (2007), *Volcano Deformation - New Geodetic Monitoring Techniques*, 476 pp., Springer.
- Eaton, J. P. (1959), A portable water-tube tiltmeter, *Bulletin of the Seismological Society of America*, 49(4), 301-316.
- Eaton, J. P. (1962), *Crustal structure and volcanism in Hawaii*, Wiley Online Library.
- Eaton, J. P., and K. J. Murata (1960), How volcanos grow, *Science*, 132, 925-938.
- Economides, M. J., and K. G. Nolte (2000), *Reservoir stimulation*, Wiley New York.

- Ellsworth, W. L. (2013), Injection-Induced Earthquakes, *Science*, *341*, doi:10.1126/science.1225942.
- Eshelby, J. D. (1957), The determination of the elastic field of an ellipsoidal inclusion, and related problems, *Proc. R. Soc. London*, *241*, 376-396.
- Evans, E. L., J. P. Loveless, and B. J. Meade (2015), Total variation regularization of geodetically and geologically constrained block models for the Western United States, *Geophysical Journal International*, *202*(2), 713-727.
- Evans, E. L., and B. J. Meade (2012), Geodetic imaging of coseismic slip and postseismic afterslip: Sparsity promoting methods applied to the great Tohoku earthquake, *Geophysical Research Letters*, *39*, doi:10.1029/2012gl051990.
- Ewing, T. E. (1990), *Tectonic map of Texas*, Bureau of Economic Geology, University of Texas at Austin.
- Faith, J. R., C. D. Blome, M. P. Pantea, J. O. Puckette, T. Halihan, N. Osborn, S. Christenson, and S. Pack (2010), Three-dimensional geologic model of the Arbuckle-Simpson Aquifer, south-central Oklahoma *Rep. 2331-1258*, US Geological Survey.
- Fan, Z., P. Eichhubl, and J. F. Gale (2016), Geomechanical analysis of fluid injection and seismic fault slip for the Mw 4. 8 Timpson, Texas, earthquake sequence, *Journal of Geophysical Research: Solid Earth*, *121*(4), 2798-2812.
- Fialko, Y., Y. Khazan, and M. Simons (2001), Deformation due to a pressurized horizontal circular crack in an elastic half-space, with applications to volcano geodesy, *Geophysical Journal International*, *146*(1), 181-190, doi:10.1046/j.1365-246X.2001.00452.x.
- Figueiredo, M. A., J. M. Bioucas-Dias, and R. D. Nowak (2007), Majorization–minimization algorithms for wavelet-based image restoration, *IEEE Transactions on Image processing*, *16*(12), 2980-2991.
- Fiske, R. S., and W. T. Kinoshita (1969), Inflation of kilauea volcano prior to its 1967-1968 eruption, *Science*, *165*(3891), 341-349, doi:10.1126/science.165.3891.341.
- Franceschetti, G., and R. Lanari (1999), *Synthetic aperture radar processing*, 324 pp., CRC Press, Boca Raton, Florida.
- Francis, P., and C. Oppenheimer (2004), *Volcanoes* (2nd Edition), edited, Oxford University Press, New York, Oxford.
- Franklin, J. N. (1970), Well-posed stochastic extensions of ill-posed linear problems, *J. Math. Anal. Appl.*, *31*, 682-716.
- Frohlich, C. (2012), Two-year survey comparing earthquake activity and injection-well locations in the Barnett Shale, Texas, *Proceedings of the National Academy of Sciences*, *109*(35), 13934-13938.
- Frohlich, C., C. Hayward, B. Stump, and E. Potter (2011), The Dallas-Fort Worth Earthquake Sequence: October 2008 through May 2009, *Bulletin of the Seismological Society of America*, *101*(1), 327-340, doi:10.1785/0120100131.

- Frohlich, C., J. I. Walter, H. DeShon, B. Stump, C. Hayward, and M. Hornbach (2016), A Historical Review of Induced Earthquakes in Texas, *Seismological Research Letters*, 87(4), 1022-1038, doi:10.1785/0220160016.
- Fujii, T., and I. Kushiro (1977), Density, viscosity, and compressibility of basaltic liquid at high pressures, in Annual Report of the Director 1976-1977 *Rep.*, 419-424 pp, Geophysical Laboratory, Carnegie Institution, Washington, D. C.
- Gale, J. F., and L. A. Gomez (2007), Late opening-mode fractures in karst-brecciated dolostones of the Lower Ordovician Ellenburger Group, west Texas: recognition, characterization, and implications for fluid flow, *AAPG bulletin*, 91(7), 1005-1023.
- Gaul, L., M. Kögl, and M. Wagner (2003), *Boundary element methods for engineers and scientists: an introductory course with advanced topics*, Springer-Verlag Berlin Heidelberg, New York.
- Geertsma, J. (1973), A basic theory of subsidence due to reservoir compaction: the homogeneous case, *Verhandelingen Kon. Ned. Geol. Mijnbouwk. Gen*, 28, 43-62.
- Gholami, A., and H. Siahkoohi (2010), Regularization of linear and non-linear geophysical ill-posed problems with joint sparsity constraints, *Geophysical Journal International*, 180(2), 871-882.
- Goebel, T. H. W., M. Weingarten, X. Chen, J. Haffener, and E. E. Brodsky (2017), The 2016 Mw5.1 Fairview, Oklahoma earthquakes: Evidence for long-range poroelastic triggering at > 40 km from fluid disposal wells, *Earth and Planetary Science Letters*, 472, 50-61, doi:10.1016/j.epsl.2017.05.011.
- Golub, G. H., and C. F. Van Loan (2012), *Matrix computations*, JHU Press.
- Gonnermann, H. M., J. H. Foster, M. Poland, C. J. Wolfe, B. A. Brooks, and A. Miklius (2012), Coupling at Mauna Loa and Kilauea by stress transfer in an asthenospheric melt layer, *Nature Geoscience*, 5(11), 826-829, doi:10.1038/ngeo1612.
- Gono, V. (2015), On shaky ground: understanding the correlation between induced seismicity and wastewater injection in the Fort Worth basin, Master thesis, The University of Texas at Austin.
- Got, J. L., J. Fréchet, and F. W. Klein (1994), Deep fault plane geometry inferred from multiplet relative relocation beneath the south flank of Kilauea, *J. Geophys. Res.*, 99(B8), 15375-15386.
- Grewal, M. S., and A. P. Andrews (2001), *Kalman Filtering : Theory and Practice Using MATLAB*, 416 pp., John Wiley & Sons, New York, N.Y.
- Grigoli, F., S. Cesca, E. Priolo, A. P. Rinaldi, J. F. Clinton, T. A. Stabile, B. Dost, M. G. Fernandez, S. Wiemer, and T. Dahm (2017), Current challenges in monitoring, discrimination, and management of induced seismicity related to underground industrial activities: A European perspective, *Reviews of Geophysics*.
- Gudmundsson, A. (1990), Emplacement of dikes, sills and crustal magma chambers at divergent plate boundaries, *Tectonophysics*, 176(3-4), 257-275.
- Gudmundsson, A. (2008), Magma-Chamber Geometry, Fluid Transport, Local Stresses and Rock Behaviour During Collapse Caldera Formation, in *Caldera Volcanism: Analysis*,

- Modelling and Response*, edited by G. Joachim, M. Joan and iacute, pp. 313-349, Elsevier.
- Gudmundsson, A. (2012), Magma chambers: formation, local stresses, excess pressures, and compartments, *Journal of Volcanology and Geothermal Research*, 237, 19-41.
- Gudmundsson, A. (2016), The mechanics of large volcanic eruptions, *Earth-Science Reviews*, 163, 72-93.
- Guglielmi, Y., F. Cappa, J. P. Avouac, P. Henry, and D. Elsworth (2015), Seismicity triggered by fluid injection-induced aseismic slip, *Science*, 348(6240), 1224-1226, doi:10.1126/science.aab0476.
- Harris, R., and P. Segall (1987), Detection of a locked zone at depth on the Parkfield, California segment of the San Andreas fault, *J. Geophys. Res.*, 92, 7945-7962.
- Healy, J. H., W. W. Rubey, D. T. Griggs, and C. B. Raleigh (1968), The Denver earthquakes, *Science*, 161, 1301-1310.
- Hefferan, K., and J. O'Brien (2010), *Earth materials*, John Wiley & Sons.
- Heliker, C., and S. Brantley (2004), The Ongoing Pu 'u 'O'o-Kupaianaha Eruption of Kilauea Volcano, Hawaii, *US Geological Survey Fact Sheet*, 3085(2).
- Hennenfent, G., E. v. d. Berg, M. P. Friedlander, and F. J. Herrmann (2008), New insights into one-norm solvers from the Pareto curve, *Geophysics*, 73(4), A23-A26.
- Hincks, T., W. Aspinall, R. Cooke, and T. Gernon (2018), Oklahoma's induced seismicity strongly linked to wastewater injection depth, *Science*, eaap7911.
- Hofmann-Wellenhof, B., and H. Moritz (2005), *Physical Geodesy*, Springer.
- Holland, A. A. (2013), Optimal Fault Orientations within Oklahoma, *Seismological Research Letters*, 84(5), 876-890, doi:10.1785/0220120153.
- Hornbach, M. J., H. R. DeShon, W. L. Ellsworth, B. W. Stump, C. Hayward, C. Frohlich, H. R. Oldham, J. E. Olson, M. B. Magnani, and C. Brokaw (2015), Causal factors for seismicity near Azle, Texas, *Nature communications*, 6.
- Hornbach, M. J., M. Jones, M. Scales, H. R. DeShon, M. B. Magnani, C. Frohlich, B. Stump, C. Hayward, and M. Layton (2016), Ellenburger wastewater injection and seismicity in North Texas, *Physics of the Earth and Planetary Interiors*, 261, 54-68, doi:10.1016/j.pepi.2016.06.012.
- Horton, S. (2012), Disposal of Hydrofracking Waste Fluid by Injection into Subsurface Aquifers Triggers Earthquake Swarm in Central Arkansas with Potential for Damaging Earthquake, *Seismological Research Letters*, 83(2), 250-260, doi:10.1785/gssrl.83.2.250.
- Hubbert, M. K., and W. W. Rubey (1959), Role of fluid pressure in mechanics of overthrust faulting, *Geol. Soc. Am. Bull.*, 70, 11-166.
- Johnson, D. J. (1992), Dynamics of Magma Storage in the Summit Reservoir of Kilauea Volcano, Hawaii, *J. Geophys. Res.*, 97(B2), 1807-1820.

- Johnson, D. J., A. A. Eggers, M. Bagnardi, M. Battaglia, M. P. Poland, and A. Miklius (2010), Shallow magma accumulation at Kilauea Volcano, Hawai'i, revealed by microgravity surveys, *Geology*, 38(12), 1139-1142, doi:10.1130/G31323.1.
- Johnson, D. J., F. Sigmundsson, and P. T. Delaney (2000), Comment on "Volume of magma accumulation or withdrawal estimated from surface uplift or subsidence, with application to the 1960 collapse of Kilauea volcano" by PT Delaney and DF McTigue, *Bulletin of Volcanology*, 61(7), 491-493.
- Johnson, K. S. (2008), Geologic history of Oklahoma, *Earth sciences and mineral resources of Oklahoma: Oklahoma Geological Survey Educational Publication*, 9, 3-5.
- Jolliffe, I. (2005), Principal Component Analysis, in *Encyclopedia of Statistics in Behavioral Science*, edited by B. S. Everitt and D. C. Howell, pp. 1580-1584, John Wiley & Sons, Chichester, England.
- Jónsson, S., H. Zebker, P. Segall, and F. Amelung (2002), Fault Slip Distribution of the 1999 Mw7.1 Hector Mine Earthquake, California, estimated from Satellite Radar and GPS Measurements, *Bull. Seismol. Soc. Am.*, 92, 1377-1389.
- Jordan, T. H., Y.-T. Chen, P. Gasparini, R. Madariaga, I. Main, W. Marzocchi, G. Papadopoulos, G. Sobolev, K. Yamaoka, and J. Zschau (2011), Operational Earthquake Forecasting: State of Knowledge and Guidelines for Utilization, *Annals of Geophysics*, 54(4), 315-391.
- Justinic, A. H., B. Stump, C. Hayward, and C. Frohlich (2013), Analysis of the Cleburne, Texas, Earthquake Sequence from June 2009 to June 2010, *Bulletin of the Seismological Society of America*, 103(6), 3083-3093, doi:10.1785/0120120336.
- Kalman, R. E. (1960), A New Approach to Linear Filtering and Prediction Problems, *ASME-Journal of Basic Engineering*, 82, 35-45.
- Keranen, K. M., H. M. Savage, G. A. Abers, and E. S. Cochran (2013), Potentially induced earthquakes in Oklahoma, USA: Links between wastewater injection and the 2011 Mw 5.7 earthquake sequence, *Geology*, 41(6), 699-702, doi:10.1130/g34045.1.
- Keranen, K. M., M. Weingarten, G. A. Abers, B. A. Bekins, and S. Ge (2014), Sharp increase in central Oklahoma seismicity since 2008 induced by massive wastewater injection, *Science*, 345(6195), 448-451.
- Kim, W.-Y. (2013), Induced seismicity associated with fluid injection into a deep well in Youngstown, Ohio, *Journal of Geophysical Research: Solid Earth*, 118(7), 3506-3518, doi:10.1002/jgrb.50247.
- King, G. C. P., R. S. Stein, and J. Lin (1994), Static stress changes and the triggering of earthquakes, *Bull. Seism. Soc. Am.*, 84, 935-953.
- Klein, F. W., R. Y. Koyanagi, J. S. Nakata, and W. R. Tanigawa (1987), The seismicity of Kilauea's magma system, *US Geol. Surv. Prof. Pap.*, 1350(2), 1019-1185.
- Langenbruch, C., and M. D. Zoback (2016), How will induced seismicity in Oklahoma respond to decreased saltwater injection rates?, *Science Advances*, 2(11), doi:10.1126/sciadv.1601542.

- Lees, J. M. (2007), Seismic tomography of magmatic systems, *Journal of Volcanology and Geothermal Research*, 167(1), 37-56.
- Lévéque, J. J., L. Rivera, and G. Wittlinger (1993), On the use of the checker-board test to assess the resolution of tomographic inversions, *Geophysical Journal International*, 115(1), 313-318.
- Lin, G., P. M. Shearer, R. S. Matoza, P. G. Okubo, and F. Amelung (2014), Three-dimensional seismic velocity structure of Mauna Loa and Kilauea volcanoes in Hawaii from local seismic tomography, *Journal of Geophysical Research-Solid Earth*, 119(5), 4377-4392, doi:10.1002/2013jb010820.
- Lisowski, M. (2007), Analytical volcano deformation source models, in *Volcano Deformation*, edited, pp. 279-304, Springer.
- Liu, Y. (2009), *Fast multipole boundary element method: theory and applications in engineering*, Cambridge university press.
- Liu, Y., S. Mukherjee, N. Nishimura, M. Schanz, W. Ye, A. Sutradhar, E. Pan, N. A. Dumont, A. Frangi, and A. Saez (2011), Recent advances and emerging applications of the boundary element method, *Applied Mechanics Reviews*, 64(3), 030802.
- Lockwood, J. P., R. I. Tilling, R. T. Holcomb, F. Klein, A. T. Okamura, and D. W. Peterson (1999), *Magma migration and resupply during the 1974 summit eruptions of Kilauea Volcano, Hawaii*, US Government Printing Office.
- Lu, Z., T. Masterlark, J. Power, D. Dzurisin, and C. Wicks (2002), Subsidence at Kiska volcano, western Aleutians, detected by satellite radar interferometry, *Geophysical Research Letters*, 29(18).
- Lundgren, P., et al. (2013), Evolution of dike opening during the March 2011 Kamoamo fissure eruption, Kilauea Volcano, Hawai'i, *Journal of Geophysical Research-Solid Earth*, 118(3), 897-914, doi:10.1002/jgrb.50108.
- Lundgren, P., S. V. Samsonov, C. M. López Velez, and M. Ordoñez (2015), Deep source model for Nevado del Ruiz Volcano, Colombia, constrained by interferometric synthetic aperture radar observations, *Geophysical Research Letters*, 42(12), 4816-4823.
- Lustig, M., D. Donoho, and J. M. Pauly (2007), Sparse MRI: The application of compressed sensing for rapid MR imaging, *Magnetic resonance in medicine*, 58(6), 1182-1195.
- Maerten, F., P. Resor, D. Pollard, and L. Maerten (2005), Inverting for slip on three-dimensional fault surfaces using angular dislocations, *Bulletin of the Seismological Society of America*, 95(5), 1654-1665, doi:doi: 10.1785/0120030181.
- Magnani, M. B., M. L. Blanpied, H. R. DeShon, and M. J. Hornbach (2017), Discriminating between natural versus induced seismicity from long-term deformation history of intraplate faults, *Science advances*, 3(11), e1701593.
- Majer, E. L., R. Baria, M. Stark, S. Oates, J. Bommer, B. Smith, and H. Asanuma (2007), Induced seismicity associated with enhanced geothermal systems, *Geothermics*, 36(3), 185-222, doi:10.1016/j.geothermics.2007.03.003.

- Malioutov, D., M. Çetin, and A. S. Willsky (2005), A sparse signal reconstruction perspective for source localization with sensor arrays, *IEEE Transactions on Signal Processing*, 53(8), 3010-3022.
- Manga, M., and C. Wang (2015), 4.12. Earthquake hydrology, *Treatise on Geophysics, second edition*. Elsevier, Oxford, 305-328.
- Marsh, B. (1981), On the crystallinity, probability of occurrence, and rheology of lava and magma, *Contributions to Mineralogy and Petrology*, 78(1), 85-98.
- Marsh, B. D. (1989), Magma Chambers, *Annual Review of Earth and Planetary Sciences*, 17(1), 439-472, doi:doi:10.1146/annurev.earth.17.050189.002255.
- Marsh, B. D. (2015), Magma Chambers in *The Encyclopedia of Volcanoes (Second Edition)*, edited by H. Sigurdsson, B. Houghton, S. McNutt, H. Rymer and J. Stix, pp. 185-201, Academic Press, Amsterdam.
- Marsh, S., and A. Holland (2016), Comprehensive fault database and interpretive fault map of Oklahoma, *Oklahoma Geol. Surv. Open-File Rept.*, 15.
- Maruyama, T. (1964), Statical elastic dislocations in an infinite and semi-infinite medium, *Bull. Earthq. Res. Inst.*, 42, 289-368.
- Masterlark, T., K. L. Feigl, M. Haney, J. Stone, C. Thurber, and E. Ronchin (2012), Nonlinear estimation of geometric parameters in FEMs of volcano deformation: Integrating tomography models and geodetic data for Okmok volcano, Alaska, *Journal of Geophysical Research: Solid Earth*, 117(B2).
- Masterlark, T., and Z. Lu (2004), Transient volcano deformation sources imaged with interferometric synthetic aperture radar: Application to Seguam Island, Alaska, *J. Geophys. Res.*, 109(B1), doi:doi: 10.1029/2003JB002568.
- McClure, M. W., and R. N. Horne (2011), Investigation of injection-induced seismicity using a coupled fluid flow and rate/state friction model, *Geophysics*, 76(6), WC181-WC198, doi:10.1190/geo2011-0064.1.
- McGarr, A. (2014), Maximum magnitude earthquakes induced by fluid injection, *Journal of Geophysical Research-Solid Earth*, 119(2), 1008-1019, doi:10.1002/2013jb010597.
- McTigue, D. F. (1987), Elastic stress and deformation near a finite spherical magma body: resolution of the point source paradox, *J. Geophys. Res.*, 92, 12931-12940.
- Menke, W. (1984), *Geophysical Data Analysis: Discrete Inverse Theory*, Academic Press, Orlando, 260 pp.
- Meyer, P. L. (1970), *Introductory Probability and Statistical Applications*, second edition ed., 367 pp., oxford & IBH
- Miklius, A., P. Cervelli, M. Sako, M. Lisowski, S. Owen, P. Segal, J. Foster, K. Kamibayashi, and B. Brooks (2005), Global positioning system measurements on the Island of Hawai'i: 1997 through 2004, *Rep. 2005-1425*, 48 pp, U.S. Geological Survey.
- Mogi, K. (1958), Relations between the eruptions of various volcanoes and the deformations of the ground surfaces around them, *Bull. Earthq. Res. Inst. (Tokyo)*, 36, 99-134.



- Montgomery-Brown, E. K., P. Segall, and A. Miklius (2009), Kilauea slow slip events: Identification, source inversions, and relation to seismicity, *Journal of Geophysical Research-Solid Earth*, 114, , B00A03, doi:10.1029/2008JB006074.
- Montgomery-Brown, E. K., D. K. Sinnett, K. M. Larson, M. P. Poland, P. Segall, and A. Miklius (2011), Spatiotemporal evolution of dike opening and decollement slip at Kilauea Volcano, Hawai'i, *Journal of Geophysical Research-Solid Earth*, 116, doi:10.1029/2010jb007762.
- Montgomery-Brown, E. K., D. K. Sinnett, M. Poland, P. Segall, T. Orr, H. Zebker, and A. Miklius (2010), Geodetic evidence for an echelon dike emplacement and concurrent slow slip during the June 2007 intrusion and eruption at Kilauea volcano, Hawaii, *Journal of Geophysical Research-Solid Earth*, 115, doi:10.1029/2009jb006658.
- Montgomery, S. L., D. M. Jarvie, K. A. Bowker, and R. M. Pollastro (2005), Mississippian Barnett Shale, Fort Worth basin, north-central Texas: Gas-shale play with multi-trillion cubic foot potential, *Aapg Bulletin*, 89(2), 155-175, doi:10.1306/091704040402.
- Mossop, A., and P. Segall (1999), Volume strain within The Geysers geothermal field, *Journal of Geophysical Research-Solid Earth*, 104(B12), 29113-29131, doi:10.1029/1999jb900284.
- Müller, G. (2001), Volume change of seismic sources from moment tensors, *Bull. Seism. Soc. Am.*, 91(4), 880-884.
- Mura, T. (2013), *Micromechanics of defects in solids*, Springer Science & Business Media.
- Murray, K. E., and A. A. Holland (2014), Inventory of class II underground injection control volumes in the midcontinent.
- Mutch, J., and D. G. Lowe (2006), Multiclass object recognition with sparse, localized features, paper presented at 2006 IEEE Computer Society Conference on Computer Vision and Pattern Recognition (CVPR'06), IEEE.
- Myer, D., D. Sandwell, B. Brooks, J. Foster, and M. Shimada (2008), Inflation along Kilauea's Southwest Rift Zone in 2006, *Journal of Volcanology and Geothermal Research*, 177(2), 418-424.
- Nikkhoo, M., and T. R. Walter (2015), Triangular dislocation: an analytical, artefact-free solution, *Geophysical Journal International*, 201(2), 1117-1139.
- Norbeck, J., and J. Rubinstein (2018), Hydromechanical earthquake nucleation model forecasts onset, peak, and falling rates of induced seismicity in Oklahoma and Kansas, *Geophysical Research Letters*, 45(7), 2963-2975.
- Norbeck, J. H., and R. N. Horne (2016), Evidence for a transient hydromechanical and frictional faulting response during the 2011 Mw 5.6 Prague, Oklahoma earthquake sequence, *Journal of Geophysical Research-Solid Earth*, 121(12), 8688-8705, doi:10.1002/2016jb013148.
- OCC (2016), Media advisory—Regional earthquake response plan for central Oklahoma and expansion of the area of interest.

- Okada, Y. (1985), Surface deformation due to shear and tensile faults in a half-space, *Bull. Seism. Soc. Am.*, 75, 1135-1154.
- Okada, Y. (1992), Internal deformation due to shear and tensile faults in a half-space, *Bull. Seism. Soc. Am.*, 82, 1018-1040.
- Owen, S., P. Segall, J. Freymueller, A. Miklius, R. Denlinger, T. Arnadottir, M. Sako, and R. Burgmann (1995), Rapid Deformation of the South Flank of Kilauea Volcano, Hawaii, *Science*, 267(5202), 1328-1332, doi:10.1126/science.267.5202.1328.
- Owen, S., P. Segall, M. Lisowski, A. Miklius, R. Denlinger, and M. Sako (2000a), Rapid deformation of Kilauea Volcano: Global Positioning System measurements between 1990 and 1996, *J. Geophys. Res.*, 105(B8), 18,983–918,998.
- Owen, S., P. Segall, M. Lisowski, A. Miklius, M. Murray, M. Bevis, and J. Foster (2000b), January 30, 1997 eruptive event on Kilauea Volcano, Hawaii, as monitored by continuous GPS, *Geophysical Research Letters*, 27(17), 2757-2760, doi:10.1029/1999gl008454.
- Parfitt, E. A., and L. Wilson (2008), *Fundamentals of Physical Volcanology*, edited, Blackwell Publishing Ltd, Oxford, UK.
- Pascal, K., J. Neuberg, and E. Rivalta (2014), On precisely modelling surface deformation due to interacting magma chambers and dykes, *Geophysical Journal International*, 196(1), 253-278, doi:10.1093/gji/ggt343.
- Patrick, M. R., T. Orr, A. J. Sutton, E. Tamar, and D. Swanson (2013), The first five years of Kīlauea's summit eruption in Halema 'ūma 'ū Crater, 2008–2013, *US Geol. Surv. Fact Sh.*, 3116(4).
- Pei, S., Z. Peng, and X. Chen (2018), Locations of Injection-Induced Earthquakes in Oklahoma Controlled by Crustal Structures, *Journal of Geophysical Research: Solid Earth*, 0(0), doi:10.1002/2017JB014983.
- Perilla-Castillo, P. (2017), Rock properties derived from analysis of earth tide strain observed in continuous pressure monitoring of the Arbuckle Group of Oklahoma.
- Peterie, S. L., R. D. Miller, J. W. Intfen, and J. B. Gonzales (2018), Earthquakes in Kansas induced by extremely far-field pressure diffusion, *Geophysical Research Letters*.
- Petersen, M. D., C. S. Mueller, M. P. Moschetti, S. M. Hoover, A. L. Llenos, W. L. Ellsworth, A. J. Michael, J. L. Rubinstein, A. F. McGarr, and K. S. Rukstales (2016), 2016 one-year seismic hazard forecast for the Central and Eastern United States from induced and natural earthquakes *Rep. 2331-1258*, US Geological Survey.
- Pietruszka, A. J., and M. O. Garcia (1999a), A rapid fluctuation in the mantle source and melting history of Kilauea Volcano inferred from the geochemistry of its historical summit lavas (1790–1982), *Journal of Petrology*, 40(8), 1321-1342.
- Pietruszka, A. J., and M. O. Garcia (1999b), The size and shape of Kilauea Volcano's summit magma storage reservoir: a geochemical probe, *Earth and Planetary Science Letters*, 167(3), 311-320.

- Pietruszka, A. J., D. E. Heaton, J. P. Marske, and M. O. Garcia (2015), Two magma bodies beneath the summit of Kilauea Volcano unveiled by isotopically distinct melt deliveries from the mantle, *Earth and Planetary Science Letters*, *413*(0), 90-100, doi:http://dx.doi.org/10.1016/j.epsl.2014.12.040.
- Poland, M., T. Huth, and A. Miklius (2009a), Source processes of short-term, transient tilt events at Kilauea Volcano, Hawaii, paper presented at AGU Fall Meeting Abstracts.
- Poland, M., A. Miklius, and E. Montgomery-Brown (2014), Magma supply, storage, and transport at shield-stage Hawaiian volcanoes, in *Characteristics of Hawaiian Volcanoes*, edited by M. Poland, T. Takahashi and C. Landowski, pp. 179-234, U.S. Geological Survey, Reston, Virginia.
- Poland, M., A. Miklius, T. Orr, J. Sutton, C. Thornber, and D. Wilson (2008), New episodes of volcanism at Kilauea Volcano, Hawaii, *Eos, Transactions American Geophysical Union*, *89*(5), 37-38.
- Poland, M. P. (2014), Time-averaged discharge rate of subaerial lava at Kilauea Volcano, Hawai'i, measured from TanDEM-X interferometry: Implications for magma supply and storage during 2011-2013, *Journal of Geophysical Research-Solid Earth*, *119*(7), 5464-5481, doi:10.1002/2014jb011132.
- Poland, M. P., A. Miklius, A. J. Sutton, and C. R. Thornber (2012), A mantle-driven surge in magma supply to Kilauea Volcano during 2003-2007, *Nature Geoscience*, *5*(4), 295-U297, doi:10.1038/Ngeo1426.
- Poland, M. P., A. J. Sutton, and T. M. Gerlach (2009b), Magma degassing triggered by static decompression at Kilauea Volcano, Hawai'i, *Geophysical Research Letters*, *36*, doi:10.1029/2009gl039214.
- Pollastro, R. M., D. M. Jarvie, R. J. Hill, and C. W. Adams (2007), Geologic framework of the Mississippian Barnett Shale, Barnett-Paleozoic total petroleum system, bend arch-Fort Worth Basin, Texas, *Aapg Bulletin*, *91*(4), 405-436, doi:10.1306/10300606008.
- Pratt, W. E., and D. W. Johnson (1926), Local subsidence of the Goose Creek oil field, *The Journal of Geology*, *34*(7, Part 1), 577-590.
- Raleigh, C. B., J. H. Healy, and J. D. Bredehoeft (1976), An Experiment in Earthquake Control at Rangely, Colorado, *191*(4233), 1230-1237 doi:DOI: 10.1126/science.191.4233.1230.
- Reasenber, P. (1985), Second-order moment of central California seismicity, 1969-1982, *Journal of Geophysical Research: Solid Earth*, *90*(B7), 5479-5495.
- Rivalta, E., and P. Segall (2008), Magma compressibility and the missing source for some dike intrusions, *Geophysical Research Letters*, *35*(4), doi:10.1029/2007gl032521.
- Ronchin, E. (2015), Finite Element Models of Volcano Deformational Systems Having Structural Complexity, Ph.D thesis, 231 pp, Universitat de Barcelona.
- Ronchin, E., T. Masterlark, J. M. Molist, S. Saunders, and W. Tao (2013), Solid modeling techniques to build 3D finite element models of volcanic systems: an example from the Rabaul Caldera system, Papua New Guinea, *Computers & Geosciences*, *52*, 325-333.

- Rubinstein, J. L., W. L. Ellsworth, A. McGarr, and H. M. Benz (2014), The 2001-Present Induced Earthquake Sequence in the Raton Basin of Northern New Mexico and Southern Colorado, *Bulletin of the Seismological Society of America*, 104(5), 2162-2181, doi:10.1785/0120140009.
- Rubinstein, J. L., and A. B. Mahani (2015), Myths and facts on wastewater injection, hydraulic fracturing, enhanced oil recovery, and induced seismicity, *Seismological Research Letters*.
- Rudnicki, J. (2002), Eshelby transformations, pore pressure and fluid mass changes, and subsidence, paper presented at Second Biot Conference on Poromechanics (Poromechanics II), Grenoble, France, August.
- Ryan, M. P. (1987a), Elasticity and contractancy of Hawaiian olivine tholeiite and its role in the stability and structural evolution of subcaldera magma reservoirs and rift systems, *Volcanism in Hawaii*, 2, 1395-1447.
- Ryan, M. P. (1987b), Neutral buoyancy and the mechanical evolution of magmatic systems, in *Magmatic Processes: Physicochemical Principles*, edited, pp. 259-287, Geochem. Soc. University Park, PA.
- Satter, A., G. M. Iqbal, and J. L. Buchwalter (2008), *Practical enhanced reservoir engineering: assisted with simulation software*, Pennwell Books, Tulsa.
- Scales, M. M., H. R. DeShon, M. B. Magnani, J. I. Walter, L. Quinones, T. L. Pratt, and M. J. Hornbach (2017), A Decade of Induced Slip on the Causative Fault of the 2015 Mw 4.0 Venus Earthquake, Northeast Johnson County, Texas, *Journal of Geophysical Research: Solid Earth*.
- Schorlemmer, D., and M. Gerstenberger (2007), RELM testing center, *Seismological Research Letters*, 78(1), 30-36.
- Scuderi, M. M., and C. Collettini (2016), The role of fluid pressure in induced vs. triggered seismicity: Insights from rock deformation experiments on carbonates, *Scientific reports*, 6, 24852.
- Segall, P. (2010), *Earthquake and volcano deformation*, 432 pp., Princeton University Press, Princeton, New Jersey.
- Segall, P., P. Cervelli, S. Owen, M. Lisowski, and A. Miklius (2001), Constraints on dike propagation from continuous GPS measurements, *J. Geophys. Res.*, 106, 19,301-319,318.
- Segall, P., E. K. Desmarais, D. Shelly, A. Miklius, and P. Cervelli (2006), Earthquakes triggered by silent slip events on Kilauea volcano, Hawaii, *Nature*, 442(7098), 71-74, doi:10.1038/Nature04938.
- Segall, P., and S. Lu (2015), Injection-induced seismicity: Poroelastic and earthquake nucleation effects, *Journal of Geophysical Research-Solid Earth*, 120(7), 5082-5103, doi:10.1002/2015jb012060.
- Shah, A. K., and G. R. Keller (2017), Geologic influence on induced seismicity: Constraints from potential field data in Oklahoma, *Geophysical Research Letters*, 44(1), 152-161.

- Shapiro, S. A. (2015), *Fluid-induced seismicity*, Cambridge University Press.
- Shapiro, S. A., O. S. Kruger, and C. Dinske (2013), Probability of inducing given-magnitude earthquakes by perturbing finite volumes of rocks, *Journal of Geophysical Research-Solid Earth*, *118*(7), 3557-3575, doi:10.1002/jgrb.50264.
- Shirzaei, M. (2013), A Wavelet-Based Multitemporal DInSAR Algorithm for Monitoring Ground Surface Motion, *Ieee Geoscience and Remote Sensing Letters*, *10*(3), 456-460, doi:Doi 10.1109/Lgrs.2012.2208935.
- Shirzaei, M. (2015), A seamless multitrack multitemporal InSAR algorithm, *Geochemistry Geophysics Geosystems*, *16*(5), 1656-1669, doi:Doi 10.1002/2015gc005759.
- Shirzaei, M., and R. Bürgmann (2012), Topography correlated atmospheric delay correction in radar interferometry using wavelet transforms, *Geophysical Research Letters*, *39*(1), doi: 10.1029/2011GL049971.
- Shirzaei, M., and R. Bürgmann (2013), Time-dependent model of creep on Hayward fault inferred from joint inversion of 18 years InSAR time series and surface creep data, *J. Geophys. Res. Solid Earth*, *118*( 1733–1746), doi:10.1002/jgrb.50149.
- Shirzaei, M., W. L. Ellsworth, K. F. Tiampo, P. J. González, and M. Manga (2016), Surface uplift and time-dependent seismic hazard due to fluid injection in eastern Texas, *Science*, *353*(6306), 1416-1419.
- Shirzaei, M., M. L. Rudolph, and M. Manga (2015), Deep and shallow sources for the Lusi mud eruption revealed by surface deformation, *Geophysical Research Letters*.
- Shirzaei, M., and T. R. Walter (2009), Randomly iterated search and statistical competency as powerful inversion tools for deformation source modeling: Application to volcano interferometric synthetic aperture radar data, *Journal of Geophysical Research-Solid Earth*, *114*, doi:Doi 10.1029/2008jb006071.
- Shirzaei, M., and T. R. Walter (2010), Time-dependent volcano source monitoring using interferometric synthetic aperture radar time series: A combined genetic algorithm and Kalman filter approach, *Journal of Geophysical Research-Solid Earth*, *115*, doi:Doi 10.1029/2010jb007476.
- Shirzaei, M., and T. R. Walter (2011), Estimating the Effect of Satellite Orbital Error Using Wavelet-Based Robust Regression Applied to InSAR Deformation Data, *Ieee Transactions on Geoscience and Remote Sensing*, *49*(11), 4600-4605, doi:Doi 10.1109/Tgrs.2011.2143419.
- Shirzaei, M., T. R. Walter, and R. Bürgmann (2013), Coupling of Hawaiian volcanoes only during overpressure condition, *Geophysical Research Letters*, doi:10.1002/grl.50470.
- Sides, I. R., M. Edmonds, J. MacLennan, D. A. Swanson, and B. F. Houghton (2014), Eruption style at Kilauea Volcano in Hawai'i linked to primary melt composition, *Nature Geosci*, *7*(6), 464-469, doi:10.1038/ngeo2140.
- Smith, A. E., and D. W. Coit (1997), Constraint-Handling Techniques - Penalty Functions, in *Handbook of Evolutionary Computation*, edited by T. Bäck, D. Fogel and Z. Michalewicz, Institute of Physics Publishing and Oxford University Press, Bristol, U.K., Chapter C5.2.

- Snee, J. E. L., and M. D. Zoback (2016), State of stress in Texas: Implications for induced seismicity, *Geophysical Research Letters*, 43(19), 10208-10214, doi:10.1002/2016gl070974.
- Stephen, M., Y. Sever, W. Bertiger, M. Heflin, K. Hurst, R. Muellerschoen, S. Wu, T. Yunk, and J. Zumberge (1996), GIPSY-OASIS II: a high precision GPS data processing system and general satellite orbit analysis tool, *Jet Propulsion Laboratory, California Institute of Technology, Pasadena, CA*.
- Sumy, D. F., E. S. Cochran, K. M. Keranen, M. Wei, and G. A. Abers (2014), Observations of static Coulomb stress triggering of the November 2011 M5.7 Oklahoma earthquake sequence, *Journal of Geophysical Research-Solid Earth*, 119(3), 1904-1923, doi:10.1002/2013jb010612.
- Swanson, D. A., W. A. Duffield, and R. S. Fiske (1976), Displacement of the south flank of Kilauea Volcano: The result of forceful intrusion of magma into the rift zones, *Profess. Paper 936 Rep.*, 1-39 pp, U. S. Geol. Surv.
- Thomas, A. L. (1993), Poly 3 D: a three-dimensional, polygonal element, displacement discontinuity boundary element computer program with applications to fractures, faults, and cavities in the Earth's crust, to the Department of Geology, Stanford University.
- Tiampo, K. F., J. B. Rundle, J. Fernández, and J. O. Langbein (2000), Spherical and ellipsoidal volcanic sources at Long Valley caldera, California, using a genetic algorithm inversion technique, *J. Volcanology Geothermal Res.*, 102, 189-206.
- Tibshirani, R. (1996), Regression shrinkage and selection via the lasso, *Journal of the Royal Statistical Society. Series B (Methodological)*, 267-288.
- Tikhonov, A. N., and V. Y. Arsenin (1977), *Solutions of Ill-Posed Problems*, V. H. Winston & Sons, Washington D.C.
- Trasatti, E., C. Giunchi, and N. P. Agostinetti (2008), Numerical inversion of deformation caused by pressure sources: application to Mount Etna (Italy), *Geophysical Journal International*, 172(2), 873-884.
- Trasatti, E., C. Giunchi, and M. Bonafede (2003), Effects of topography and rheological layering on ground deformation in volcanic regions, *J. Volcanology Geothermal Res.*, 122(1-2), 89-110.
- Trasatti, E., C. Giunchi, and M. Bonafede (2005), Structural and rheological constraints on source depth and overpressure estimates at the Campi Flegrei caldera, Italy, *Journal of volcanology and geothermal research*, 144(1), 105-118.
- Van Den Berg, E., and M. P. Friedlander (2008), Probing the Pareto frontier for basis pursuit solutions, *SIAM Journal on Scientific Computing*, 31(2), 890-912.
- van der Elst, N. J., M. T. Page, D. A. Weiser, T. H. W. Goebel, and S. M. Hosseini (2016), Induced earthquake magnitudes are as large as (statistically) expected, *Journal of Geophysical Research-Solid Earth*, 121(6), 4575-4590, doi:10.1002/2016jb012818.

- Vasco, D., C. Puskas, R. Smith, and C. Meertens (2007), Crustal deformation and source models of the Yellowstone volcanic field from geodetic data, *Journal of Geophysical Research: Solid Earth*, 112(B7).
- Vasco, D. W., L. R. Johnson, and N. E. Goldstein (1988), Using surface displacement and strain observations to determine deformation at depth, with an application to Long Valley Caldera, California, *Journal of Geophysical Research-Solid Earth and Planets*, 93(B4), 3232-3242, doi:10.1029/JB093iB04p03232.
- Vasco, D. W., C. Wicks, K. Karasaki, O. Marques, and J. B. Hulen (2002), Geodetic imaging: reservoir monitoring using satellite interferometry, *Geophysical Journal International*, 149(3), 555-571, doi:DOI 10.1046/j.1365-246X.2002.01569.x.
- Walsh, J. (2002), Subsidence above a planar reservoir, *Journal of Geophysical Research: Solid Earth*, 107(B9).
- Wang, R. J., and H. J. Kumpel (2003), Poroelasticity: Efficient modeling of strongly coupled, slow deformation processes in a multilayered half-space, *Geophysics*, 68(2), 705-717, doi:10.1190/1.1567241.
- Weingarten, M., S. Ge, J. W. Godt, B. A. Bekins, and J. L. Rubinstein (2015), High-rate injection is associated with the increase in US mid-continent seismicity, *Science*, 348(6241), 1336-1340, doi:10.1126/science.aab1345.
- Wicks, C. W., D. Dzurisin, S. Ingebritsen, W. Thatcher, Z. Lu, and J. Iverson (2002), Magmatic activity beneath the quiescent Three Sisters volcanic center, central Oregon Cascade Range, USA, *Geophysical Research Letters*, 29(7), doi:Doi 10.1029/2001gl014205.
- Wielandt, E. (2003), On the relationship between seismic moment and source volume, *Inst. of Geophys., Stuttgart Univ., Germany*. [Available at <http://www.geophys.uni-stuttgart.de/~erhard/skripte/ew/isomoment/>, accessed on May 30 2003.].
- Winters, D. W., B. D. Van Veen, and S. C. Hagness (2010), A sparsity regularization approach to the electromagnetic inverse scattering problem, *IEEE transactions on antennas and propagation*, 58(1), 145-154.
- Wright, T. L., and F. W. Klein (2006), Deep magma transport at Kilauea volcano, Hawaii, *Lithos*, 87(1-2), 50-79.
- Yang, X.-m., and P. M. Davis (1986), Deformation due to a rectangular tension crack in an elastic half-space, *Bull. Seism. Soc. Am.*, 76, 865-881.
- Yang, X. M., P. M. Davis, P. T. Delaney, and A. T. Okamura (1992), Geodetic analysis of dike intrusion and motion of the magma reservoir beneath the summit of Kilauea Volcano, Hawaii: 1970-1985, *J. Geophys. Res.*, 97, 3305-3324.
- Yang, X. M., P. M. Davis, and J. H. Dieterich (1988), Deformation from Inflation of a Dipping Finite Prolate Spheroid in an Elastic Half-Space as a Model for Volcanic Stressing, *Journal of Geophysical Research-Solid Earth and Planets*, 93(B5), 4249-4257, doi:Doi 10.1029/Jb093ib05p04249.

- Yao, H., P. Gerstoft, P. M. Shearer, and C. Mecklenbräuker (2011), Compressive sensing of the Tohoku-Oki Mw 9.0 earthquake: Frequency-dependent rupture modes, *Geophysical Research Letters*, *38*(20), n/a-n/a, doi:10.1029/2011gl049223.
- Yao, H., P. M. Shearer, and P. Gerstoft (2013), Compressive sensing of frequency-dependent seismic radiation from subduction zone megathrust ruptures, *Proceedings of the National Academy of Sciences*, *110*(12), 4512-4517.
- Yeck, W., G. Hayes, D. E. McNamara, J. L. Rubinstein, W. Barnhart, P. Earle, and H. M. Benz (2017), Oklahoma experiences largest earthquake during ongoing regional wastewater injection hazard mitigation efforts, *Geophysical Research Letters*, *44*(2), 711-717.
- Zhai, G., and M. Shirzaei (2016), Spatiotemporal model of Kīlauea's summit magmatic system inferred from InSAR time series and geometry-free time-dependent source inversion, *Journal of Geophysical Research: Solid Earth*, *121*(7), 5425-5446, doi:10.1002/2016JB012953.
- Zhai, G., and M. Shirzaei (2017), 3-D Modeling of Irregular Volcanic Sources Using Sparsity-Promoting Inversions of Geodetic Data and Boundary Element Method, *Journal of Geophysical Research: Solid Earth*, *122*(12), 10,515-510,537, doi:doi:10.1002/2017JB014991.
- Zhai, G., and M. Shirzaei (2018), Fluid Injection and Time-Dependent Seismic Hazard in the Barnett Shale, Texas, *Geophysical Research Letters*, *45*(10), 4743-4753, doi:10.1029/2018GL077696.
- Zhao, H., N. B. Givens, and B. Curtis (2007), Thermal maturity of the Barnett Shale determined from well-log analysis, *AAPG bulletin*, *91*(4), 535-549.
- Zou, H., and T. Hastie (2005), Regularization and variable selection via the elastic net, *Journal of the Royal Statistical Society: Series B (Statistical Methodology)*, *67*(2), 301-320.
- Zumberge, J. F., M. B. Heflin, D. C. Jefferson, M. M. Watkins, and F. H. Webb (1997), Precise point positioning for the efficient and robust analysis of GPS data from large networks, *Journal of Geophysical Research: Solid Earth*, *102*(B3), 5005-5017, doi:10.1029/96JB03860.



## APPENDIX A

### SUPPLEMENTARY INFORMATION FOR CHAPTER 2

### Text A.1 Definition of Green's Function of PCD

Assuming a homogenous and isotropic elastic half space, the displacement at point  $\mathbf{x}$  on the free surface, due to dilatational point source at location  $\mathbf{x}'$ , takes the form [Lu *et al.*, 2002],

$$u_i(x_1, x_2, x_3 = 0) = C * S_i$$

$$S_i = \frac{x_i - x'_i}{[(x_1 - x'_1)^2 + (x_2 - x'_2)^2 + (x_3 - x'_3)^2]^{3/2}}, i = 1, 2, 3. \quad (\text{A.1})$$

Equation (A.1) shows that the displacement at the free surface is a linear function of source strength,  $C$ .  $C$  is proportional to the volume change or pressure change in a reservoir, as well as pressure change inside a confined aquifer and the thermoelastic deformation change produced by distributed temperature changes at depth. Here, the volume change distribution is solved for [Segall, 2010], and  $C$  in equation (A.1) is replaced with

$$C = \frac{1 - \vartheta}{\pi} dv \quad (\text{A.2})$$

where  $\vartheta$  is Poisson's ratio and  $dv$  is the volume change.

### Text A.2 Construction of Laplacian Smoothing Matrix

Equation (2.2) does not provide a robust and unique solution due to the design matrix being "ill-conditioned" [Bjerhammar, 1973]. This issue can be resolved through regularization [Tikhonov and Arsenin, 1977], which considers an additional constraint, such as the second derivative of parameters, to stabilize the solution of equation (2.2). This regularization function is quantified through Laplacian smoothing operator  $D$ , as shown in equation (2.4). Laplacian operator can be computed using a simple numerical finite-difference approximation. Figure A.12 illustrates how the Laplacian smoothing operator for the array of PCD is constructed. Using 3-D Delaunay triangulation, all the neighbors, i.e. surrounding PCDs with volume change  $V_j$  ( $j = 1, 2, \dots, m$ ), are identified to  $i$ th PCD with volume change  $V_i$ . All second-order derivatives are averaged with respect to a fixed neighbor PCD, shown as  $V_1$ . Thus, the Laplacian smoothing operator of  $i$ th PCD is defined as

$$\nabla^2 V_i = \frac{1}{m-1} \sum_{j=2}^m \frac{\frac{V_j - V_i}{H_{ij}} - \frac{V_i - V_1}{H_{i1}}}{H_{j1}} \quad (\text{A.3})$$

where  $H_{ij}$  is the spatial distance between  $i$ th PCD and its  $j$ th neighbor.  $H_{j1}$  is the spatial distance between the first and  $j$ th neighbor.  $H_{i1}$  is the spatial distance between  $i$ th PCD and its first neighbor. The spatial distances are calculated using 3-D coordinates of PCDs.

### Text A.3 Solving Slip History on the Decollement

The deformation signal due to slip on the decollement is characterized by long wavelengths and is more in the north-south direction compared to that of the magmatic activities at Kilauea's summit [Shirzaei *et al.*, 2013]. Given the distinct characteristics of the signals affecting Kilauea's south flank, a  $L_1$ -norm minimization approach can be used to invert GPS data and solve for the depth and slip history of the decollement.  $L_1$ -norm is chosen here because it is less sensitive to outliers [Marshall and Bethel, 1996], which are signals due to magmatic activity at Kilauea's summit. Through this step, it is to investigate whether the slip rate varies on the decollement during the observation period. To model the slip on the decollement, a subhorizontal rectangular dislocation model [Okada, 1985] with uniform seaward motion is used. This model is constrained using only GPS stations near the

shoreline (black triangles and station PGF3 and PGF5 in Figure 2.2a) that also span the time period of InSAR time series. The observed displacement at these stations is mostly caused by slip on the decollement. To optimize the slip at each time step, a Genetic Algorithm (GA) is applied, which is a nonlinear optimization algorithm [Shirzaei and Walter, 2009]. It minimizes the  $L_1$ -norm of the difference between observed and modeled surface deformation. This inversion is run for each time step, which provides a time series of slip on the decollement.

The long-term rate of slip on the decollement is relatively steady at  $11 \pm 1$  cm/year. This slip rate is estimated using linear regression based on the solved slip history. Variance–covariance analysis is used to estimate the uncertainty of slip rate.

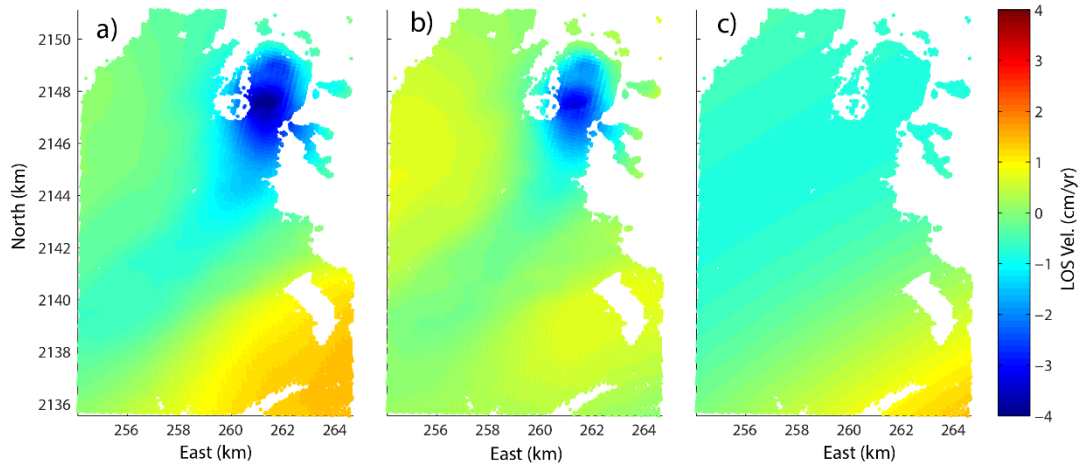


**Figure A.1.** (a) The observed InSAR LOS velocity at the Kilauea south flank. (b) The corrected InSAR LOS velocity after the effect of long-term slip on the decollement is removed. (c) The difference between panel A and B.

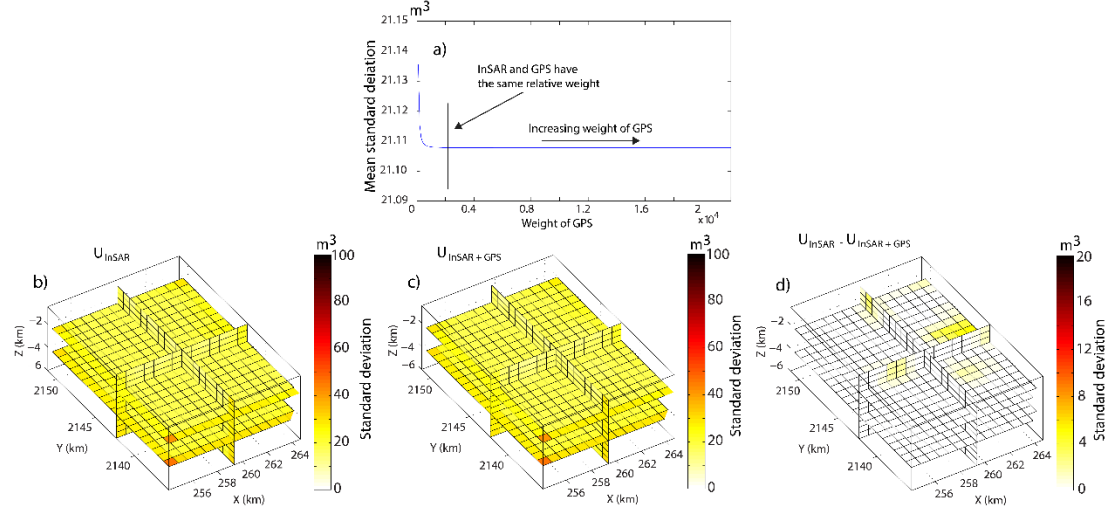


**Figure A.2.** Distribution of the standard deviations associated with volume change inversion obtained through variance–covariance analysis. (a) Mean standard deviation of the volume change as a function of GPS relative weight. The value at which GPS and InSAR have same relative weight is shown using the vertical black line. 3-D distribution of the standard deviations are shown considering (b) only InSAR, (c) both InSAR and GPS with equal weight, and (d) difference between Figure A.2b and Figure A.2c.

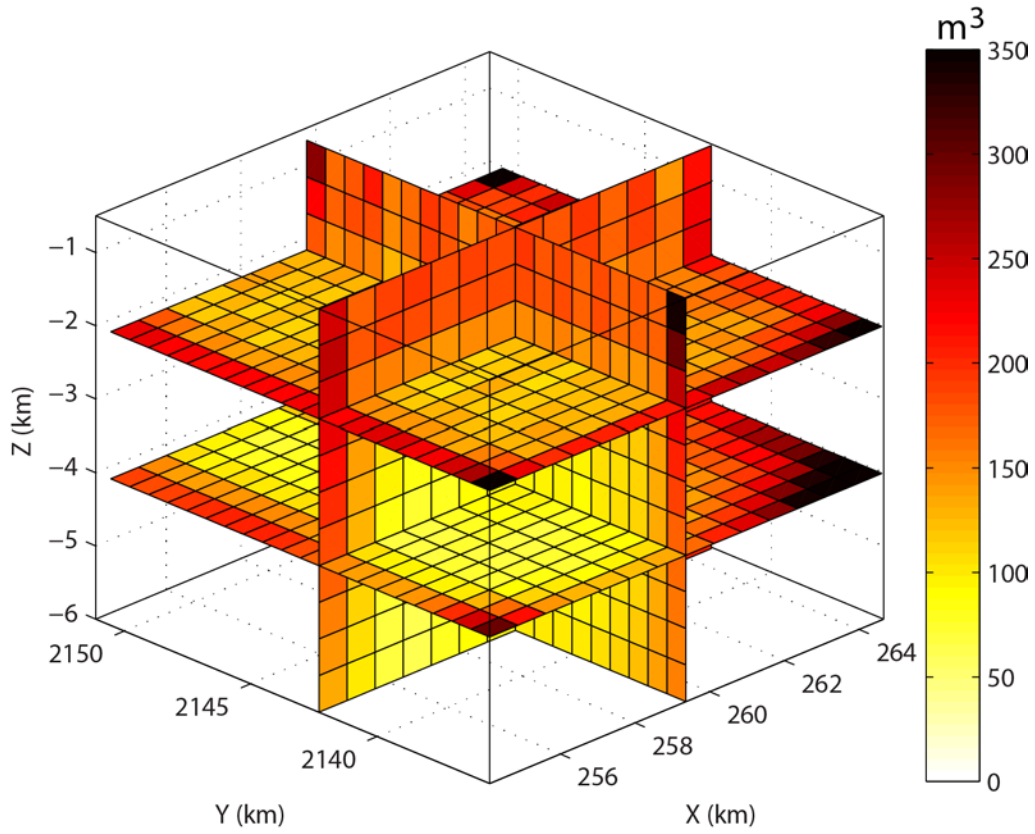


**Figure A.3.** Distribution of the standard deviations associated with the inverted volume change distribution obtained through bootstrapping as a result of data gap and observation noise. The data used for bootstrapping is InSAR LOS displacement between first and last time steps. The noise added is 5 mm based on InSAR time series analysis.

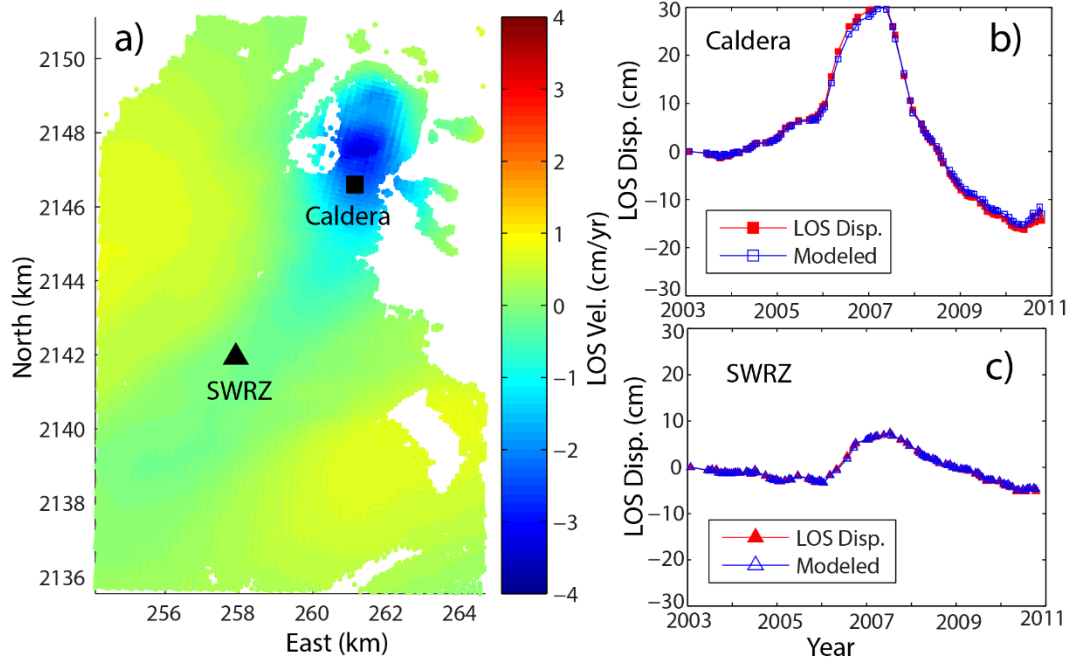


**Figure A.4.** (a) Observed LOS velocity for Kilauea summit area. (b, c) LOS displacement time series and predicted LOS displacement time series using the inverted volume change at the summit caldera and SWRZ, respectively.

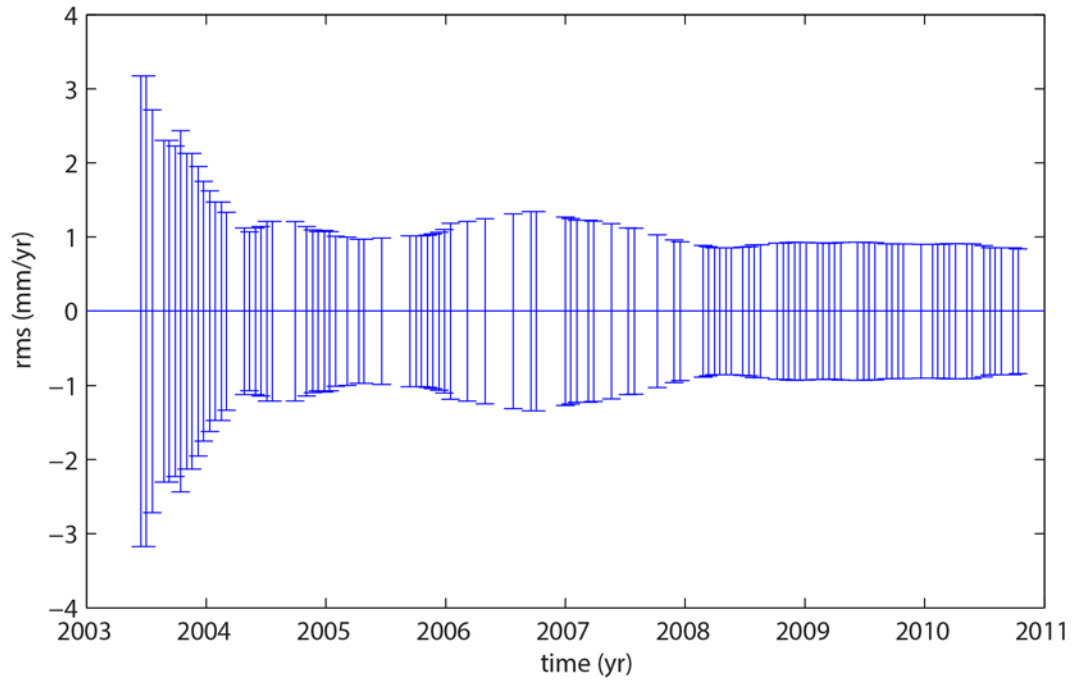


**Figure A.5.** Model misfit Root Mean Square (RMS) for all time steps, obtained by inverting for the rate of volume change at each time step.



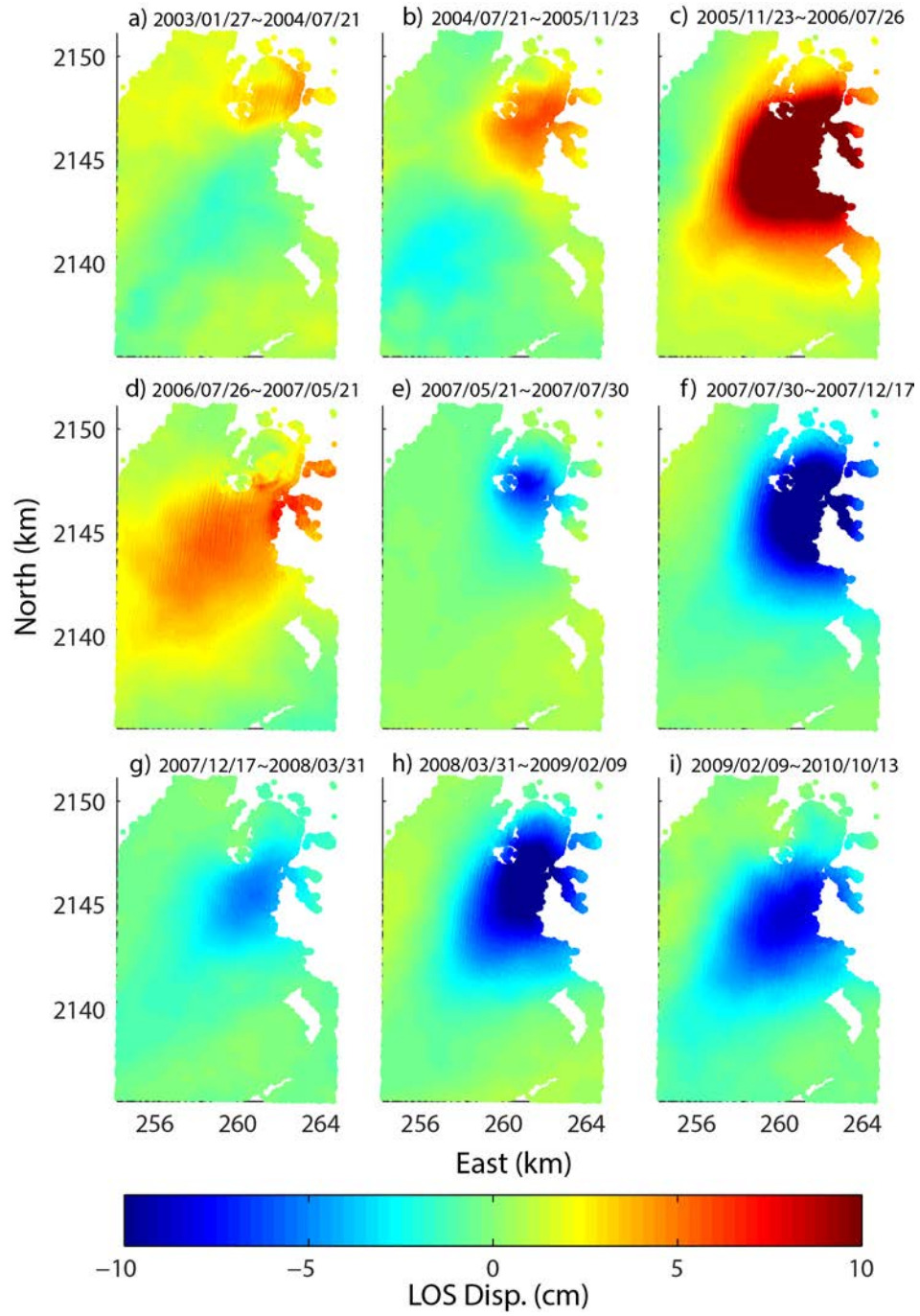


**Figure A.6.** Observed LOS displacement for the nine consecutive periods shown also in Figure 2.3.

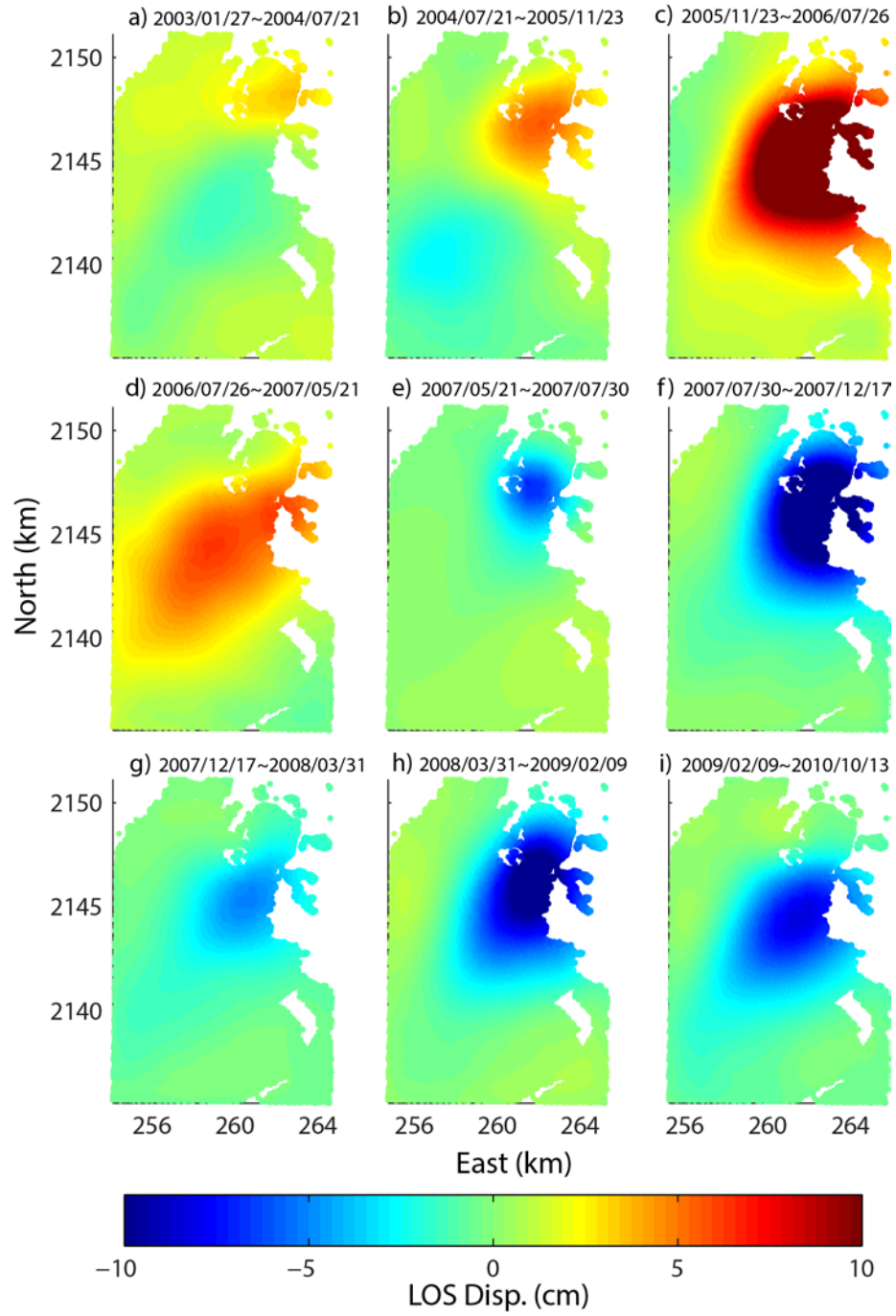


**Figure A.7.** Modeled surface LOS displacement for the nine consecutive periods shown in Figure A.6.

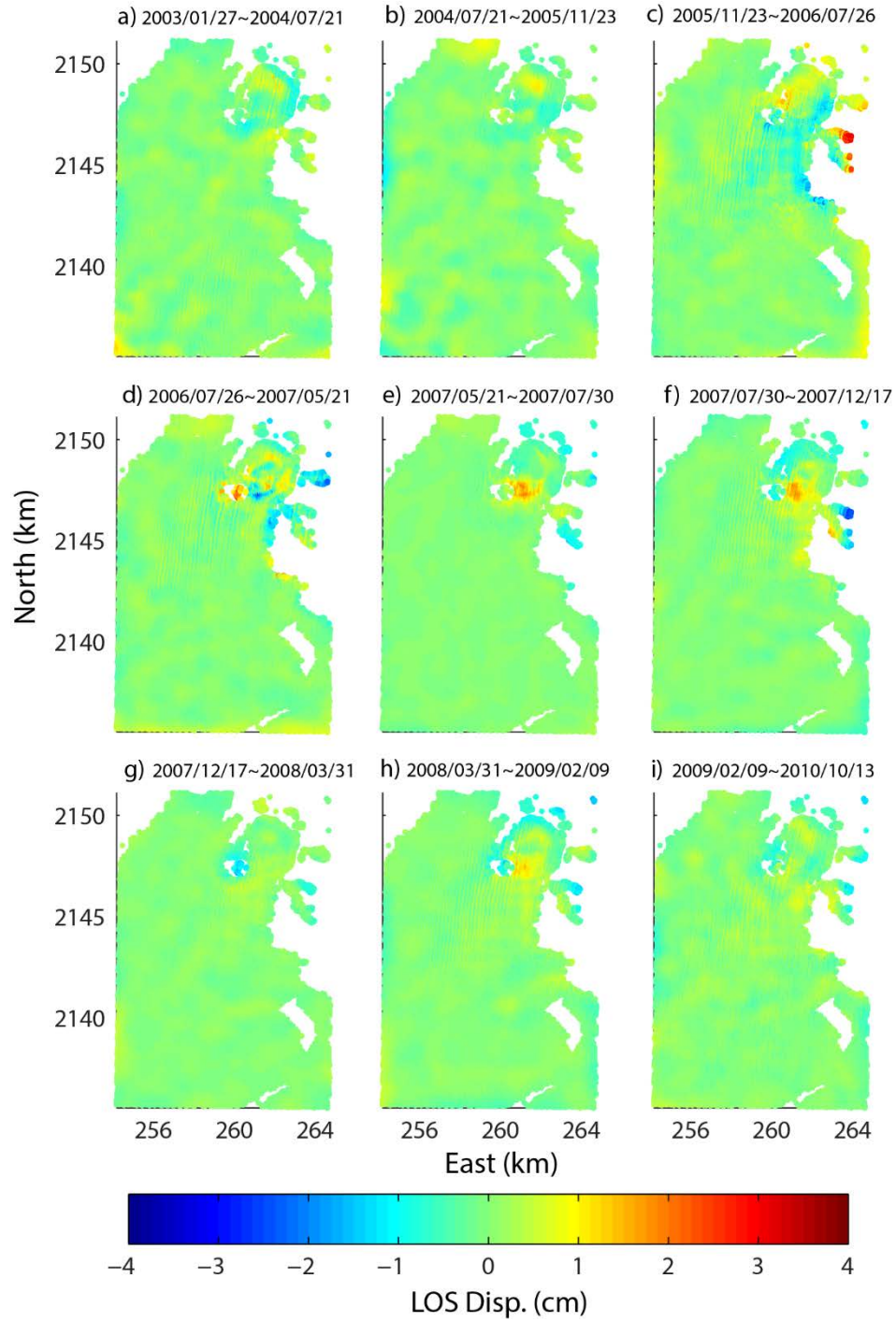


**Figure A.8.** Misfit (observed – modeled) for nine consecutive periods shown in Figures A.6 and A.7.

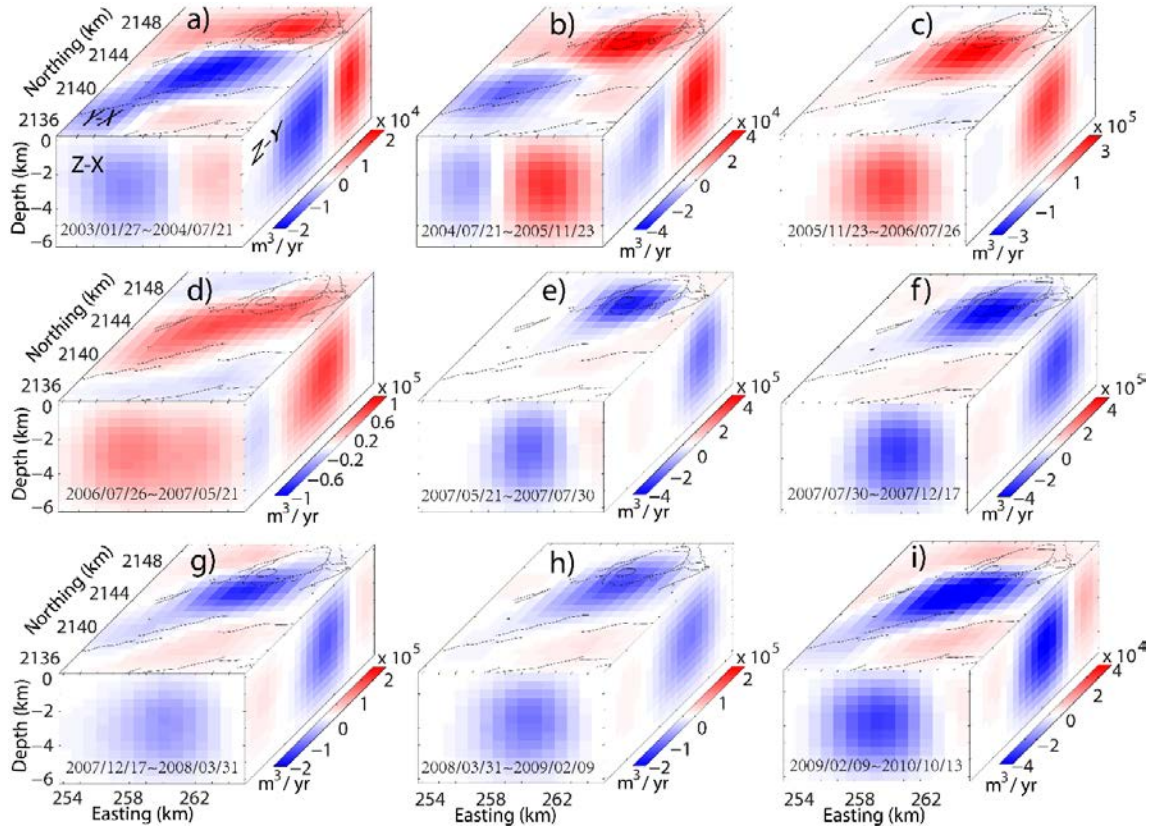


**Figure A.9.** Integrated major volume change rates in three directions for nine consecutive periods shown in Figures 2.3 and A.6. Y–X plane: integrated volume change in depth direction; Z–X plane: integration in north–south direction; Z–Y plane: integration in east–west direction. The color bar scales vary for different time period to highlight the temporally variable pattern of volume change rate distribution.



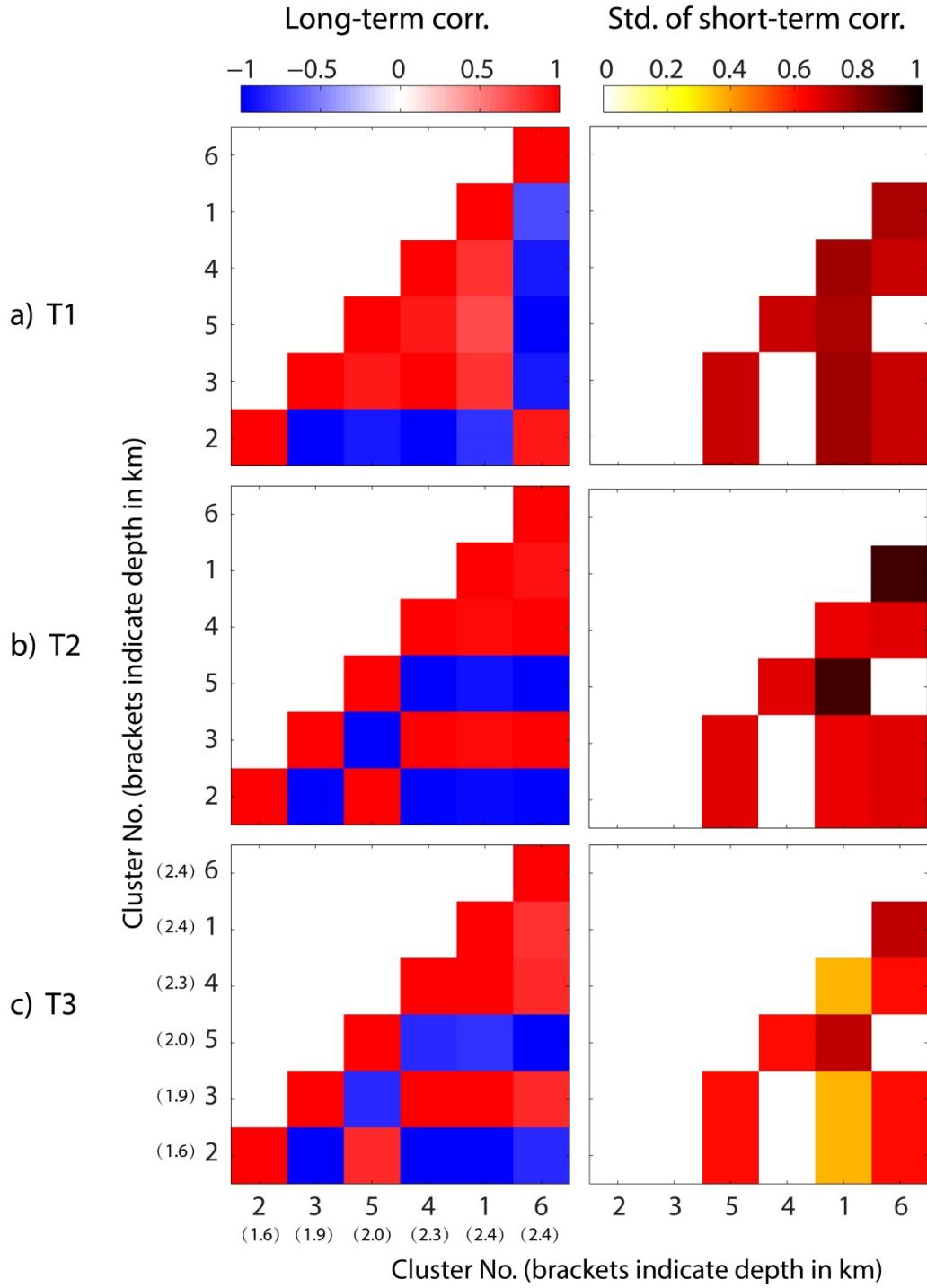


**Figure A.10.** Estimated intermediate-term correlation coefficient and standard deviation of the short-term correlation between time series of volume changes of every two clusters for the three identified time periods.

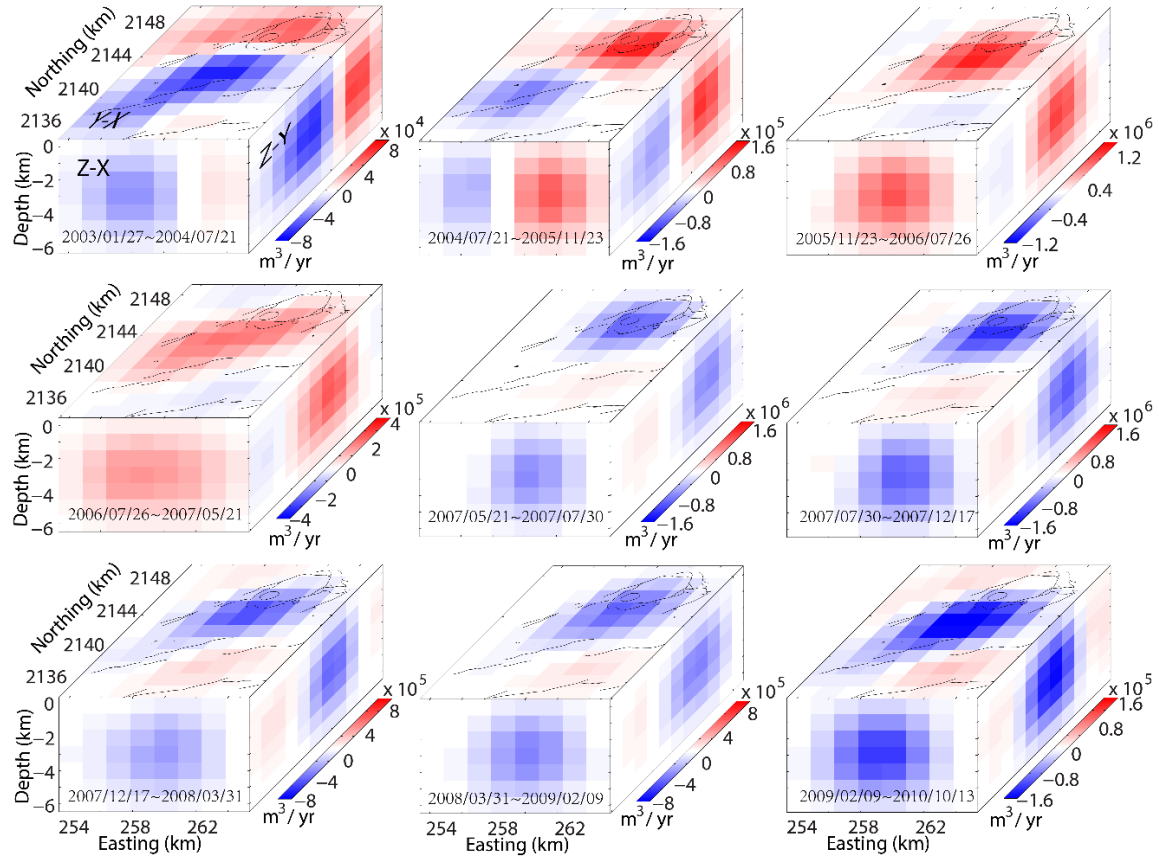


**Figure A.11.** Same as Figure A.9, except that the spacing between PCDs is doubled.

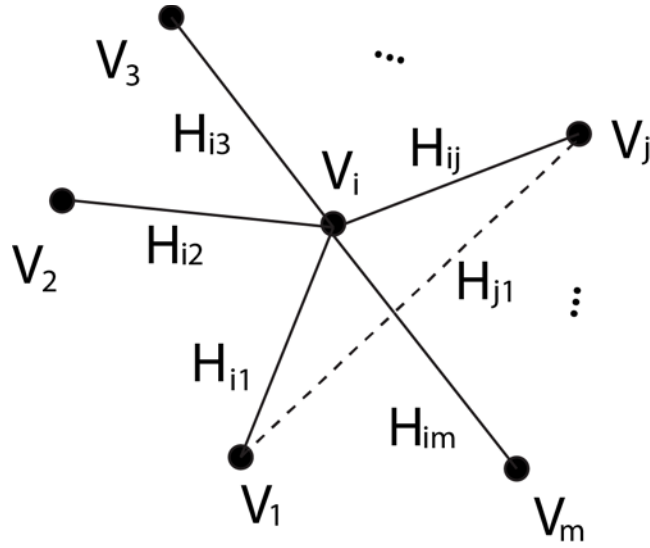


**Figure A.12.** Schematic view of implemented finite-difference approach to calculate the Laplacian smoothing operator.

## APPENDIX B

### SUPPLEMENTARY INFORMATION FOR CHAPTER 3



### Text B.1 Mathematical Relationship Between $\Delta V_{cr}$ and $\Delta V_{ch}$

Considering a finite source with an irregular shape subjected to uniform internal pressure and assuming an isotropic, homogeneous, Poisson-solid half-space, the relationship between crack volume change and mechanical chamber volume change can be derived. The constitutional equation of linear elasticity with strain  $\epsilon_{ij}$  and stress  $\sigma_{ij}$  is

$$\sigma_{ij} = \lambda \epsilon_{kk} \delta_{ij} + 2\mu \epsilon_{ij} \quad (\text{B.1})$$

where  $\delta_{ij}$  is Kronecker delta,  $\lambda$  and  $\mu$  are Lamé constants. Then

$$\sigma_{kk} = 3\lambda \epsilon_{kk} + 2\mu \epsilon_{kk} = 3\kappa \epsilon_{kk} \quad (\text{B.2})$$

where the host rock bulk modulus  $\kappa = \lambda + \frac{2\mu}{3}$ . Using the method of *Eshelby* [1957],  $\epsilon_{ij}^T$  is the stress-free strain that the inclusion would undergo in the absence of the matrix, and  $\epsilon_{ij}^C$  is the constrained strain in the inclusion when it is embedded in the matrix. The stress inside the inclusion is  $\sigma_{ij}^I$ :

$$\sigma_{ij}^I = \lambda(\epsilon_{kk}^C - \epsilon_{kk}^T) \delta_{ij} + 2\mu(\epsilon_{ij}^C - \epsilon_{ij}^T) \quad (\text{B.3})$$

So,

$$\sigma_{kk}^I = 3\kappa(\epsilon_{kk}^C - \epsilon_{kk}^T) \quad (\text{B.4})$$

The internal pressure is defined as  $P = -\sigma_{kk}^I/3$ , then

$$P = \kappa(\epsilon_{kk}^T - \epsilon_{kk}^C) \quad (\text{B.5})$$

Generally, a finite inclusion is taken as reference, so  $P$  is replaced with pressure change  $\Delta P$  and thus

$$\Delta P = \kappa(\epsilon_{kk}^T - \epsilon_{kk}^C) \quad (\text{B.6})$$

Following the definition of magma chamber compressibility,  $\beta_{ch}$  [Segall, 2010; Segall et al., 2001], then

$$\beta_{ch} = \frac{\Delta V_{ch}}{V} * \frac{1}{\Delta P} \quad (\text{B.7})$$

Where  $V$  is volume of cavity (inclusion) and  $\Delta V_{ch}$  is mechanical chamber volume change.

Traction-free volume change  $\Delta V^T$  is equivalent to crack volume change  $\Delta V_{cr}$  of a magma chamber [Müller, 2001; Wielandt, 2003], and constrained volume change of inclusion  $\Delta V^C$  corresponds to mechanical chamber volume change  $\Delta V_{ch}$ , here

$$\epsilon_{kk}^T = \frac{\Delta V^T}{V} = \frac{\Delta V_{cr}}{V} \quad (\text{B.8})$$

$$\epsilon_{kk}^C = \frac{\Delta V^C}{V} = \frac{\Delta V_{ch}}{V} \quad (\text{B.9})$$

Combine equations (B.6–B.9), and define host rock compressibility  $\beta_{hr} = \frac{1}{\kappa}$ , then

$$\Delta V_{ch} = \frac{\Delta V_{cr}}{(1 + \beta_{hr}/\beta_{ch})} \quad (\text{B.10})$$

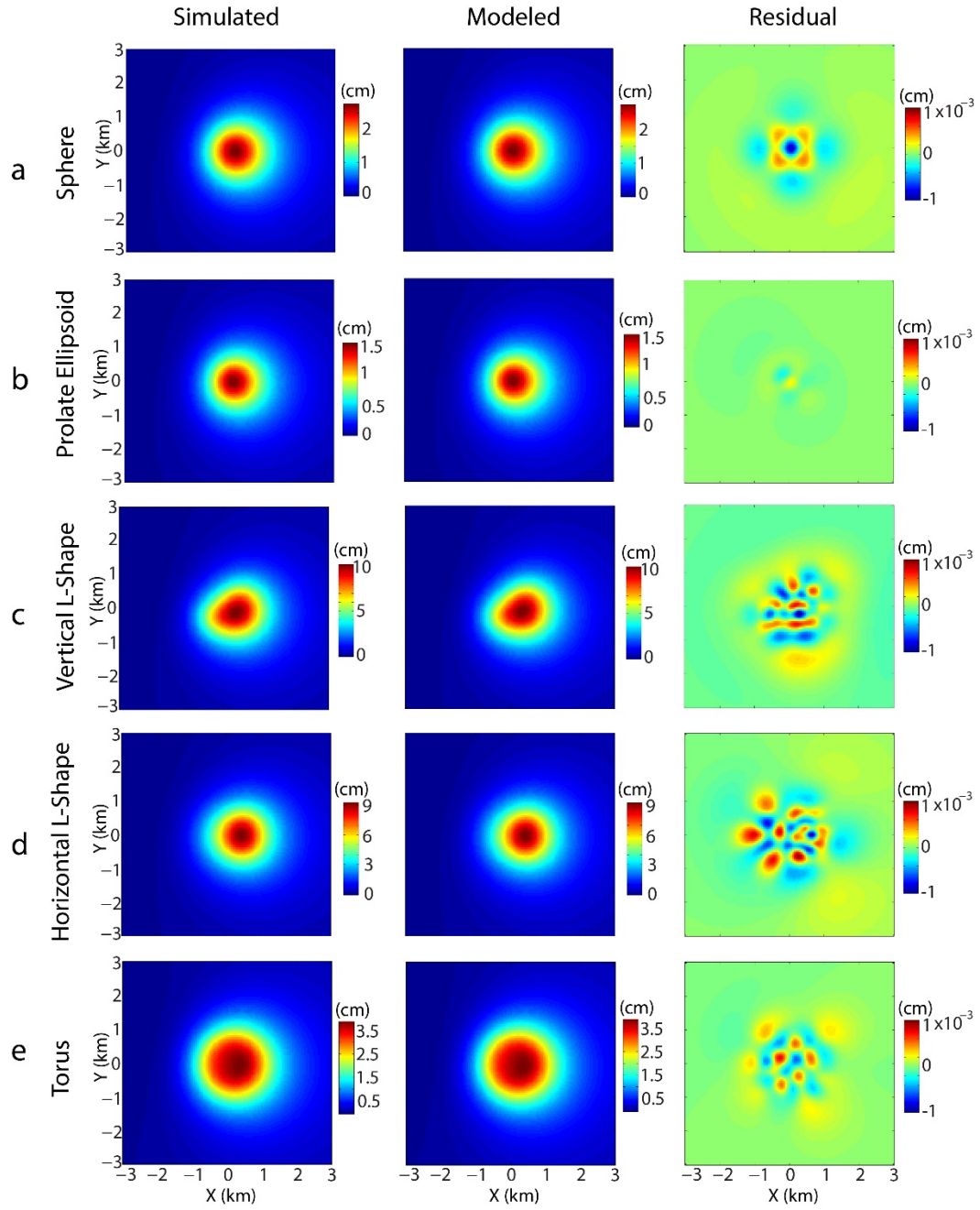


**Figure B.1.** Data fit for the synthetic tests shown in Figure 3.4 without considering observation noise.

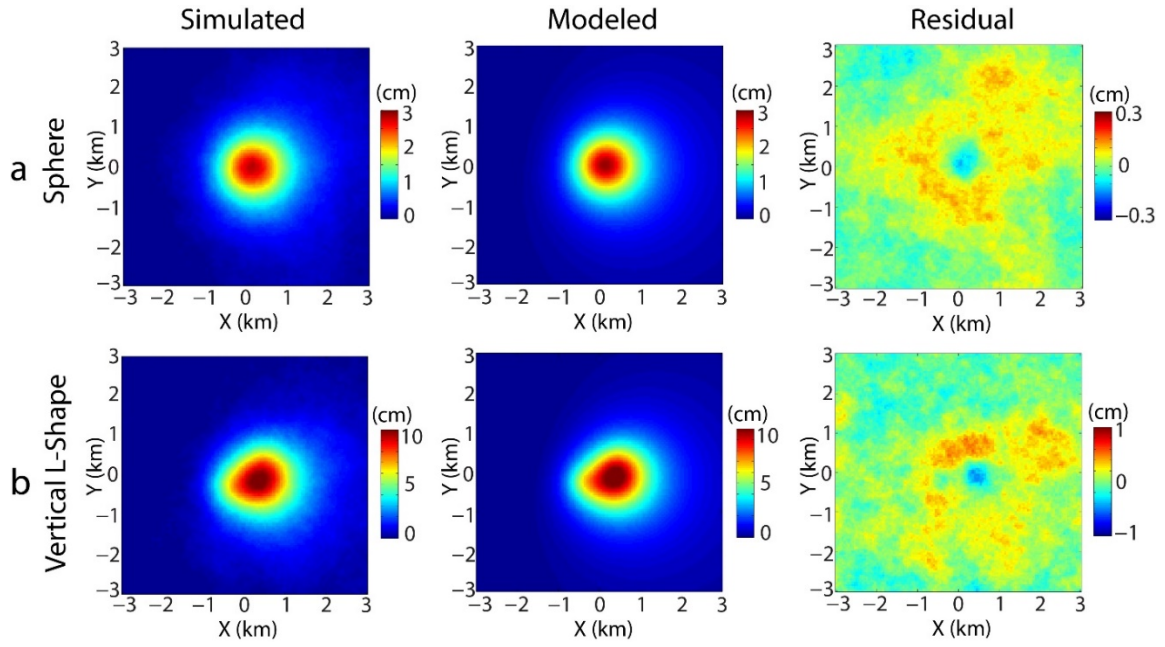


**Figure B.2.** Data fit for synthetic tests shown in Figure 3.5 considering 5% colored noise added to simulated observations.

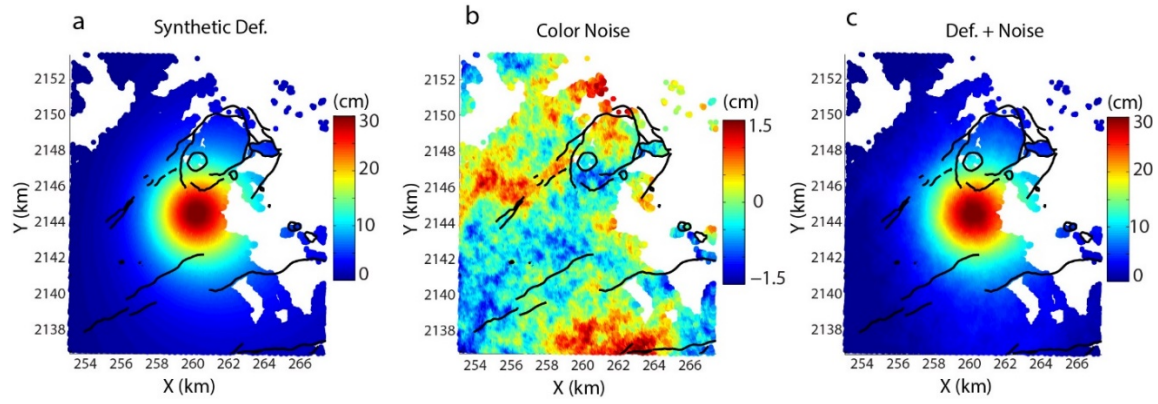


**Figure B.3.** Simulated surface deformation in descending viewing geometry associated with synthetic spherical source used for calibration. (a) Surface LOS deformation calculated from forward modeling referred to Kilauea summit area. (b) Simulated color noise for InSAR data. (c) The addition of Figures B.3a and B.3b.

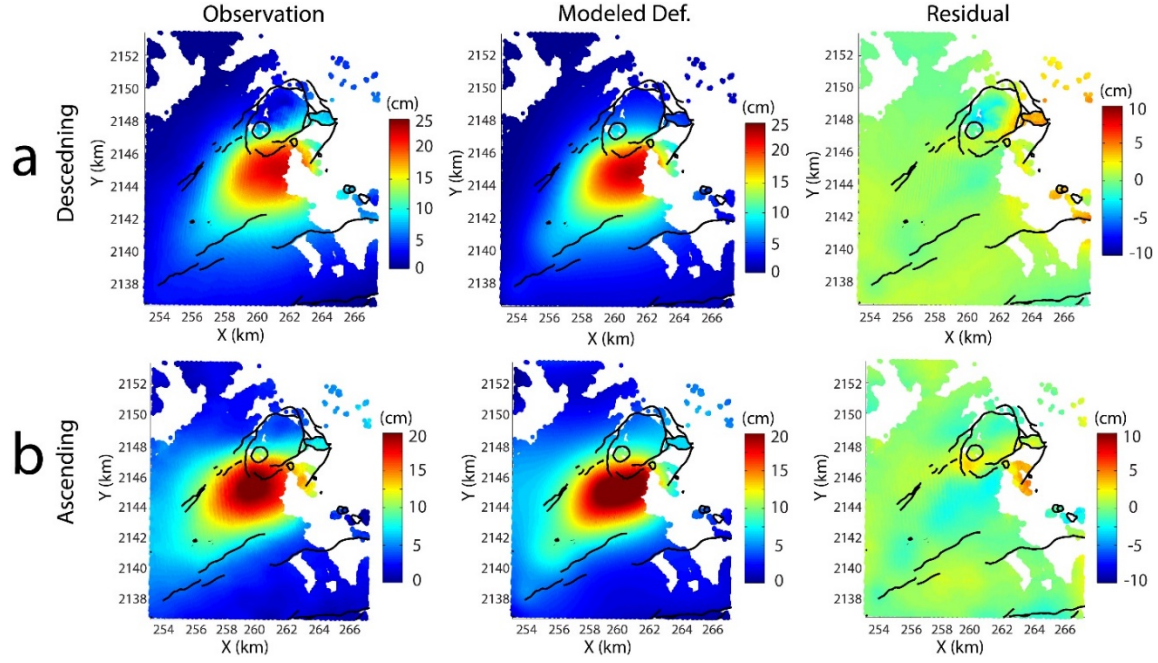


**Figure B.4.** Data fit for the sparsity-promoting inversion for the uplift period. (a, b) Results for descending and ascending measurements, respectively. In each row, the 1<sup>st</sup> column is observed surface LOS displacement, the 2<sup>nd</sup> column is predicted surface LOS displacement, and the 3<sup>rd</sup> column is the model misfit.

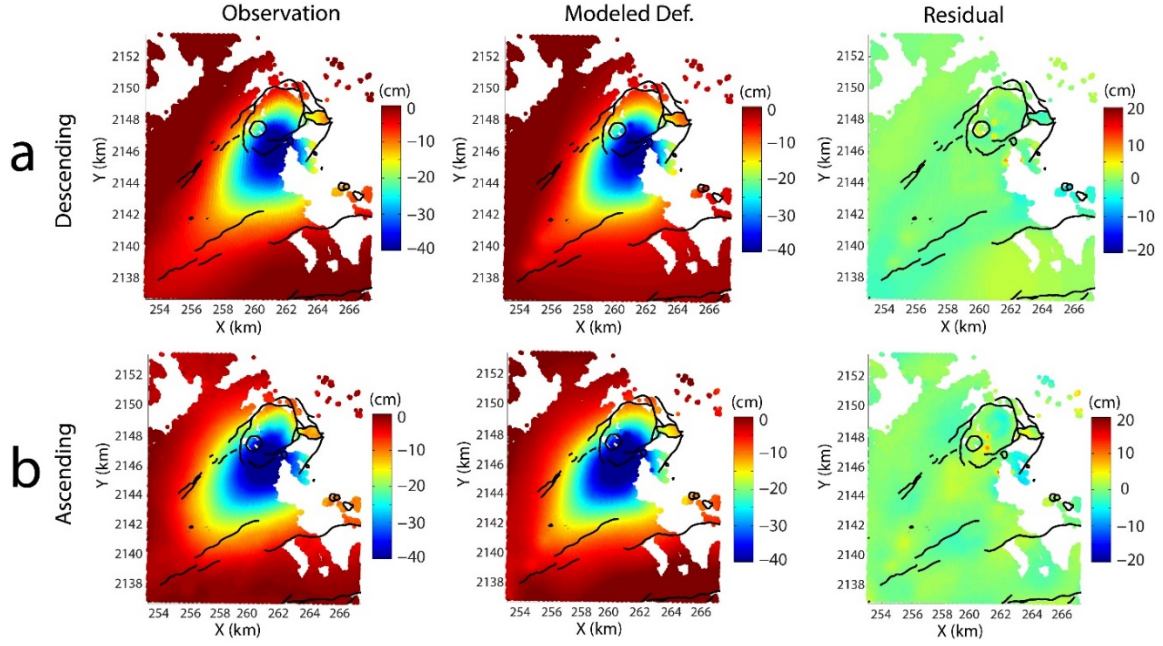


**Figure B.5.** Data fit for the sparsity-promoting inversion for the subsidence period. (a, b) Results for descending and ascending measurements, respectively. In each row, the 1<sup>st</sup> column is observed surface LOS displacement, the 2<sup>nd</sup> column is predicted surface LOS displacement, and the 3<sup>rd</sup> column is the model misfit.



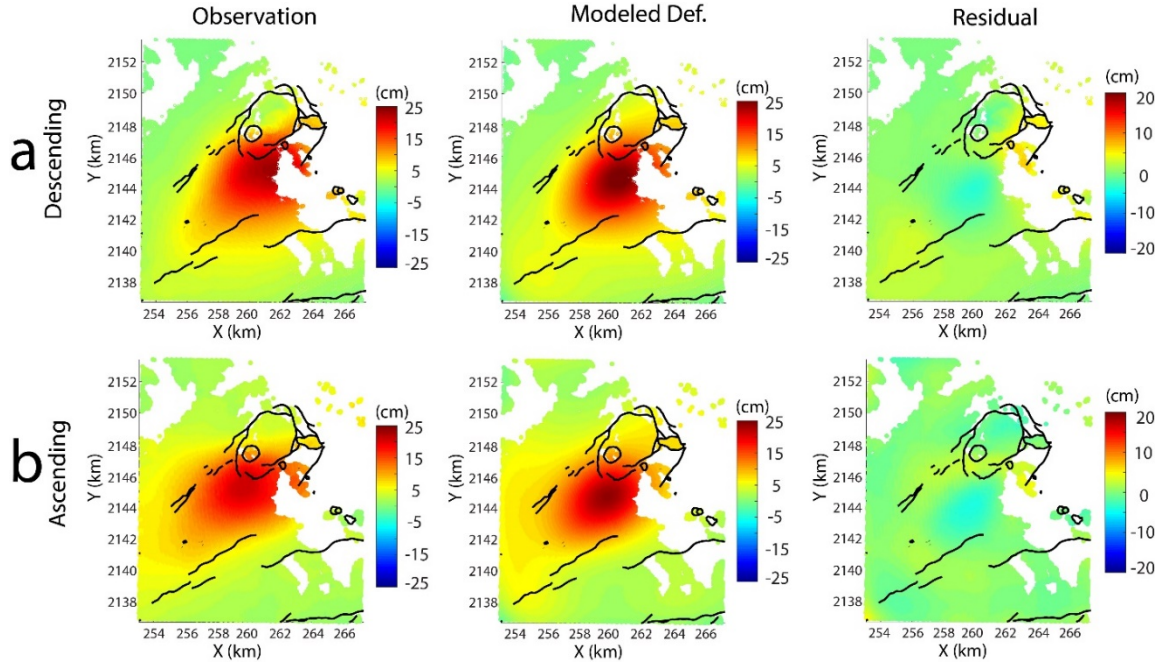


**Figure B.6.** Data fit for the BEM modeling for the uplift period. (a, b) Results for descending and ascending measurements, respectively. In each row, the 1<sup>st</sup> column is observed surface LOS displacement, the 2<sup>nd</sup> column is predicted surface LOS displacement, and the 3<sup>rd</sup> column is the model misfit.

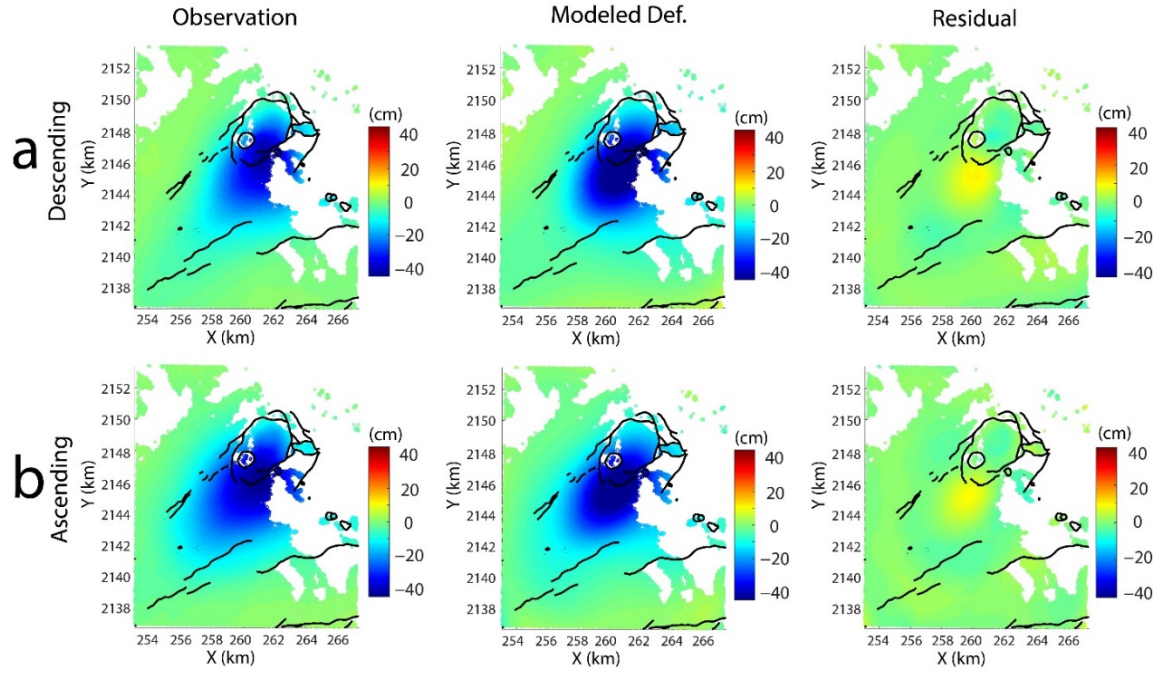


**Figure B.7.** Data fit for the BEM modeling for the subsidence period. (a, b) results for descending and ascending measurements, respectively. In each row, the 1<sup>st</sup> column is observed surface LOS displacement, the 2<sup>nd</sup> column is predicted surface LOS displacement, and the 3<sup>rd</sup> column is the model misfit.



## APPENDIX C

### SUPPLEMENTARY INFORMATION FOR CHAPTER 4

### Text C.1 Lithostratigraphy

The Fort Worth Basin locates between the northeast-trending Ouachita fold belt and Bend arch along the southern North American continental margin [Ewing, 1990]. The main oil and gas production sites are in the northern part of the Fort Worth Basin. Within the basin, the Mississippian Barnett Shale sits directly on the Ordovician Viola Limestone or Ellenburger Limestone which overlie Precambrian crystalline granite basement [Pollastro *et al.*, 2007]. Resting on the Barnett Shale, there are formations including the Pennsylvanian Canyon Group, Strawn sandstone, Atoka sandstone, Bend, and Marble Falls Limestone. Atop the Canyon Group is the Permian Cisco Group, which is overlaid by the Cretaceous undifferentiated layer. Figure C.2A shows the stratigraphic columns. The average thickness of the Barnett shale is  $\sim 100$  m and that of the Ellenburger formation is  $\sim 1000$ – $1500$  m based on well logs in the Fort Worth basin [Montgomery *et al.*, 2005; Pollastro *et al.*, 2007]. The isopach shows that the average depth of the bottom of the Barnett Shale formation (or the top of the Ellenburger formation) is  $\sim 2.2$  km within the study area [Pollastro *et al.*, 2007; Zhao *et al.*, 2007]. The lithostratigraphy is simplified by considering five horizontal layers as shown in Figure C.2B.

### Text C.2 Parameter Determination

A layered linear poroelastic model is used to constrain the spatiotemporal evolution of poroelastic stresses and pore pressure. Each layer is characterized by five parameters, including shear modulus, drained and undrained Poisson ratio, Skempton's pore pressure coefficient, and hydraulic diffusivity. The choices of shear modulus, Poisson ratios, and Skempton's coefficient in the study area are referred to Shirzaei *et al.* [2016]. The hydraulic diffusivity is constrained using local hydrogeological information and can be determined using hydraulic conductivity  $K$  and specific storage  $S_s$ :

$$D = \frac{K}{S_s} \quad (C.1)$$

The hydraulic conductivity can be expressed using intrinsic permeability  $K_i$ :

$$K = \frac{K_i \rho_f g}{\eta} \quad (C.2)$$

where,  $\rho_f$  is the fluid density;  $g$  is the gravitational constant;  $\eta$  is the dynamic viscosity of fluid. Also, the specific storage is given by following expression:

$$S_s = \rho_f g (\beta_s + n\beta_f) \quad (C.3)$$

where  $\beta_s$  and  $\beta_f$  are the compressibilities of solid medium and fluid;  $n$  is the porosity.

Substituting equations (C.2) and (C.3) into equation (C.1), then

$$D = \frac{K_i}{\eta(\beta_s + n\beta_f)} \quad (C.4)$$

The values of compressibility and porosity for different layers in the model are acquired based on geological information compiled by Hornbach *et al.* [2016]. If a layer contains different geological formations, the average value is calculated as model input. The hydraulic diffusivity is estimated assuming a compressibility of  $4.6 \times 10^{-10} \text{ Pa}^{-1}$  for brine fluid and an average matrix compressibility of  $7.0 \times 10^{-10} \text{ Pa}^{-1}$  for dolomitic limestone [Hornbach *et al.*, 2015]. A value of  $1.1 \times 10^{-3} \text{ Pa} \cdot \text{s}$  is used for fluid viscosity  $\eta$ . The final list of the hydrogeological parameters is given in Figure C.2C.

### Text C.3 Implementation of Numerical Simulations

The formulation provided by *Wang and Kümpel* [2003] is used to simulate the spatial and temporal evolution of poroelastic stresses and pore pressure due to monthly time series of injected volumes (Figure 4.1) in a layered poroelastic half space (Figure C.2). This method solves equations (4.1) and (4.2) using a spectral element method and calculates time-dependent axisymmetric pore pressure and poroelastic strain tensor in a 3-D cylindrically coordinate system. For each well, a radial domain of 200 km with 50 radial samples and a time span of 18 years between 2007 and 2025 with 150 temporal samples are defined. To reduce the computation load, only the results at the depth of 3.5 km are output. Then a tensor transformation is applied to compute strain tensor in a Cartesian coordinate system (see equation (7) of *Fan et al.* [2016]). Afterward, the pore pressure and transformed poroelastic strain associated with each well are resampled on a grid of 2.0 by 1.6 degrees (Figure 4.2) with a cell size of 0.05 by 0.04 degrees in longitude and latitude directions, respectively. The stress tensor is estimated using the constitutive equations of linear elasticity and the elastic parameters in Figure C.2.

Given the geometry of receiver fault and its coefficient of friction (Table C.1), the Coulomb failure stress can be computed using USGS package Coulomb 3.3.

Seismicity rate  $R$  (rate of seismicity relative to the background seismicity rate) is evaluated using equation (4.4). Using the set of parameters provided in Table C.1 and the stressing rate obtained from the time-dependent coulomb stress change, the MATLAB function ode45 is applied to solve the differential equation and estimate  $R$  between 2007 and 2025 with 1000 samples.

To estimate time-dependent earthquake probability due to total Coulomb failure stress change, equation (4.5) is applied to all grid cells of the poroelastic model, which allows calculating the magnitude exceedance probability as a function of time and location. The background seismicity rate (equation (4.7)) is calculated using the set of parameters given in Table C.1.

### Text C.4 Modeling of Fluid Production at Azle

The records of fluid production at 120 wells are obtained in Azle area, as mentioned by *Hornbach et al.* [2015] (Figure C.7). The data are originally reported in G-10 forms by RRC and contain one value of flowback volume at each well per year. Here, it is assumed that production at each well maintains a constant annual rate during the study period of 2007–2015. To evaluate the associated pressure and poroelastic stresses, a similar modeling procedure is implemented as that used with injection data. The modeling results are shown in Figures C.8–C.12.

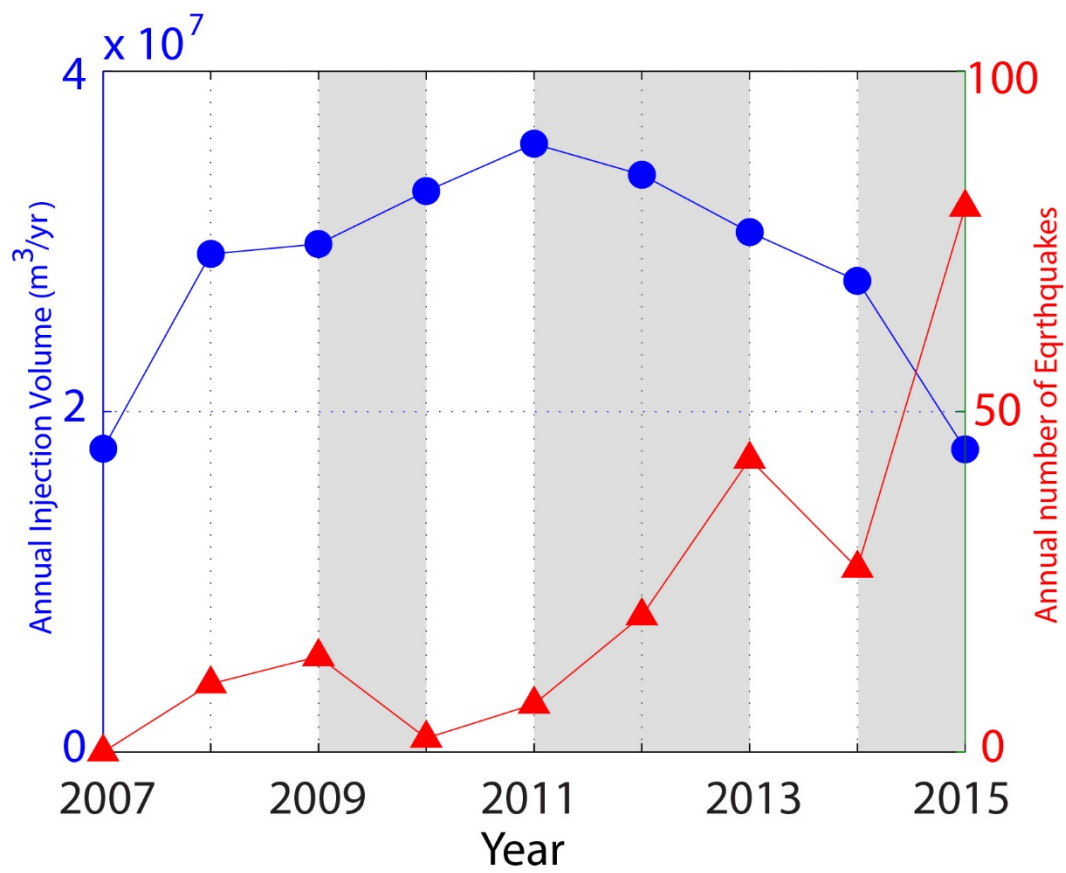


**Figure C.1.** Time series of the annual total volume of injected fluid versus number of earthquakes. Grey shadings indicate periods of anticorrelation between injected volume and earthquake counts. Earthquakes are compiled from ComCat.

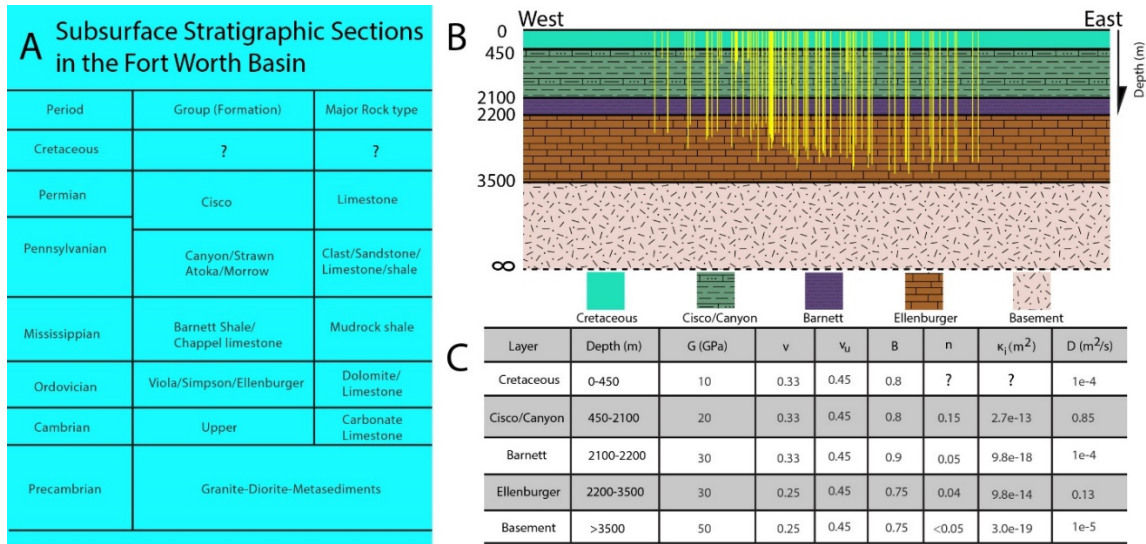


**Figure C.2.** (A) Subsurface lithostratigraphic information associated with the Barnett Shale. (B) East–west cross section showing the simplified five-layer model characterizing the study area. Vertical yellow lines indicate the depth extent of injection wells. (C) Geomechanical parameters used to characterize each layer.

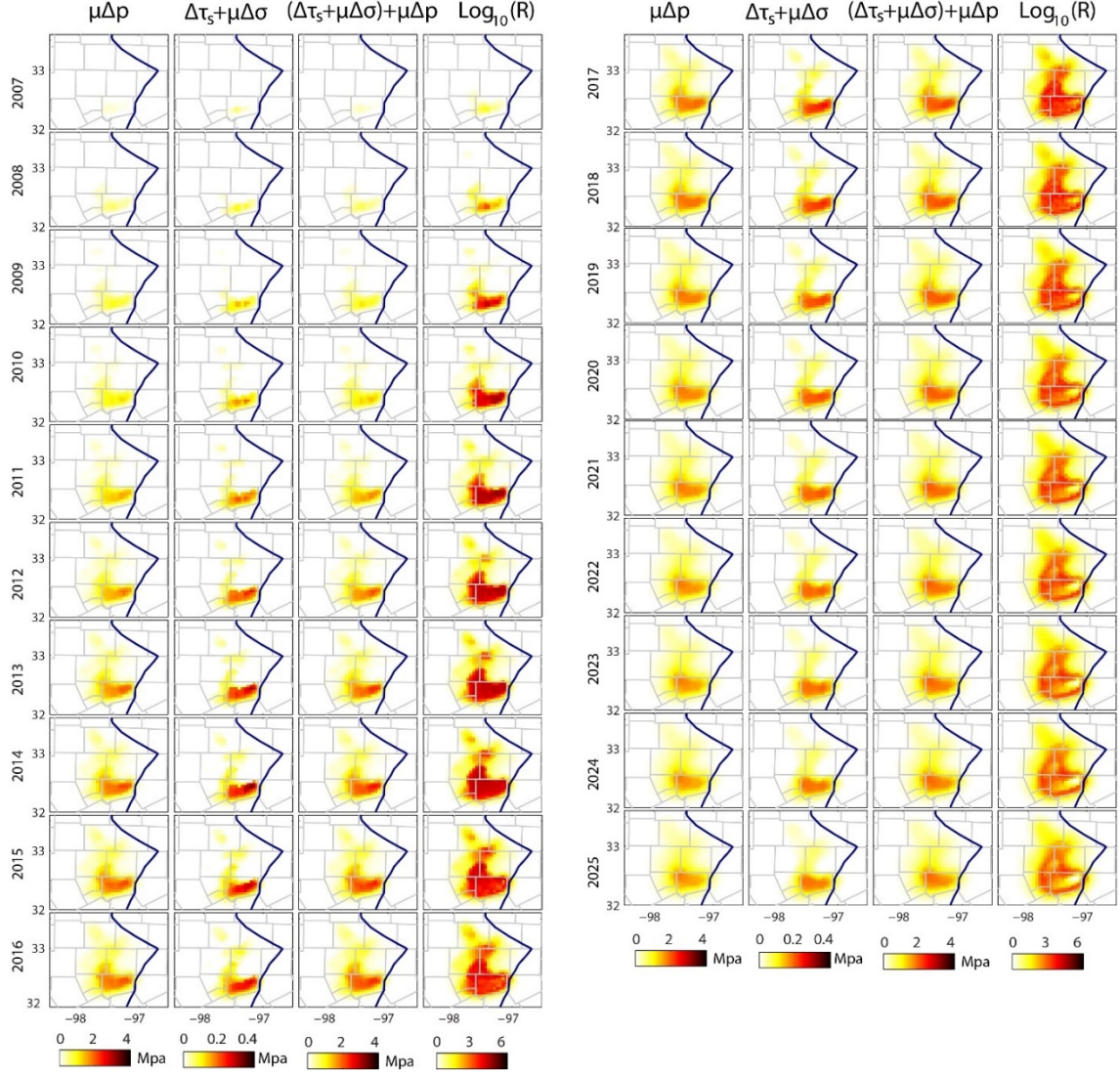


**Figure C.3.** Yearly Snapshots (end of each year) show distribution of modeled cumulative  $\mu\Delta p$ ,  $\Delta\tau_s + \mu\Delta\sigma$ ,  $(\Delta\tau_s + \mu\Delta\sigma) + \mu\Delta p$ , and  $\text{Log}_{10}(R)$ .  $\mu\Delta p$  is the coulomb failure stress change due to pore pressure change, scaled with the coefficient of friction;  $\Delta\tau_s + \mu\Delta\sigma$  is the coulomb failure stress change due to poroelastic stress change;  $(\Delta\tau_s + \mu\Delta\sigma) + \mu\Delta p$  is the total coulomb failure stress change;  $\text{Log}_{10}(R)$  is the logarithm of seismicity rate.

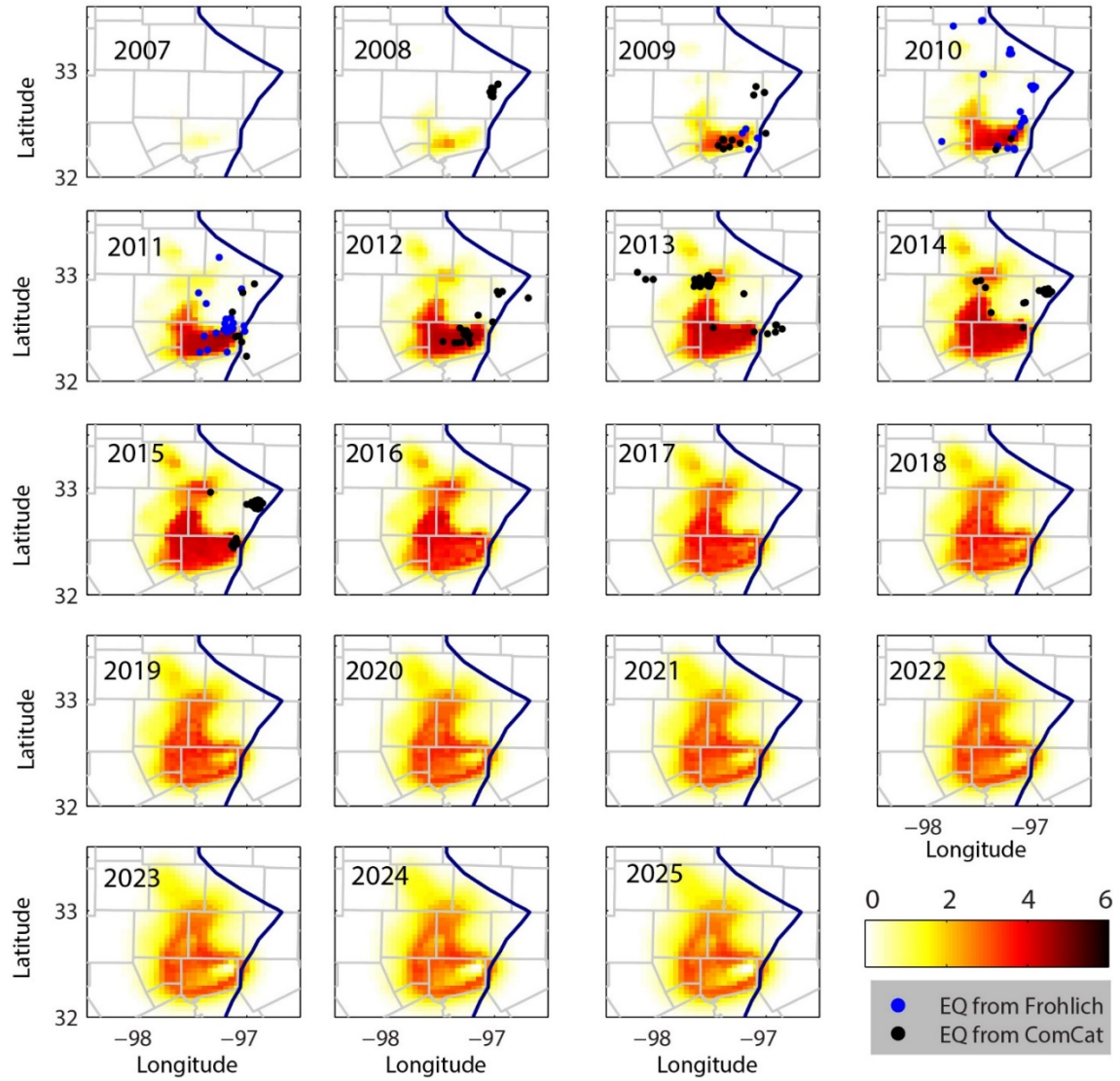


**Figure C.4.** Yearly snapshots (end of each year) of relative earthquake exceedance probability of magnitude larger than 4.0 ( $M \geq 4.0$ ), which is defined by the ratio between probability due to injection and reference probability. Note that the plots show the  $\log_{10}$  of relative probability.



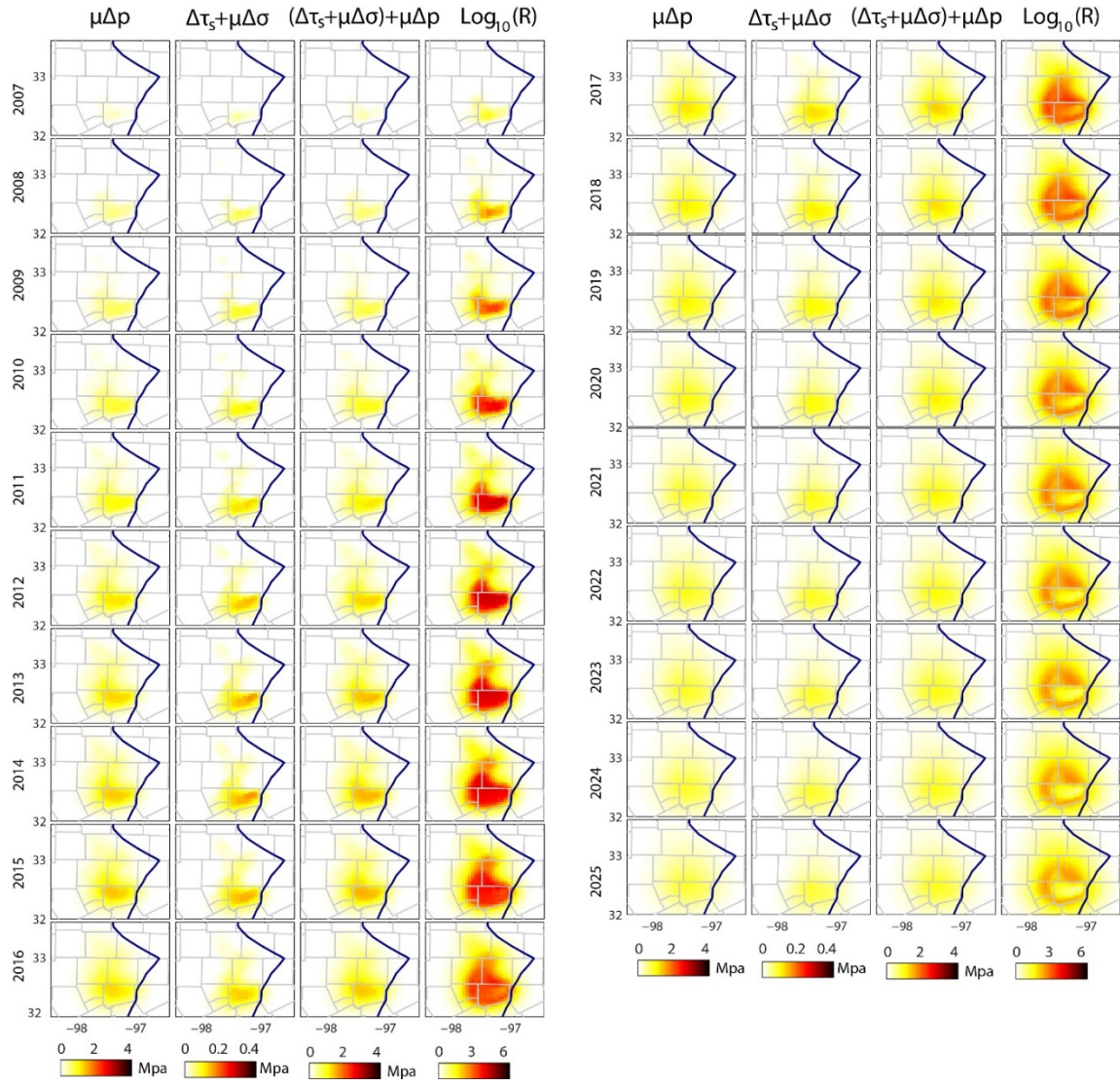


**Figure C.5.** Similar plot as Figure C.3 for hydraulic diffusivity of  $0.7 \text{ m}^2/\text{s}$ .



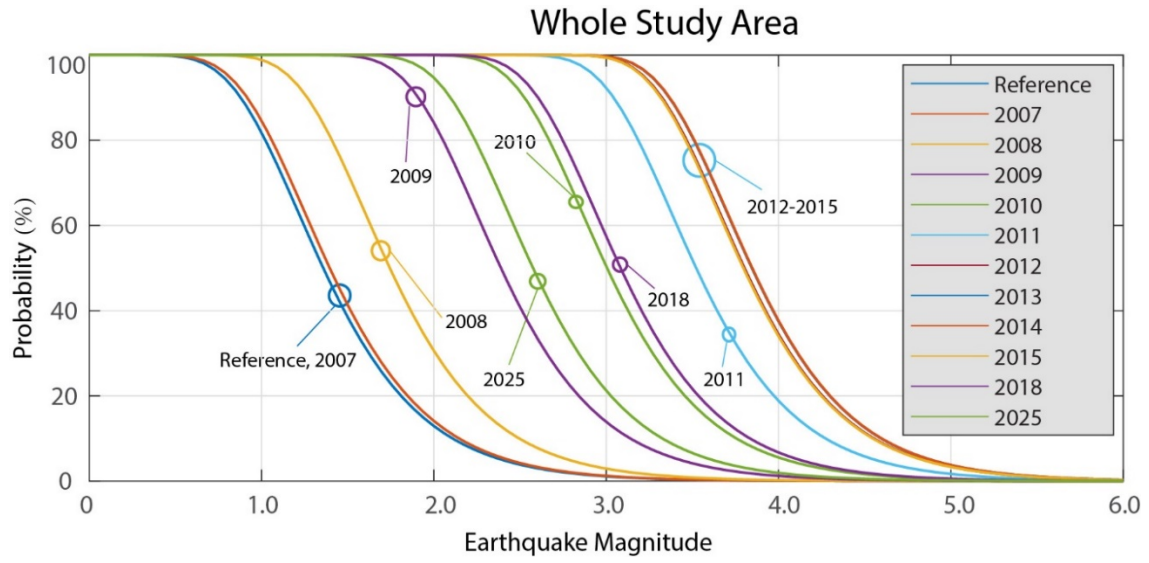


**Figure C.6.** Annual earthquake magnitude exceedance probabilities for the whole study area, assuming a hydraulic diffusivity of  $0.7 \text{ m}^2/\text{s}$  to Ellenburger formation consistent with the end-member compressibility of rock matrix pore space as provided by *Hornbach et al.* [2015].

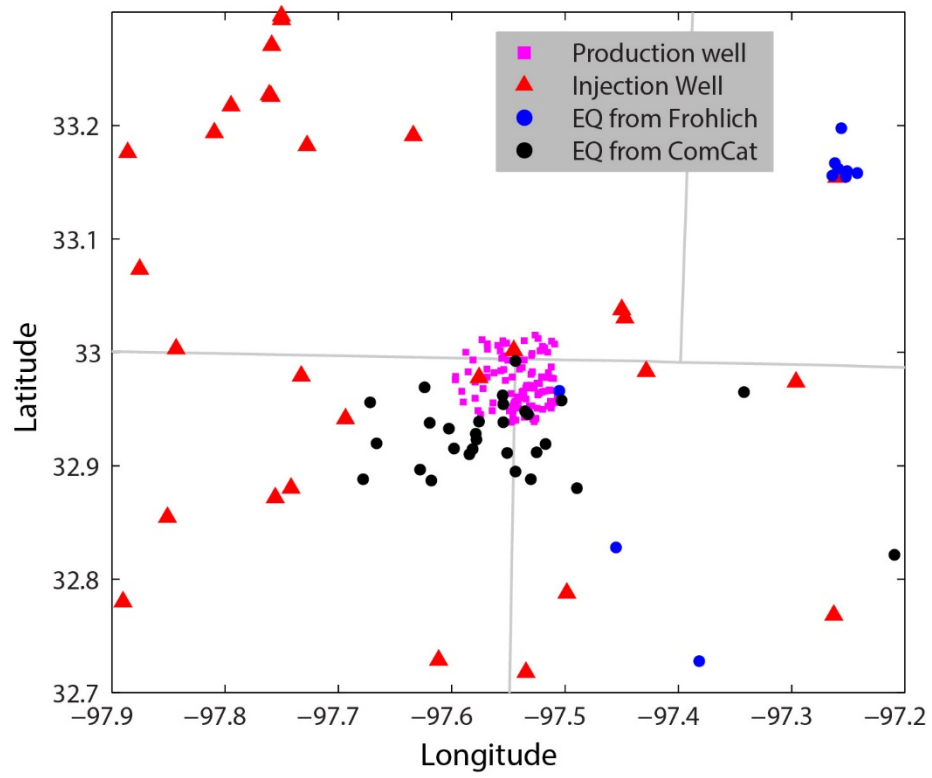


**Figure C.7.** Production well locations at Azle, as used by *Hornbach et al.* [2015].

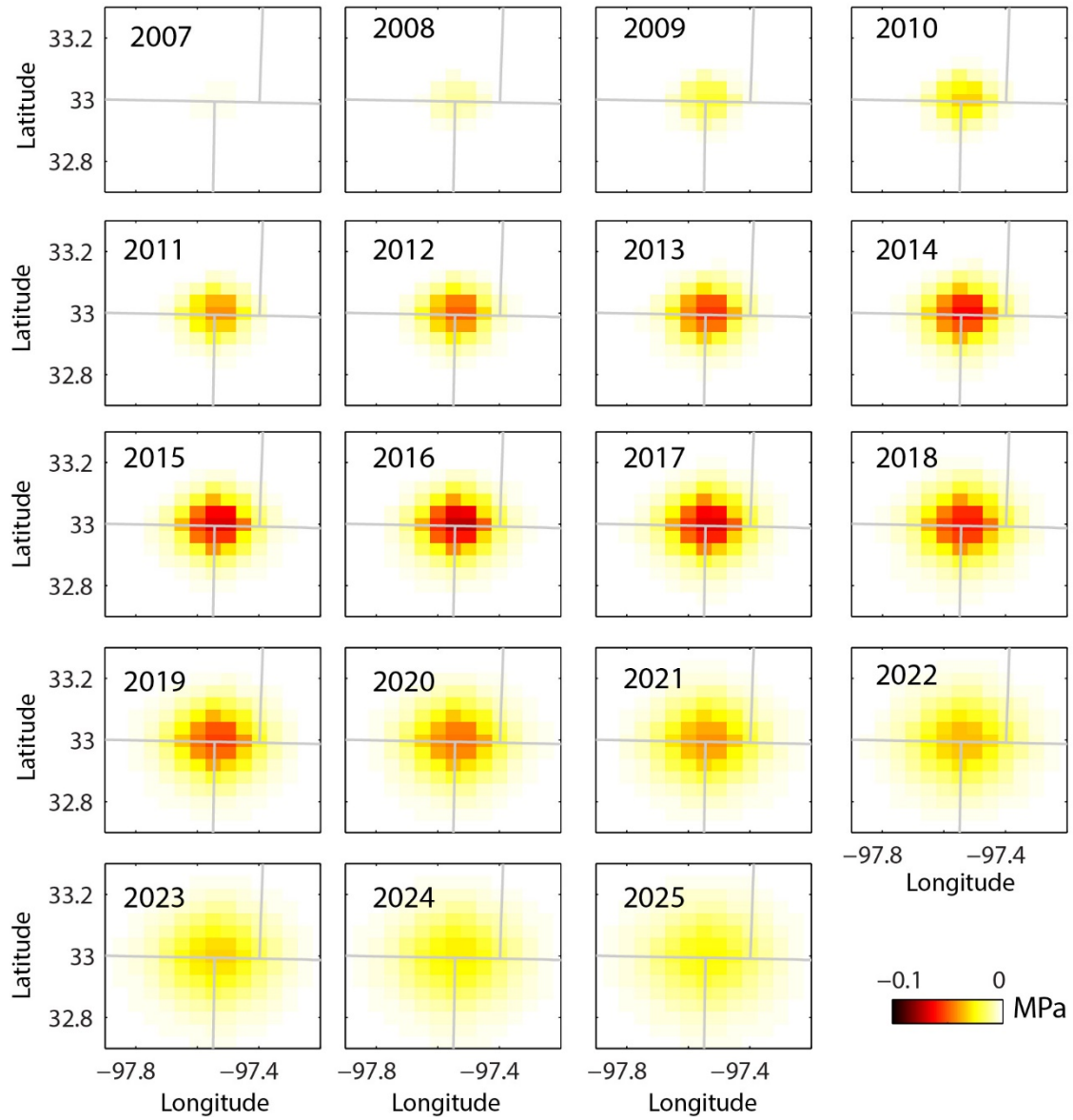


**Figure C.8.** Yearly snapshots (end of each year) of total coulomb stress change due to fluid production at Azle.

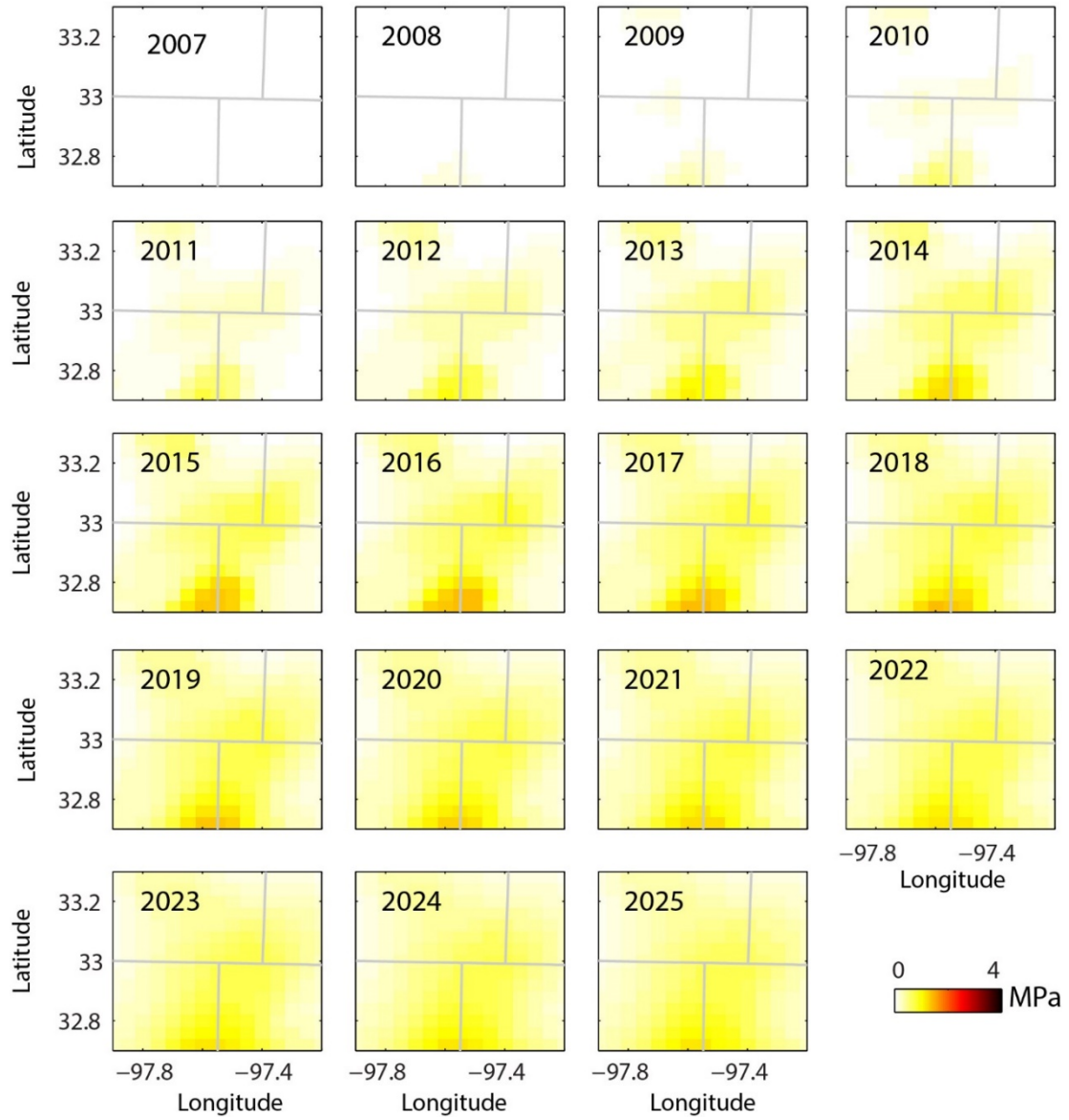


**Figure C.9.** Yearly snapshots (end of each year) of total coulomb stress change due to both injection and production at Azle.

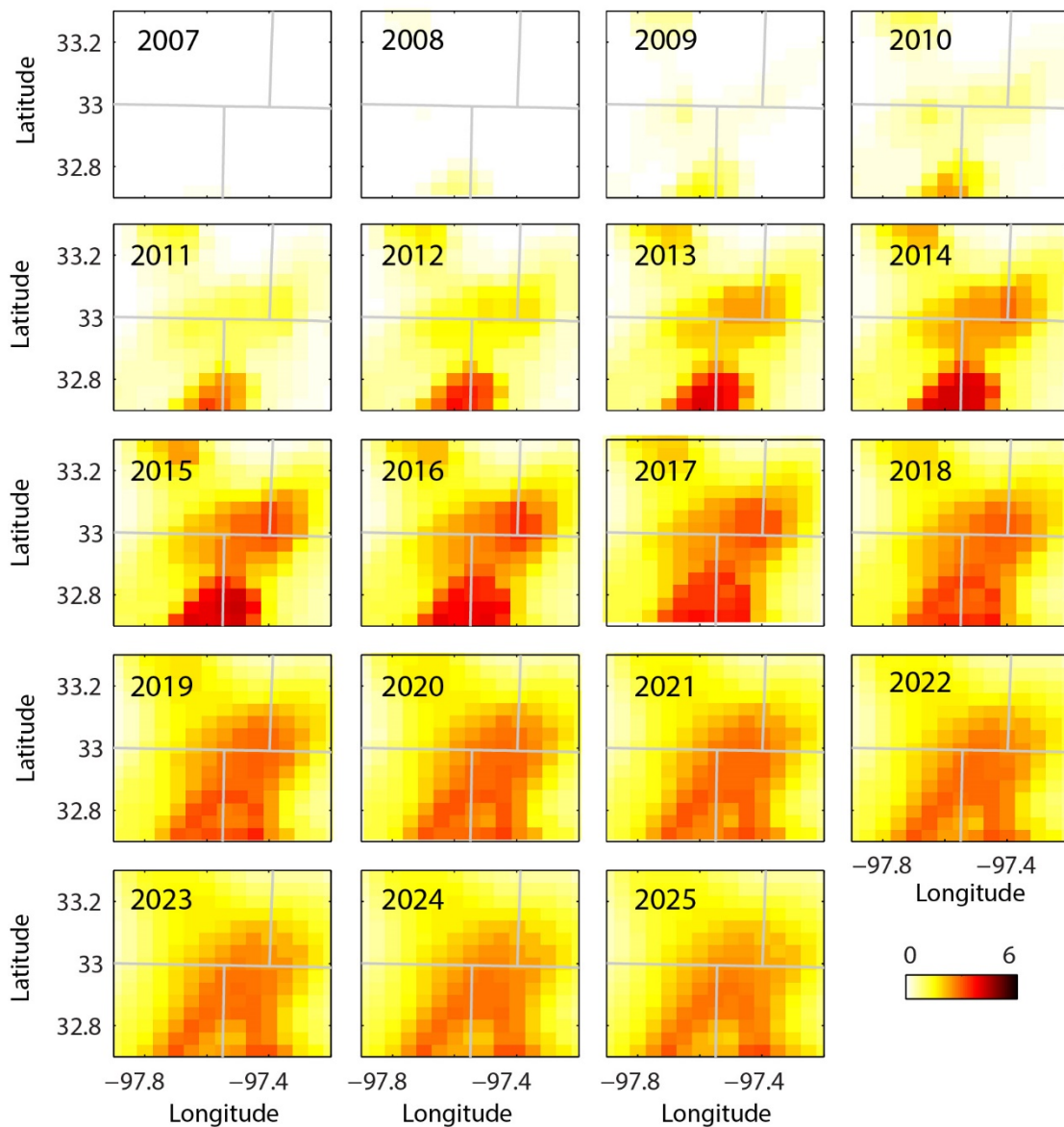


**Figure C.10.** Yearly snapshots (end of each year) of seismicity rate due to both injection and production at Azle.

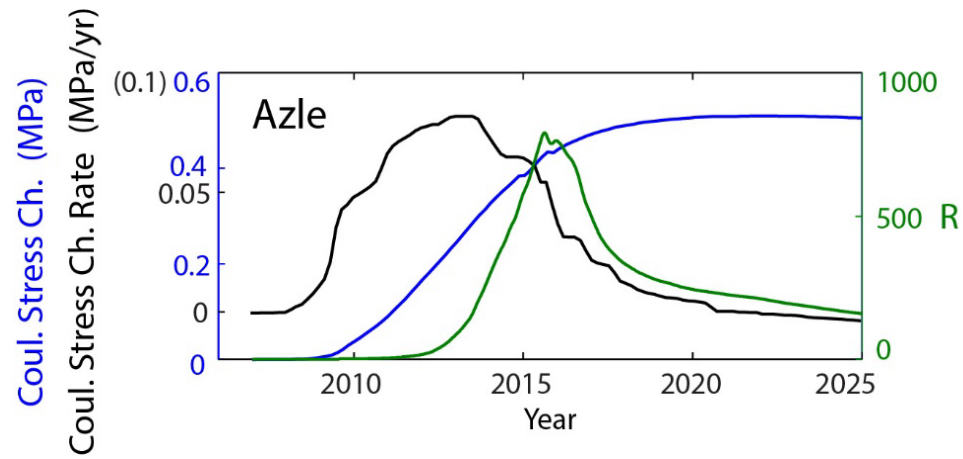


**Figure C.11.** Time series of total Coulomb failure stress change, Coulomb stressing rate, and relative seismicity rate due to combined effect of injection and production at Azle.

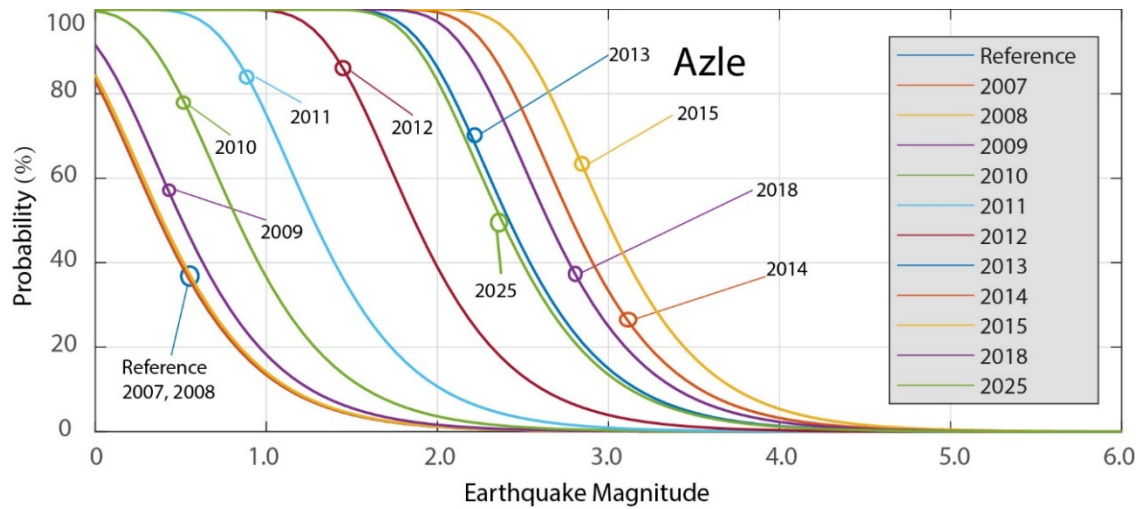


**Figure C.12.** Annual earthquake magnitude exceedance probabilities due to both injection and production at Azle, which can be compared with Figure 4.4c, where only the exceedance probabilities due to injection are provided.

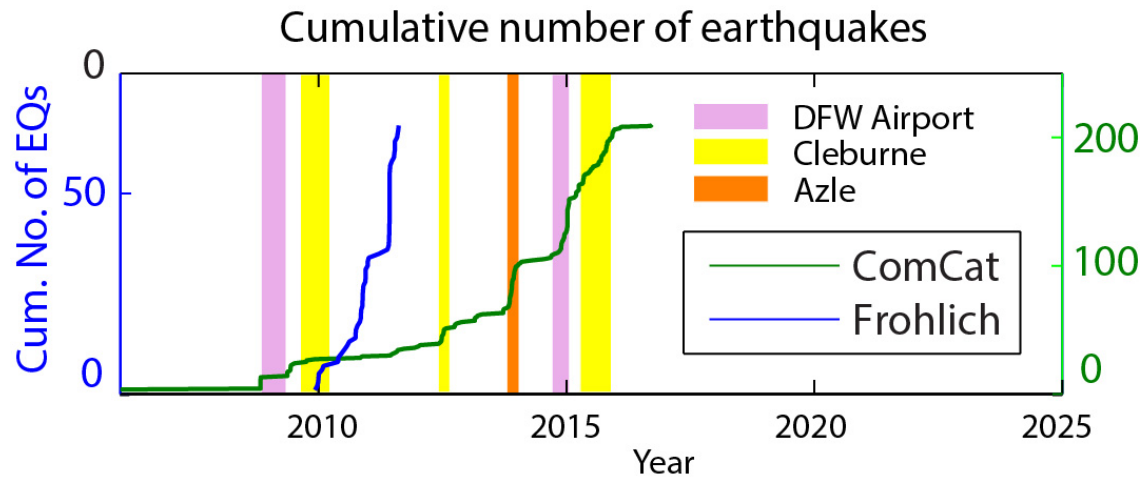


**Figure C.13.** Cumulative number of earthquakes compiled from ComCat (green) and *Frohlich* [2012] (blue) catalogues. Vertical color bars indicate the durations of earthquake sequences occurred in DFW Airport (purple), Cleburne (yellow), and Azle (orange).



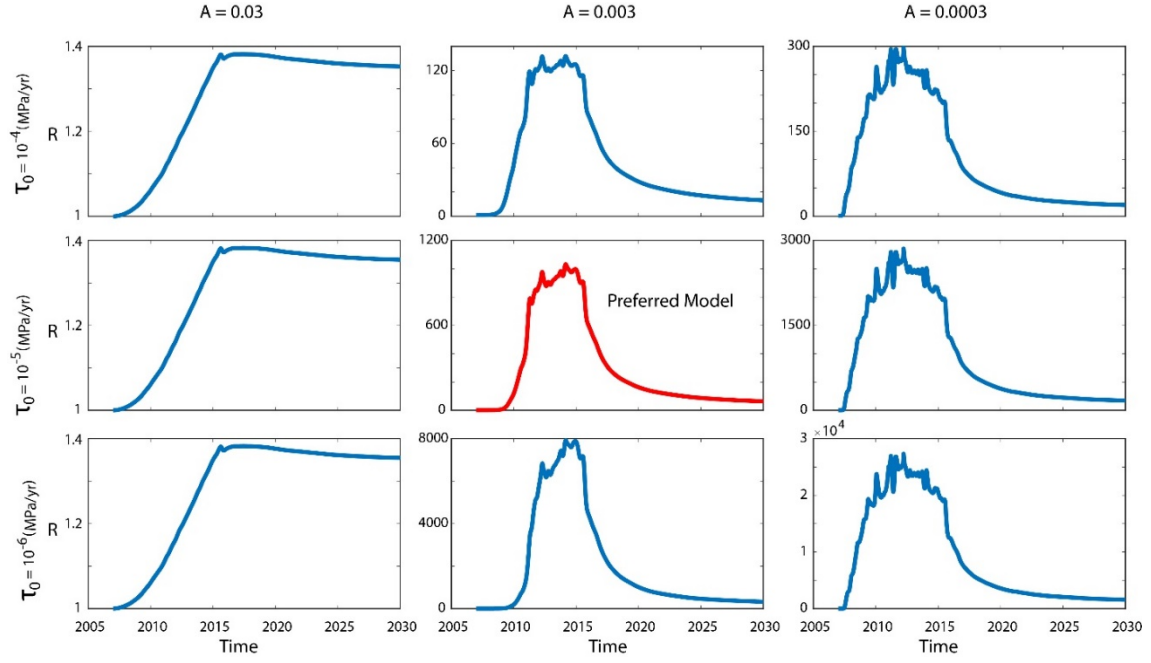


**Figure C.14.** Time series of average seismicity rate over the whole study area using different combinations of frictional parameter  $A$  and background stressing rate  $\tau_0$ . The middle panel corresponds to the preferred parameters used in this study and provided in Table C.1.

**Table C.1** The set of parameters used for modeling the Coulomb failure stress change, seismicity rate, and earthquake magnitude exceedance probability.

Receiver Fault Geometry	
Strike	220°
Dip	65°
Rake	−90°
$\mu$	0.6
Parameters for Seismicity Rate Modeling	
$\dot{\tau}_0$	10 <sup>−5</sup> MPa/year
$\bar{\sigma}$	35 MPa
$A$	0.003
Parameters of Gutenberg–Richter law for Background Seismicity Rate in Barnett Shale	
$k$	10 <sup>1.3</sup> /year
$b$	1.09

**Table C.2** Parameters of injection wells. bpd = BBLS/day, E = Ellenburger, S = Shallow injection. Data are compiled from Railroad Commission of Texas.

UIC#	API#	Max Vol. (bpd)	Max Pres. (psig)	Inject. Dep. (ft)	Latitude	Longitude	County	Injection layer
96543	12132868	3500	2000	9025	33.074458	-97.185708	Denton	E
97701	12132954	25000	3500	10675	33.154601	-97.260306	Denton	E
94754	22130983	25000	3100	7789	32.339149	-97.662307	Hood	E
94942	22100019	10000	2550	5816	32.518664	-98.012928	Hood	E
95424	22131029	10000	2550	5816	32.518672	-98.012279	Hood	E
95664	22131054	30000	2763	6776	32.339908	-97.885999	Hood	E
95808	22131048	25000	2000	7900	32.323077	-97.873181	Hood	E
96415	22131109	25000	3300	8325	32.318405	-97.856356	Hood	E
96673	22131113	25000	2900	7375	32.333426	-97.682529	Hood	E
96785	22131206	30000	3250	8000	32.5081	-97.64855	Hood	E
98847	22131584	25000	3575	7327	32.528838	-97.797734	Hood	E
98889	22131585	30000	3560	6849	32.364587	-97.714078	Hood	E
98944	22131364	25000	2900	7873	32.457515	-97.648201	Hood	E
97038	22131173	20000	3100	6850	32.539093	-97.774521	Hood	E
94929	25130249	35000	3500	8050	32.374266	-97.543196	Johnson	E
94931	25130219	20000	3708	8468	32.395508	-97.400416	Johnson	E
95462	25131020	37000	4300	10050	32.440134	-97.252898	Johnson	E
95581	25130481	25000	3800	9408	32.336824	-97.314534	Johnson	E
96091	25130696	10000	4832	9747	32.311911	-97.516865	Johnson	E
96184	25130509	5000	3400	8600	32.314799	-97.520873	Johnson	E
96321	25130815	20000	3800	9800	32.384985	-97.368873	Johnson	E
96368	25130834	25000	4000	10400	32.449607	-97.130839	Johnson	E
96487	25130895	30000	3500	8605	32.274189	-97.467896	Johnson	E
96488	25130897	30000	3500	8925	32.379499	-97.375507	Johnson	E
96597	25130385	25000	3500	8752	32.520656	-97.604511	Johnson	E
97039	25130953	25000	4000	10200	32.286167	-97.178823	Johnson	E
97089	25131305	30000	4000	11000	32.517649	-97.107017	Johnson	E
97113	25131266	15000	2300	9575	32.307925	-97.380068	Johnson	E
97813	25131443	25000	3000	7820	32.190891	-97.583517	Johnson	E
98399	25132059	25000	3600	9000	32.534126	-97.426356	Johnson	E
98425	25132327	30000	2500	10247	32.446472	-97.252357	Johnson	E
98632	25132450	25000	4200	10813	32.423145	-97.154627	Johnson	E
98954	25132402	30000	5500	11850	32.518889	-97.102547	Johnson	E
99562	25133189	25000	3000	8100	32.374574	-97.534147	Johnson	E
99676	25134121	N/A	N/A	11516	32.51211	-97.174789	Johnson	E
99950	25133335	30000	2500	9107	32.514192	-97.437592	Johnson	E
93369	25130127	9000	2900	8307	32.404077	-97.419281	Johnson	E
94930	25130299	15000	2900	8558	32.325958	-97.380685	Johnson	E
96725	25131021	25000	3500	9875	32.376273	-97.20734	Johnson	E
95078	25130489	30000	3750	8750	32.522049	-97.603382	Johnson	E
95502	25130428	20000	3000	8750	32.518058	-97.577462	Johnson	E
8096	36730852	175	1000	1548	32.925629	-97.928569	parker	S
60651	36732202	N/A	N/A	5229	32.994756	-98.053152	parker	E
62594	36732996	N/A	N/A	1100	32.854673	-97.850907	parker	S
72444	36733071	130	350	925	32.872013	-97.755851	parker	S
77529	36733002	400	445	1619	32.990867	-97.957528	parker	S
96159	36734430	20000	3475	8985	32.728775	-97.611551	parker	E
96233	36733920	30000	3300	8300	32.88026	-97.741798	parker	E

96496	36734054	25000	3420	7590	32.619429	-97.690614	parker	E
96568	36733992	20000	3800	9050	32.678804	-97.57094	parker	E
96729	36734072	30000	3267	8268	32.912066	-98.030216	parker	S
97827	36733999	25000	3400	8400	32.941547	-97.693803	parker	E
97860	36734555	25000	3000	7250	32.708734	-97.941833	parker	E
98090	36734467	25000	3400	9075	32.586134	-97.680318	parker	E
99421	36734709	25000	2500	9250	32.780163	-97.890161	parker	E
100265	36734693	25000	2600	8697	32.977895	-97.575961	parker	E
100495	36734251	20000	2400	8114	32.701533	-97.948643	parker	E
96606	36733859	25000	2000	8400	32.9792	-97.732716	Parker	E
95809	36733790	25000	2000	7900	32.596564	-97.686955	parker	E
96561	36734085	25000	3400	8400	32.590938	-97.684641	parker	E
95124	43931228	25000	3500	9400	32.983263	-97.428339	Tarrant	E
96924	43931801	30000	3600	10250	32.717895	-97.534446	Tarrant	E
97422	43932114	10000	3750	8250	32.768395	-97.262923	Tarrant	E
97642	43932003	25000	4400	11175	32.946644	-97.033312	Tarrant	E
97865	43932466	25000	2500	9099	32.69247	-97.523727	Tarrant	E
98070	43932779	25000	3400	8400	32.787702	-97.498444	Tarrant	E
100852	43934128	25000	4000	9750	32.973828	-97.296287	Tarrant	E
98402	43932673	25000	5023	12211	32.852997	-97.050932	Tarrant	E
29944	49700730	N/A	N/A	2905	33.317443	-97.650566	Wise	S
41166	49700741	200	500	1596	33.176365	-97.886005	Wise	S
84862	49733986	3000	1050	2280	33.313839	-97.792492	Wise	S
92294	49735024	4000	680	2000	33.217429	-97.794798	Wise	S
92686	49735063	4500	668	1427	33.225988	-97.759523	Wise	S
92809	49735119	10000	900	2260	33.322912	-97.795280	Wise	S
93165	49735241	3000	575	1300	33.193744	-97.809590	Wise	S
93178	49735209	4000	500	1991	33.296776	-97.750228	Wise	S
93251	49735252	6624	680	1734	33.227052	-97.760982	Wise	S
93533	49735433	4000	1000	2250	33.317361	-97.799711	Wise	S
95065	49735723	5000	750	2725	33.420295	-97.443924	Wise	S
95129	49735807	20000	3600	8880	33.182446	-97.727675	Wise	E
95391	49736875	10000	3670	9120	33.001791	-97.545337	Wise	E
95423	49735858	N/A	N/A	2706	33.003186	-97.843204	Wise	S
97741	49736296	25000	3600	8200	33.293548	-97.750235	Wise	E
98309	49736317	25000	3400	9550	33.191176	-97.633855	Wise	E
99840	49736872	N/A	N/A	10200	33.03043	-97.447156	Wise	E
94263	49735690	10000	1125	2800	33.037893	-97.449885	Wise	S
100492	49737190	N/A	N/A	3400	33.39655	-97.811043	Wise	E
95745	49735925	5000	1300	2900	33.404475	-97.796325	Wise	S
96768	42530115	25000	2000	7900	32.263529	-97.702682	Somervell	E
97071	42530132	25000	2000	6384	32.272181	-97.673432	Somervell	E
96898	42530122	20000	3150	8100	32.292548	-97.624002	Somervell	E
100281	42530200	25000	3042	7792	32.289321	-97.629718	Somervell	E
95567	33732039	5000	1425	3105	33.455816	-97.776894	Montague	S
95519	33733760	20000	1450	3450	33.477969	-97.798551	Montague	S
95950	33733781	20000	1275	3200	33.503733	-97.797757	Montague	S
98868	9734005	15000	1600	2550	33.451025	-97.295232	Cooke	S

**Table C.3** Earthquake catalog obtained from ComCat.

Date	Latitude	Longitude	Depth	Magnitude	RMS
5/31/1997	33.182	-95.966	5	3.4	0.72
1/25/2002	34	-97.53	5	2.6	0
4/7/2003	33.892	-97.695	5	2.9	1.08
10/31/2008	32.8	-97.016	5	2.6	0.63
10/31/2008	32.836	-97.029	5	3	0.67
10/31/2008	32.871	-96.971	5	2.6	0.22
10/31/2008	32.755	-97.017	5	2.5	1.08
10/31/2008	32.799	-97.045	5	2.6	0.69
10/31/2008	32.832	-97.012	5	2.9	0.56
10/31/2008	32.831	-97.028	5	2.9	1.32
10/31/2008	32.788	-97.028	5	2.9	0.8
11/1/2008	32.766	-97.035	5	2.5	1.02
11/1/2008	32.874	-96.968	5	2.7	0.61
5/16/2009	32.795	-97.016	8.7	3.3	0.84
5/16/2009	32.85	-97.095	5	3	1.18
5/16/2009	32.77	-97.117	5	2.7	1.43
5/16/2009	32.795	-97.016	5	2.6	0
6/2/2009	32.352	-97.403	5	2.8	0
6/7/2009	32.285	-97.345	5	2.6	0.4
6/8/2009	32.35	-97.4	5	2.4	0
6/9/2009	32.266	-97.402	5	2.3	0.27
6/9/2009	32.35	-97.4	5	2	0
6/27/2009	32.297	-97.451	5	2.4	0.64
7/10/2009	32.35	-97.32	5	2	0
9/30/2009	32.356	-97.406	5	2.4	0.91
10/1/2009	32.318	-97.243	5	2.3	0.47
12/5/2009	32.412	-97.004	5	2.9	0.87
11/8/2010	32.26	-97.39	5	2.5	0.53
11/12/2010	32.361	-97.249	5	2.1	1.2
6/12/2011	32.236	-97.002	5	2.7	1.46
6/25/2011	32.37	-97.049	5	2.5	0.74
7/17/2011	32.424	-97.084	5	3	0.44
8/1/2011	32.913	-96.929	5	2.2	1.4
8/7/2011	32.832	-97.037	5	2.6	0.63
9/23/2011	32.648	-97.135	5	2.4	1.25
12/7/2011	32.418	-97.106	5	2.7	0.95
1/6/2012	32.782	-96.685	5	2.1	0.98
1/18/2012	32.372	-97.487	5	3.3	0.79
6/4/2012	32.36	-97.344	5	2.3	0.97
6/15/2012	32.462	-97.273	5	3.3	0.79
6/23/2012	32.401	-97.246	5	2.1	0.14
6/24/2012	32.474	-97.289	5	3.5	1.04
6/25/2012	32.443	-97.272	5	2.3	0.65
6/26/2012	32.357	-97.232	5	2.5	1.04
6/29/2012	32.367	-97.311	5	2.3	0.82
7/6/2012	32.43	-97.276	5	2.7	0.45
7/10/2012	32.476	-97.266	5	2.4	1.18
7/10/2012	32.445	-97.291	5	2.8	0.5
7/11/2012	32.438	-97.237	5	2.1	0.46
7/13/2012	32.499	-97.323	5	2.7	0.78
7/28/2012	32.363	-97.376	6.4	2.2	0.87

9/30/2012	32.842	-96.976	5	3.4	0.68
9/30/2012	32.815	-96.962	5	3.1	0.72
10/1/2012	32.841	-96.93	5	2.3	1.13
10/17/2012	32.557	-97.019	6	2.7	1.02
11/20/2012	32.622	-97.157	5	2.3	1.02
2/24/2013	32.462	-96.912	5	2.5	1.21
2/24/2013	32.527	-96.911	5	2.6	0.73
2/24/2013	32.446	-96.987	5.1	2.7	1.63
3/10/2013	32.503	-97.499	4.3	2.7	0.53
3/17/2013	32.491	-96.85	2.4	2.6	0.64
4/18/2013	31.817	-97.088	0	2.1	0.98
9/21/2013	33.957	-97.136	6.6	2.8	1.04
9/22/2013	33.984	-97.162	5	2.6	0.63
9/23/2013	33.9544	-97.1107	8.93	3.2	1.15
9/23/2013	33.946	-97.161	5	3.4	1.17
10/16/2013	32.5272	-96.9032	5	2.4	0.39
11/1/2013	32.8213	-97.2095	5	2.1	0.72
11/2/2013	32.4647	-97.1154	5	2	0.9
11/6/2013	32.9194	-97.5175	5	2.6	0.58
11/6/2013	32.8884	-97.6784	5	2.6	0.83
11/8/2013	32.9556	-97.6719	5	2.8	0.56
11/9/2013	32.8873	-97.618	5	2.3	1.18
11/9/2013	32.9197	-97.6665	5	3	0.91
11/11/2013	32.9923	-97.5436	5	2.8	0.8
11/13/2013	32.9574	-97.5029	5	2.6	0.49
11/19/2013	32.9328	-97.6024	5	2.4	0.71
11/19/2013	32.9101	-97.5845	5	2.8	0.76
11/20/2013	32.9116	-97.5509	5	3.6	0.71
11/21/2013	32.9232	-97.578	5	2.1	0.46
11/23/2013	32.9152	-97.5983	5	2.9	0.63
11/25/2013	32.8968	-97.6281	5	3.3	0.93
11/26/2013	32.9479	-97.5353	5	2.8	0.59
11/26/2013	32.8882	-97.5299	5	3	0.95
11/26/2013	32.9692	-97.6237	3.36	2.8	1
11/28/2013	32.9553	-98.1312	4.96	3.6	0.51
11/28/2013	33.0204	-98.2091	4.98	2.8	0.53
11/29/2013	32.9118	-97.5251	5	3.1	1.34
12/3/2013	32.9387	-97.5545	5	2.7	0.63
12/8/2013	32.9144	-97.5817	4.99	3.6	0.53
12/9/2013	32.9576	-98.0594	5	3.7	0.85
12/10/2013	32.8951	-97.5437	5	2.7	0.85
12/11/2013	33.6998	-96.7133	5	2.7	0.33
12/13/2013	33.7031	-96.6921	5	2.6	1.1
12/14/2013	33.7122	-96.8048	4.69	2.7	0.51
12/15/2013	32.9379	-97.6196	5.05	2.9	0.9
12/17/2013	32.9543	-97.5546	5	2.1	0.69
12/22/2013	32.9619	-97.5552	5	3.3	0.58
12/23/2013	32.9284	-97.5789	6.39	3.3	0.44
1/11/2014	32.8802	-97.4895	5	2.2	1.13
1/13/2014	32.9391	-97.576	2	3.1	0.4
1/28/2014	32.9454	-97.5328	5	3	0.58
2/2/2014	32.6451	-97.4354	4.99	2.4	0.62
4/17/2014	32.869	-96.8991	5	2.5	0.61
7/20/2014	32.8386	-96.8669	3.23	2.2	0.81
9/7/2014	32.7397	-97.1132	4.12	2.4	0.53

9/11/2014	32.8153	-96.9178	5	2.8	0.93
9/12/2014	32.7335	-97.1299	5	2.5	0.68
10/1/2014	32.8499	-96.9824	6.56	2.1	0.45
10/28/2014	32.8431	-96.9058	5	2.4	0.74
11/10/2014	32.8183	-96.8902	5	2.3	1.1
11/15/2014	32.8481	-96.9576	5	2.6	0.53
11/23/2014	32.8346	-96.8932	3.96	3.3	0.46
11/23/2014	32.8449	-96.9343	8.01	2.5	0.5
11/24/2014	32.846	-96.8955	5	2.4	0.15
11/25/2014	32.8481	-96.9013	5	2.2	0.55
11/25/2014	32.8404	-96.8922	2.58	2.7	0.88
11/30/2014	32.5035	-97.1328	5	3.4	0.41
12/2/2014	32.836	-96.893	5	2.7	1.23
12/10/2014	32.8621	-96.9338	5	2	0.5
12/12/2014	32.8501	-96.8902	3.02	2.7	0.63
12/15/2014	32.8412	-96.9009	4.16	2.7	0.52
12/17/2014	32.8507	-96.9193	5	2.6	0.41
12/19/2014	32.8245	-96.9317	8.13	2.4	1.26
12/20/2014	32.8304	-96.9188	3.18	2.4	0.48
12/30/2014	32.8372	-96.9132	3.09	2.7	0.57
1/2/2015	32.8438	-96.9034	2.25	2.4	0.45
1/6/2015	32.8487	-96.8883	5	2.3	0.33
1/6/2015	32.835	-96.9027	5.93	3.5	0.19
1/7/2015	32.847	-96.8922	5	3.6	0.52
1/7/2015	32.8085	-96.8962	8.24	2.9	0.55
1/7/2015	32.8485	-96.9375	5	2.7	0.2
1/7/2015	32.8564	-96.8819	5	1.7	0.5
1/7/2015	32.8588	-96.9174	5	2.4	0.56
1/7/2015	32.8512	-96.8844	5	1.6	0.16
1/7/2015	32.8417	-96.9131	5	3.1	0.72
1/7/2015	32.8473	-96.8896	4.27	2.3	0.27
1/7/2015	32.8367	-96.9063	5	2.7	1.19
1/7/2015	32.8464	-96.9171	7.24	2.7	0.36
1/8/2015	32.8375	-96.9	5	1.9	0.46
1/8/2015	32.8282	-96.9008	5	2.3	0.34
1/8/2015	33.968	-97.299	8.3	2.5	0.49
1/8/2015	32.4778	-97.0944	5	2.6	1.15
1/9/2015	32.8418	-96.8936	5.03	2.4	0.49
1/12/2015	32.8175	-96.8769	5	2.4	0.54
1/14/2015	32.8396	-96.8998	5	1.9	0.5
1/18/2015	32.852	-96.9378	5	2.2	0.55
1/20/2015	32.8492	-96.9152	9.83	2.3	0.17
1/20/2015	32.8615	-96.9093	8.77	2.6	0.44
1/20/2015	32.8257	-96.9011	8.96	3	0.68
1/20/2015	32.8526	-96.9265	8.32	2.5	0.43
1/23/2015	32.8904	-96.8967	8.74	2.2	0.43
2/27/2015	32.8254	-96.8928	5	3.1	0.78
3/8/2015	32.8364	-96.9026	5	2.2	0.61
3/12/2015	32.8775	-96.9129	8.17	2.4	0.22
3/12/2015	32.8839	-96.9075	5	2	0.37
3/14/2015	32.8565	-96.9251	5	2.7	0.63
3/25/2015	32.4646	-97.1445	6.62	2.6	0.55
4/2/2015	32.8543	-96.9392	5	2.7	0.52
4/2/2015	32.8579	-96.9345	7.86	3.3	0.46
4/3/2015	32.8575	-96.9117	5	2.5	0.72

4/3/2015	32.8678	-96.934	5.74	2.3	0.49
4/3/2015	32.8826	-96.8772	5	2.2	0.28
5/3/2015	32.8511	-96.9514	5	3.2	0.56
5/3/2015	32.8561	-96.891	5	2.5	0.7
5/4/2015	32.8589	-96.852	5	2.1	0.84
5/4/2015	32.8613	-96.8716	5	2.7	0.78
5/7/2015	32.4817	-97.1006	2.54	4	0.79
5/9/2015	32.854	-96.8903	5	2.7	0.68
5/10/2015	32.5005	-97.0942	4.94	2.4	0.85
5/18/2015	32.8675	-96.9566	5	3.3	0.73
6/13/2015	32.8726	-96.9038	5	2.3	0.93
6/15/2015	32.5299	-97.101	5	2.4	0.87
6/27/2015	32.8723	-96.907	5	2.3	0.82
6/28/2015	32.8505	-97.0002	5	2.1	0.52
7/13/2015	32.8351	-96.939	5	2.4	0.89
7/16/2015	32.8533	-96.9417	5	1.8	0.57
8/12/2015	32.8465	-96.9122	9.78	2.7	0.3
8/25/2015	32.8363	-96.9467	5	2.1	0.47
8/25/2015	32.8552	-96.9412	5	2.2	0.65
8/31/2015	32.8463	-96.9359	5	1.8	0.53
9/12/2015	32.8427	-96.9185	5	2.5	0.56
9/12/2015	32.8281	-96.933	5	2.2	0.95
9/14/2015	32.8785	-96.901	5	2	0.59
9/16/2015	32.8411	-96.9448	5	2.1	0.52
9/22/2015	32.8838	-96.9187	5	2.4	0.4
10/1/2015	32.8119	-96.922	5	2.7	0.58
10/4/2015	32.8633	-96.9174	5	2.1	0.81
10/18/2015	32.8733	-96.9165	6.53	2.4	0.34
10/19/2015	32.8755	-96.9134	5	2.7	0.61
10/19/2015	32.8659	-96.9394	5	2.3	0.44
10/23/2015	32.4889	-97.1324	7.57	2.1	0.08
10/23/2015	32.4429	-97.1262	5.13	2.6	0.39
10/27/2015	32.8725	-96.924	5	2.3	0.39
10/28/2015	32.8608	-96.9495	5	2.2	0.51
10/29/2015	32.8435	-96.9109	8.67	2.5	0.36
11/3/2015	32.8566	-96.9525	5	2.2	0.5
11/15/2015	32.8476	-96.9288	8.72	2	0.24
11/16/2015	32.8702	-96.9488	5	2.4	0.92
12/3/2015	32.8576	-96.9236	5	2.8	0.6
12/4/2015	32.8655	-96.9028	5.66	2.6	0.3
12/4/2015	32.8648	-96.9196	5	2.1	0.44
12/6/2015	32.8752	-96.921	5.7	2.1	0.39
12/7/2015	32.8186	-96.9185	5	2.8	0.49
12/17/2015	32.8465	-96.9682	5	2.1	0.29
12/17/2015	32.965	-97.3421	5	3	0.55



**Table C.4** Earthquake catalog obtained from *Froblich* [2012].

Date	Latitude	Longitude	Depth	Magnitude	RMS
2009/12/05	32.368	-97.082	5	2.9	0.62
2009/12/22	32.454	-97.193	5	N/A	0.80
2009/12/30	32.263	-97.161	5	N/A	0.24
2010/01/01	32.416	-97.222	5	N/A	0.97
2010/01/02	32.474	-97.164	5	2.1	0.42
2010/01/27	32.614	-97.161	5	1.9	0.46
2010/02/06	32.552	-97.128	5	N/A	0.53
2010/05/25	32.531	-97.121	5	2.1	0.46
2010/05/26	32.858	-97.038	5	N/A	0.70
2010/06/17	32.270	-97.279	5	N/A	0.47
2010/07/11	32.966	-97.505	5	N/A	1.46
2010/07/30	33.416	-97.787	5	N/A	0.69
2010/08/16	32.263	-97.218	5	N/A	0.45
2010/09/30	32.288	-97.372	5	N/A	0.26
2010/10/01	32.259	-97.213	5	N/A	0.47
2010/10/03	32.270	-97.220	5	N/A	0.43
2010/10/15	32.511	-97.148	5	N/A	0.61
2010/11/01	32.822	-97.042	5	N/A	0.51
2010/11/08	32.293	-97.372	5	2.5	0.28
2010/11/08	32.290	-97.374	5	N/A	0.30
2010/11/12	32.290	-97.374	5	2.1	0.34
2010/11/20	33.158	-97.242	5	2.3	0.34
2010/11/21	33.155	-97.252	5	2.1	0.58
2010/11/23	32.334	-97.895	5	N/A	0.09
2010/11/23	32.848	-97.018	5	2.4	0.80
2010/11/24	33.156	-97.264	5	N/A	0.57
2010/11/26	33.159	-97.252	5	N/A	0.53
2010/12/11	33.160	-97.251	5	2.3	0.58
2010/12/13	32.855	-97.064	5	2.5	0.32
2010/12/13	33.167	-97.262	5	N/A	0.51
2010/12/14	33.198	-97.256	5	N/A	0.44
2010/12/29	33.463	-97.525	5	N/A	0.41
2010/12/29	33.471	-97.514	5	N/A	0.43
2011/01/04	33.162	-97.259	5	N/A	0.48
2011/03/25	32.540	-97.209	5	N/A	0.45
2011/05/23	32.469	-97.020	5	N/A	0.72
2011/06/01	32.292	-97.368	5	N/A	0.37
2011/06/03	32.425	-97.401	5	N/A	0.24
2011/06/03	32.274	-97.187	5	N/A	0.49
2011/06/06	32.271	-97.443	5	N/A	1.30
2011/06/06	32.462	-97.187	5	N/A	0.26
2011/06/06	32.513	-97.146	5	N/A	0.63
2011/06/07	32.491	-97.145	5	2.2	0.66

2011/06/07	32.582	-97.195	5	N/A	0.45
2011/06/07	32.470	-97.178	5	2.2	0.60
2011/06/07	32.465	-97.187	5	N/A	0.78
2011/06/07	32.484	-97.157	5	N/A	0.62
2011/06/07	32.454	-97.289	5	N/A	1.03
2011/06/07	32.496	-97.130	5	2.2	0.71
2011/06/07	32.504	-97.143	5	2.4	0.56
2011/06/07	32.547	-97.127	5	N/A	0.47
2011/06/07	32.502	-97.149	5	N/A	0.62
2011/06/07	32.511	-97.140	5	N/A	0.61
2011/06/07	32.493	-97.145	5	2.4	0.66
2011/06/09	32.500	-97.146	5	N/A	0.60
2011/06/10	32.828	-97.455	5	N/A	0.73
2011/06/12	32.495	-97.151	5	2.7	0.58
2011/06/25	32.480	-97.151	5	2.4	0.71
2011/07/09	32.483	-97.149	5	N/A	0.29
2011/07/13	32.520	-97.029	5	N/A	1.05
2011/07/17	32.488	-97.171	5	3.0	0.63
2011/07/17	32.494	-97.161	5	N/A	0.61
2011/07/17	32.593	-97.147	5	N/A	0.22
2011/08/01	32.865	-97.049	5	2.2	0.24
2011/08/07	32.864	-97.050	5	2.6	0.27
2011/08/12	32.728	-97.382	5	N/A	1.17
2011/08/14	32.483	-97.215	5	N/A	1.21

## APPENDIX D

### SUPPLEMENTARY INFORMATION FOR CHAPTER 5

### Text D.1 Background Seismicity

The parameters characterizing the seismicity before the increase in earthquakes are explored separately in CO and WO (Figure D.13). The Gutenberg-Richter frequency-magnitude relationship was constructed using a maximum likelihood estimation method and found a  $k$ -value of  $10^{2.71}$  within an area size of  $\sim 25,000 \text{ km}^2$  and a  $b$ -value of 1.09 for CO (Figure D.14). The seismicity data within WO did not allow such an estimation since the number of earthquakes is too few to construct a frequency-magnitude curve. Nonetheless, the estimated  $b$ -value for the combined region of CO and WO is consistent with that obtained for CO [Langenbruch and Zoback, 2016], thus the same  $b$ -value of 1.09 was assumed for WO. The background seismic productivity levels in CO and WO are different (Figure D.15). The seismic productivity in WO is obtained by scaling that of CO with a factor equal to the ratio between annual seismicity rate in WO and CO zones, giving a  $k$  value of  $\sim 10^{1.7}$  within an area size of  $\sim 12,000 \text{ km}^2$  for WO.

### Text D.2 Earthquake Magnitude-Time Simulation

For a region of size  $S$ , assuming the background earthquake magnitude-frequency relationship remains homogeneous in both space and time, the absolute seismicity rate as a function of stress changes due to fluid injection can be given by scaling the background seismicity with relative seismicity rate. Thus, the earthquake count per unit area per unit time per unit magnitude is given by

$$R(\mathbf{x}, t, M) = \frac{\ln(10)kb10^{-bM}}{S_0} R(\mathbf{x}, t) \quad (\text{D.1})$$

where  $k$  is the background seismicity rate of magnitude  $\geq 0$ , describing the productivity level within the measurable region  $S_0$ ,  $b$  is the slope of frequency-magnitude relationship, characterizing the earthquake size distribution. The total number of earthquakes per unit time per unit magnitude for specific region  $S$  is given by integration over the entire area

$$R(t, M) = \int_S R(\mathbf{x}, t, M) d\mathbf{x} = \frac{\ln(10)kb10^{-bM}}{S_0} \int_S R(\mathbf{x}, t) d\mathbf{x} \quad (\text{D.2})$$

To simulate magnitude-time distribution that is governed by the function of  $R(t, M)$ , time  $t$  is discretized into  $N_t$  evenly spaced time samples  $[t_1, t_2, \dots, t_i, \dots, t_{N_t}]$  with time interval length of  $\Delta t = t_{i+1} - t_i$  and define the minimum magnitude  $M_{min}$  and maximum magnitude  $M_{max}$  for the purpose of mimicking probability distribution. Firstly, for the time interval  $[t_i, t_{i+1}]$ , the total number of earthquakes from  $M_{min}$  to  $M_{max}$  is calculated:

$$N(t_i) = \int_{M_{min}}^{M_{max}} \int_{t_i}^{t_{i+1}} R(t, M) dt dM \quad (\text{D.3})$$

Secondly, for the same time interval  $[t_i, t_{i+1}]$ , the cumulative probability distribution is defined as a function of earthquake magnitude  $M$ :

$$P(M; t_i) = 1 - \frac{\int_M^{M_{max}} \int_{t_i}^{t_{i+1}} R(t, M) dt dM}{\int_{M_{min}}^{M_{max}} \int_{t_i}^{t_{i+1}} R(t, M) dt dM} \quad (\text{D.4})$$

Based on the number of earthquakes  $N(t_i)$  and probability distribution function  $P(M; t_i)$  for time interval  $[t_i, t_{i+1}]$ , the magnitudes of the  $N(t_i)$  events can be determined using a random sampling method [Meyer, 1970]. Similarly, the associated event times of the  $N(t_i)$  earthquakes are randomly sampled from the time interval  $[t_i, t_{i+1}]$ . This procedure is

iteratively applied to all the defined time intervals to obtain a united magnitude-time distribution.

#### Text D.3 Time-dependent Earthquake Magnitude Exceedance Probability

Assuming a nonhomogeneous Poisson process for earthquake occurrence, the probability of at least one event larger than  $M$  in time interval  $[t_1, t_2]$  over region  $S$  is

$$P_{\geq M}(t_1, t_2, S) = 1 - \exp[-N_{\geq M}(t_1, t_2, S)] \quad (\text{D.5})$$

where,  $N_{\geq M}(t_1, t_2, S)$  is the expected number of  $\geq M$  earthquakes during  $[t_1, t_2]$  over region  $S$ , which is given by integration over space and time:

$$N_{\geq M}(t_1, t_2, S) = \int_{t_1}^{t_2} \int_S \frac{k10^{-bM}}{S_0} R(\mathbf{x}, t) d\mathbf{x} dt \quad (\text{D.6})$$

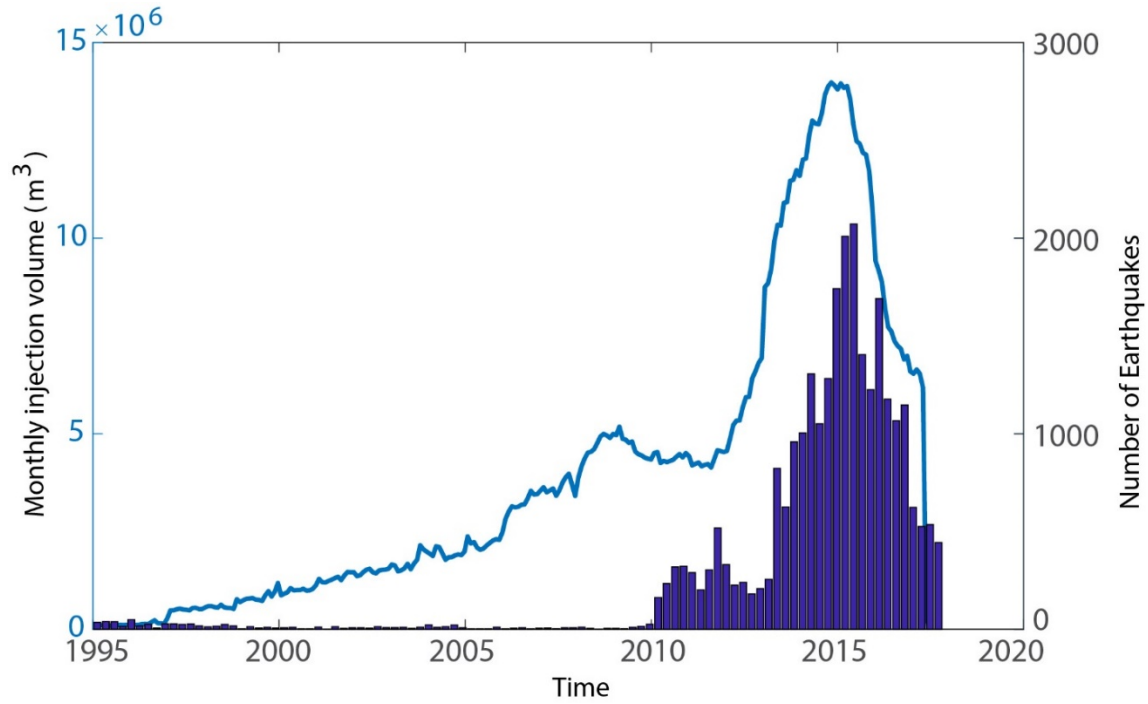


**Figure D.1.** Monthly injection volume and histogram of observed seismicity during 1995-2017. Time series of total monthly injection rate within north-central Oklahoma is obtained by summation of Arbuckle disposal well injection data from Oklahoma Corporation Commission, comparable to previous studies [Langenbruch and Zoback, 2016]. Seismicity catalog is compiled from Oklahoma Geological Survey. M0+ earthquakes without declustering are shown in the histogram.

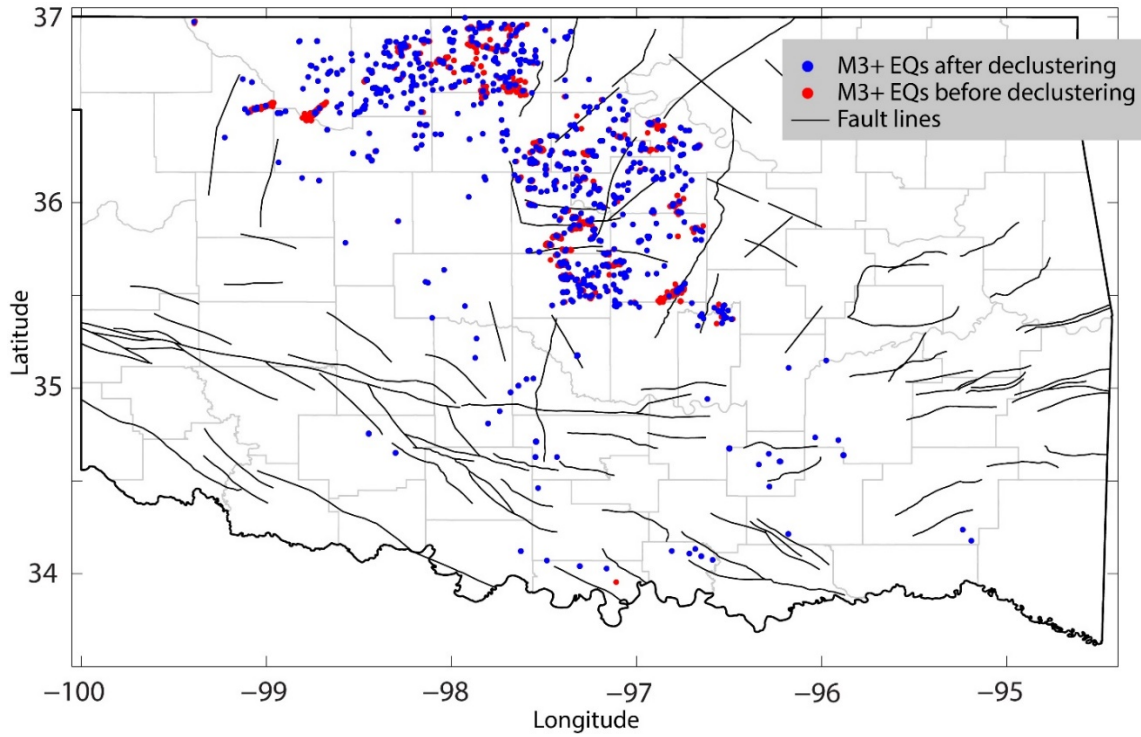


**Figure D.2.** Earthquake declustering. Red dots show all the recorded M3+ earthquakes. Declustered M3+ earthquakes are shown as blue dots. Black lines are mapped faults. Declustering is implemented using a maximum look-ahead time of 30 days and using an average location uncertainty of 1.5 km for epicenter and 2.0 km for depth.

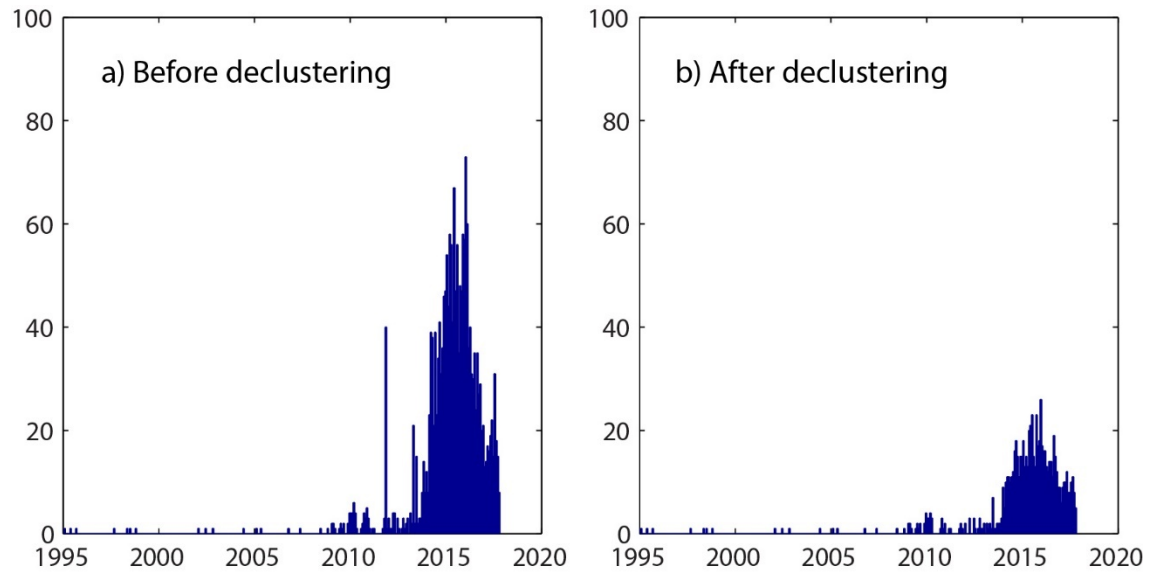


**Figure D.3.** Histograms of M3+ earthquakes. (a) Histogram of recorded M3+ earthquakes before declustering. (b) Histogram of declustered M3+ earthquakes.



Subsurface Stratigraphic Sections			
Period	Group (Formation)	Major Rock type	Aquifer unit
Permian	Post-Simpson	Sandstone	Shallow Aquifer
Pennsylvanian			
Mississippian Devonian Silurian Upper Ordovician		Shale/Carbonate	Confining layer
Middle Ordovician		Simpson	Sandstone/ Carbonate
Lower Ordovician	Arbuckle		
Cambrian	Timbered Hills		
Precambrian	Granite		Confining layer

**Figure D.4.** Subsurface stratigraphic information in Oklahoma. Shown are time-stratigraphic, rock-stratigraphic, geologic, and model stratigraphic units.

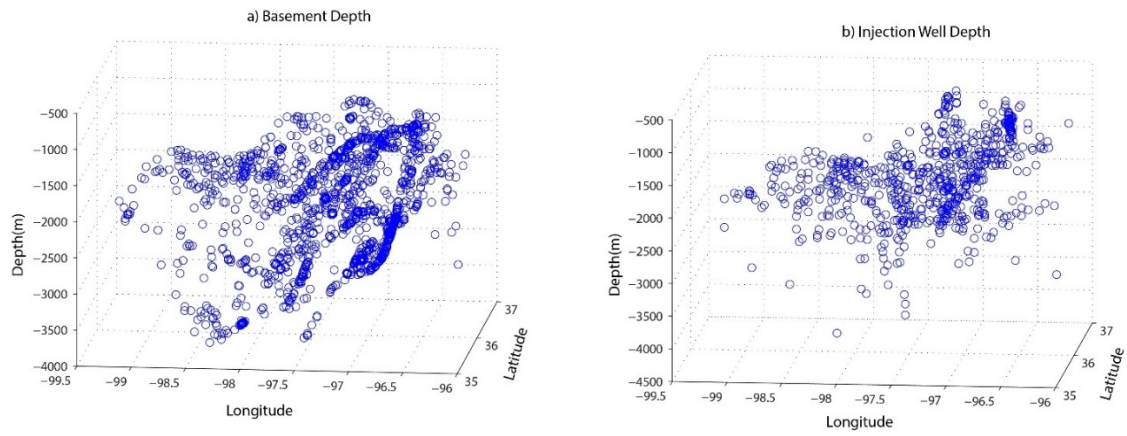


**Figure D.5.** Basement depth and injection well depth. (a) 3-D distribution of depth samples of basement interface. (b) 3-D distribution of injection depth of Arbuckle wells.

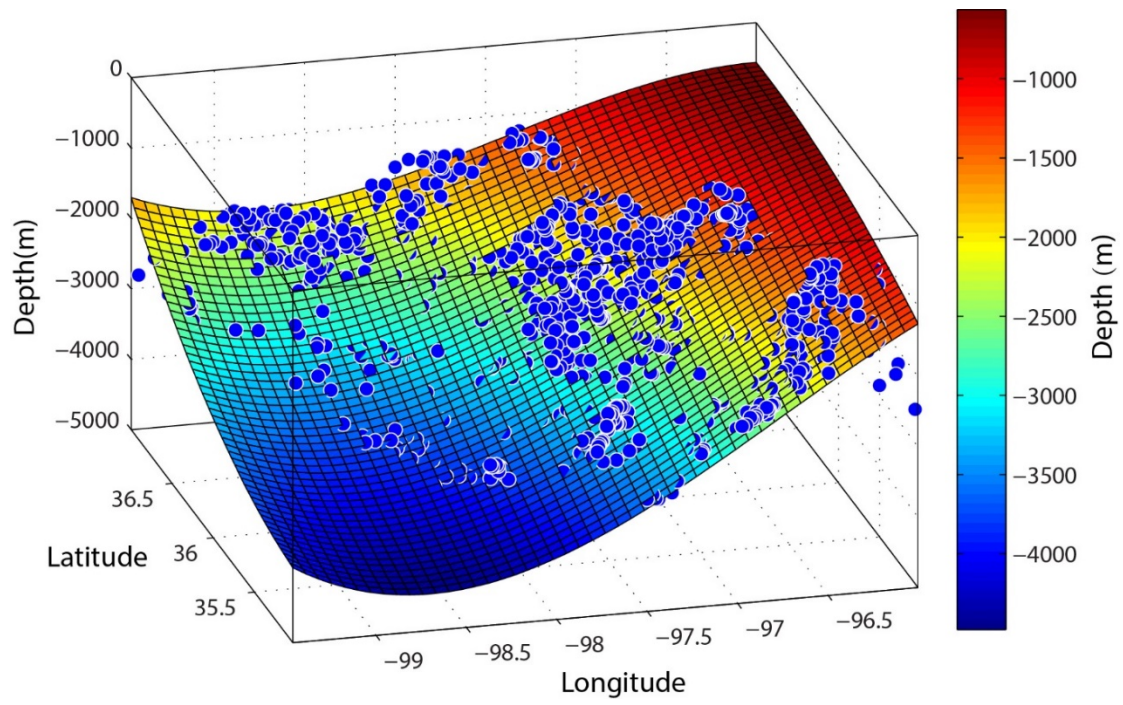


**Figure D.6.** The fitted surface of basement interface. The polynomial curve is applied to fit a curved surface to the samples of basement interface.

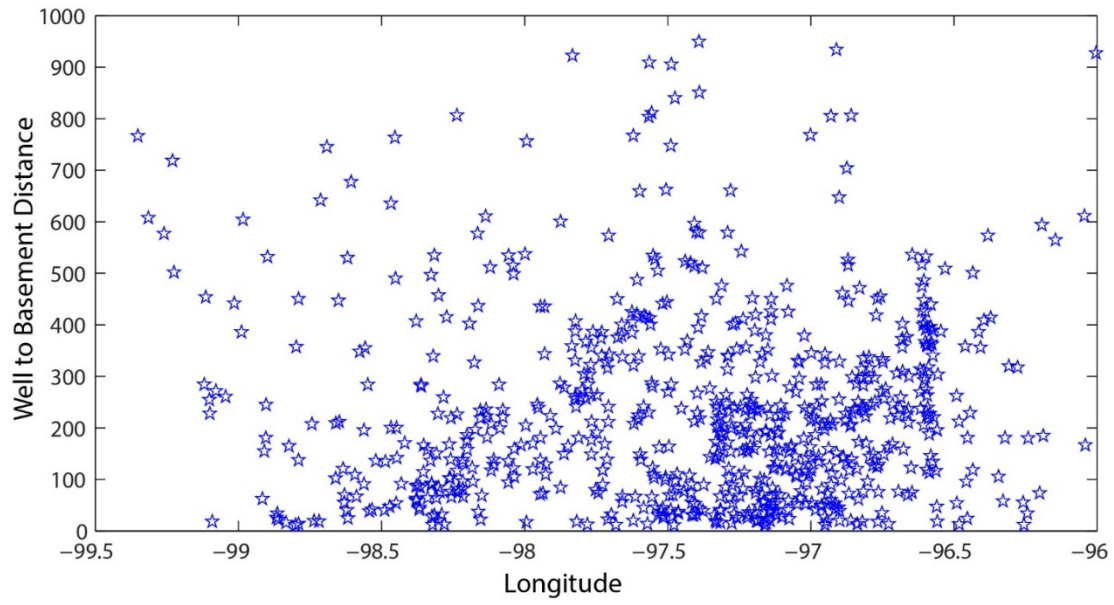


**Figure D.7.** Well bottom to basement relative distance. The relative distance between the well injection depth to the fitted basement interface. The x-axis shows longitude of the injection well.

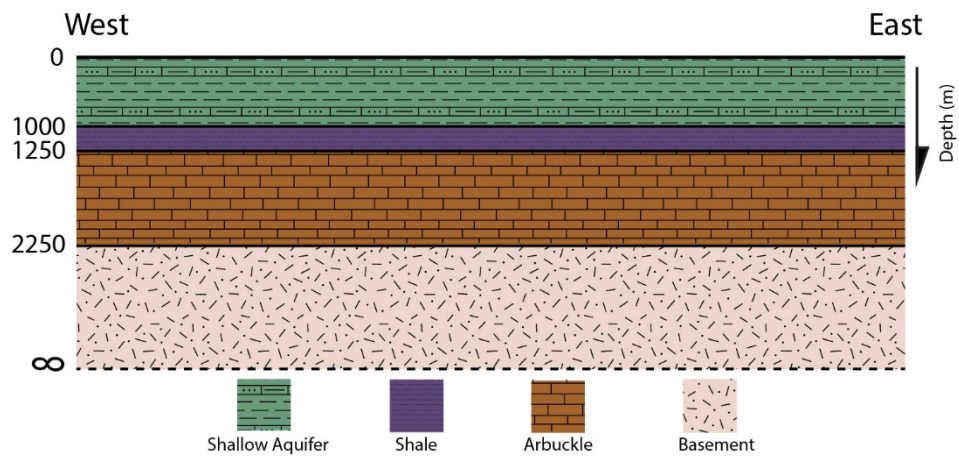


**Figure D.8.** Profile of layered model. Four-layer hydrogeological model characterized by shallow aquifer, impermeable shale, high-permeability carbonate Arbuckle group, and granite basement.

Layer	Depth (m)	G (GPa)	$\nu$	$\nu_u$	B	D (m <sup>2</sup> /s)
Shallow Aquifer	0-1000	10	0.25	0.45	0.8	0.1
Shale	1000-1250	10	0.25	0.45	0.9	1e-3
Arbuckle	1250-2250	20	0.25	0.45	0.75	1.5 (co) 4.0 (wo)
Basement	>2250	30	0.25	0.45	0.75	1e-4

**Figure D.9.** Mechanical parameters of the layered hydrogeological model. Each layer is characterized by the shear modulus, drained Poisson ratio, undrained Poisson, Skempton coefficient, and hydraulic diffusivity.

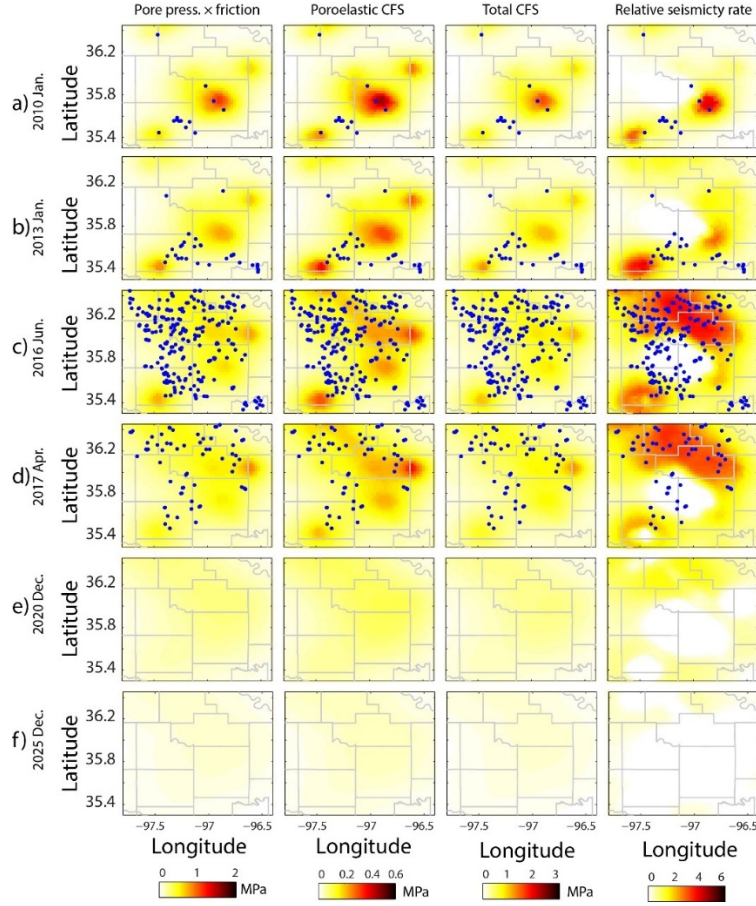


**Figure D.10.** Snapshots of poroelastic modeling result and seismicity rate in CO. Snapshots are at three epochs-2010 January (a), 2013 January (b), and 2016 June (c)-before injection shut-in, one epoch-2017 April (d)-at injection shut-in, and two epochs-2010 December (e) and 2025 December (f) after injection shut-in. Four columns are pore pressure scaled with friction coefficient (first column), CFS due to poroelastic stresses (second column), total CFS (third column), and relative seismicity rate (fourth column), respectively. Blue dots are the locations of incremental occurrence of M3+ earthquakes. Hydraulic diffusivity of  $1.5 \text{ m}^2/\text{s}$  is used for poroelastic model output in CO. CFS is calculated using northeast trending optimal fault geometry with a frictional coefficient of 0.6. Relative seismicity rate is simulated assuming a background stressing rate of  $10^{-5} \text{ MPa/year}$  based on geodetic studies [Calais *et al.*, 2006].



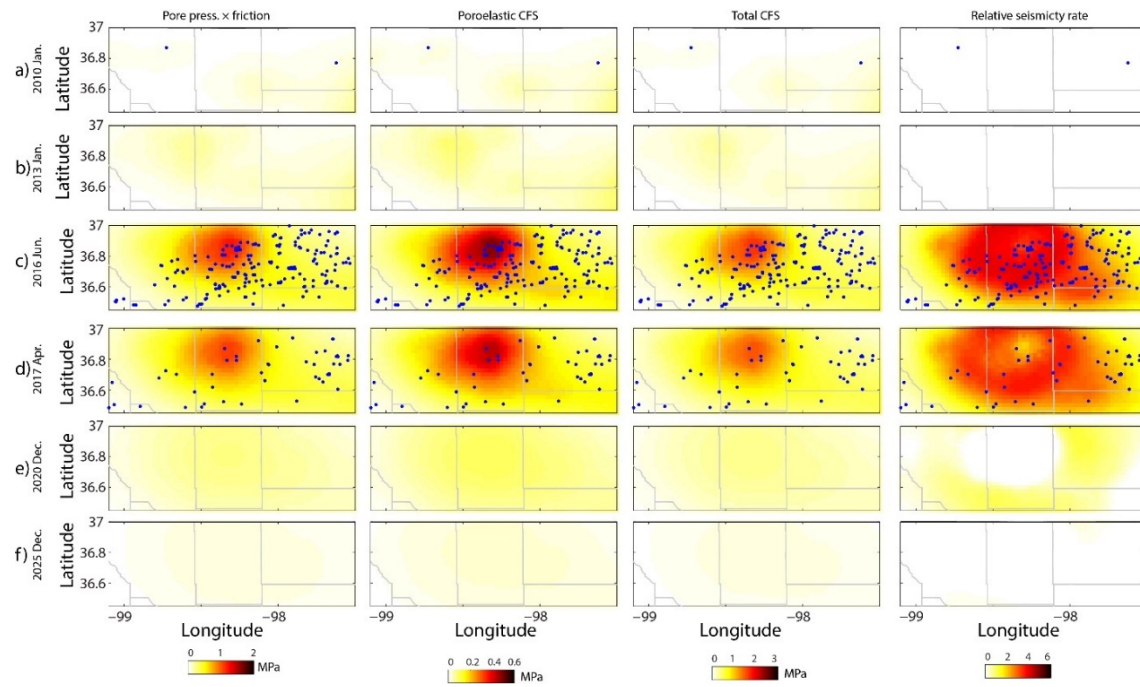


**Figure D.11.** Snapshots of poroelastic modeling result and seismicity rate in WO. Same figure as Figure D.10 but for WO. Hydraulic diffusivity of  $4.0 \text{ m}^2/\text{s}$  is used for poroelastic model output in WO.



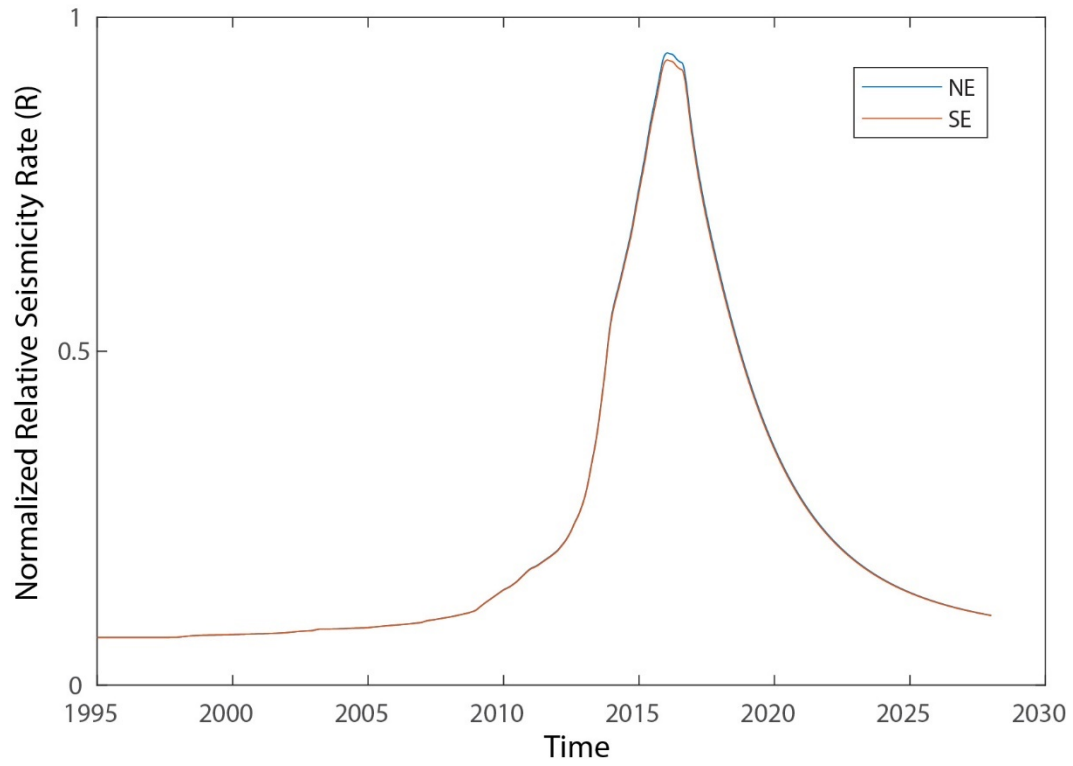


**Figure D.12.** Comparison of relative seismicity rate using different fault geometry. Normalized seismicity rate in the Pawnee region using northeast and southeast trending fault geometries.

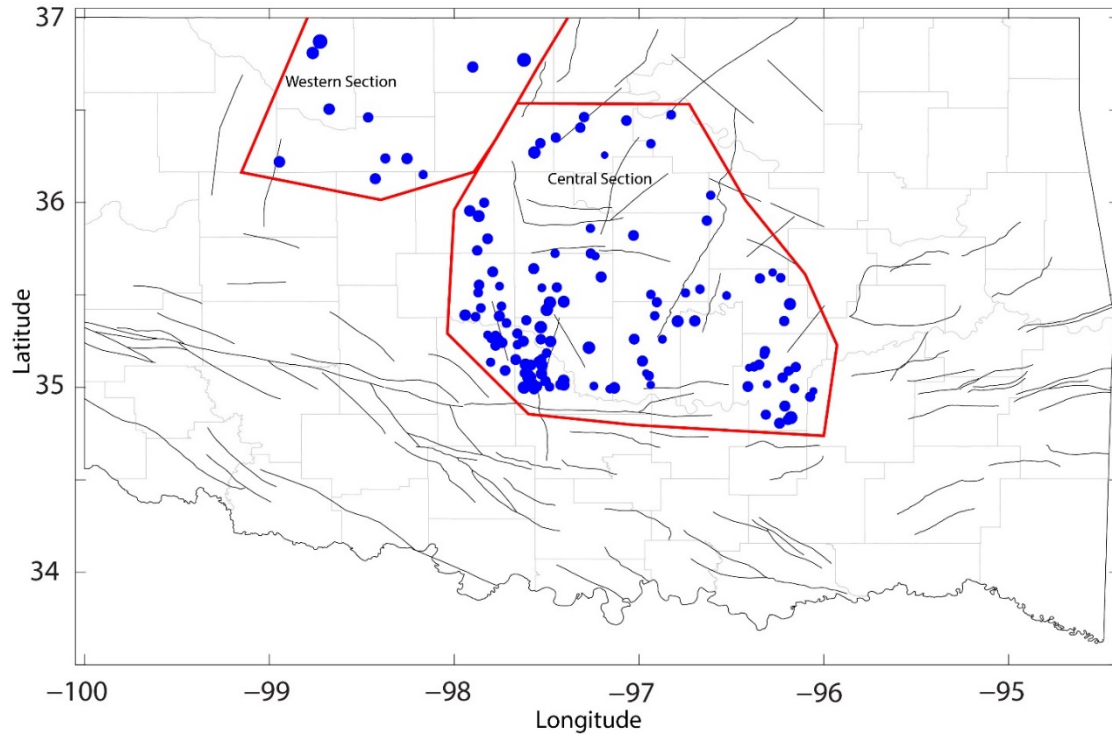


**Figure D.13.** Background seismicity prior to 2008. Two regions are defined to calculate the background a-value scaled with area and b-value of Gutenberg-Richter law in CO and WO. Blue dots are the background seismicity.

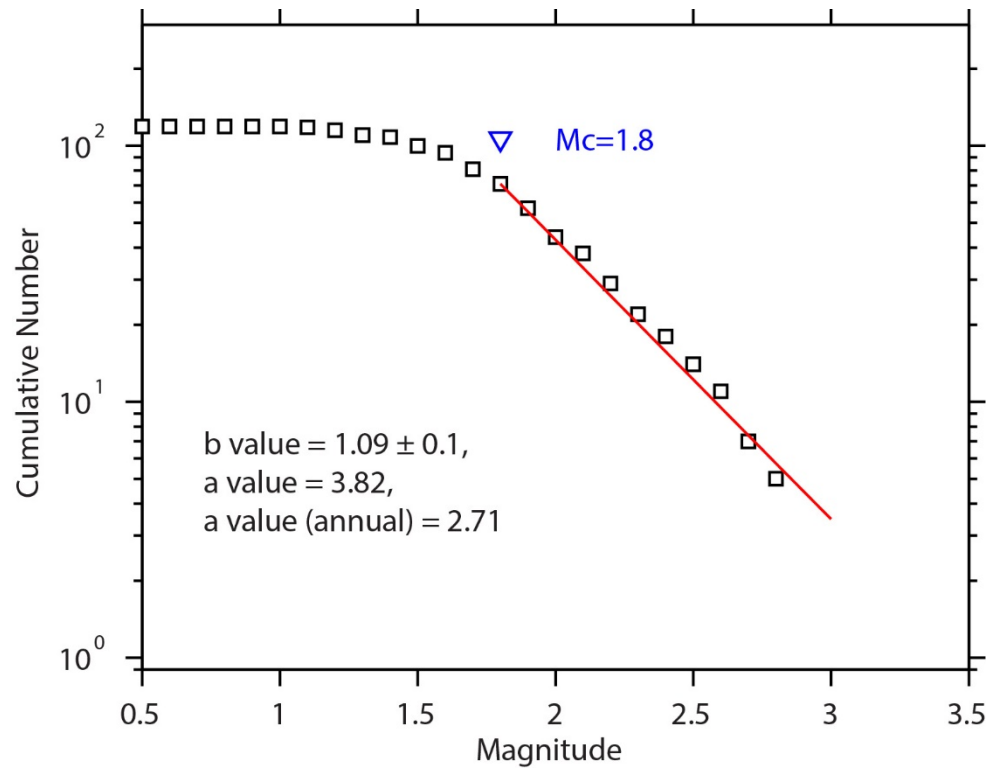


**Figure D.14.** Gutenberg-Richter law for CO. Background seismicity prior to 2008 in CO is used to implement the linear fitting.

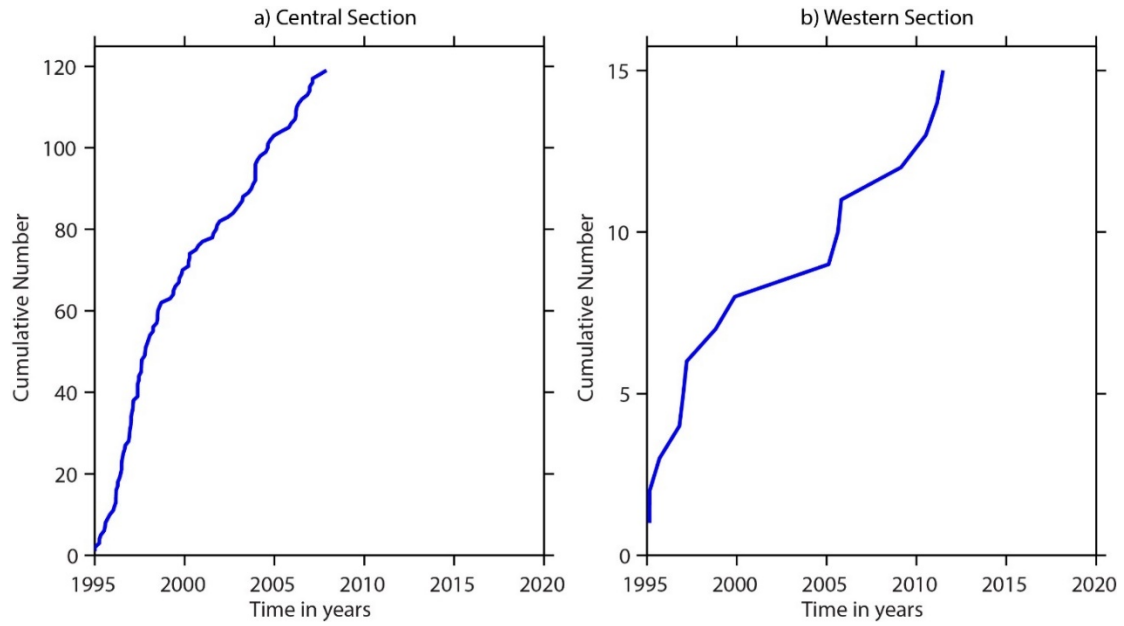


**Figure D.15.** Cumulative background earthquake number. (a) Cumulative earthquake number before 2008 (critical time of CO) corresponding to the central polygon in Figure D.13. (b) Cumulative earthquake number before 2013 (critical time of WO) corresponding to the western polygon in Figure D.13.

## APPENDIX E

### APPENDIX REFERENCES

- Bjerhammar, A. (1973), *Theory of errors and generalized matrix inverse*, 127-128 pp., Elsevier publishing company, Amsterdam.
- Calais, E., J. Y. Han, C. DeMets, and J. M. Nocquet (2006), Deformation of the North American plate interior from a decade of continuous GPS measurements, *Journal of Geophysical Research-Solid Earth*, 111(B6), doi:10.1029/2005jb004253.
- Eshelby, J. D. (1957), The determination of the elastic field of an ellipsoidal inclusion, and related problems, *Proc. R. Soc. London*, 241, 376-396.
- Ewing, T. E. (1990), *Tectonic map of Texas*, Bureau of Economic Geology, University of Texas at Austin.
- Fan, Z., P. Eichhubl, and J. F. Gale (2016), Geomechanical analysis of fluid injection and seismic fault slip for the Mw 4.8 Timpson, Texas, earthquake sequence, *Journal of Geophysical Research: Solid Earth*, 121(4), 2798-2812.
- Frohlich, C. (2012), Two-year survey comparing earthquake activity and injection-well locations in the Barnett Shale, Texas, *Proceedings of the National Academy of Sciences*, 109(35), 13934-13938.
- Hornbach, M. J., H. R. DeShon, W. L. Ellsworth, B. W. Stump, C. Hayward, C. Frohlich, H. R. Oldham, J. E. Olson, M. B. Magnani, and C. Brokaw (2015), Causal factors for seismicity near Azle, Texas, *Nature communications*, 6.
- Hornbach, M. J., M. Jones, M. Scales, H. R. DeShon, M. B. Magnani, C. Frohlich, B. Stump, C. Hayward, and M. Layton (2016), Ellenburger wastewater injection and seismicity in North Texas, *Physics of the Earth and Planetary Interiors*, 261, 54-68, doi:10.1016/j.pepi.2016.06.012.
- Langenbruch, C., and M. D. Zoback (2016), How will induced seismicity in Oklahoma respond to decreased saltwater injection rates?, *Science Advances*, 2(11), doi:10.1126/sciadv.1601542.
- Lu, Z., T. Masterlark, J. Power, D. Dzurisin, and C. Wicks (2002), Subsidence at Kiska volcano, western Aleutians, detected by satellite radar interferometry, *Geophysical Research Letters*, 29(18).
- Marshall, J., and J. Bethel (1996), Basic concepts of L1 norm minimization for surveying applications, *Journal of surveying engineering*, 122(4), 168-179.
- Meyer, P. L. (1970), *Introductory Probability and Statistical Applications*, second edition ed., 367 pp., oxford & IBH
- Montgomery, S. L., D. M. Jarvie, K. A. Bowker, and R. M. Pollastro (2005), Mississippian Barnett Shale, Fort Worth basin, north-central Texas: Gas-shale play with multi-trillion cubic foot potential, *Aapg Bulletin*, 89(2), 155-175, doi:10.1306/091704040402.
- Müller, G. (2001), Volume change of seismic sources from moment tensors, *Bull. Seism. Soc. Am.*, 91(4), 880-884.
- Okada, Y. (1985), Surface deformation due to shear and tensile faults in a half-space, *Bull. Seism. Soc. Am.*, 75, 1135-1154.

- Pollastro, R. M., D. M. Jarvie, R. J. Hill, and C. W. Adams (2007), Geologic framework of the Mississippian Barnett Shale, Barnett-Paleozoic total petroleum system, bend arch-Fort Worth Basin, Texas, *Aapg Bulletin*, 91(4), 405-436, doi:10.1306/10300606008.
- Segall, P. (2010), *Earthquake and volcano deformation*, 432 pp., Princeton University Press, Princeton, New Jersey.
- Segall, P., P. Cervelli, S. Owen, M. Lisowski, and A. Miklius (2001), Constraints on dike propagation from continuous GPS measurements, *J. Geophys. Res.*, 106, 19,301-319,318.
- Shirzaei, M., W. L. Ellsworth, K. F. Tiampo, P. J. González, and M. Manga (2016), Surface uplift and time-dependent seismic hazard due to fluid injection in eastern Texas, *Science*, 353(6306), 1416-1419.
- Shirzaei, M., and T. R. Walter (2009), Randomly iterated search and statistical competency as powerful inversion tools for deformation source modeling: Application to volcano interferometric synthetic aperture radar data, *Journal of Geophysical Research-Solid Earth*, 114, doi:Doi 10.1029/2008jb006071.
- Shirzaei, M., T. R. Walter, and R. Bürgmann (2013), Coupling of Hawaiian volcanoes only during overpressure condition, *Geophysical Research Letters*, doi:10.1002/grl.50470.
- Tikhonov, A. N., and V. Y. Arsenin (1977), *Solutions of Ill-Posed Problems*, V. H. Winston & Sons, Washington D.C.
- Wang, R. J., and H. J. Kämpel (2003), Poroelasticity: Efficient modeling of strongly coupled, slow deformation processes in a multilayered half-space, *Geophysics*, 68(2), 705-717, doi:10.1190/1.1567241.
- Wielandt, E. (2003), On the relationship between seismic moment and source volume, *Inst. of Geophys., Stuttgart Univ., Germany*. [Available at <http://www.geophys.uni-stuttgart.de/~erhard/skripte/ew/isomoment/>, accessed on May 30 2003.].
- Zhao, H., N. B. Givens, and B. Curtis (2007), Thermal maturity of the Barnett Shale determined from well-log analysis, *AAPG bulletin*, 91(4), 535-549.